sPHENIX Conceptual Design Report

CD-1 Review Release
May 11, 2018

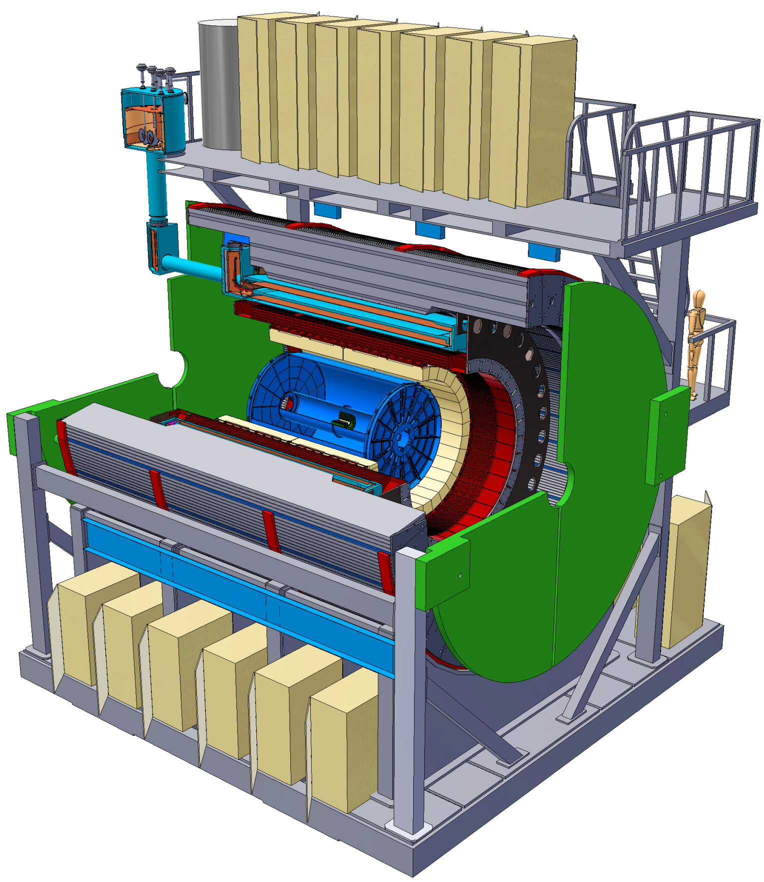

Executive Summary

sPHENIX[1] is a proposal for a major upgrade to the PHENIX experiment at RHIC capable of measuring jets, jet correlations and upsilons to determine the temperature dependence of transport coefficients of the quark-gluon plasma. The detector needed to make these measurements require electromagnetic and hadronic calorimetry for measurements of jets, a high resolution and low mass tracking system for reconstruction of the Upsilon states, and a high speed data acquisition system.

This document describes a design for a detector capable of carrying out this program of measurements built around the BaBar solenoid. As much as possible, the mechanical, electrical, and electronic infrastructure developed for the PHENIX experiment from 1992-2016 is reused for sPHENIX. The major new systems are the superconducting magnet, a high precision tracking system, and electromagnetic and hadronic calorimeters.

The central tracking system consists of a small Time Projection Chamber with up to four layers of silicon strip detector within the inner radius. The feasibility of the detector and electronics is being evaluated through simulation, design, and prototyping.

The electromagnetic calorimeter is a compact tungsten-scintillating fiber design located inside the solenoid. The outer hadronic calorimeter consists of of steel and scintillator in a somewhat novel arrangement in which scintillator tiles with light collected by wavelength shifting fiber are sandwiched between tapered absorber plates that project nearly radially from the interaction point. The calorimeters use a common set of silicon photomultiplier photodetectors and amplifier and digitizer electronics.

The detector is being designed with an eye on upgrades and enhancements which can extend the physics reach of the detector. The presently expected DOE funding is only sufficient for approximately 75% of the electromagnetic calorimeter, although outside contributions appear likely to restore the full scope. The design of a precision silicon vertex detector which enables a large menu of physics, has been developed by a consortium of institutions, and the design of an additional longitudinal layer of hadronic calorimetry has been developed so that it could be instrumented if additional funding becomes available.

The detector design has been evaluated by means of GEANT4 simulation and measurements with a continuing program of bench and beam tests prototypes of the detectors. Simulation, prototyping, and testing of components is continuing to finalize the baseline design.

Contents

 CONTENTS

Chapter 1

Scientific Objective and Performance

Results from RHIC and the LHC indicate that a new state of matter is formed in ultra-relativistic collisions of heavy nuclei. Initial temperatures $T > 300$ MeV [2] at RHIC and $T > 420$ MeV [3] at the LHC have been extracted from the spectrum of directly-emitted photons from the system. The formation of this state, called the quark-gluon plasma (QGP), was predicted by Lattice QCD and various models and to have existed at similar temperatures prior to the formation of hadrons just microseconds after the Big Bang.

The temperature scales at RHIC and LHC result in an intrinsically non-perturbative system. The difference in the initial temperature created in RHIC and LHC collisions is expected to be associated with changes in the nature of the QGP being probed. Such changes in the properties of the system must be determined in order to properly characterize the new QGP state of matter. Furthermore, to understand the many-body collective effects in the QGP and their temperature dependence near the transition temperature requires considerable further investigation.

The scientific objective of the sPHENIX experiment [1] is to gain an understanding of the evolution of the system and its coupling strength at RHIC from the initial high temperatures, where short distance scales prevail, through expansion and cooling to the transition temperature and longer distance scales. This will be accomplished by using hard-scattered partons that traverse the medium and the Upsilon states to investigate the medium at the different length scales. The fragmentation products of partons in the form of jets and the three Upsilon states, which span a large range in binding energy and size, are complementary and excellent probes for this purpose. The variables in this investigation are the temperature of the QGP, the length scale probed in the medium, and the virtuality of the hard process.

The QGP is expected to transform from a weakly-coupled system at high temperature to a more strongly-coupled system near T_c. In general, for many systems a change in coupling strength is related to quasi-particle excitations or strong coherent fields. To study these phenomena usually requires that the medium be investigated at a variety of length scales. The collisions at RHIC and the LHC involve a time evolution during which the temperature decreases as the QGP expands. Determination of the temperature dependence of the properties of the QGP is expected to come from calculations that describe simultaneously all observables measured at both energies. Typically, all the non-scaling behavior is found near the transition. It is therefore crucial to perform measurements near the phase transition and compare with results from experiments done farther above T_c.

These measurements at RHIC will provide information complementary to those at the LHC. The measurement of jets over the broadest possible energy scale is key to investigating the potential quasi-particle nature of the QGP. Jets at the LHC reach the highest energies, the largest initial virtualities, and large total energy loss to probe the shortest distance scales. The lower underlying event activity at RHIC will allow extension of jet measurements to lower energies and lower initial virtualities than at LHC, thus probing the important longer distance scales in the medium. Figure 1.1 (left), which will be discussed in more detail in Section 1.4, displays as a function of temperature the expected evolution of virtuality in vacuum, from medium contributions, and combined for a QGP. Figure 1.1 (right) shows a scenario for what may be resolved in the QGP by probing at the length scales indicated by the magnifying glasses on the left. In addition to the investigation of jets, precision measurements of the three Upsilon states will allow further insight and understanding of the behavior on different distance scales.

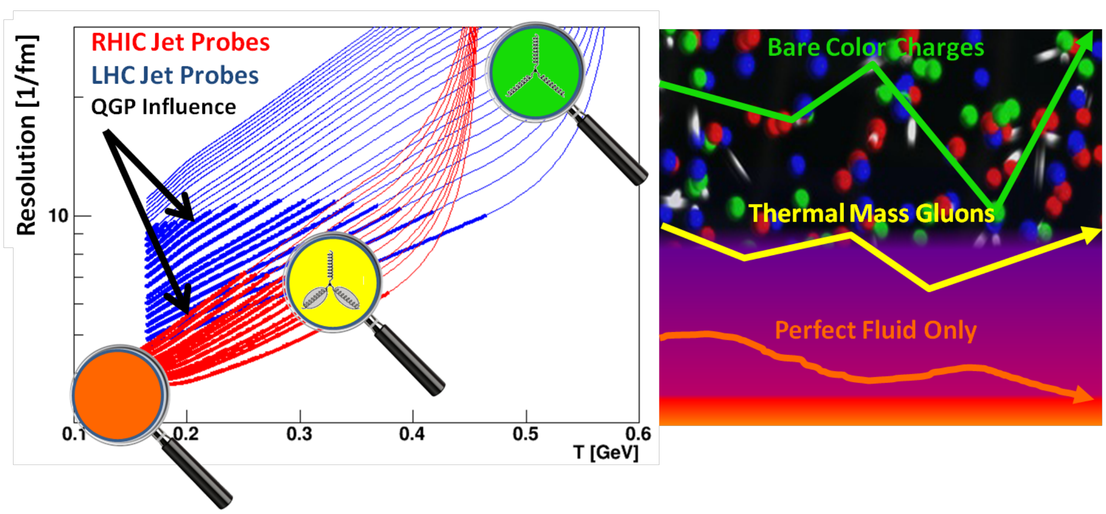

Figure 1.1: Virtuality evolution as a function of temperature as represented (left) by the resolution of jet probes at the LHC (blue curves) and at RHIC (red curves). The potential range of influence of the QGP that is being investigated is represented by the bolder curves for each case. The magnified views are meant to represent pQCD scattering from bare quarks and gluons in the medium (green), scattering from thermal gluons (yellow), and a final state integration over all possible objects probed in the medium (orange). (right) Graphical depiction of the objects being probed at the various resolutions on the left.

In this Chapter we start by presenting our current understanding of the role of the coupling strength in the QGP, how it can be probed at different length scales, the temperature dependence of a few observables of the QGP and the evolution of parton virtuality in the QGP. We then present the case for utilizing hard-scattering (parton) probes to constrain theories and compare a few examples of theoretical calculations with recent LHC data and their differing predictions for RHIC. We relate these aspects to specific observables that can be measured with sPHENIX. These include fragmentation functions from photon-jet correlations, hadron-jet and di-jet measurements, open heavy flavor jets and beauty quarkonia. We conclude with the rates and other performance measures of sPHENIX that will enable precision measurements to be made across a comprehensive jet and quarkonium program at RHIC.

1.1 Towards Understanding the Coupling Strength of the QGP

It was originally thought that even at temperatures as low as 2–5 T_c, the QGP could be described by a weakly-coupled perturbative approach, despite being quite far from energy scales typically associated with asymptotic freedom. One very surprising result discovered at RHIC was the fluid-like flow of the QGP [4], in stark contrast to some expectations that the QGP would behave as a weakly-coupled gas of quarks and gluons. RHIC and LHC heavy ion experiments have since provided a wealth of data for understanding the physics of the QGP.

The QGP created in heavy ion collisions expands and cools, eventually passing through the phase transition to a state of hadrons, which are then measured by experiment. Extensive measurements of the radial and flow coefficients of various hadrons, when compared to hydrodynamics calculations, imply a very small ratio of shear viscosity to entropy density, η/s [5]. In the limit of very weak coupling (i.e., a non-interacting gas), the shear viscosity is quite large as particles can easily diffuse across a velocity gradient in the medium. Stronger inter-particle interactions inhibit diffusion to the limit where the strongest interactions result in a very short mean free path and thus almost no momentum transfer across a velocity gradient, resulting in almost no shear viscosity.

The shortest possible mean free path is of order the de Broglie wavelength, which sets a lower limit on η/s [6]. A more rigorous derivation of the limit $\eta/s \geq 1/4\pi$ has been calculated within string theory for a broad class of strongly coupled gauge theories by Kovtun, Son, and Starinets (KSS) [7]. Viscous hydrodynamic calculations assuming η/s to be temperature independent through the heavy ion collision time evolution are consistent with the experimental data where η/s is within 50% of this lower bound for strongly coupled matter [5, 8, 9, 10, 11, 12]. Even heavy quarks (i.e., charm and beauty) are swept up in the fluid flow and theoretical extractions of the implied η/s are equally small [13].

Other key measures of the coupling strength to the medium can be found in the passage of a hard-scattered parton through the QGP. As the parton traverses the medium it accumulates transverse momentum as characterized by $\hat{q} = d(\Delta p_T^2)/dt$ and transfers energy to the medium via collisions as characterized by $\hat{e} = dE/dt$. Once in vacuum, the hard-scattered parton creates a conical shower of particles referred to as a jet. In the QGP, the lower energy portion of the shower may eventually be equilibrated into the medium, thus giving a window on the rapid thermalization process in heavy ion collisions. This highlights part of the reason for needing to measure the fully reconstructed jet energy and the correlated particle emission with respect to the jet at all energy scales. In particular, coupling parameters such as $\hat{q}$ and $\hat{e}$ are scale dependent and must take on weak-coupling values at high enough energies and strong-coupling values at thermal energies.

Continued developments in techniques for jet reconstruction in the environment of a heavy ion collision have allowed the LHC experiments to reliably recover jets down to 40 GeV [14, 15], which is well within the range of reconstructed jet energies at RHIC in the future. This overlap opens the possibility of studying the QGP at the same scale but under different conditions of temperature and coupling strength.

Apart from the temperature and coupling strength differences in the medium created at RHIC and the LHC, the difference in the steepness of the hard scattering p_T spectrum plays an important role. The less steeply falling spectrum at the LHC has the benefit of giving the larger reach in p_T with reconstructed jets expected up to 1 TeV. At RHIC, the advantage of the more steeply falling spectrum is the greater sensitivity to the medium coupling and QGP modifications of the parton shower. This greater sensitivity may enable true tomography in particular with engineering selections for quarks and/or gluons with longer path length through the medium. In addition, for correlations, once a clean direct photon or jet tag is made, the underlying event is 2.5 times smaller at RHIC compared to the LHC thus giving cleaner access to the low energy remnants of the parton shower and possible medium response. Therefore one focus of this proposal is the measurement of jet probes of the medium as a way of understanding the coupling of the medium, the origin of this coupling, and the mechanism of rapid equilibration.

1.2 Probing Different Length Scales in the QGP

In electron scattering, the length scale is set by the virtuality of the exchanged photon, Q^2. By varying this virtuality one can obtain information over an enormous range of scales: from pictures of viruses at length scales of 10^{-5} meters, to the partonic make-up of the proton in deep inelastic electron scattering at length scales of less than 10^{-18} meters.

For the case of hard-scattered partons in the quark-gluon plasma, the length scale probed is initially set by the virtuality of the hard-scattering process. Thus, at the highest LHC jet energies, the parton initially probes a very short length scale. Then as the evolution proceeds, the length scale is set by the virtuality of the gluon exchanged with the color charges in the medium, as shown in the circular diagram on the right of Figure 1.2. However, if the exchanges are coherent, the total coherent energy loss through the medium may set the length scale.

If the length scale being probed is very small then one expects scattering directly from

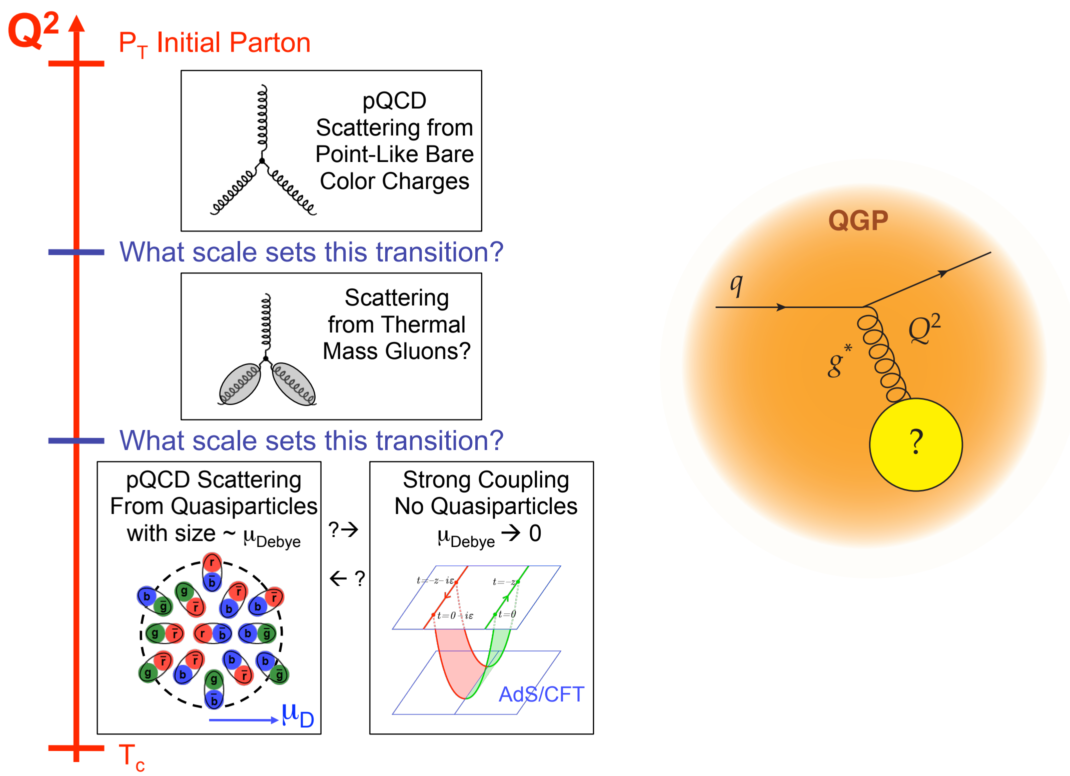

Figure 1.2: Interaction scale for the interaction of partons with the QGP and possibilities for the recoil objects. (left) Diagram of the net interaction of a parton with the medium and the range of possibilities for the recoil objects as a function of Q^2. (right) Diagram for a quark exchanging a virtual gluon with an unknown object in the QGP. This highlights the uncertainty for what sets the scale of the interaction and what objects or quasiparticles are recoiling.

point-like bare color charges, most likely without any influence from quasiparticles or deconfinement. This can be seen in Figure 1.2 (left). As one probes longer length scales, the scattering may be from thermal mass gluons and eventually from possible quasiparticles with size of order the Debye screening length (lower in Figure 1.2). In Ref. [16], Rajagopal states that "at some length scale, a quasiparticulate picture of the QGP must be valid, even though on its natural length scale it is a strongly-coupled fluid. It will be a challenge to see and understand how the liquid QGP emerges from short-distance quark and gluon quasiparticles." This is the challenge to be met by sPHENIX.

The extension of jet measurements over a wide range of energies and with different medium temperatures again gives one the largest span along this axis. What the parton is scattering from in the medium is tied directly to the balance between radiative energy loss and inelastic collisional energy loss in the medium (encoded in $\hat{q}$ and $\hat{e}$). In the limit that the scattering centers in the medium are infinitely massive, one only has radiative energy loss—as was assumed for nearly 10 years to be the dominant parton energy loss effect. In the model of Liao and Shuryak [17], the strong coupling near the quark-gluon plasma transition is due to the excitation of color magnetic monopoles, and this should have a significant influence on the collisional energy loss and equilibration of soft partons into the medium.

In a model by Coleman-Smith [18, 19] consisting of parton showers propagating in a medium of deconfined quarks and gluons, one can directly vary the mass of the effective scattering centers and extract the resulting values for $\hat{e}$ and $\hat{q}$. Figure 1.3 shows $T\hat{e}/\hat{q}$ as a function of the mass of the effective scattering centers in the medium in this model. In the limit of infinitely massive scattering centers, the interactions are elastic and no energy is transferred to the medium.

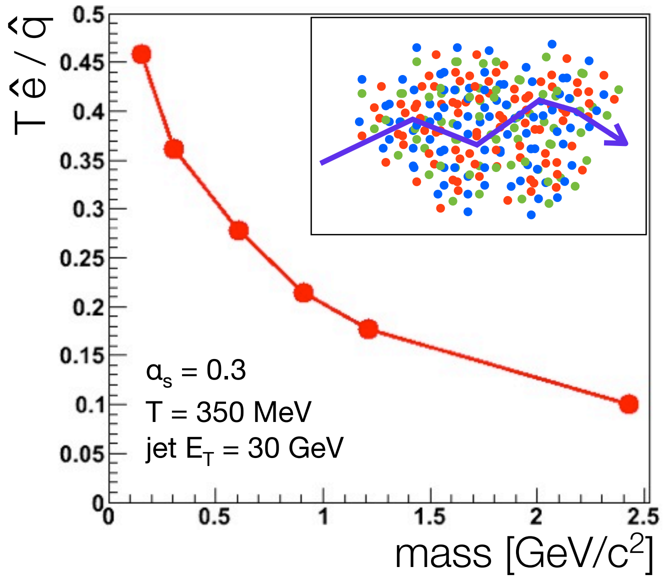

Figure 1.3: $T\hat{e}/\hat{q}$ as a function of the mass of the effective scattering centers in the medium. As the mass increases, the parton is less able to transfer energy to the medium and the ratio drops.

1.3 The Temperature Dependence of the QGP

1.3.1 Shear viscosity to entropy density ratio

It is well known that near a phase boundary familiar substances governed by quantum electrodynamics demonstrate interesting behavior such as the rapid change in the shear viscosity to entropy density ratio, η/s, near the critical temperature, T_c. This is shown in Figure 1.4 (left) for water, nitrogen, and helium [20]. Despite the eventual transition to superfluidity at temperatures below T_c, η/s for these materials remains an order of magnitude above the conjectured quantum bound of Kovtun, Son, and Starinets (KSS) derived

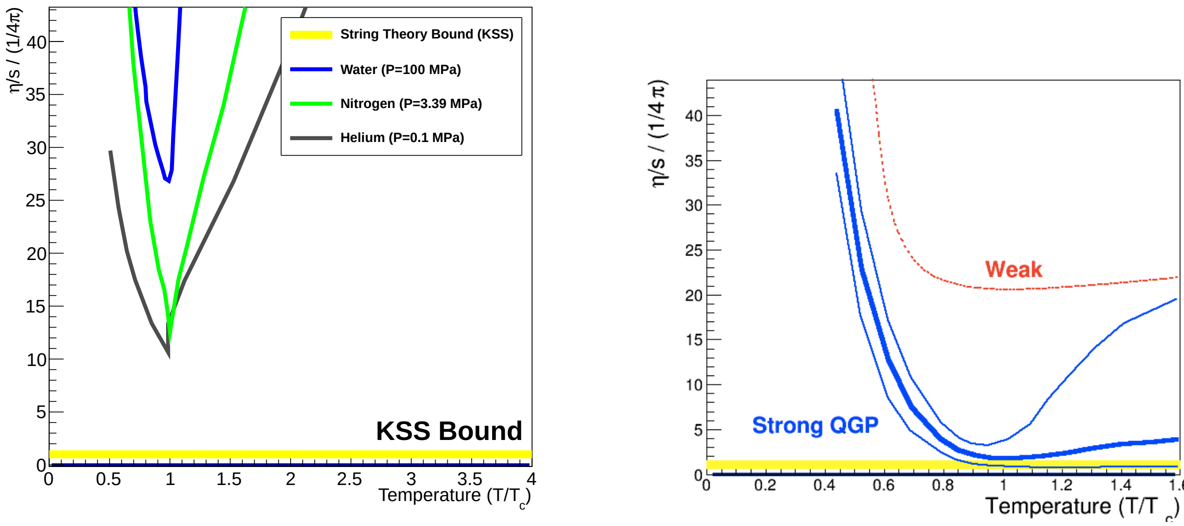

Figure 1.4: (left) The ratio of shear viscosity to entropy density, η/s, normalized by the conjectured KSS bound as a function of the reduced temperature, T/T_c, for water, nitrogen, and helium. The cusp for Helium corresponds to the case at the critical pressure. (right) Calculation for a weakly-coupled system (pQCD) and for various models of a strongly-coupled QGP.

from string theory [7]. Such observations provide a deeper understanding of the nature of these materials: for example the coupling between the fundamental constituents, the degree to which a description in terms of quasiparticles is important, and the description in terms of normal and superfluid components.

The dynamics of the QGP are dominated by Quantum Chromodynamics and the experimental characterization of the dependence of η/s on temperature will lead to a deeper understanding of strongly coupled QCD near this fundamental phase transition. Theoretically, perturbative calculations in the weakly-coupled limit indicate that η/s decreases slowly as one approaches T_c from above, but with a minimum still a factor of 20 above the KSS bound [21].

Hydrodynamic modeling of the bulk medium does provide constraints on η/s, and recent work has been done to understand the combined constraints on η/s as a function of temperature utilizing both RHIC and LHC flow data sets [22, 23, 24, 25] and result in values near the KSS bound around T_c as seen in Figure 1.4 (right).

1.3.2 Jet probe parameters

The above discussion was focused on η/s as the measure of the coupling strength of the QGP. However, both η/s and jet probe parameters such as $\hat{q}$ and $\hat{e}$ are sensitive to the underlying coupling of the matter, but in distinct ways. Establishing for example the behavior of $\hat{q}$ around the critical temperature is therefore essential to a deep understanding of the QGP. Hydrodynamic modeling may eventually constrain $\eta/s(T)$ very precisely, though it will not provide an answer to the question of the microscopic origin of the strong coupling (something naturally available with jet probes).

Since the expected scaling of $\hat{q}$ with temperature is such a strong function of temperature, jet quenching measurements should be dominated by the earliest times and highest temperatures. In order to have sensitivity to temperatures around 1–2 T_c, measurements at RHIC are needed in contrast to the LHC where larger initial temperatures are produced, as depicted graphically in Figure 1.1. In addition, the ability of RHIC to provide high luminosity heavy-ion collisions at a variety of center of mass energies can be exploited to probe the detailed temperature dependence of quenching right in the vicinity of T_c.

Theoretical developments constrained simultaneously by data from RHIC and the LHC have been important in discriminating against some models with very large $\hat{q}$, see Ref. [26] and theory references therein. Models such as PQM and ASW with very large values of $\hat{q}$ have been ruled out by the combined constraint. Shown in the left panel of Figure 1.5 is a recent compilation of four theoretical calculations with a directly comparable extraction of $\hat{q}$. It is notable that a number of calculations favor an increased coupling strength near the transition temperature. Developments on the theory and experimental fronts have significantly narrowed the range of $\hat{q}$[27]. This theoretical progress lends credence to the case that the tools will be available on the same time scale as sPHENIX data to have precision determinations of $\hat{q}$ and then ask deeper additional questions about the quark-gluon plasma and its underlying properties.

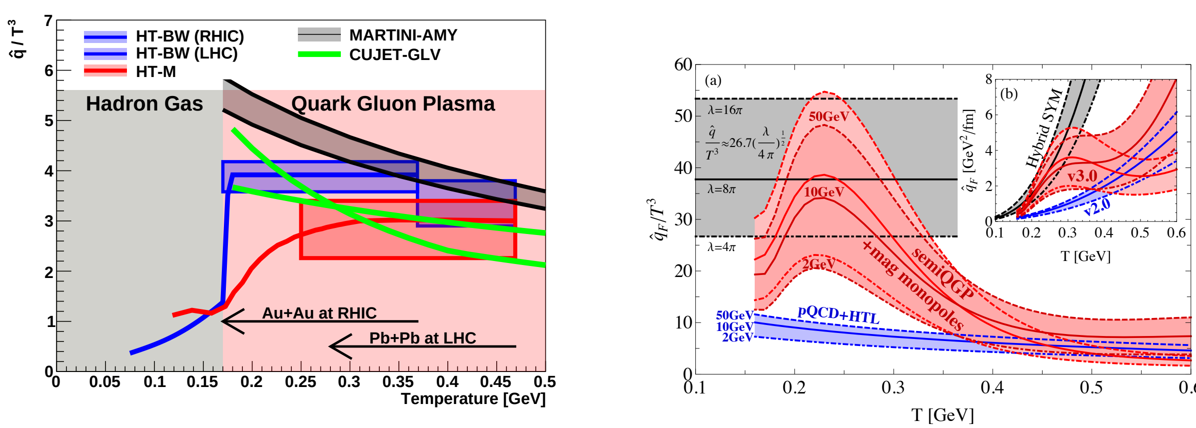

Figure 1.5: Calculations of $\hat{q}/T^3$ vs temperature, constrained by RHIC and LHC R_{AA} data — including near T_C enhancement scenarios of $\hat{q}/T^3$. (left) Calculations from four jet quenching frameworks constrained by RHIC and LHC R_{AA} data with results for $\hat{q}/T^3$ as a function of temperature. Details of the calculation are given in Ref. [27]. (right) Results from calculations within CUJET 3.0 with magnetic monopole excitations that result in enhanced coupling near T_c. Plotted are the constraints on $\hat{q}/T^3$ as a function of temperature as shown in Ref. [28]

Ref. [29] states that "Comparing weak coupling scenarios with data, NTC [near T_C enhancement] is favored. An answer to this question will require a systematic picture across several different high p_T observables." In Ref. [17], Liao and Shuryak use RHIC measurements of single hadron suppression and azimuthal anisotropy to infer that "the jet quenching is a few times stronger near T_c relative to the quark-gluon plasma at $T > T_c$."

Most recently this strong coupling picture with color magnetic monopole excitations has been implemented within CUJET 3.0 for a broader comparison with experimental observables and previous theory calculations [28]. Shown in Figure 1.5 (right panel) are results from their constrained RHIC and LHC data fit for the temperature dependence of the scaled quenching power $\hat{q}/T^3$.

Within the jet quenching model WHDG [30], the authors constrain $\hat{q}$ by the PHENIX π^0 nuclear modification factor. They find the prediction scaled by the expected increase in the color charge density created in higher energy LHC collisions when compared to the ALICE results [31] over-predicts the suppression. This over-prediction based on the assumption of an unchanging probe-medium coupling strength led to the title of Ref. [30]: "The surprisingly transparent sQGP at the LHC." They state that "one possibility is the sQGP produced at the LHC is in fact more transparent than predicted." Similar conclusions have been reached by other authors [32, 33, 34]. Recently work has been done to incorporate the running of the QCD coupling constant [35].

It is important to note that most calculations predict a stronger coupling near the transition, even if just from the running of the coupling constant α_s. The goal is to determine experimentally the degree of this effect. Lower energy data at RHIC also provides important constraints – see for example Refs. [36, 37]. The full set of experimental observables spanning the largest range of collision energy, system size, and path length through the medium is needed to determine the coupling strength as a function of temperature.

1.4 Evolution of Parton Virtuality in the QGP

The initial hard-scattered parton starts out very far off-shell and in e^+e^-, $p+p$ or $p+\overline{p}$ collisions the virtuality evolves in vacuum through gluon splitting down to the scale of hadronization. In heavy ion collisions, the vacuum virtuality evolution is interrupted at some scale by scattering with the medium partons which increase the virtuality with respect to the vacuum evolution. Figure 1.1 (left) shows the expected evolution of virtuality in vacuum, from medium contributions, and both combined (in a QGP).

If this picture is borne out, it "means that [a] very energetic parton hardly notices the medium for the first 3–4 fm of its path length [38]." Spanning the largest possible range of virtuality (initial hard process Q^2) is very important, but complementary measurements at both RHIC and LHC of produced jets at the same virtuality (around 50 GeV) will test the interplay between the vacuum shower and medium scattering contributions.

In some theoretical frameworks — for example Refs [39, 40, 41] — the parton splitting is simply dictated by the virtuality and in vacuum this evolves relatively quickly from large to small scales. The Q evolution means that the jet starts out being considerably off mass shell when produced, and this off-shellness is reduced by successive splits to less virtual partons. In these calculations, the scattering with the medium modifies this process of parton splitting. The scale of the medium as it relates to a particular parton is $\hat{q}$ times the parton lifetime (this is the mean transverse momentum that the medium may impart to the parent and daughter partons during the splitting process). When the parton's off-shellness is much larger than this scale, the effect of the medium on this splitting process is minimal. As the parton drops down to a lower scale, the medium begins to affect the parton splitting more strongly.

Shown in Figure 1.6 (left) is the single hadron R_{AA} measured in central Au+Au collisions at 200 GeV and in heavy ion collisions at other beam energies. One can see in Figure 1.6 (right) that inclusion of the virtuality evolution for the YAJEM calculation leads to a 50% rise in R_{AA} from 20–40 GeV/c, and a 100% rise in the HT-M calculation. A strong rise in R_{AA} measured at higher p_T at the LHC has been observed, and measurement of the effect within the same framework at RHIC is a key test of this virtuality evolution description. It is notable that the JEWEL calculation, which accurately describes the rising R_{AA} at the LHC [42], results in a nearly flat R_{AA} over the entire p_T range at RHIC. As detailed in Ref. [43, 44], many formalisms assuming weakly coupled parton probes are able to achieve an equally good description of the single-inclusive hadron (R_{AA}) data at RHIC and the LHC. The single high p_T hadron suppression constrains the $\hat{q}$ value within a model, but is not able to discriminate between different energy loss mechanisms and formalisms for the calculation. sPHENIX will perform precision measurements of charged hadrons over an extended p_T range, as shown in the projected uncertainties, that will strongly discriminate between the various energy loss mechanisms and model assumptions about the virtuality evolution in the medium.

1.5 Current Jet Probe Measurements

Jet quenching (i.e., the significant loss of energy for partons traversing the QGP) was discovered via measurements at RHIC of the suppression of single hadron yields compared to expectations from $p+p$ collisions [45, 46]. Since the time of that discovery there has been an enormous growth in jet quenching observables that have also pushed forward a next generation of analytic and Monte Carlo theoretical calculations to confront the data.

Two-hadron correlations measure the correlated fragmentation between hadrons from within the shower of one parton and also between the hadrons from opposing scattered partons. These measurements, often quantified in terms of a nuclear modification I_{AA} [47, 48, 49], have been a challenge for models to describe simultaneously [50].

The total energy loss of the leading parton provides information on one part of the parton-

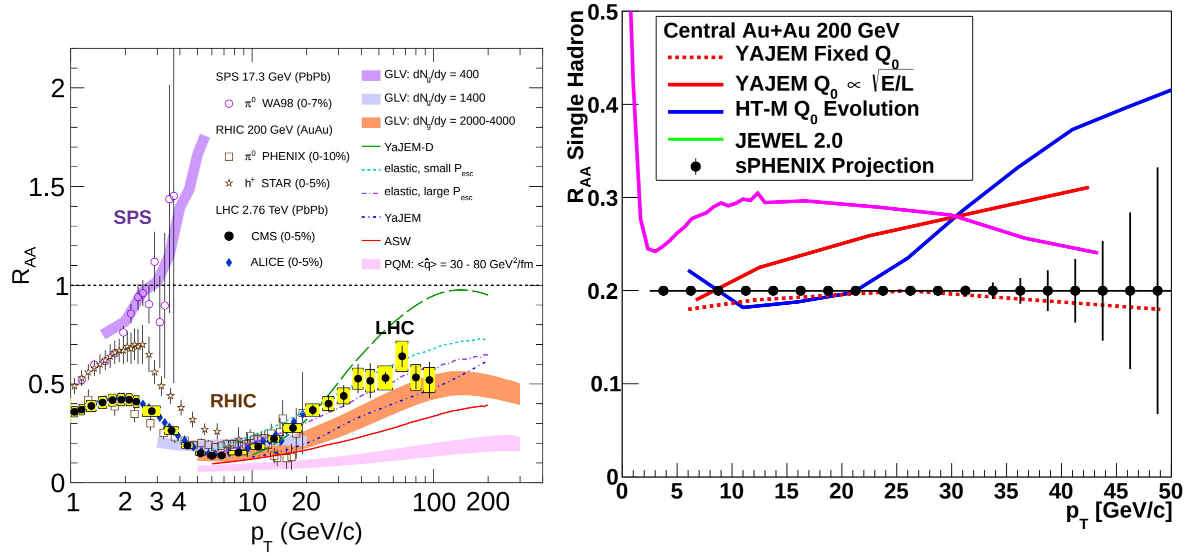

Figure 1.6: (left) The nuclear modification factor R_{AA} as a function of transverse momentum in A+A collisions at the SPS, RHIC, and LHC. Comparisons with various jet quenching calculations as detailed in Ref. [26] and references therein are shown. The simultaneous constraint of RHIC and LHC data is a powerful discriminator. (right) Predictions of R_{AA} for single hadrons to $p_T \sim 50$ GeV/c in central Au+Au at 200 GeV. Also shown are the projected sPHENIX uncertainties.

medium interaction. Key information on the nature of the particles in the medium being scattered from is contained in how the soft (lower momentum) part of the parton shower approaches equilibrium in the QGP. This information is accessible through full jet reconstruction, jet-hadron correlations, di-jets and γ-jet correlation observables.

The measurements of fully reconstructed jets and the particles correlated with the jet (both inside and outside the jet) are crucial to testing the various models and their energy loss mechanisms. Not only does the strong coupling influence the induced radiation from the hard parton (gluon bremsstrahlung) and its inelastic collisions with the medium, but it also influences the way soft partons are transported by the medium outside of the jet cone as they fall into equilibrium with the medium. Thus, the jet observables combined with correlations are a means to access directly the coupling of the hard parton to the medium and the parton-parton coupling for the medium partons themselves.

1.5.1 LHC results

The first results from the LHC based on reconstructed jets in heavy ion collisions were the centrality-dependent dijet asymmetries measured by ATLAS [51] and CMS [52] as shown on the left panels of Figures 1.7 and 1.8. The measured dijet asymmetry A_J is defined by ATLAS as $A_J = (E_1 - E_2)/(E_1 + E_2)$ and $A_J = (p_1 - p_2)/(p_1 + p_2)$ by CMS. These results indicate a substantial broadening of the dijet asymmetry A_J distribution for increasingly central Pb+Pb collisions and a lack of modification to the dijet azimuthal correlations (not shown). The broadening of the A_J distribution points to substantial energy loss for jets and the unmodified azimuthal distribution shows that the opposing jet $\Delta\phi$ distribution is not broadened as it traverses the matter.

Direct photon-jet measurements are also a powerful tool to study jet quenching. Unlike dijet measurements the photon passes through the matter without losing energy, providing a cleaner measure of the expected jet p_T [53]. CMS has results for photons with $p_T >$ 60 GeV/c correlated with jets with $p_T >$ 30 GeV/c [54]. Though with modest statistical precision, the measurements indicate energy transported outside the $R = 0.3$ jet cone through medium interactions. Similar results from the ATLAS experiment again indicate a shift of the energy outside the opposing jet cone.

Reconstructed jets have significantly extended the kinematic range for jet quenching studies at the LHC, and quenching effects are observed up to the highest reconstructed jet energies ($>$ 300 GeV) [55]. They also provide constraints on the jet modification that are not possible with particle-based measurements. For example, measurements from ATLAS constrain the modification of the jet fragmentation in Pb+Pb collisions from vacuum fragmentation to be small [56]. CMS results on jet-hadron correlations have shown that the lost energy is recovered in low p_T particles far from the jet cone [52]. The lost energy is transported to very large angles and the remaining jet fragments as it would in the vacuum.

1.5.2 RHIC results

There are preliminary results on fully reconstructed jets from both STAR [57, 58, 59, 60] and PHENIX experiments [61, 62]. However, a comprehensive jet detector, such as sPHENIX, with large, uniform acceptance and a high-rate capability can be combined with the newly completed increase in RHIC luminosity to perform these key measurements definitively to access this important physics. In addition to extending the RHIC observables to include fully reconstructed jets and γ-jet correlations, theoretical development is required for converging to a coherent 'standard model' of the medium coupling strength and the nature of the probe-medium interaction. In the next section, we present predictions for a sample of future RHIC measurements based on theory that has been calibrated through successful reproduction of recent LHC measurements.

1.6 Using Jets at RHIC to Constrain Theoretical Calculations

The theoretical community is actively working to understand the details of probe-medium interactions. Much work has been carried out by the Topical Collaboration on Jet and Electromagnetic Tomography of Extreme Phases of Matter in Heavy-ion Collisions [63]. The challenge is to understand not only the energy loss of the leading parton, but how the parton shower evolves in medium and how much of the lost energy is re-distributed in the QGP. Monte Carlo approaches have been developed (as examples [64, 65, 66, 19, 67, 68]) to overcome specific theoretical hurdles regarding analytic parton energy loss calculations and to couple these calculations with realistic models of the QGP space-time evolution. Theoretical calculations attempting to describe the current data from RHIC and LHC have yet to reconcile some of the basic features. Some models include large energy transfer to the medium as heat (for example [69]) while others utilize mostly radiative energy loss (for example [70, 71]). Measurements at RHIC energies with jets over a different kinematic range allow specific tests of the different mechanisms.

Jets provide a rich spectrum of physics observables, ranging from single-jet observables such as R_{AA}, to correlations of jets with single particles and correlations of trigger jets with other jets in the event. Triggers ranging from single hadrons to ideally reconstructed jets are used to form correlations with hadrons or another jet in the event. Different triggers demonstrate different degrees of surface bias in the production point of the "dijet", i.e. the hard-scattering vertex location, and this bias itself has been used as leverage in the investigation of the properties of the medium. Examples of different trigger biases that can be exploited have been presented in calculations by Renk [72].

In this section, we present a brief review of a subset of calculations that employ different mechanisms for jet-medium interactions. These are compared to jet observables that still need to be measured at RHIC, with an emphasis on their particular sensitivity to the underlying physics, and represent the potential constraining power of a comprehensive jet physics program by sPHENIX at RHIC.

1.6.1 Di-jet Asymmetry

Results of calculations from Coleman-Smith and collaborators [18, 19] for the dijet asymmetry A_J at the LHC are presented along with the data in Figure 1.7 (left) [18]. The parton showers are extracted from PYTHIA (with hadronization turned off) and then embedded into a deconfined QGP, modeled at constant temperature using the VNI parton cascade [73] with fixed $\alpha_s = 0.3$. One feature of the calculation is that it provides the ability to track the time evolution of each individual parton, not only the scattered partons from the shower, but also partons from the medium, which through interactions can contribute particles to the reconstructed jets. Jets in the calculation are reconstructed with the anti-k_T algorithm with radius parameter $R = 0.5$ and then smeared by a simulated jet resolution of $100\%/\sqrt{E}$, and with requirements of $E_{T1} > 120$ GeV and $E_{T2} > 50$ GeV on the leading and sub-leading jet, respectively. The calculated A_J distributions reproduce the CMS experimental data [52].

In Figure 1.7 (right panel) the calculation is repeated with a medium temperature appropriate for RHIC collisions and with RHIC observable jet energies, $E_{T1} > 20$ GeV and $R = 0.2$. The calculation is carried out for different coupling strengths α_s between partons in the medium themselves and the parton probe and medium partons. The variation in the value of α_s should be viewed as changing the effective coupling in the many-body environment of the QGP. It is interesting to note that in the parton cascade BAMPS the authors find that an effective coupling of $\alpha_s \approx 0.6$ is required to describe the bulk medium flow [74]. These results indicate sizable modification to the dijet asymmetry and thus excellent sensitivity to the effective coupling to the medium at RHIC energies.

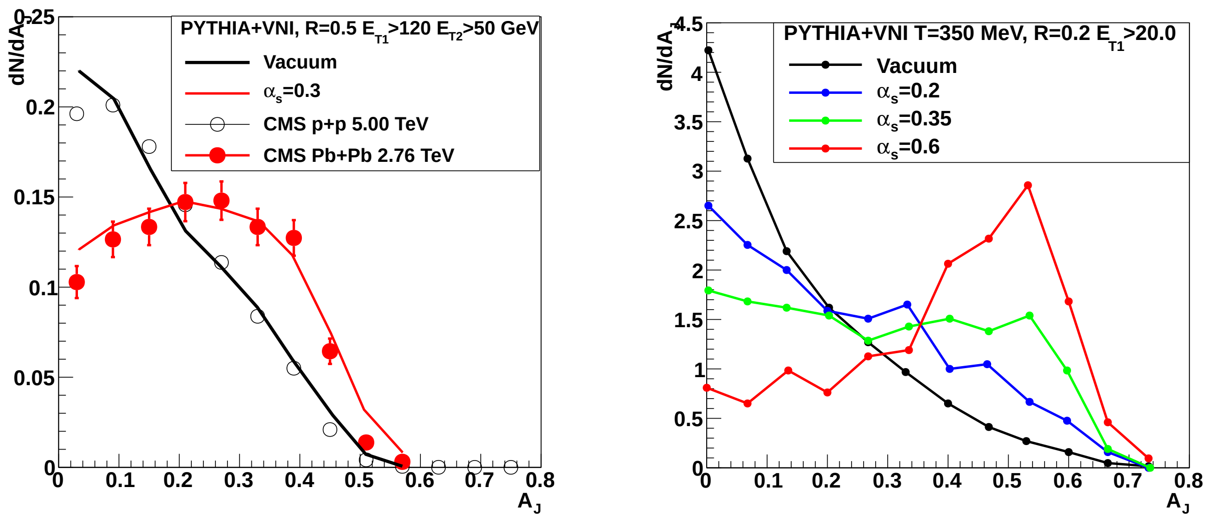

Figure 1.7: (left) Calculation in VNI parton cascade of dijet A_J with $T = 0.35$ GeV and $\alpha_s = 0.3$ compared to the CMS data [18]. (right) Calculation for RHIC jet energies, $E_{T,1} > 20$ GeV, for a circular geometry of radius 5 fm of A_J for different values of α_s increasing to $\alpha_s = 0.6$ (red line) [75].

The results of calculations for A_J from two other groups are presented in Figure 1.8. In the calculation of Qin and collaborators [76, 77] a differential equation governing the evolution of the radiated gluon distribution is solved to predict the propagation of the jet through the medium. Energy contained inside the jet cone is lost by dissipation through elastic collisions and by scattering of shower partons to larger angles. The model calculations of Young, Schenke and collaborators [66] utilize a jet shower Monte Carlo, referred to as MARTINI [78], and embed the shower on top of a hydrodynamic space-time background, using the model referred to as MUSIC [79]. Each of the above approaches reproduce the A_J data measured at LHC quite well [80, 76] as shown in Figure 1.8 (left). Figure 1.8 (right) shows the jet energy dependence of A_J predicted for RHIC energy di-jets with

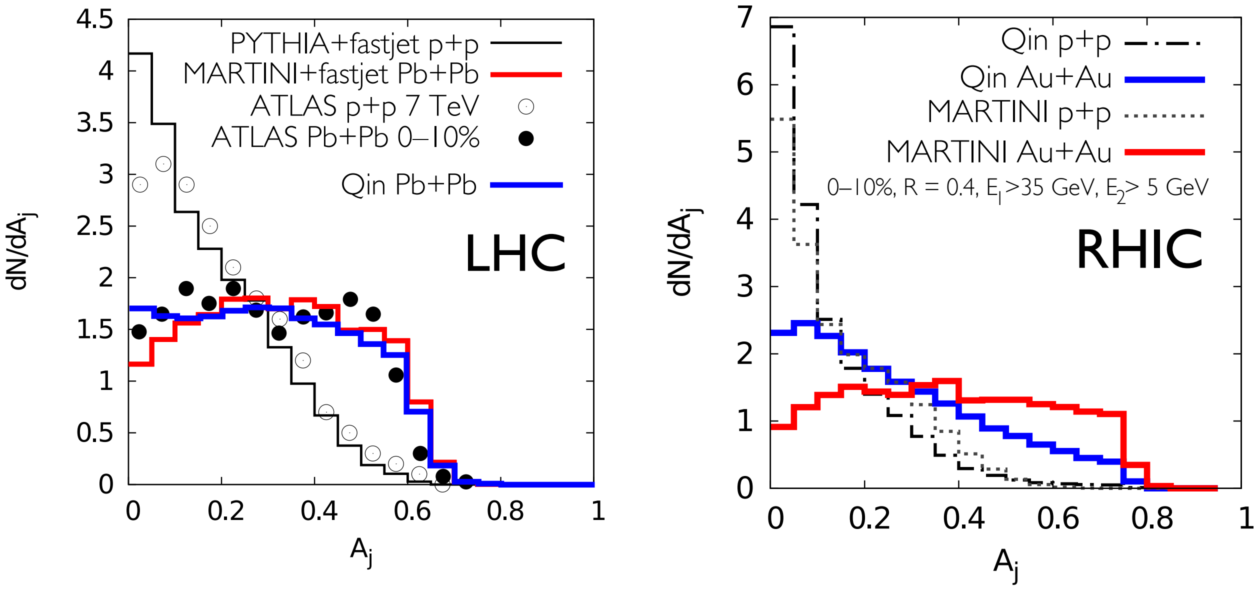

Figure 1.8: A_J distributions in MARTINI+MUSIC [81] and the model of Qin et al. [77]. (left) Comparison of A_J calculations in MARTINI+MUSIC and by Qin et al for Pb+Pb collisions at 2.76 TeV (red line, Qin et al; blue line, MARTINI+MUSIC). Both calculations show a similar broad A_J distribution. (right) Same as left panel, but for Au+Au collisions at 200 GeV (with leading jet $E_T > 35$ GeV). These results indicate a substantially different modification predicted by these models for di-jets propagating through the QGP at RHIC.

$E_{T1} > 35$ GeV with $E_{T2} > 5$ GeV by the two model calculations. A significant difference in shape is observed between the two models at RHIC energy with a peak developing at small A_J in the Qin et al. model while the MARTINI+MUSIC calculation retains a shape similar to those seen at the LHC energy.

1.6.2 Jet Shapes

Calculations from Vitev and collaborators [82, 83, 84] predict a jet radius R and energy dependence for inclusive jet R_{AA}, in contrast to the results from Qin et al. Vitev et al. utilize a Next-to-Leading-Order (NLO) calculation and consider not only final-state inelastic parton interactions in the QGP, but also parton energy loss effects from the cold nuclear matter. This can be seen in Figure 1.9, which exhibits significant radius and energy dependences. Because the high energy jets originate from hard scattering of high Bjorken x partons, a modest energy loss of these partons results in a reduction in the inclusive jet yields. At RHIC cold nuclear matter measurements will be made with p+Au running in sPHENIX at the same collision energy to determine the strength of cold nuclear matter and any other effects as a baseline to the heavy ion measurements.

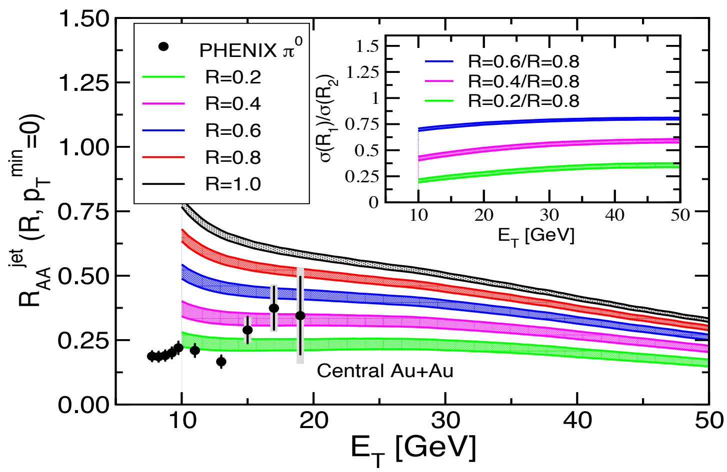

Figure 1.9: Calculations from Vitev et al. for the inclusive jet R_{AA} as a function of the jet energy and radius. Also shown for reference are PHENIX π^0 R_{AA} results. Inset presents ratios for jets of various radii relative to those measured with R = 0.8.

1.7 Fragmentation Functions

1.7.1 Direct photon-jet correlations

Ideally, one would like to understand how a quark or gluon of known energy interacts while traversing the QGP and the redistribution of energy and particles both longitudinal and transverse to the initial parton direction. The initial quark energy can be identified from binary scattering kinematics by measuring its direct photon [53] scattering "partner" on the opposite side. One can study fully reconstructed jets opposite the photon for various jet radii to investigate the redistribution in transverse energy. ATLAS has presented results on photon-jet R_{AA}. A suppression of the away-side jet is observed for two different jet-radius parameters.

Figure 1.10 presents the result of calculations of the event distribution of the ratio of the reconstructed jet energy (with $R = 0.3$) relative to the direct photon energy [85]. The authors note: "The steeper falling cross sections at RHIC energies lead not only to a narrow z_{J_γ} distribution in $p+p$ collisions but also to a larger broadening and shift in $\left\langle z_{J_\gamma} \right\rangle$ in A+A collisions." This results in a greater sensitivity to the redistribution of energy, which is again sensitive to the balance of processes including radiative and collisional energy loss. With an underlying event energy at RHIC that is a factor of 2.5 lower than that at the LHC, sPHENIX will be able to reconstruct jets over a very broad range of radii and energies opposite the direct photons. Shown in Figure 1.11 are the projected sPHENIX photon - jet correlation uncertainties measured differentially with respect to the path length through the QGP.

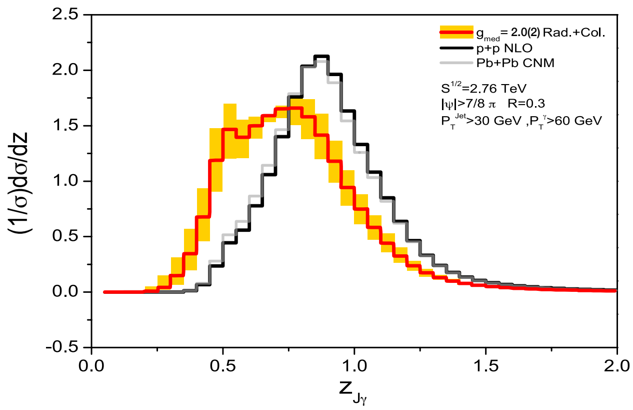

Figure 1.10: Calculations by Vitev et al. of the vacuum and medium-modified z_{J_γ} distributions for direct photon-triggered reconstructed jet events at LHC (left) and RHIC (right) energies [85].

With charged particle tracking one can also measure the longitudinal redistribution of hadrons opposite the direct photon. sPHENIX will have excellent statistical reach for such direct photon measurements.

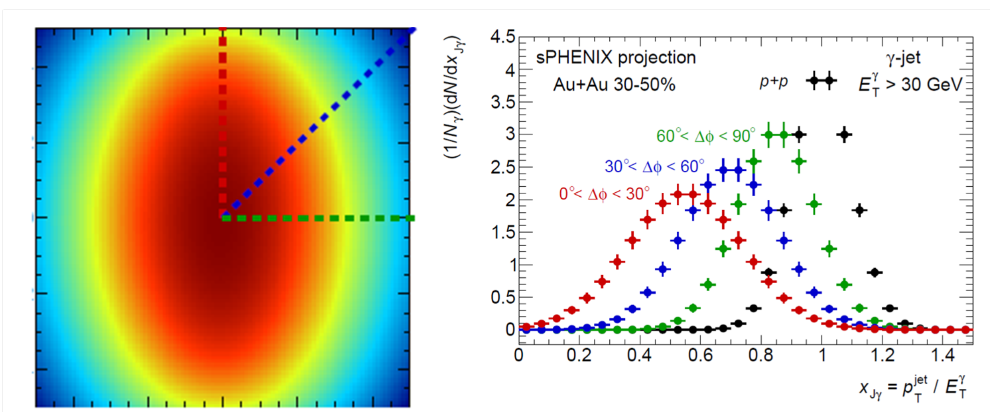

Figure 1.11: Schematic of different potential path lengths through the QGP (left) and projected sPHENIX uncertainties in the photon-jet channel for these different length scales traversed in the QGP.

At the same time, it is advantageous to measure modified fragmentation functions within inclusive reconstructed jets and via correlations as well. The original predictions of jet quenching in terms of induced forward radiation had the strongest modification in the longitudinal distribution of hadrons from the shower (i.e., a substantial softening of the fragmentation function). One may infer from the nuclear suppression of π^0 in central Au+Au collisions $R_{AA} \approx 0.2$ that the high z (large momentum fraction carried by the hadron) showers are suppressed.

1.7.2 Hadron-jet correlations

In sPHENIX, fragmentation functions via precision charged-track measurements are available from high-z, where the effects are predicted to be largest, to low-z where medium response and equilibration effects are relevant. The independent measurement of jet energy (via calorimetry) and the hadron p_T via tracking is important. This independent determination also dramatically reduces the fake-track contribution by the coincidence required with a high energy jet.

One can also access somewhat less directly this transverse and longitudinal redistribution of energy and particles via trigger high p_T hadrons and narrow reconstructed jets. Such measurements have been undertaken by STAR [86]. The large kinematic reach of sPHENIX will provide very high statistics observables that span a reach where the opposing parton is mostly a gluon near 20 GeV with increasing quark fraction for higher energy triggers. This is another complement between the kinematics at RHIC and the LHC as shown in Figure 1.12 that compares the quark-quark, quark-gluon, gluon-gluon relative contributions as a function of p_T.

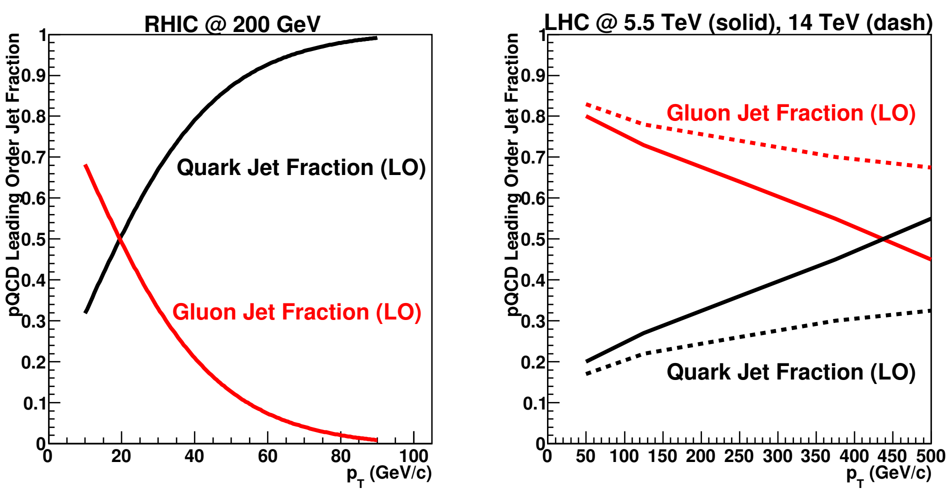

Figure 1.12: Comparison of the fraction of quark and gluon jets from leading order pQCD calculations as a function of transverse momentum for RHIC (left) and LHC (right) energies.

1.8 Heavy Quark Jets

The motivation for studying heavy flavor jets in heavy ion collisions is to understand the processes involved in parton-medium interactions and to further explore the issue of *strong versus weak* coupling [87]. As elaborated in Section 1.2, a major goal is understanding the constituents of the medium and how fast partons transfer energy to the medium.

Heavy quarks are particularly sensitive to the contribution of collisional energy loss, due to suppressed radiative energy loss from the "dead cone" effect [88]. Measurements of beauty-tagged jets and reconstructed D mesons over the broadest kinematic reach will enable the disentangling of $\hat{q}$ and $\hat{e}$.

There are important measurements currently being made of single electrons from semileptonic D and B decays and direct D meson reconstruction with the current PHENIX VTX and STAR Heavy Flavor Tracker (HFT). The sPHENIX program can significantly expand the experimental acceptance and physics reach of this program with its ability to reconstruct full jets with a heavy flavor tag. The rates for heavy flavor production from perturbative QCD calculations [89] are shown in Figure 1.13.

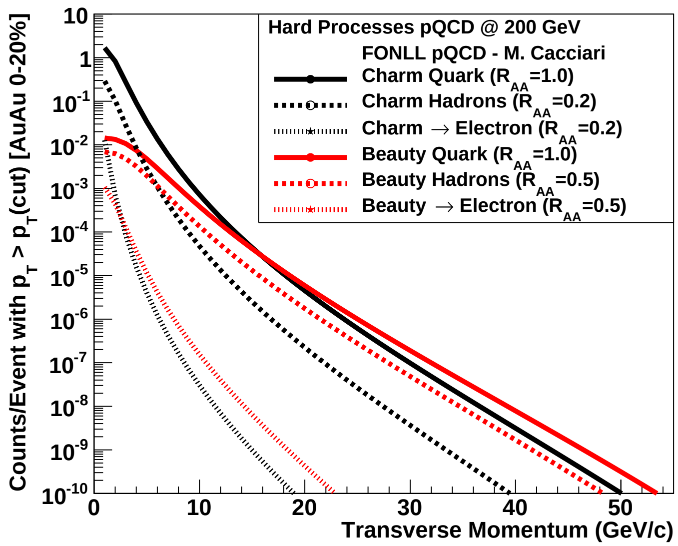

Figure 1.13: FONLL calculations [89] for heavy flavor (charm and beauty) jets, fragmentation hadrons (D, B mesons primarily), and decay electrons as a function of transverse momentum. The rates indicate expected counts for p_T above a minimum transverse momentum threshold, $p_T(cut)$, as a function of $p_T(cut)$ for Au+Au 0–20% central collisions.

Calculations including both radiative and collisional energy loss for light quark and gluon jets, charm jets, and beauty jets have been carried out within the CUJET 2.0 framework [90]. The resulting R_{AA} values in central Au+Au at RHIC and Pb+Pb at the LHC for π, D, B mesons are shown as a function of p_T in Figure 1.14. The mass orderings are a convolution of different initial spectra steepness, different energy loss mechanisms, and the final fragmentation. Measurements of D mesons to high p_T and reconstructed beauty-tagged jets at RHIC will provide particularly sensitive constraints in a range where, due to their large masses, the charm and beauty quark velocities are not near the speed of light.

The tagging of charm and beauty jets has an extensive history in particle physics experiments. There are multiple ways to tag heavy flavor jets. First is the method of tagging via

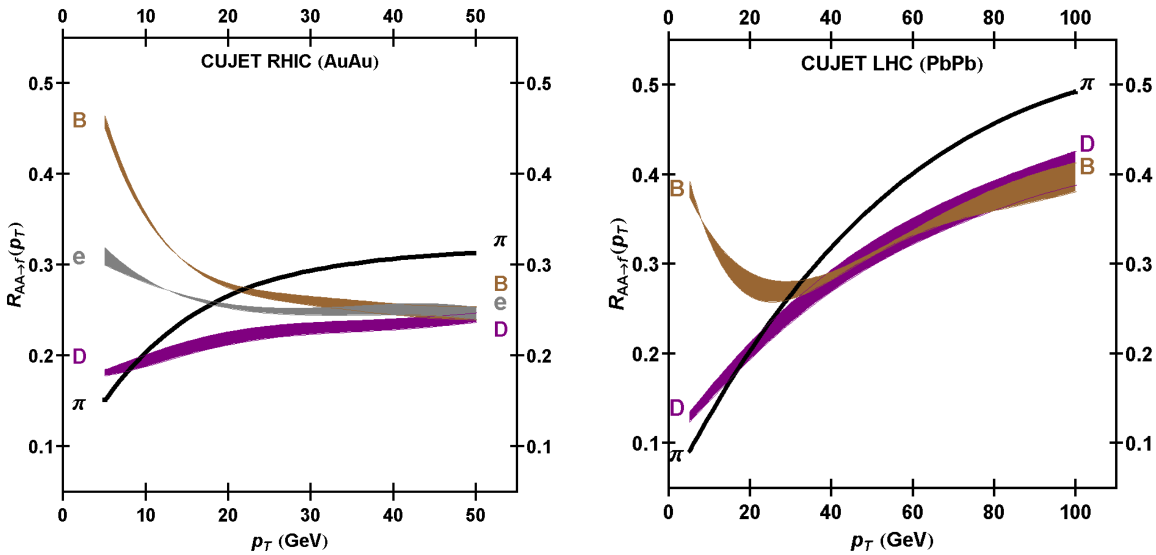

Figure 1.14: Calculations within the CUJET 2.0 [90] framework of the R_{AA} in central Au+Au collisions at RHIC (left) and Pb+Pb collisions at the LHC (right), with light, charm and beauty hadrons and electrons shown as separate curves.

the selection of a high p_T electron with a displaced vertex inside the jet. In minimum bias Au+Au collisions at $\sqrt{s_{NN}} = 200$ GeV, the fraction of inclusive electrons from D and B meson decays is already greater than 50% for $p_T > 2$ GeV/c. The sPHENIX tracking can confirm the displaced vertex of the electron from the collision point, further enhancing the signal. Since the semileptonic branching fraction of D and B mesons is approximately 10%, this method provides a reasonable tagging efficiency. Also, the relative angle of the lepton with respect to the jet axis provides a useful discriminator for beauty jets as well, due to the decay kinematics. Second, the direct reconstruction of D mesons is possible within sPHENIX (see Figure 4.37 of Ref. [1]).

The third method utilizes jets with many tracks that do not point back to the primary vertex. This technique is detailed by the $D0$ collaboration to identify beauty jets at the Tevatron [91, 92], and employed with variations by ATLAS and CMS at the LHC. This method exploits the fact that most hadrons with a beauty quark decay into multiple charged particles all with a displaced vertex. The performance metrics for tagged beauty jets are given in Section 4.7 of Ref. [1]).

Measurements at the LHC provide tagging of heavy flavor probes as well – initial results on beauty tagged jets from CMS are shown in Figure 1.15. As detailed in Ref. [93], beauty tagged jets at the LHC come from a variety of initial processes. In fact, most often a tagged beauty jet does not have a back-to-back partner beauty jet. At RHIC energies the pair creation process represents $\sim 35\%$ of the beauty jet cross-section, which is a larger fractional contribution than at the LHC, though flavor excitation still produces $\sim 50\%$ of all b-jets at RHIC. Measurements at RHIC offer a different mixture of initial processes, and

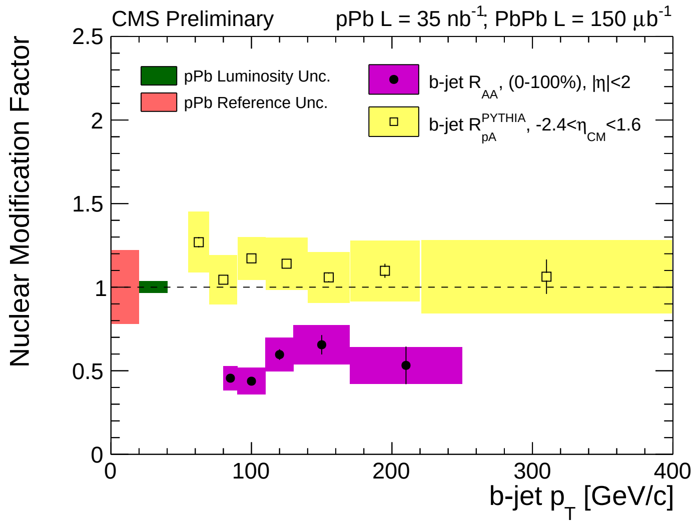

Figure 1.15: CMS results on the R_{AA} for beauty tagged jets in Pb+Pb collisions at the LHC.

thus kinematics, when looking at correlated back-to-back jets including heavy flavor tags, and will complement similar measurements at the LHC to constrain theories.

1.9 Quarkonia in the QGP

Motivated by a desire to observe the suppression of J/ψ production by color screening in the QGP an extensive program of J/ψ measurements in A+A collisions has been carried out at the SPS ($\sqrt{s_{NN}} = 17.3$ GeV) and RHIC ($\sqrt{s_{NN}} = 200$ GeV) and the LHC ($\sqrt{s_{NN}} = 2.76$ TeV). Strong suppression is observed at all three energies, but it has become clear that the contribution of color screening to the observed modification cannot be uniquely determined without a good understanding of two strong competing effects.

The first of these, the modification of the J/ψ production cross section in a nuclear target, has been addressed at RHIC using d+Au collisions and at the SPS using p+Pb collisions, and is being addressed at the LHC using p+Pb collisions. A more recently recognized complicating effect arises from the possibility that previously unbound heavy quark pairs could coalesce into bound states due to interactions with the medium. This introduces the possibility that if a sufficient density of heavy quark pairs is produced initially, then coalescence of heavy quarks may increase the production cross section beyond the initial population of bound pairs [94].

Using p+Pb and d+Au data as a baseline, and under the assumption that cold nuclear matter (CNM) effects can be factorized from hot matter effects, the suppression in central collisions due to the presence of hot matter in the final state has been estimated to be about 25% for Pb+Pb at the SPS [95], and about 50% for Au+Au at RHIC [96], both measured at midrapidity. The first J/ψ data in Pb+Pb collisions at $\sqrt{s_{NN}} = 2.76$ TeV have been measured from ALICE [97]. Interestingly, the suppression in central collisions is far greater at RHIC than at the LHC. This is qualitatively consistent with a predicted [94] strong coalescence component due to the very high $c\bar{c}$ production rate in a central collision at LHC. There is great promise that, with CNM effects estimated from p+Pb data, comparison of these data at widely spaced collision energies will lead to an understanding of the role of coalescence.

1.9.1 Upsilon State Measurements

Upsilon measurements have a distinct advantage over charmonium measurements as a probe of deconfinement in the quark-gluon plasma. The Υ(1S), Υ(2S) and Υ(3S) states can all be observed with comparable yields via their dilepton decays. Therefore, it is possible to compare the effect of the medium simultaneously on three bottomonium states—all of which have quite different radii and binding energies.

At the LHC, CMS has measured Upsilon modification data at midrapidity in Pb+Pb collisions at 2.76 TeV that indicate strong differential suppression of the 2S and 3S states relative to the 1S state [98]. ALICE has measured the $\Upsilon(1S)$ modification at forward rapidity in Pb+Pb collisions at 2.76 GeV [99], and in p+Pb collisions at 5.02 TeV [100]. With longer Pb+Pb runs, and corresponding p+Pb modification data to establish a CNM baseline, the LHC measurements will provide an excellent data set within which the suppression of the three upsilon states relative to p+Pb can be measured simultaneously at LHC energies.

At RHIC, upsilon measurements have been hampered by a combination of low cross sections and acceptance, and insufficient momentum resolution to resolve the three states. So far, there are measurements of the modification of the three states combined in Au+Au by PHENIX [101] and STAR [102]. However a mass-resolved measurement of the modifications of the three upsilon states at $\sqrt{s_{NN}} = 200$ GeV would be extremely valuable for several reasons.

First, the core QGP temperature is approximately $2T_c$ at RHIC at 1 fm/c and is at least 30% higher at the LHC (not including the fact that the system may thermalize faster) [103]. This temperature difference results in a different color screening environment. Figure 1.16 shows the temperature as a function of time for the central cell in Au+Au and Al+Al collisions at 200 GeV and Pb+Pb collisions at 2.76 TeV from hydrodynamic simulations that include earlier pre-equilibrium dynamics and post hadronic cascade [104]. Superimposed are the lattice expected dissociation temperatures with uncertainties for the three upsilon states. The significant lever arm in temperature between RHIC and LHC, and the use of either centrality or system size, allow one to bracket the expected screening behavior.

Second, the bottomonium production rate at RHIC is lower than that at the LHC by ~ 100 [96]. As a result, the average number of $b\bar{b}$ pairs in a central Au+Au collision at RHIC is ~ 0.05 versus ~ 5 in central Pb+Pb at the LHC. Qualitatively, one would

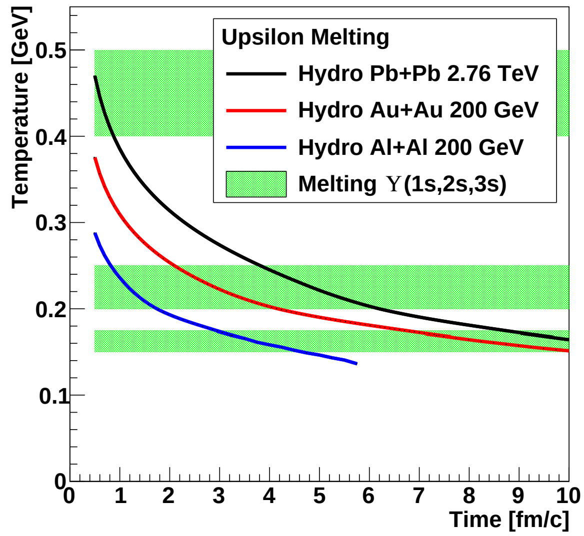

Figure 1.16: Temperature as a function of time for the central cell in Au+Au and Al+Al collisions at 200 GeV and Pb+Pb collisions at 2.76 TeV from hydrodynamic simulations that include earlier pre-equilibrium dynamics and post hadronic cascade [104]. Superimposed are the lattice expected dissociation temperatures with uncertainties for the three upsilon states.

expect this to effectively remove at RHIC any contributions from coalescence of bottom quarks from different hard processes, making the upsilon suppression at RHIC dependent primarily on color screening and CNM effects. This seems to be supported by recent theoretical calculations [105] where, in the favored scenario, coalescence for the upsilon is predicted to be significant at the LHC and small at RHIC.

Finally, it is of interest at RHIC energy to directly compare the modifications of the J/ψ and the $\Upsilon(2S)$ states as a way of constraining the effects of coalescence by studying two states - in the same temperature environment - that have very similar binding energies and radii, but quite different underlying heavy quark populations.

An example theoretical calculation for both RHIC and the LHC is shown in Figure 1.17 indicating the need for substantially improved precision and separation of states in the temperature range probed at RHIC.

STAR has constructed a Muon Telescope Detector (MTD) to measure muons at midrapidity [106]. The MTD has coverage over $|\eta| < 0.5$, with about 45% effective azimuthal coverage. The MTD will have a muon to pion enhancement factor of 50–100, and the mass resolution will provide a clean separation of the ϒ(1S) from the ϒ(2S+3S), and likely the ability to separate the ϒ(2S) and ϒ(3S) by fitting. While STAR has already taken data in the 2014 run with the MTD installed, the upgrade to sPHENIX will provide better mass resolution and approximately 10 times higher yields per run for upsilon measurements. An

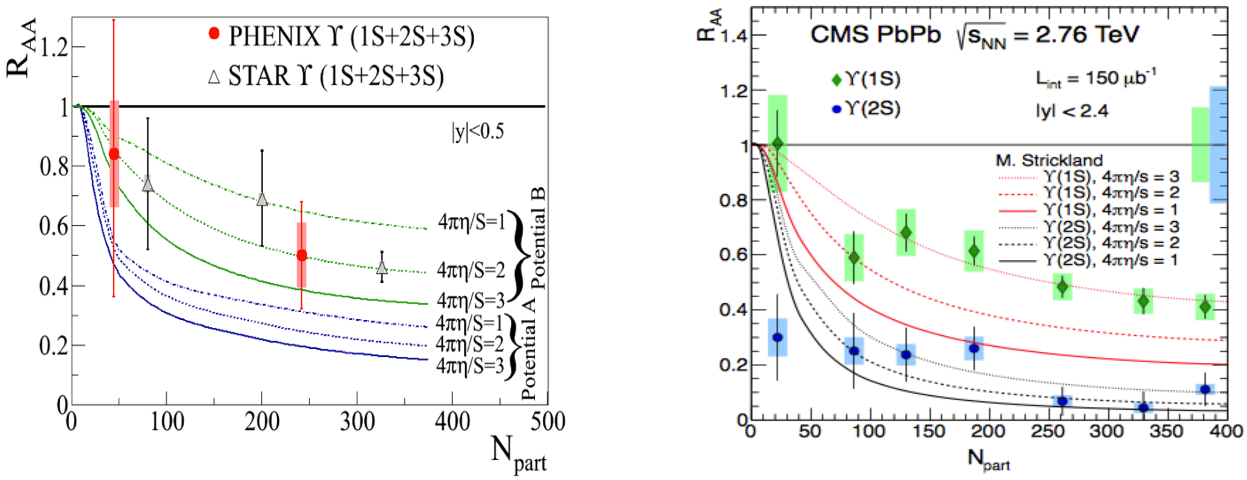

Figure 1.17: Calculations for Upsilon state suppression at RHIC and LHC energies as a function of collision centrality. The current state of measurements are also shown from PHENIX, STAR and CMS.

example of the estimated statistical precision is shown in Figure 1.18. In concert with the expected higher statistics results from the LHC experiments, sPHENIX data will provide the required precision to discriminate models of breakup in the dense matter and the length scale probed in the medium.

1.9.2 Quarkonia in p(d) + A collisions

Measurements of quarkonia production in proton-nucleus collisions have long been considered necessary to establish a cold nuclear matter baseline for trying to understand hot matter effects in nuclear collisions. It has become clear, however, that the physics of p+A collisions is interesting in its own right [96]. Modification of quarkonia production in a nuclear target has been described by models that include gluon saturation effects (see for example [107]), breakup of the forming quarkonia by collisions with nucleons in the target [108, 109], and partonic energy loss in cold nuclear matter [110]. These mechanisms, which are all strongly rapidity and collision energy dependent, have been used, in combination, to successfully describe J/ψ and $\Upsilon(1S)$ data in $p(d)$+A collisions.

The observation of what appears to be hydrodynamic effects in p+Pb collisions at the LHC [111, 112, 113] and d+Au collisions at RHIC [114] has raised questions about the longstanding assumption that $p(d)$+A collisions are dominated by cold nuclear matter effects. For quarkonia, it raises the obvious question: does the small hot spot produced in the $p(d)$+A collision affect the quarkonia yield? Recent measurements of the modification of quarkonia excited states in $p(d)$+A collisions have produced unexpected and puzzling results.

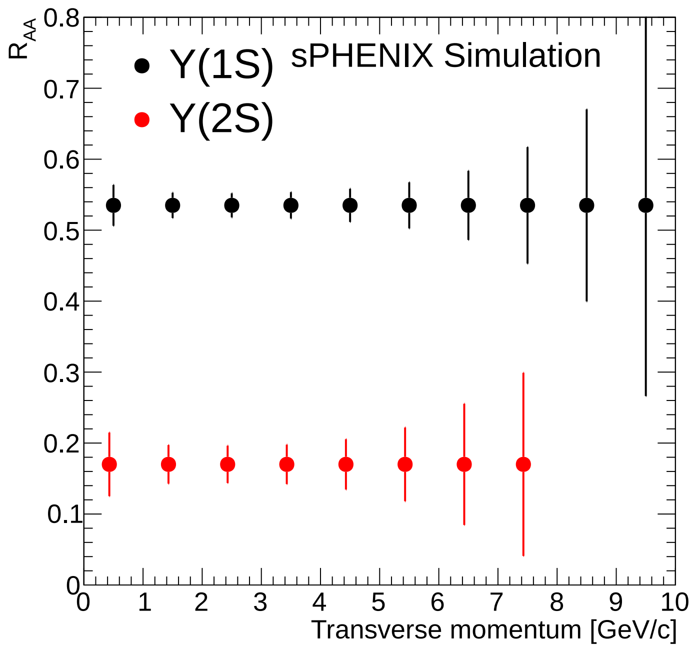

Figure 1.18: Estimate of the statistical precision of a measurement of the Υ(1S) and Υ(2S) states in the 10% most central Au+Au collisions using sPHENIX, assuming that the measured R_{AA} is equal to the results of a recent theory calculation by Strickland & Barzow. This plot was made for 250 billion recorded minimum bias Au+Au events. As is the case for the CMS experiment at the LHC, measurements of the yield of the Υ(3S) state in sPHENIX will be extremely challenging due to its very strong suppression in central collisions.

The situation has become more interesting with the release of data from CMS on production of Upsilon excited states in p+Pb collisions. They find that the $\Upsilon(2S)$ to $\Upsilon(1S)$ ratio is suppressed by about 20% in minimum bias p+Pb collisions, while for the $\Upsilon(3S)$ the differential suppression in minimum bias collisions is about 30%. The effect will be considerably larger in the most central collisions, but data showing the centrality dependence are not released yet.

A comprehensive p+A collision program with sPHENIX will provide Upsilon measurements in p+Au collisions at RHIC energy with all three states resolved from each other.

1.10 Jet Rates and Physics Reach

In order to realize the proposed comprehensive program of jet probes, direct photon-tagged jets, and Upsilon measurements requires very high luminosities and the ability to sample events without selection biases. [1] In addition to the Upsilon capabilities summarized in Figure 1.18, the extensive set of reconstructed jet measurements made available by sPHENIX will provide detailed information about the quark-gluon plasma properties, dynamics, time evolution, and structure at 1–2 T_c. The theoretical bridgework needed to connect these measurements to the interesting and unknown medium characteristics of deconfined color charges is under active construction by many theorists. Combining this work with new results from the flexible and high luminosity RHIC collider facility can produce new discoveries in heavy ion collisions with an appropriate set of baseline measurements provided sPHENIX apparatus is constructed. The sPHENIX jet detector at RHIC is best able to take advantage of these opportunities.

1.10.1 Inclusive jet rates

The inclusive jet yield within $|\eta| < 1.0$ in 0–20% central Au+Au collisions at 200 GeV has been calculated for p+p collisions by Vogelsang in a Next-to-Leading-Order (NLO) perturbative QCD formalism [117] and scaled by the expected number of binary collisions. This is presented in Figure 1.19. Also shown are results from the calculation for π^0 and direct and fragmentation photon yields. The bands correspond to the renormalization scale uncertainty in the calculation (i.e., $\mu, \mu/2, 2\mu$). Figure 1.19 provides the counts per event with p_T larger than the value on the x-axis for the most central 20% Au+Au collisions at $\sqrt{s_{NN}} = 200$ GeV. With 20 billion events per RHIC year for this centrality selection, this translates into jet samples from 20–80 GeV and direct photon statistics out beyond 40 GeV. It is notable that within the acceptance of the sPHENIX detector, over 80% of the inclusive jets will also be accepted dijet events. The necessary comparable statistics are available with 10 weeks of p+p and 10 weeks of p+Au running.

1.10.2 Constraining the path length through the medium

An observable that has been especially challenging for energy loss models to be able to reproduce is the azimuthal anisotropy of π^0 production with respect to the reaction plane. A weak dependence on the path length in the medium is expected from radiative energy loss. This translates into a small elliptic flow v_2 value for high p_T particles, and thus would

[1] The effect of the completed stochastic cooling upgrade to the RHIC accelerator [115] has been incorporated into the RHIC beam projections [116]. Utilizing these numbers and accounting for accelerator and experiment uptime and the fraction of collisions within $|z| < 10$ cm, the nominal full acceptance range for the detector, the sPHENIX detector can record 100 billion Au+Au minimum bias collisions in a one-year 22 week run. With the latest luminosity projections, for the purely calorimetric jet and γ-jet observables with modest trigger requirements, one can sample 0.6 trillion Au+Au minimum bias collisions Note that the PHENIX experiment has a nearly dead-timeless high-speed data acquisition and trigger system that has already sampled tens of billions of Au+Au minimum bias collisions, and maintaining this high rate performance with the additional sPHENIX components is an essential design feature.

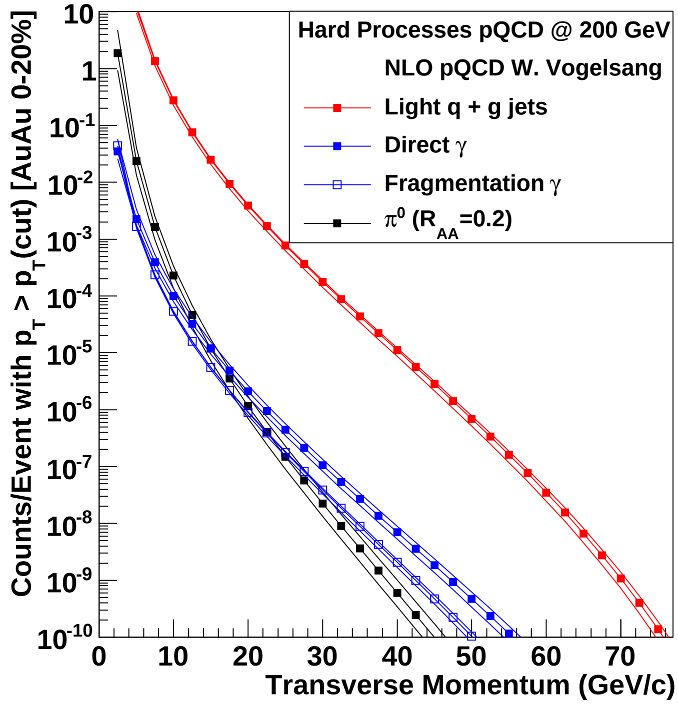

Figure 1.19: Jet, photon and π^0 rates for $|\eta| < 1.0$ from NLO pQCD [117] calculations scaled to Au+Au central collisions for $\sqrt{s_{NN}} = 200$ GeV . The scale uncertainties on the pQCD calculations are shown as additional lines. Ten billion Au+Au central collisions correspond to one count at 10^{-10} at the bottom of the y-axis range. A nominal 22 week RHIC run corresponds to 20 billion central Au+Au events.

represent only a modest difference in parton energy loss when traversing a short versus long path length in the QGP.

A strong path length dependence is naturally described by strongly-coupled energy-loss models [118, 119]. Note that one can obtain a larger v_2 by using a stronger coupling, larger $\hat{q}$, but at the expense of over-predicting the average level of suppression. New strong coupling models [120, 121] will need to confront the full set of observables measured at RHIC.

The measurement of jet quenching observables, as a detailed function of orientation with respect to the reaction plane, is directly sensitive to the coupling strength and the path length dependence of any modification to the parton shower. In addition, medium response may be optimally measured in mid-central collisions where there is a lower underlying event and where the medium excitations are not damped out over a longer time evolution as in more central collisions or which may be the case also at LHC. Shown in Figure 1.20 are projected uncertainties from sPHENIX for the direct photon and reconstructed jet

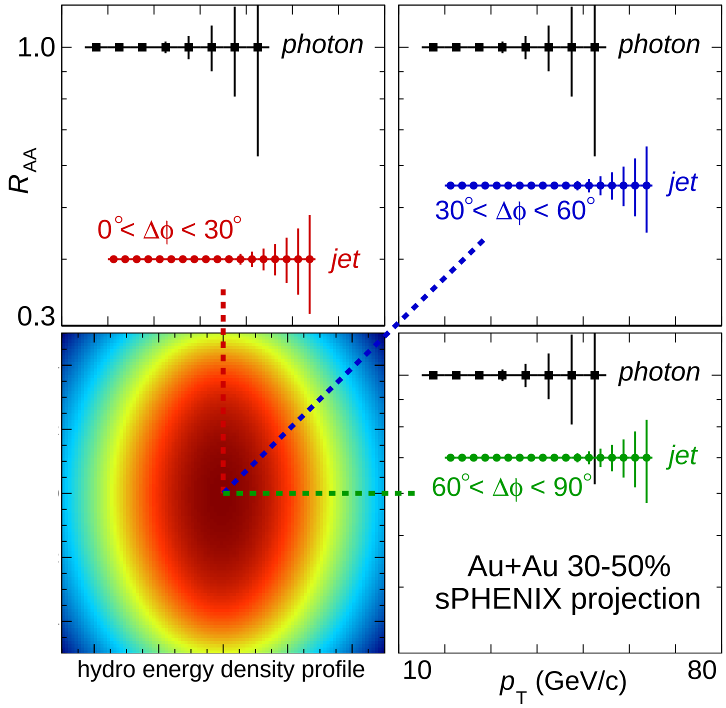

Figure 1.20: Demonstration of the statistical reach for azimuthally-sensitive hard probes measurements in sPHENIX. Each panel shows the projected statistical uncertainty for the R_{AA} of inclusive jets and photons, with each a panel a different $\Delta\phi$ range with respect to the reaction plane in 30–50% Au+Au events. sPHENIX would additionally have tremendous statistical reach in the analogous charged hadron R_{AA}.

observables in three orientation selections. One expects no orientation dependence for the direct photons and the question is whether the unexpectedly large dependence for charged hadrons persists in reconstructed jets up to the highest p_T. Note that the same measurements can be made for beauty tagged jets, charged hadrons up to 50 GeV/c, and a full suite of correlation measurements including jet-jet, hadron-jet, γ-jet.

All measurements in heavy ion collisions are the result of emitted particles integrated over the entire time evolution of the reaction, covering a range of temperatures. Similar to the hydrodynamic model constraints, the theory modeling for jet probes requires a consistent temperature and scale dependent model of the quark-gluon plasma and is only well constrained by precision data through different temperature evolutions, as measured at RHIC and the LHC.

1.10.3 Rates for Direct Photons

Measurement of direct photons requires them to be separated from the other sources of inclusive photons, largely those from π^0 and η meson decay. The left panel of Figure 1.21 shows the direct photon and π^0 spectra as a function of transverse momentum for both $\sqrt{s} = 200$ GeV and 2.76 TeV $p+p$ collisions. The right panels show the γ/π^0 ratio as a function of p_T for these energies with comparison PHENIX measurements at RHIC. At the LHC, the ratio remains below 10% for $p_T < 50$ GeV while at RHIC the ratio rises sharply and exceeds one at $p_T \approx 30$ GeV/c. In heavy ion collisions the ratio is further enhanced because the π^0s are significantly suppressed. Taking the suppression into account, the γ/π^0 ratio at RHIC exceeds one for $p_T > 15$ GeV/c. The large signal to background means that it will be possible to measure direct photons with the sPHENIX calorimeter alone, even before applying isolation cuts. Beyond measurements of inclusive direct photons, this enables measurements of γ-jet correlations and γ-hadron correlations.

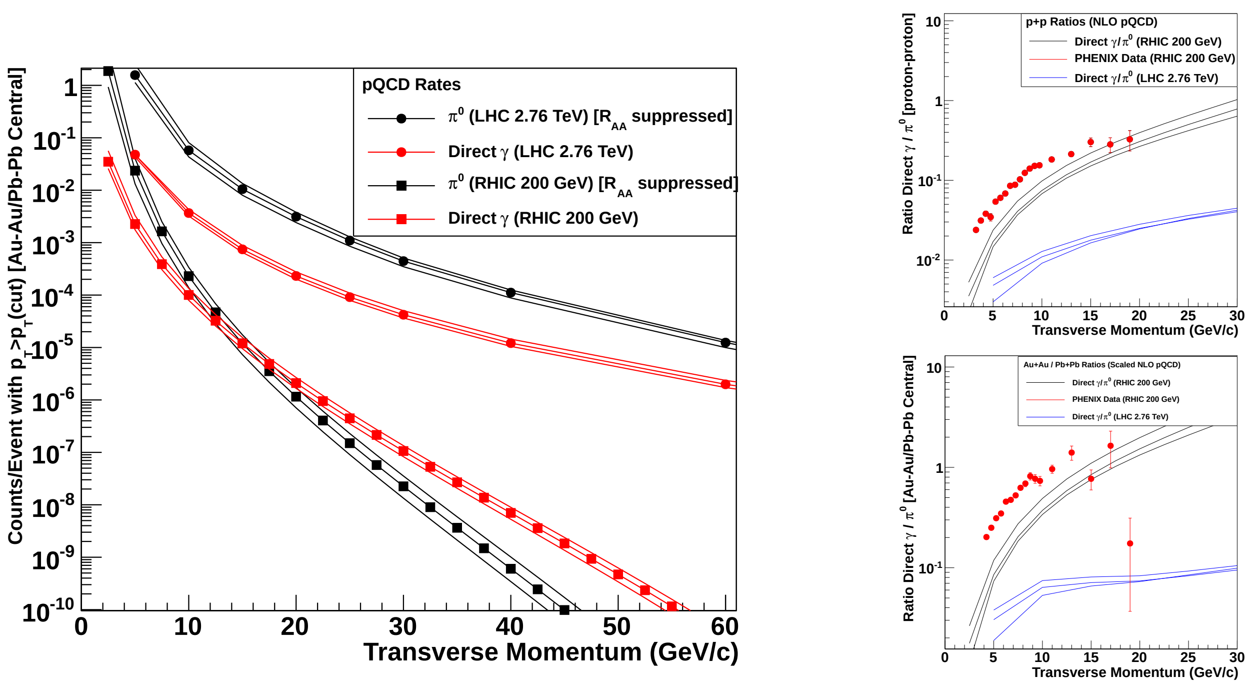

Figure 1.21: NLO pQCD calculations of direct photons and π^0 for RHIC and LHC. The plot on the left shows the counts per event in Au+Au or Pb+Pb collisions (including the measured R_{AA} suppression factor for π^0). The upper (lower) panel on the right shows the direct γ to π^0 ratio in $p+p$ (Au+Au or Pb+Pb) collisions, in comparison with measurements from the PHENIX experiment at RHIC [122, 123].

1.10.4 Hard probe statistics and range in p_T

Figure 1.22 summarizes the current and future state of hard probes measurements in A+A collisions in terms of their statistical reach, showing the most up to date R_{AA} measurements of hard probes in central Au+Au events by the PHENIX Collaboration plotted against statistical projections for sPHENIX channels measured after the first two years of data-taking. While these existing measurements have greatly expanded our knowledge of the QGP created at RHIC, the overall kinematic reach is constrained to < 20 GeV even for the highest statistics measurements. Figure 1.23 shows the expected range in p_T for sPHENIX as compared to measurements at the LHC. Due to the superior acceptance, detector capability and collider performance, sPHENIX will greatly expand the previous kinematic range studied at RHIC energies (in the case of inclusive jets, the data could extend to 80 GeV/c, four times the range of the current PHENIX π^0 measurements) and will allow access to new measurements entirely (such as fully reconstructed b-tagged jets).

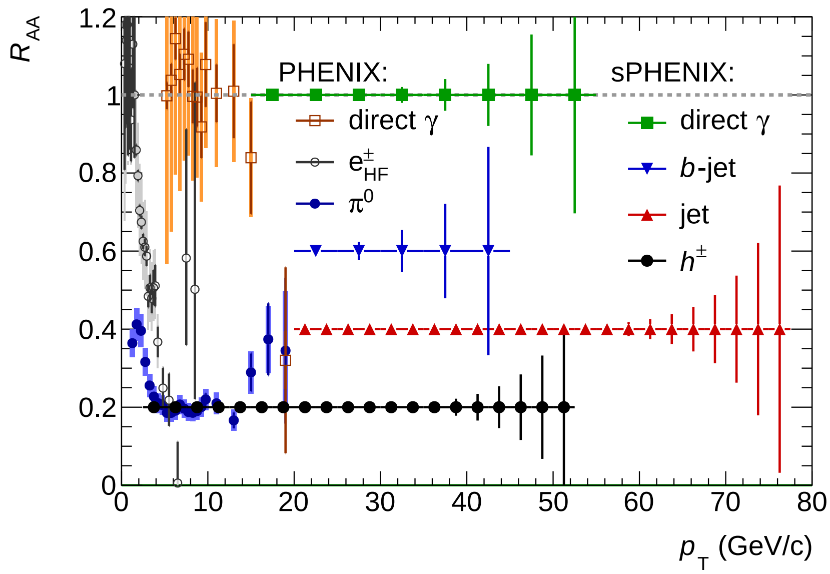

Figure 1.22: Statistical projections for the R_{AA} of various hard probes vs p_{T} in 0–20% Au+Au events with the sPHENIX detector after two years of data-taking, compared with a selection of current hard probes data from PHENIX.

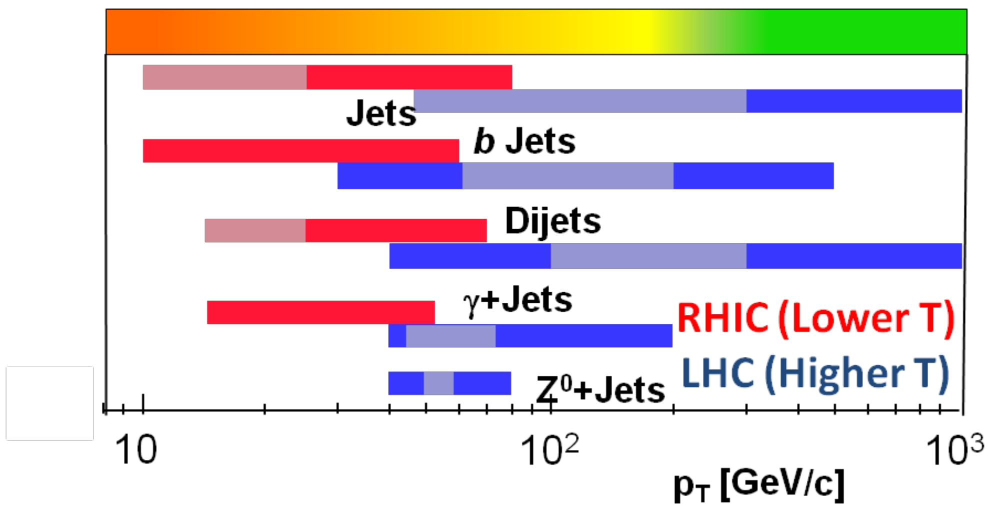

Figure 1.23: Anticipated range in p_T of various hard probe measurements using sPHENIX at RHIC (red) and measurements made at the LHC (blue). The color strip across the top corresponds to the regions presented initially in Figure 1.1 (left) for scattering in the medium from bare quarks and gluons (green), from thermal gluons (yellow), and integration over all possible objects that are probed (orange).

Chapter 2

Detector Overview

The sPHENIX Detector is a cylindrical detector covering $|\eta| \leq 1.1$ and the full azimuth. It is designed to use the former BaBar superconducting solenoid to contain an inner tracking system out to 80 cm in radius followed by a electromagnetic calorimeter and the first of two longitudinal segments of a hadronic calorimeter. The second longitudinal segment of the hadronic calorimeter, which also serves as the magnet flux return, surrounds the magnet cryostat.

sPHENIX has been designed to collect a large sample of events in Au+Au and p+p collisions at RHIC to measure jets, jets correlations, and Upsilon production and decay and satisfy a set of performance requirements that are needed to carry out the physics program described in Chapter 1. The sPHENIX physics program rests on several key measurements, particularly measurements of jets with calorimetry and tracking which can cleanly separate the Upsilon states; the requirements that drive any particular aspect of the detector performance come from a broad range of considerations related to those measurements. A comprehensive assessment of the physics requirements has led to the development of the reference design shown in Figure 2.1.

The primary components of the sPHENIX reference design are as follows.

Magnetic Solenoid Built for the BaBar experiment at SLAC, the magnet became available after the termination of the BaBar program. The cryostat has an inner radius of 140 cm and is 33 cm thick, and can produce a central field of 1.5 T.

Tracking system The tracking system consist of three components:

Time Projection Chamber A TPC with an outer radius of about 80 cm measures space points on charged tracks which provides momentum resolution which can separate the Upsilon states in decays to e^+e^-.

Intermediate Tracking The Intermediate Tracker is a silicon strip detector consisting of up to four layers which can measure space points on charged tracks inside

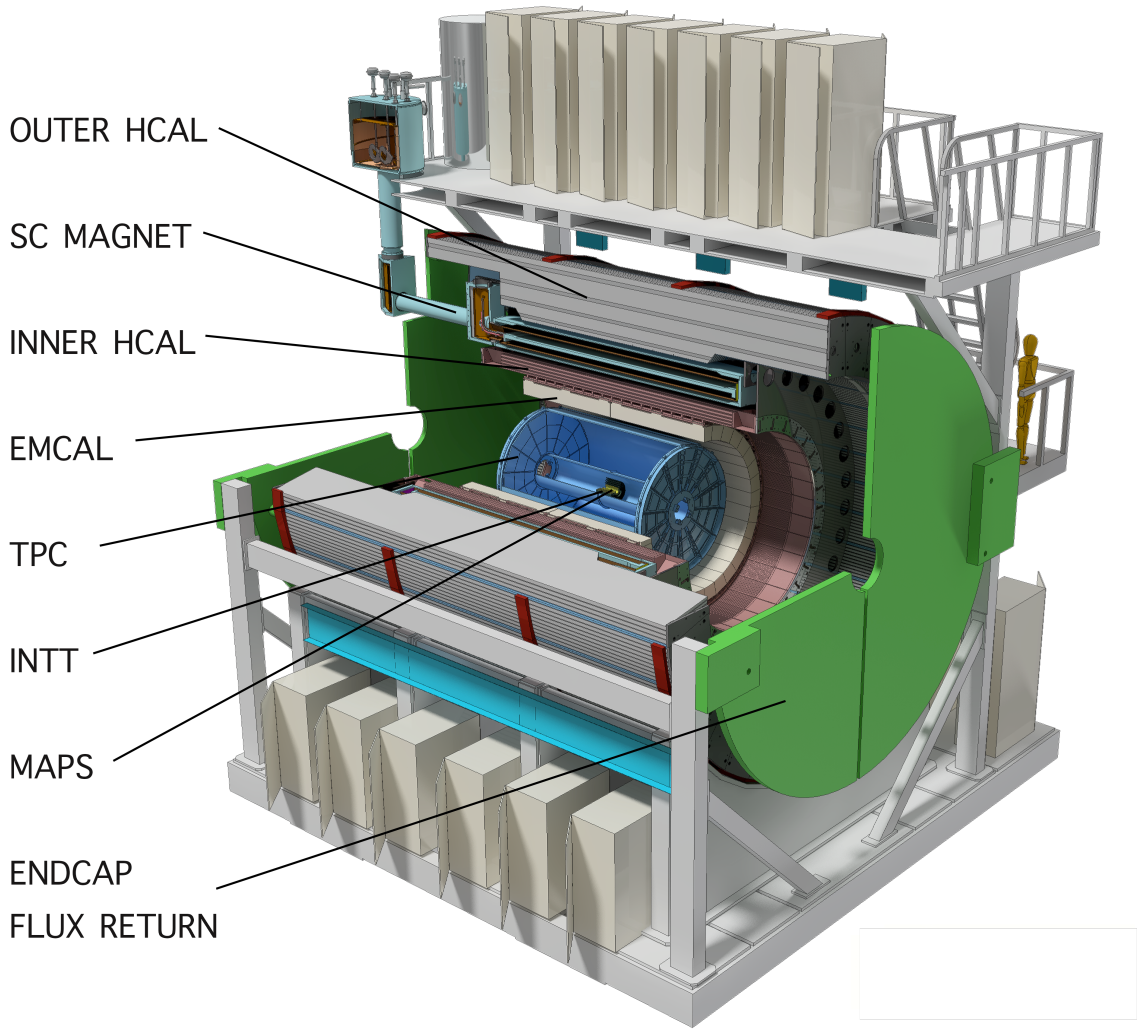

Figure 2.1: View of the sPHENIX detector with its component subdetectors.

the inner radius of the TPC for robust tracking even in a high multiplicity heavy ion collision with time resolution that can separate pileup in the TPC. This detector is based on commercial silicon sensors read out with the FPHX ASIC developed for the PHENIX FVTX detector and is a RIKEN and RIKEN-Brookhaven Research Center contribution to the sPHENIX experiment.

MAPS Vertex Detector A Monolithic Active Pixel (MAPS) vertex detector in close proximity to the beam pipe is to provide high precision vertex measurements for measurement of displaced vertices from decays of particles containing b and c quarks, and provide additional precisely measured space points for charged particle tracking. This detector is being proposed and developed as a separate upgrade to the sPHENIX proposal, based on duplicating as much as possible the ALICE Inner Tracking System (ITS) detector.

Electromagnetic Calorimeter Tungsten-scintillating fiber sampling calorimeter inside the magnet bore read out with silicon photo-multipliers. The calorimeter has a small Molière radius and short radiation length. allowing for a compact design.

Inner Hadronic Calorimeter Sampling calorimeter of non-magnetic metal and scintillator located inside the magnet bore, which is not part of the DOE funded proposal, but which could be instrumented at a later time with non-DOE funding.

Outer Hadronic Calorimeter Sampling calorimeter of magnet steel scintillator located outside the cryostat which doubles as the flux return for the solenoid.

In the following list we provide a high-level mapping between physics aims and various detector requirements. The justification for these requirements is then discussed in more detail in subsequent sections.

Upsilons The key to the physics is high statistics p+p, p+A, and A+A data sets, with mass resolution and signal-to-background sufficient to separate the three states of the Υ family.

- large geometric acceptance ($\Delta\phi = 2\pi$ and $|\eta| < 1.1$)
- high rate data acquisition (15 kHz)
- trigger for electrons from $\Upsilon \rightarrow e^+e^-$ ($>$ 90% efficiency) in p+p and p+A
- track reconstruction efficiency $>$ 90% and purity $>$ 90% for $p_T > 3$ GeV/c
- momentum resolution of 1.2% for p_T in the range 4-10 GeV/c.
- electron identification with efficiency $>$ 70% and charged pion rejection of 90:1 or better in central Au+Au at $p_T = 4$ GeV/c.

Jets The key to the physics is to cover jet energies of 20–70 GeV, for all centralities, for a range of jet sizes, with high statistics and performance insensitive to the details of jet fragmentation.

- energy resolution $< 120\%/\sqrt{E_{\rm jet}}$ in p+p for $R = 0.2$–0.4 jets
- energy resolution $< 150\%/\sqrt{E_{\rm jet}}$ in central Au+Au for $R = 0.2$ jets
- energy scale uncertainty $<$ 3% for inclusive jets
- energy resolution, including effect of underlying event, such that scale of unfolding on raw yields is less than a factor of three
- measure jets down to $R = 0.2$ (segmentation no coarser than $\Delta\eta \times \Delta\phi \sim 0.1 \times 0.1$)

- underlying event influence event-by-event (large coverage HCal/EMCal) (ATLAS method)
- energy measurement insensitive to softness of fragmentation (quarks or gluons) — HCal + EMCal
- jet trigger capability in $p+p$ and $p+A$ without jet bias (HCal and EMCal)
- rejection ($>$ 95%) of high p_T charged track backgrounds (HCal)

Dijets The key to the physics is large acceptance in conjunction with the general requirements for jets as above

- $>$ 80% containment of opposing jet axis
- $>$ 70% full containment for $R = 0.2$ dijets
- R_{AA} and A_J measured with $<$ 10% systematic uncertainty (also key in $p+A$, onset of effects)

Fragmentation functions The key to the physics is unbiased measurement of jet energy

- excellent tracking resolution out to $>$ 40 GeV/c ($dp/p < 0.2\% \times p$)
- independent measurement of p and E ($z = p/E$)

Heavy quark jets The key to the physics is tagging identified jets containing a displaced secondary vertex

- precision DCA ($<$ 100 microns) for electron $p_T > 4$ GeV/c
- electron identification for high $p_T > 4$ GeV/c

Direct photon The key to the physics is identifying photons

- EMCal segmentation $\Delta\eta \times \Delta\phi \sim 0.024 \times 0.024$
- EMCal resolution for photon ID $<$ 8% at 15 GeV
- EMCal cluster trigger capability in $p+p$ and $p+A$ with rejections $>$ 100 for $E_\gamma > 10$ GeV

High statistics Ability to sample high statistics for $p+p$, $p+A$, $A+A$ at all centralities — requires high rate, high throughput DAQ (15 kHz).

In the following sections, we detail the origin of key requirements.

2.1 Acceptance

The large acceptance and high rate of sPHENIX are key enablers of the physics program detailed in Chapter 1. The total acceptance of the detector is determined by the requirement of high statistics jet measurements and the need to fully contain both single jets and dijets. To fully contain hadronic showers in the detector requires both large solid angle coverage and a calorimeter deep enough to fully absorb the energy of hadrons up to 70 GeV.

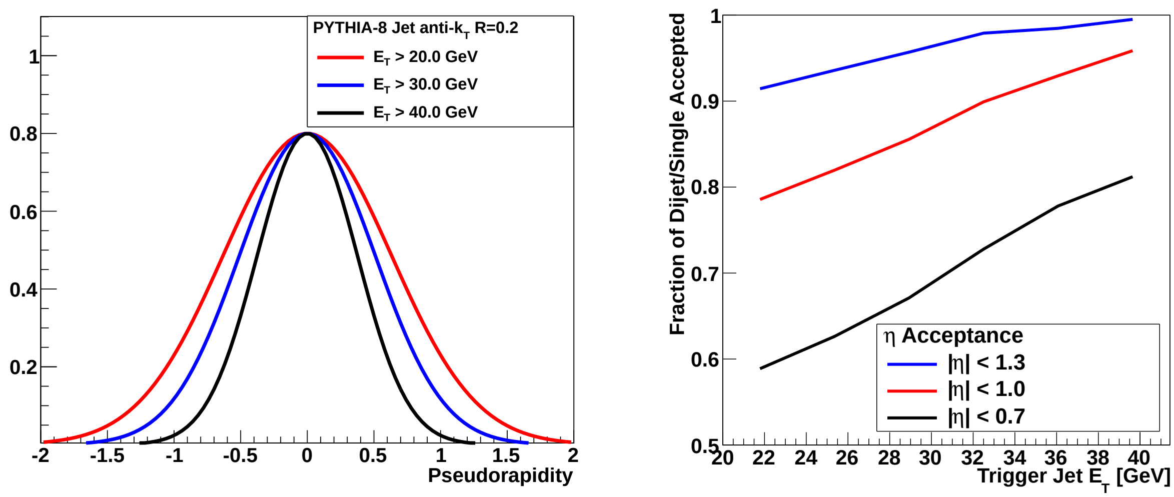

Figure 2.2: (Left) Pseudorapidity distribution of PYTHIA jets reconstructed with the FASTJET anti-k$_T$ and R=0.2 for different transverse energy selections. (Right) The fraction of PYTHIA events where the leading jet is accepted into a given pseudorapidity range where the opposite side jet is also within the acceptance. Note that the current PHENIX acceptance of $|\eta| < 0.35$ corresponds to a fraction below 30%.

The PYTHIA event generator has been used to generate a sample of p+p at 200 GeV events which can be used to demonstrate the pseudorapidity distribution of jets. The left panel in Figure 2.2 shows the pseudorapidity distribution of jets with E_T above 20, 30, and 40 GeV. The right panel in Figure 2.2 shows the fraction of events where a trigger jet with E_T greater than a given value within a pseudorapidity range has an away side jet with $E_T > 5$ GeV accepted within the same coverage. In order to efficiently capture the away side jet, the detector should cover $|\eta| < 1$, and in order to fully contain hadronic showers within this fiducial volume, the calorimetry should cover slightly more than that. Given the segmentation to be discussed below, the calorimeters are required to cover $|\eta| < 1.1$.

It should be noted that reduced acceptance for the away-side jet relative to the trigger suffers not only a reduction in statistics for the dijet asymmetry and γ-jet measurements but also results in a higher contribution of low energy fake jets (upward fluctuations in the background) in those events where the away side jet is out of the acceptance. For the latter effect, the key is that both jet axes are contained within the acceptance, and then events can be rejected where the jets are at the edge of the detector and might have partial energy capture.

2.2 Segmentation

Jets are reconstructed from the four-vectors of the particles or measured energies in the event via different algorithms, and with a typical size $R = \sqrt{\Delta\phi^2 + \Delta\eta^2}$. In order to reconstruct jets down to radius parameters of $R = 0.2$ a segmentation in the hadronic calorimeter of $\Delta\eta \times \Delta\phi = 0.1 \times 0.1$ is required. The electromagnetic calorimeter segmentation should be finer as driven by the measurement of direct photons for γ-jet correlation observables. The compact electromagnetic calorimeter design being considered for sPHENIX has a Molière radius of ~ 15 mm, and with a calorimeter at a radius of about 100 cm, this leads to an optimal segmentation of $\Delta\eta \times \Delta\phi = 0.024 \times 0.024$ in the electromagnetic section.

2.3 Energy Resolution

The requirements on the jet energy resolution are driven by considerations of the ability to reconstruct the inclusive jet spectra and dijet asymmetries and the fluctuations on the fake jet background. The total jet energy resolution is typically driven by the hadronic calorimeter resolution and many other effects including the bending of charged particles in the magnetic field out of the jet radius. Expectations of jet resolutions approximately 1.2 times worse than the hadronic calorimeter resolution alone are typical.

In a central Au+Au event, the average energy within a jet cone of radius $R = 0.2$ ($R = 0.4$) is approximately 10 GeV (40 GeV) resulting in an typical RMS fluctuation of 3.5 GeV (7 GeV). This sets the scale for the required reconstructed jet energy resolution, as a much better resolution would be dominated by the underlying event fluctuations regardless. A measurement of the jet energy for $E = 20$ GeV with $\sigma_E = 120\% \times \sqrt{E} = 5.4$ GeV gives a comparable contribution to the underlying event fluctuation. A full study of the jet energy resolution with a GEANT4 simulation of the detector configuration has been performed and is discussed in the sPHENIX proposal required and is presented in the Physics Performance chapter of the sPHENIX Proposal [1].

Different considerations set the scale of the energy resolution requirement for the EMCal. The jet physics requirement is easily met by many EMCal designs. For the direct γ-jet physics, the photon energies being considered are $E_\gamma > 10$ GeV where even a modest $\sigma_E/E = 12\%/\sqrt{E}$ represents only a blurring of 400 MeV. In Au+Au central events, the typical energy in a 3×3 tower array is also approximately 400 MeV. These values represent a negligible performance degradation for these rather clean photon showers even in central Au+Au events.

Most of these physics measurements require complete coverage over a large range of rapidity and azimuthal angle ($\Delta\eta \leq 1.1$ and $\Delta\phi = 2\pi$) with good uniformity and minimal dead area. The calorimeter should be projective (at least approximately) in η. For a compact detector design there is a trade-off in terms of thickness of the calorimeter and Molière radius versus the sampling fraction and, therefore, the energy resolution of the device. Further optimization if these effects will be required as we work towards a final design.

2.4 Tracking

The requirements on tracking capabilities are tied to three particular elements of the sPHENIX physics program. The measurement of the upsilon family of quarkonia states, heavy flavor tagged jets, and fragmentation functions at high and at low z, together set the performance specification for the sPHENIX Tracker.

To fully utilize the available luminosity, the tracking systems should have large, uniform acceptance and be capable of fast readout. Measuring fragmentation functions at low z means looking for possibly wide angle correlations between a trigger jet and a charged hadron. This places only moderate requirements on the momentum resolution ($\Delta p/p \simeq 1\% \cdot p$), but reinforces the requirement of large acceptance.

Fragmentation functions at high z place more stringent requirements on momentum resolution and can be a design constraint at momenta well above 10 GeV/c. In order to unfold the full fragmentation function, $f(z)$, the smearing due to momentum uncertainty should be very small compared to the corresponding smearing due to the calorimetric jet measurement for a cleanly identified jet. For a 40 GeV jet this condition is satisfied by a tracking momentum resolution of $\Delta p/p \simeq 0.2\% \cdot p$ or better.

The measurement of the Υ family places the most stringent requirement on momentum resolution below 10 GeV/c. The large mass of the upsilon means that one can focus primarily on electrons with momenta of $\sim 4-10$ GeV/c. The $\Upsilon(3S)$ has about 3% higher mass than the $\Upsilon(2S)$ state; to distinguish them clearly one needs invariant mass resolution of $\sim$100 MeV, or $\sim$ 1%. This translates into a momentum resolution for the daughter $e^{\pm}$ of $\sim$ 1.2% in the range $4-10$ GeV/c.

The Υ measurement also generates requirements on the purity and efficiency of electron identification. The identification needs to be efficient because of the low cross section for Υ production at RHIC, and it needs to have high purity against the charged pion background to maintain a good signal to background ratio. Generally speaking, this requires minimizing track ambiguities by optimizing the number of tracking layers, their spacing, and the segmentation of the strip layers. Translating this need into a detector requirement can be done only by performing detailed simulations with a specific tracking configuration, followed by evaluation of the tracking performance.

Tagging heavy-flavor jets introduces the additional tracking requirement of being able to measure the displaced vertex of a D or B meson decay. The $c\tau$ for D and B decays is 123 μm and 457 μm, respectively, and the displaced vertex needs to be identified with a resolution sufficient to distinguish these decays against backgrounds.

2.5 Triggering

The jet energy should be available at the Level-1 trigger as a standard part of the PHENIX dead-timeless Data Acquisition and Trigger system. This triggering ability is important as one requires high statistics measurements in proton-proton, proton-nucleus, light nucleus-light nucleus, and heavy nucleus-heavy nucleus collisions with a wide range of luminosities. It is important to have combined EMCal and HCal information available so as to avoid a specific bias on the triggered jet sample.

Chapter 3

TPC

3.1 Physics requirements

Four elements of the sPHENIX physics program drive the performance parameters of sPHENIX tracking. Three of these, the measurement of the Upsilon family of quarkonia states, fragmentation functions at high and at low z, and heavy flavor tagged jets together set the momentum resolution spec for the tracker . The fourth element, the tagging of heavy-flavor jets, requires that the inner tracking system has the ability to measure the displaced vertex of a D or B meson decay. In addition, to fully utilize the available RHIC luminosity the tracking systems should have large, uniform acceptance and be capable of fast readout.

The measurement of the Υ family places the most stringent requirement on momentum resolution at lower momentum. The large mass of the Upsilon means that one can primarily focus on electrons with momenta of $\sim 4-8$ GeV/c. The $\Upsilon(3S)$ has about 3% higher mass than the $\Upsilon(2S)$ state and to distinguish them clearly one needs invariant mass resolution of ∼100 MeV, or $\sim$ 1%. This translates into a momentum resolution for the daughter $e^{\pm}$ of $\sim$ 1.2% in the range $4-8$ GeV/c.

The Υ measurement also generates requirements on the purity and efficiency of electron identification. The identification needs to be efficient because of the low cross section for Υ production at RHIC, and it needs to have high purity against the charged hadron background to maintain a good signal to background ratio. This requires minimizing track ambiguities. For a continuous tracking device such as a TPC one must optimize the two-track separation through the appropriate choice of granularity of the readout plane, and control of space charge and pile-up effects. Translating this need into a detector requirement can be done only by performing detailed simulations with a specific tracking configuration, followed by evaluation of the tracking performance.

Fragmentation functions at high z also place stringent requirements on momentum resolution and at larger momentum than the Υ reconstructions. In order to unfold the full fragmentation function, $f(z)$, the smearing due to momentum uncertainty should be very small compared to the corresponding smearing due to the calorimetric jet measurement for a cleanly identified jet. For a 40 GeV jet this condition is satisfied by a tracking momentum resolution of $\Delta p/p \simeq 0.2\% \cdot p$ or better.

Measuring fragmentation functions at low z requires looking for possibly wide angle correlations between a trigger jet and a charged hadron. This places only moderate requirements on the momentum resolution ($\Delta p/p \simeq 1\% \cdot p$), but reinforces the requirement of large acceptance.

Tagging heavy-flavor jets introduces the additional tracking requirements. At minimum this demands the ability to measure the displaced track originating from a D or B meson decay. The $c\tau$ for D and B decays is 123 μm and 457 μm, respectively, and the displaced track would need to be identified with a resolution sufficient to distinguish these decays against backgrounds. Furthermore, heavy-flavor jet identification algorithms such as DCA-counting methods require multiple large DCA tracks to be found simultaneously within a jet and will require a large single track efficiency to keep the overall identification suitably efficient. Other heavy flavor jet identification methods such as those based on fully reconstructing individual secondary vertices can place additional demands on the individual track position resolution and impact the inner pixel segmentation.

3.2 General Remarks about Tracking

3.2.1 Magnetic Field

The field produced by the Babar magnet is shown in Figure 3.1. The sPHENIX application of this coil is rather close to the original BaBar design with an EMCAL inside the coil and tracking extending to ~78 cm. A standard solenoid with length equal to diameter has significant radial magnetic field components at each end and thereby does not produce an idealized field shape. A return yoke with a small opening (*e.g.* STAR) will compensate for this shortcoming while severely limiting possibilities for upgrades in the forward direction. The BaBar magnet attacks this classic problem by using an increased winding density at each end, thereby sacrificing uniformity of the field at large radius, for an extended "sweet spot" of field in the middle. Thus the region in which sPHENIX plans to install tracking features a close-to-ideal magnetic field shape. It should further be noted that the calculations of Figure 3.1 are done with a return yoke that allows for future upgrades in the forward direction.

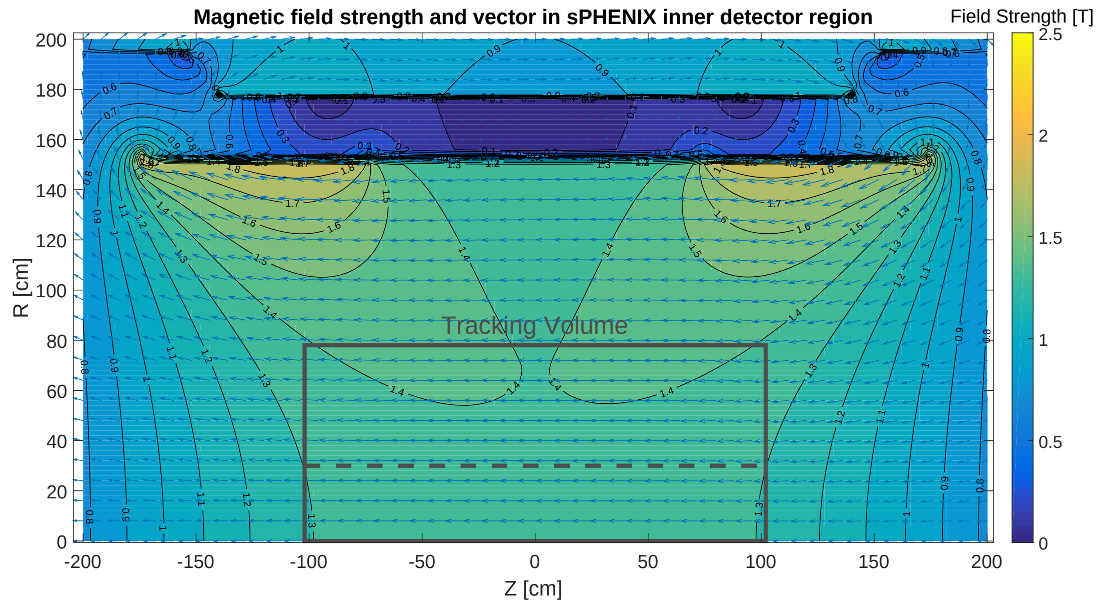

Figure 3.1: The BaBar magnet field superimposed with the dimensions of the tracker volume. This calculation includes the effect of the field return as envisioned for future upgrades (forward arm spectrometer). The dashed line indicates the inner radius of the TPC tracking volume.

3.3 TPC Design Overview

The TPC design follows the classical cylindrical double-sided TPC layout used in several other experiments, with a central membrane electrode located at the middle of the interaction region dividing the TPC into two mirror-symmetric volumes, as shown in fig. 3.2.

In each such volume the readout plane is located on the endcap inner surface, facing the gas volume. The electric field, transporting primary ionization to the readout plane is formed by the membrane electrode set to the highest voltage bias on one side and by the the readout plane at ground potential on the other. The electrical drift field is constrained by the field cage along the inner and the outer cylindrical surfaces of the TPC.

The two mirror-symmetric parts of the TPC form a common gas volume filled with the gas mixture, which transports primary ionization to the readout plane on each TPC endcap surface. The same gas that transports primary ionization also serves as the medium for the amplification elements located in front of the readout planes. These amplification elements are built based on several layers of micropattern gaseous detectors.

Other TPC subsystems directly related to the main volume are the channel readout system; high voltage distribution systems for the drift field and for the amplification elements; gas circulation, control and purification system; TPC calibration systems. Operation and

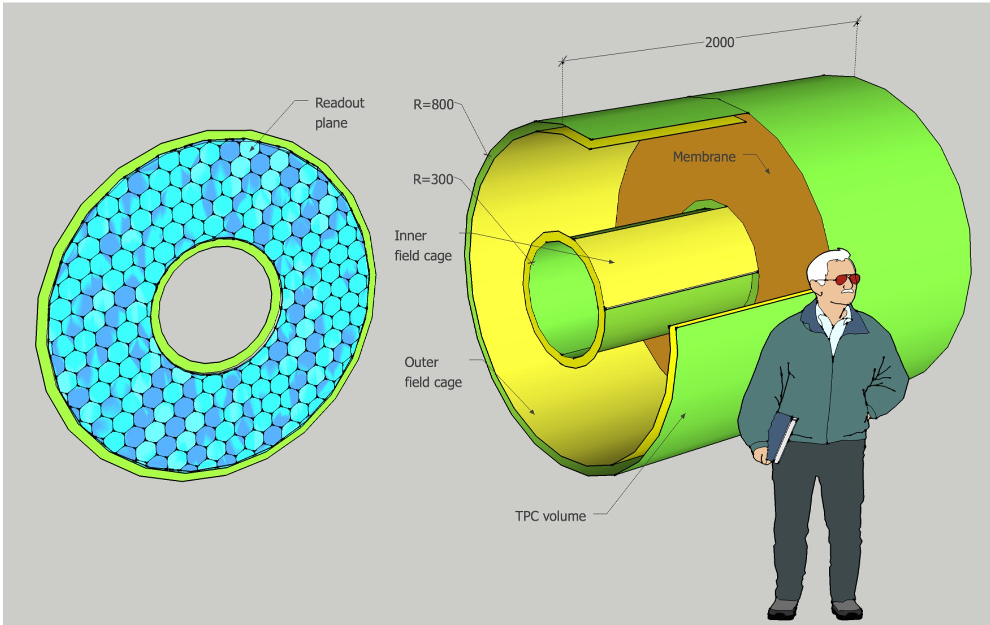

Figure 3.2: Schematic layout of TPC main elements.

Size	end/TPC	sector/end	cards/sector	channels/card	channels/TPC
R1	2	12	5	256	30720
R2	2	12	8	256	49152
R3	2	12	12	256	73728
TOTAL					**153600**

Table 3.1: Table summarizing TPC module and channel counts.

readout of different service subsystems requires a TPC slow control system.

Each end of the TPC will be divided into 12 azimuthal segments and three radial segments. This size of GEM chamber is well established in multiple experiments and should lead to stable and reliable operation. Charge from individual pads will be collected by SAMPA chips (developed by ALICE) on the so-called FEE cards. Each FEE will house 8 SAMPA chips and thereby 256 channels. The R1, R2, and R3 modules support 5, 8, and 12 FEE cards respectively. Thus, the total number of channels for the TPC is 153,600. These channel counts are summarized in Table 3.1

Data flowing from each TPC sector (25 cards) will be collected into a Data Aggregation Module (DAM) wherein clustering algorithms will be performed prior to the data entering the main sPHENIX DAQ stream.

3.4 TPC Simulations

The TPC simulations we have performed target a realistic representation of the cluster size and two-hit resolution based on design parameters *which are consistent with those described in the previous section*.

At the very high luminosities expected during sPHENIX operation, the charge collection time in the TPC causes charge from multiple different collisions to be drifting in the TPC at any given time. The time window for the configuration used for these simulations is $\pm 13.2\ \mu s$. At a Au+Au collision rate of 200 kHz the number of "pileup" events is typically 3 to 8, and they add very substantially to the occupancy in the TPC. In p+p collisions it is far higher, but the multiplicity per event is much lower. The simulation results presented here are for Au+Au, and to simulate the detector performance in high luminosity events we use central (0-4 fm impact parameter) Au+Au collisions as the triggered event, and a 200 kHz minimum bias collision rate to add pileup event charge.

GEANT4 is used to record energy deposits in a cylindrical volume of gas. In the results shown below, the volume was filled with a Ne:CF_4 mixture (90:10) operated with a drift voltage of 400 V/m and a drift speed of 8 $cm/\mu s$. The energy deposits are recorded in discrete radial regions of the cylindrical volume. For each region, a Poisonnian random number of ionization electrons are produced along the track trajectory according to measured values of the average ionization per energy deposit for the simulated gas. Because highly angled tracks deposit energy along an extended path in z within each radial layer, they have an important effect on the occupancy in the TPC. Therefore the primary ionization is broken up into segments in z that are drifted independently. Each segment of the primary ionization is then randomly diffused in 3 dimensions. The average diffusion is then added in quadrature with a constant diffusion to emulate diffusion during the amplification stage of readout.

The $r - \phi$ readout is simulated using a plane of "zigzag" pads having the planned geometry of the chevron pads, so that charge sharing is properly accounted for. The charge distribution at the pad plane from each drifted z segment is divided between pads using an analytic formula that provides the fraction of the charge distribution on a pad as a function of distance from the pad centerline. For the z direction, the analogue timing response of the SAMPA chip is simulated with different rise and fall times that approximate the measured response of the chip. In these simulations a SAMPA peaking time of 80 ns is assumed. The resulting time distribution is broken up into ADC time bins, and the bins are assigned a z location based on the drift velocity. The charge is digitized into a 12-bit ADC for each pad, directly in proportion to the number of diffused electrons reaching the pad (gain fluctuations are not currently simulated).

After the pad ADC has been recorded in each time bin, clustering is performed to group (pad,time-bin) pairs into 3-dimensional detector hits to be passed to the track-finding algorithm. The current cluster finding algorithm is designed to operate in a high occupancy environment and can separate overlapping clusters as long as the cluster centroids are separated approximately 1.5 sigma of the cluster width. This performance is sufficient to guarantee close to 100% cluster reconstruction efficency in high pile-up Au+Au events up to a channel occupancy of $\approx$ 40%.

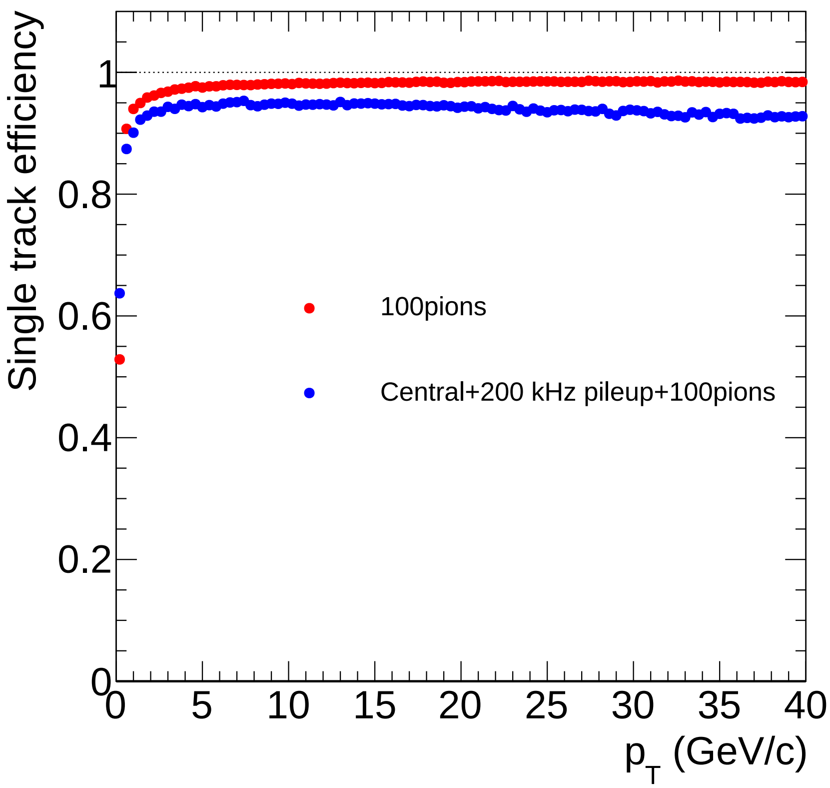

Figure 3.3: comparison of the track reconstruction efficiency for the simulated TPC for pions between 0 and 40 GeV/c in standalone 100 pion events, and embedded in central (0-4 fm) Au+Au collisions with event pileup from 200 kHz Au+Au collision rate. Even in the very high occupancy environment the tracking efficiency is $\approx$ 94%.

In addition to the TPC, the silicon strip INTT inner layers are included in the tracking setup. The clustering is performed on the silicon hits by finding groups of contiguous strips within a sensor.

From the clusters charged particle trajectories are reconstructed by a seeded kalman filter based algorithm comprised of the following steps:

- A 5-dimensional Hough transform is employed to locate clusters from helical hit patterns in the TPC arising from tracks bending through the solenoid field to seed the track reconstruction.
- Track seeds are propagated outside-in from the TPC. to the optional inner silicon based detectors by a Kalman filter [124] based pattern recognition algorithm.

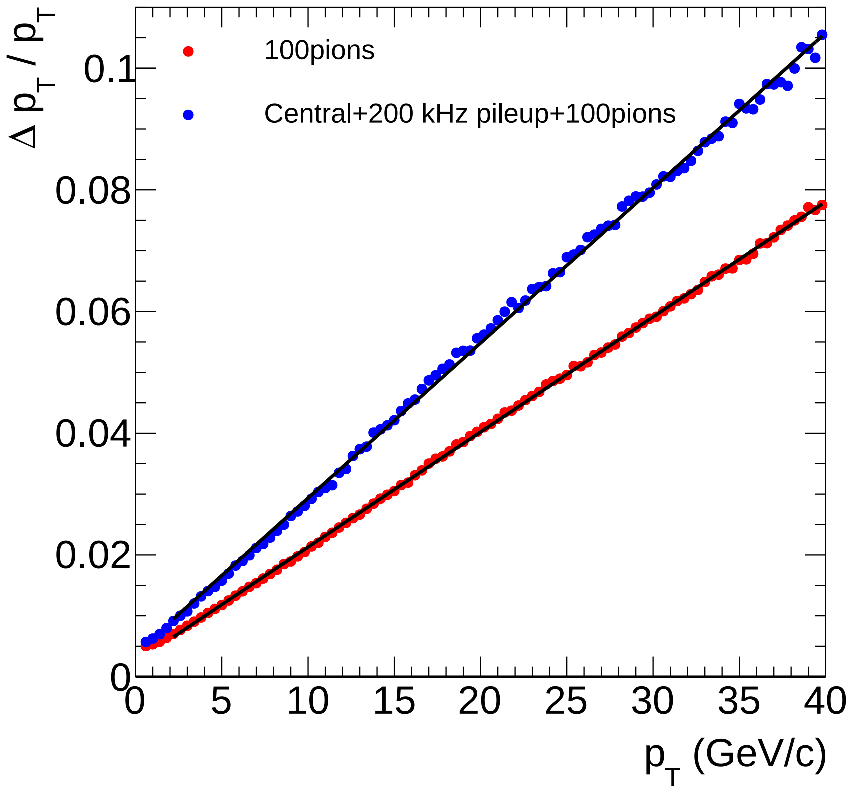

Figure 3.4: comparison of the momentum resolution of the simulated TPC for pions between 0 and 40 GeV/c in standalone 100 pion events, and embedded in central (0-4 fm) Au+Au collisions with event pileup from 200 kHz Au+Au collision rate.

- Iteration of the first two steps using looser seeding criteria in subsequent iterations.
- Clusters belonging to the same track are fit using a Kalman-filter-based generic track-fitting toolkit [125], to extract track parameters including displacement at the vertex and the momentum vector at vertex.
- All tracks are fed into a generic tracking fitting toolkit, RAVE [126], to determine the locations of the primary and secondary vertices's.

The performance of the detector in simulations is illustrated here by several figures. Figure 3.3 provides a comparison of track reconstruction efficiency for simulated events consisting of a central (0-4 fm impact parameter) HIJING collision, plus pileup from minimum bias HIJING collisions assuming a collision rate of 200 kHz. The track reconstruction efficiency is evaluated for 100 pions (p_T = 0-40 GeV/c) embedded in the central event. Reconstructed tracks are required to have a reconstructed p_T within 4σ of the truth p_T. The track efficiency is compared with that for low occupancy events, containing only the 100 pions. Figure 3.4 compares p_T resolution at low and high occupancies obtained from

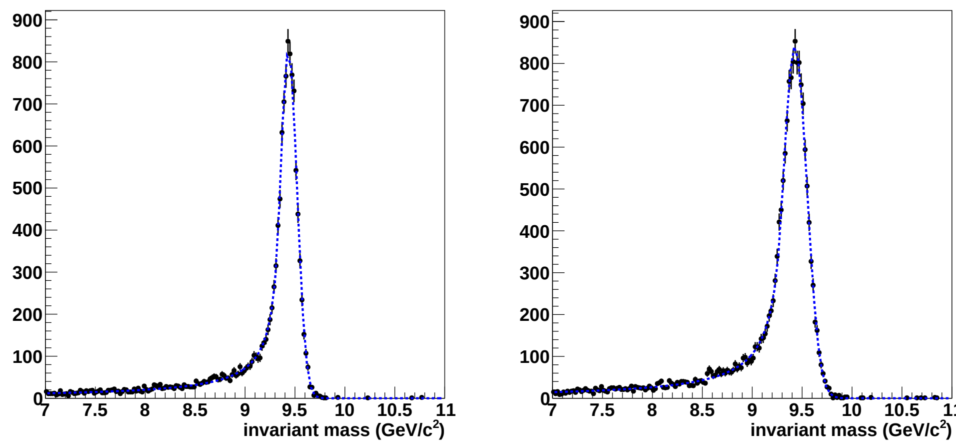

Figure 3.5: Upsilon 1S mass spectrum and resolution for the simulated TPC in low multiplicity events (100 pions), where the mass resolution is 85 MeV, is shown on the left. The mass resolution averaged over a store is about 120 MeV with the current very simple clustering algorithm, and is shown on the right.

the same simulations. Figure 3.5 shows the mass spectrum for reconstructed $\Upsilon(1S)$ decays, where on the left the Upsilons were embedded in low occupancy 100 pion events, and on the right they were embedded in the high occupancy environment of a central Au+Au collision with the collision rate integrated over a four hour store. The mass resolution is about 85 MeV in low occupancy events, but increases to about 120 MeV at the highest occupancies. This increase is caused by overlaps of TPC clusters in the highest occupancy case. The present clustering algorithm locates local maxima in the Z vs r-ϕ distribution and follows the distribution in all directions until the signal falls below threshold, or starts to rise again. Then the cluster centroid is evaluated using a weighted sum of the hits in the cluster. This very simple algorithm finds clusters with very good efficiency, but the precision of the centroid determination suffers from even small overlaps of clusters. We are investigating clustering algorithms that will provide better cluster centroid precision at high occupancy.

We have also tested the effect of high TPC occupancy on the performance of the tracking system if the proposed MVTX detector is added to sPHENIX. The goal is to understand whether the TPC as a tracker will work well in high occupancy events with a displaced vertex detector. The results for the $r\phi$ track vertex resolution are shown in Figure 3.6. Results for the track vertex resolution in the z direction are shown in Figure 3.7. The track vertex resolution shows little effect from the high occupancy except for the DCA resolution in the z direction at high momentum, where it is nevertheless still very good.

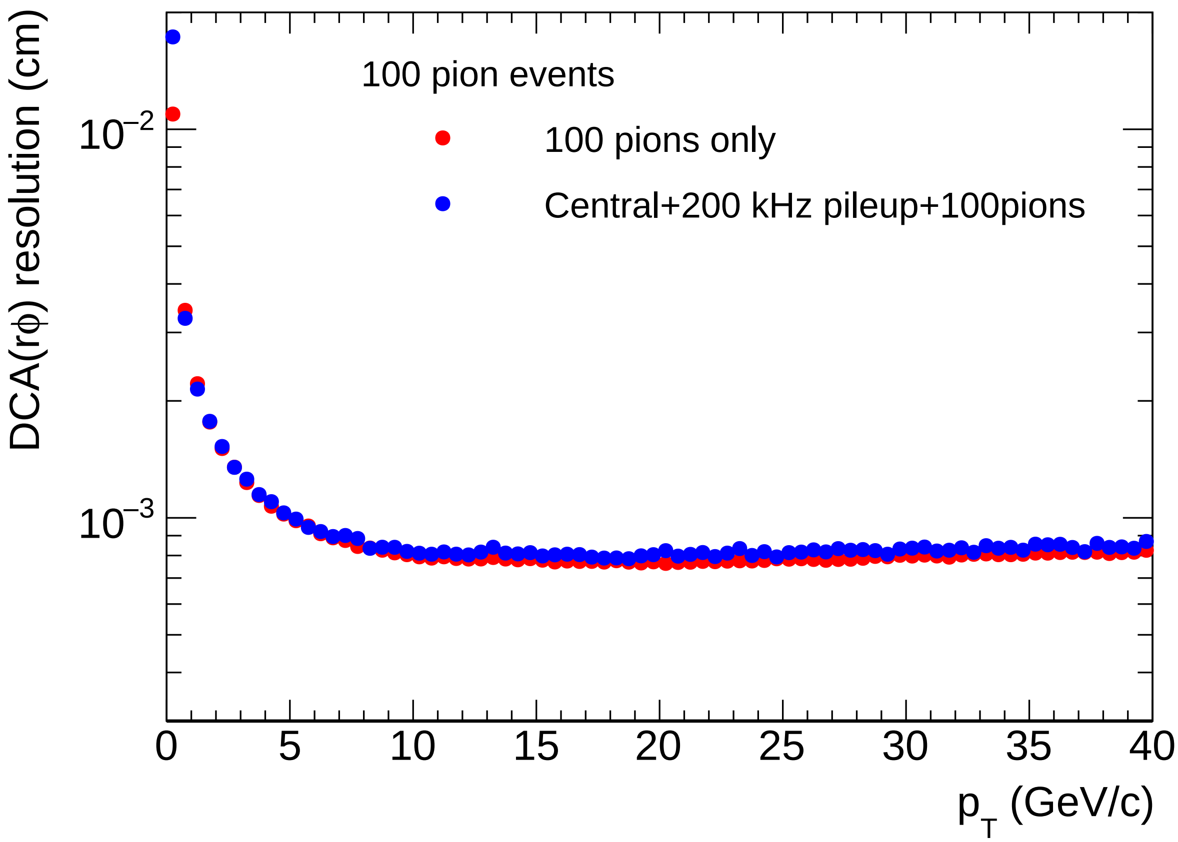

Figure 3.6: comparison of the DCA resolution in the $r\phi$ plane for a tracker consisting of the TPC and the proposed MVTX pixel barrel and the INTT silicon strip detectors. The comparison is for pions between 0 and 40 GeV/c in standalone 100 pion events, and embedded in central (0-4 fm) Au+Au collisions with event pileup from 200 kHz Au+Au collision rate.

3.5 TPC Design Details

3.5.1 Design Drivers

The TPC system must supply sPHENIX with excellent pattern recognition and excellent momentum resolution in order to meet all the physics goals. As detailed below, this is a challenging task, but not insurmountably so. Figure 3.8 shows in 3D model form the location of the TPC. Because the TPC is sandwiched between the EMCAL on the outside radius and the silicon detectors on the inside, the radial extent of the TPC is limited to $20\ cm \rightarrow 78\ cm$.

The radial extent along with the polar angle direction ($\eta < \pm 1.1\ units$) defines the TPC envelope as indicated in Figure 3.9, compliant with the sPHENIX envelope control specifications. As compared to prior TPC detectors used in heavy ion physics (STAR, ALICE) the

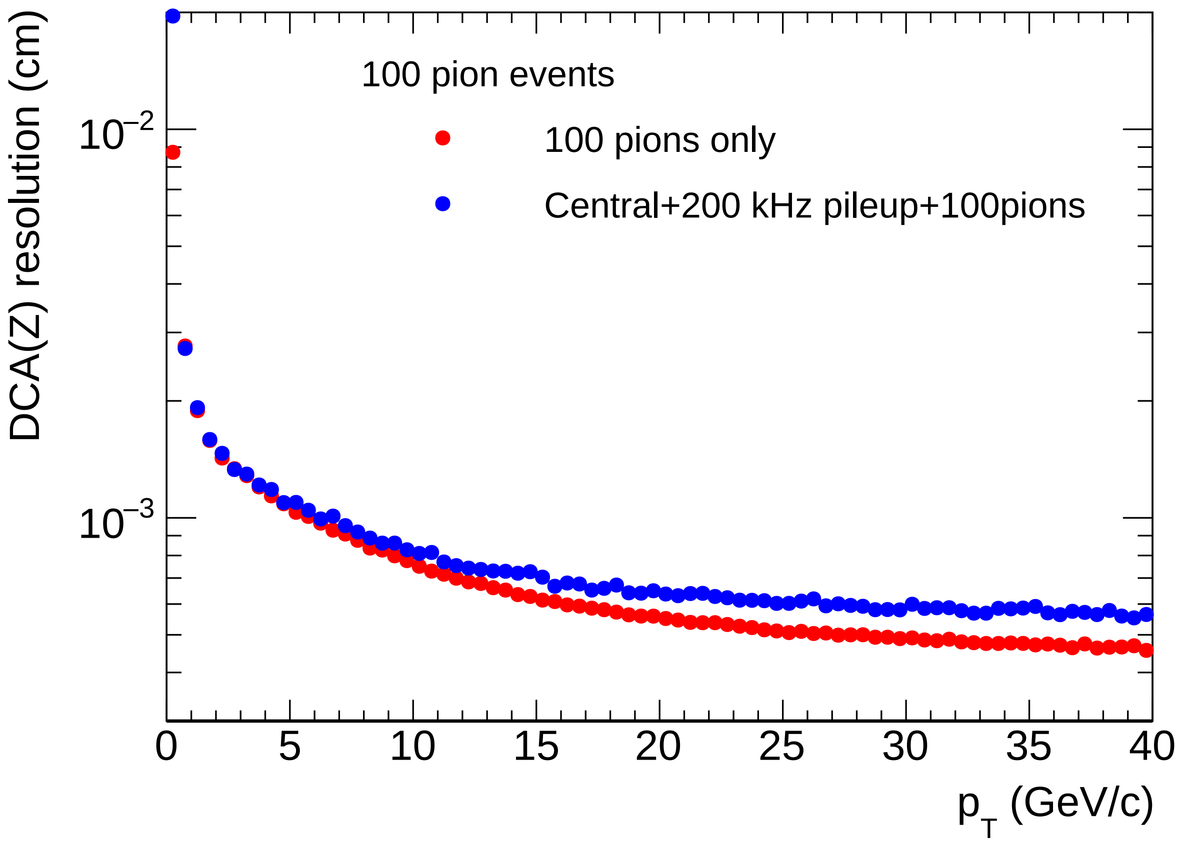

Figure 3.7: comparison of the DCA resolution in the z direction for a tracker consisting of the TPC and the proposed MVTX pixel barrel and the INTT silicon strip detectors. The comparison is for pions between 0 and 40 GeV/c in standalone 100 pion events, and embedded in central (0-4 fm) Au+Au collisions with event pileup from 200 kHz Au+Au collision rate.

sPHENIX will be rather small and is thereby referred to as a ”compact” TPC. while aspects of being compact simplify the detector construction (*e.g.* not requiring a scaffold to reach the detector top), others present challenges. In particular, a short gas length adversely affects the $\frac{dE}{dx}$ resolution and yields a small lever arm for momentum measurements.

Figures 3.3, 3.4 and 3.5 show simulations of the performance of the TPC and indicate that, as simulated, we meet or exceed all specifications. This performance is despite the short lever arm, but requires that the end-of-day resolution of the TPC should be better than 200 μm in the $r - \phi$ direction. While not significantly beyond the bounds of what has been previously achieved, we must maintain this performance in the face of high collision rates and possibly high space charge effects.

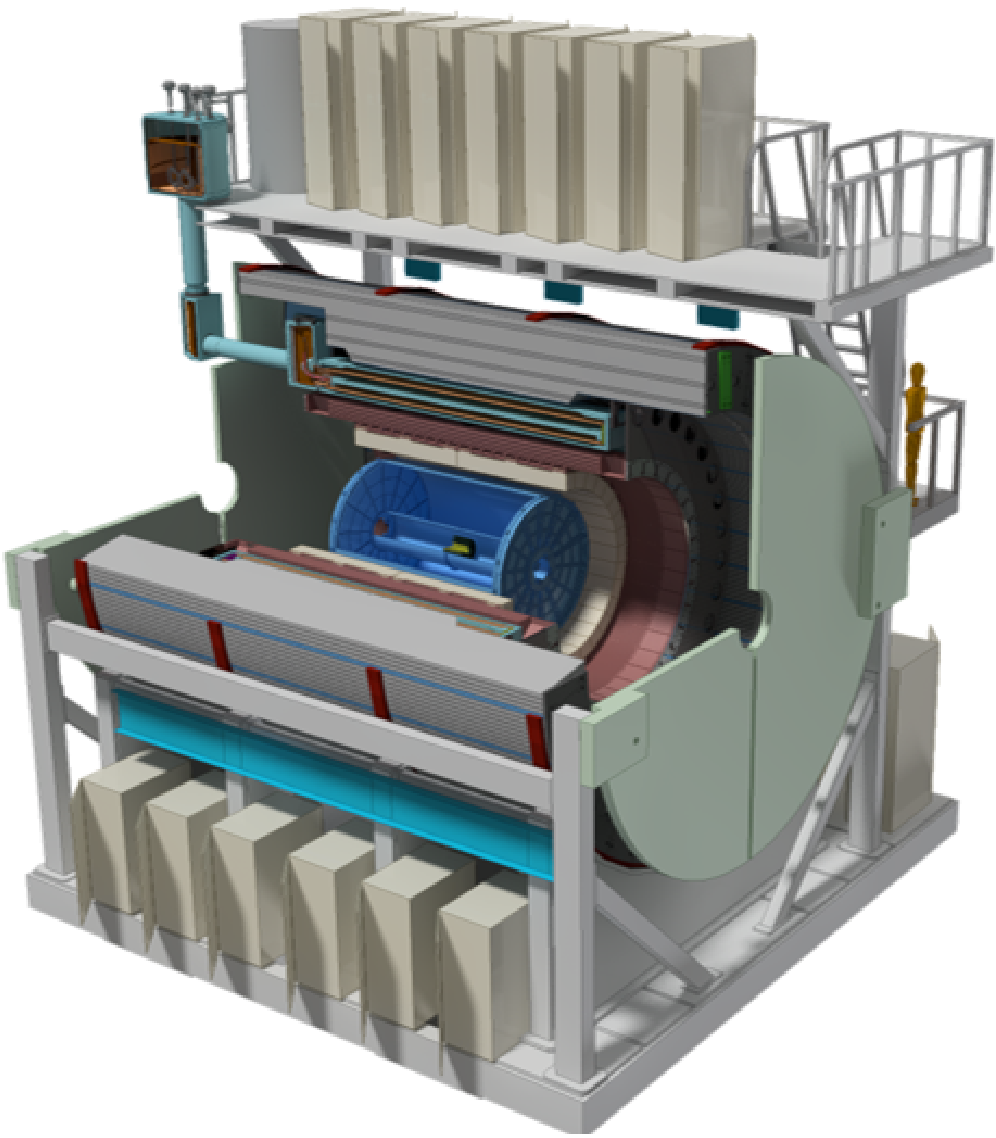

Figure 3.8: Schematic layout of the sPHENIX experiment. The TPC is presented as the central blue cylinder.

3.5.2 Limiting Space Charge Effects

Figure 3.10 summarizes the geometrical overview of the TPC. Tracking is accomplished by digitizing the after-avalanche electron clouds that impinge upon the amplification stage after having drifted away from the central membrane. Because of the enormous positive charge left in the gas volume following avalanche (here expected to be 2000X the primary charge), any TPC design must specifically deal with the positive ions to eliminate or at least minimize their impact on the TPC drift field. Traditionally this issues is handled by a so-called ”gating grid” whose bias can be set to either allow the flow and electrons (and

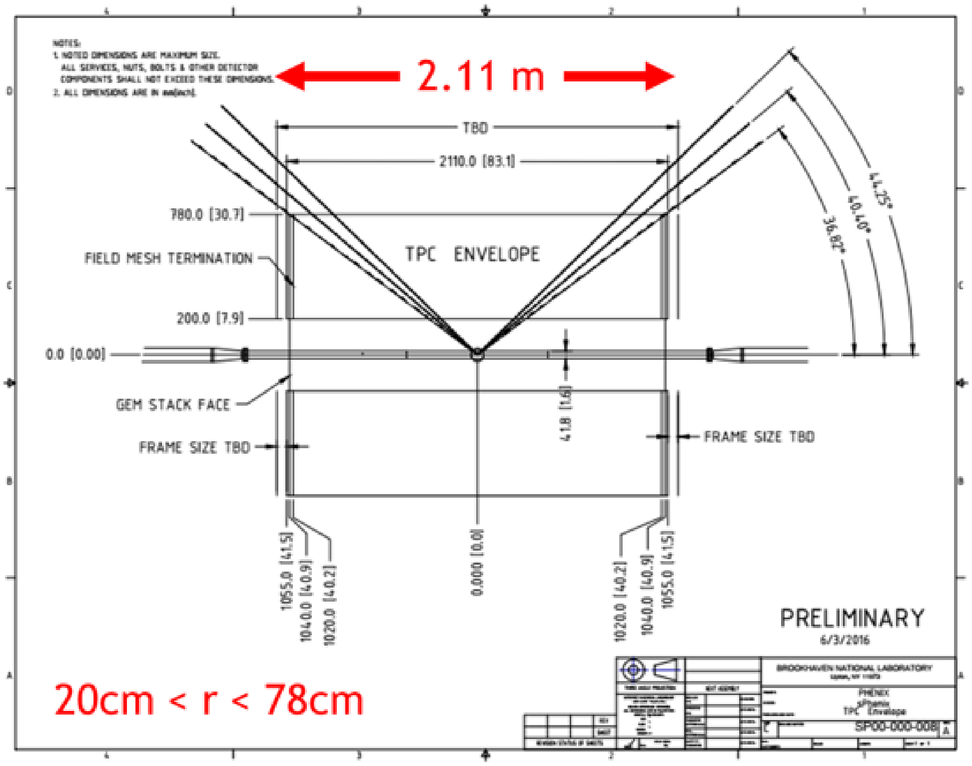

Figure 3.9: The outer limit of the TPC radial space (20 cm to 78 cm)is bounded by the INTT and EMCAL detectors and allows for an as-yet-unspecified future 10 cm PID upgrade device. The length is defined by the $\eta < \pm 1.1$ sPHENIX aperture.

ions) or deny this flow. A traditional TPC therefore operates by opening the gating grid upon receipt of a trigger, holding it open for a time sufficient to collect electrons with the largest drift time (*i.e.* those originating near the central membrane), and then closing it for a time period sufficient to block all avalanche-induced positive ions from entering the main TPC gas volume. Because of the ”off-time” for responding to positive ions, traditional TPC’s are considered somewhat slow devices.

A new concept in limiting Ion Back Flow (IBF, or avalanched-induced positive ions) has been pioneered by the ALICE collaboration and is expected to be brought online by them prior to first data-taking with sPHENIX. With the advent of MPGD (Micro-Pattern Gas Detector) technology a breakthrough is possible in IBF handling. As indicated in Figure 3.11, the avalanche stage of a gas detector can be made using a stack of Gas-Electron Multiplier (GEM) foils. Each foil contributes a small fraction of the total gain, which is achieved only when avalanching through the full stack. However, through clever manipulation of the electric fields between GEM foils (”transfer” fields) one can generate a condition whereby only a very small fraction of the positive ions are able to drift back into the main detector volume. In this way, the detector can be kept fully live at all times.

Unfortunately, the MPGD-based avalanche scheme is not 100% effective at blocking posi-

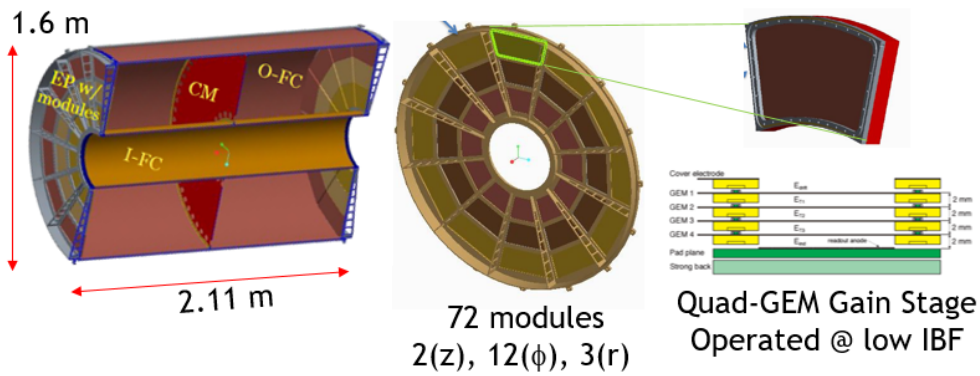

Figure 3.10: Ionization drifts away from the central membrane of the TPC and impinges upon the avalanche chambers located at each end. The end plates are segmented into 12 azimuthal and 3 radial segments, making a total of 72 modules in total. Each module is a quad-GEMstack operated in a low IBF configuration.

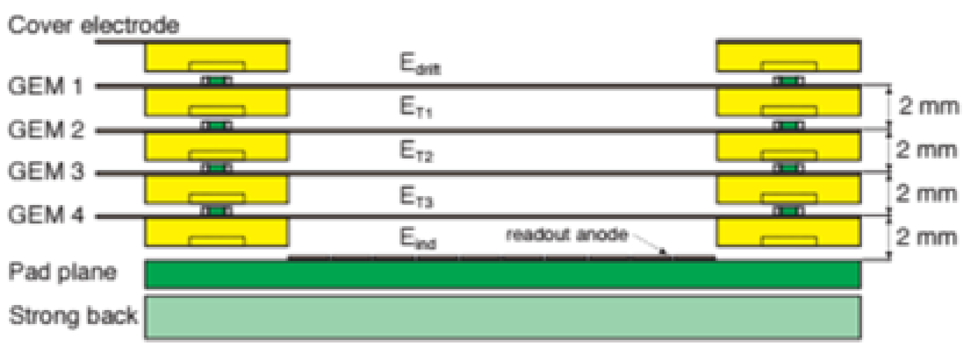

Figure 3.11: This figure shows the final design of the ALICE avalanche modules using a quad-GEMstack. We expect to operate similar chambers or perhaps a hybrid μMEGA arrangement.

tive ions from entering the gas volume. Figure 3.12 illustrates the problem. charge from the primary ionization (indicated by blue lines) is released into the gas volume. The positive ions will drift toward the central membrane with some having short paths and others longer. Conversely, all IBF positive ions begin at the avalanche chambers and therefore drift through the entire TPC gas volume. Because of the large disparity in drift velocity between the fast electrons and slow ions, the TPC effectively ”stores” a past time history of ionization in the form of pancakes of charge that slowly drift toward the central membrane. Even in the case of upgraded ALICE working optimally, when operating at a gain of 2000 and an IBF fraction of 1%, the IBF positive charge will exceed the primary by a factor of 20X. Thus, all possible precautions and design considerations must be applied to the IBF issue.

The analytical expression for space charge density in radius and z, developed by STAR,

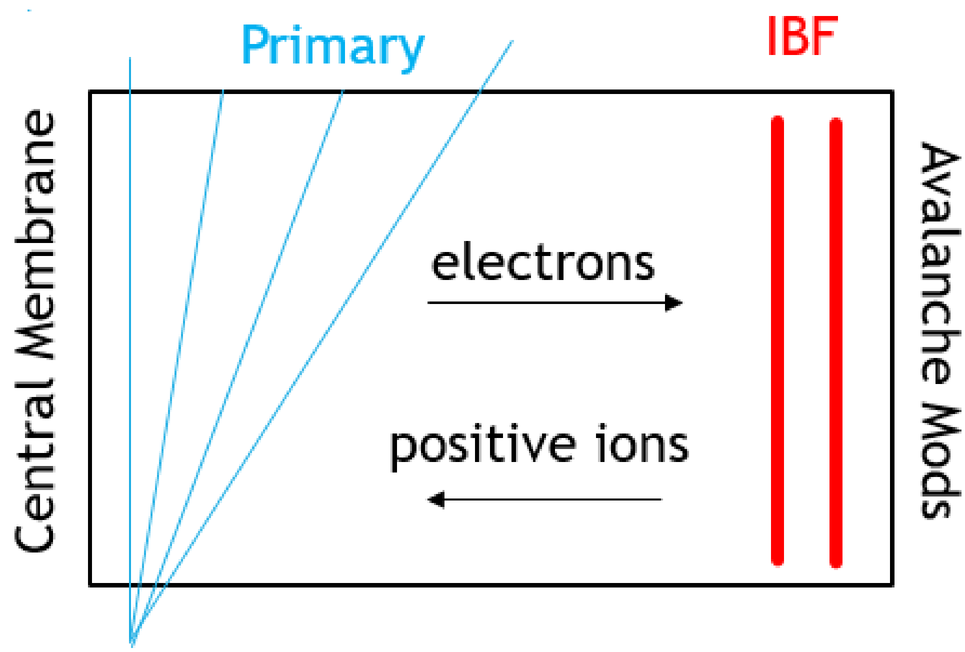

Figure 3.12: All ionization produces both signal electrons and positive ions. Primary ionization sets the lower limit to TPC space charge. However, even small percentage back flows from the avalanche stage (here represented by the red "pancakes" of drifting charge) contribute significantly to the overall space charge and will likely be the dominant source.

has the form:

$$\rho(r,z) \propto \frac{I \cdot M \cdot R}{v_{ion}} \left[\frac{1 - \frac{z}{Z_{tot}} + e}{r^2} \right] \tag{3.1}$$

where $1 - \frac{z}{Z_{tot}}$ accounts for primary ionization and e accounts for IBF. Figure 3.13 shows the relative contributions of the two forms of space charge. The left panel shows the result from only primary ionization. The right panel shows the effect of adding only 1% IBF at a gain of 2000X. The space charge comes overwhelmingly from the non-absorbed fraction of avalanche charge. For this reason, we put our initial TPC design efforts into minimizing IBF. The following sections summarize each of the design steps we have used to combat and minimize IBF.

3.5.2.1 Ion Drift Velocity

In general, the ion drift velocity is given by the expression:

$$\vec{v_{ion}} = K\vec{E} \tag{3.2}$$

where K is the ion mobility and $\vec{E}$ is the electric field. Although the ion mobility is, in principle, a function of the applied field, for all practical values of drift field, the ion

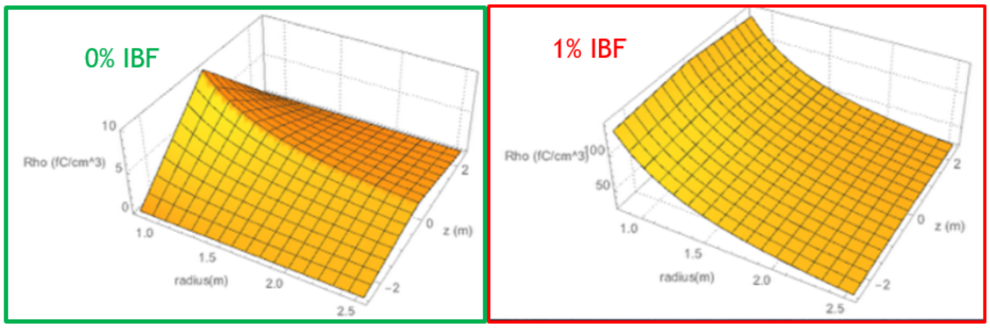

Figure 3.13: The left panel shows the anticipated space charge in the TPC resulting from only primary charges with a minimum bias collision rate of 100 kHZ. The right panel shows the result if one assumes 1% IBF from the avalanche stage operating with a gain of 2000.

mobility is a constant. Therefore, the initial attack on space charge involves maximizing the ion drift velocity by maximizing both the mobility and electric field strength. Figure 3.14 shows the ion mobility in pure gases as a function of mass. Clearly the fastest gases have the lowest mass, driving us toward Ne as the principle noble gas component for sPHENIX. The right hand plot in the same Figure shows the accuracy by which one can predict ion drift velocity in gas mixtures using Blanc's Law:

$$\frac{1}{K_{tot}} = \frac{f_1}{K_1} + \frac{f_2}{K_2} + \frac{f_3}{K_3} + ... \qquad (3.3)$$

Blanc's law is analogous to the formula for resistors in parallel. We can apply law to compare ion drift velocities across experiments as shown in the table below:

Gas	K ($\frac{cm^2}{Volt \cdot sec}$)	v_D $\left(E = 130\frac{V}{cm}\right)$	v_D $\left(E = 400\frac{V}{cm}\right)$
Ar	1.51	196	604
Ar-CH_4 90:10	1.56	203(STAR)	624
Ar-CO_2 90:10	1.45	189	582
Ne	4.2	546	1680
Ne-CH_4 90:10	3.87	503	1547
Ne-CO_2 90:10	3.27	425	1307(ALICE)
He	10.2	1326	4080
He-CH_4 90:10	7.55	981	3019
He-CO_2 90:10	5.56	722	2222
T2K	1.46	190(ILC)	584

It is clear that the space charge issues in STAR and ALICE are of an entirely different nature. in STAR, the ion mobility is low enough that the positive argon ions from the primary charge generate track distortions. In ALICE, both the noble gas choice (Ne instead of Ar) and the high drift field, dramatically reduce the distortions due to the space charge from the primary ionization. After upgrade, ALICE will struggle primarily with the ion back flow from the amplification stage.

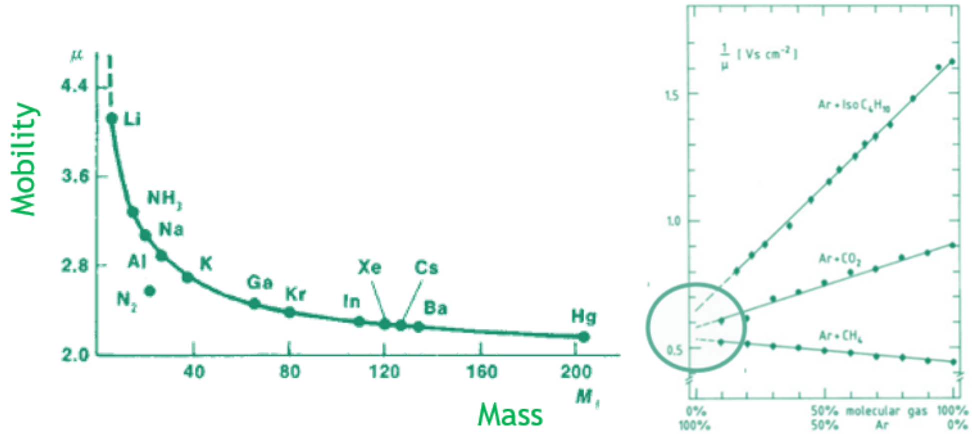

Figure 3.14: The left panel shows the mass dependence of positive ion mobility, clearly favoring light gases for high mobility and thereby low space charge. The right panel shows the effectiveness of Blanc's Law for calculating ion mobility in gas mixtures.

3.5.2.2 GEMstack Operating Point

ALICE has done extensive studies of the characteristics of IBF using a quad GEMstack. Their results are summarized in Figure 3.15. The vertical axis is an energy resolution measure based upon ^{55}Fe measurements. The 5.6 keV gamma from ^{55}Fe would be expected to have a fractional width $\frac{\sigma}{mean}$ of roughly 8%. However, one sees that in the limits of lowest ion back flow, the resolution worsens significantly. Understanding this effect is simple. In the ALICE configuration, any positive ions created by the top GEM will be coupled directly in to the drift volume. Therefore, lowering the gain in the first GEM is the most effective way to lower the IBF. However, fractional gain fluctuations are maximized at low gain, thereby spoiling energy resolution. Despite the many different running configurations represented in this plot, all fall basically atop the energy resolution vs IBF compromise curve.

For ALICE this is a critical consideration since their TPC's main function is the measurement of specific ionization, $\frac{dE}{dx}$. For sPHENIX the case is significantly simpler since our physics goals do not require a precision $\frac{dE}{dx}$ measurement. We therefore choose to operate our GEMstacks at the lowest point measured by ALICE, 0.3% IBF.

3.5.2.3 Field Cage Entrance Window

The finger-physics explanation of the effects of space charge in the TPC volume is simple: Positive ions attract electrons and thereby distort their trajectories toward the "middle" radius of the TPC. A more careful consideration reminds us that if space were filled with a uniform charge density, that there would be no net force on the electron. Therefore we are lead to the simple picture that space charge distortions maximize at both the inner

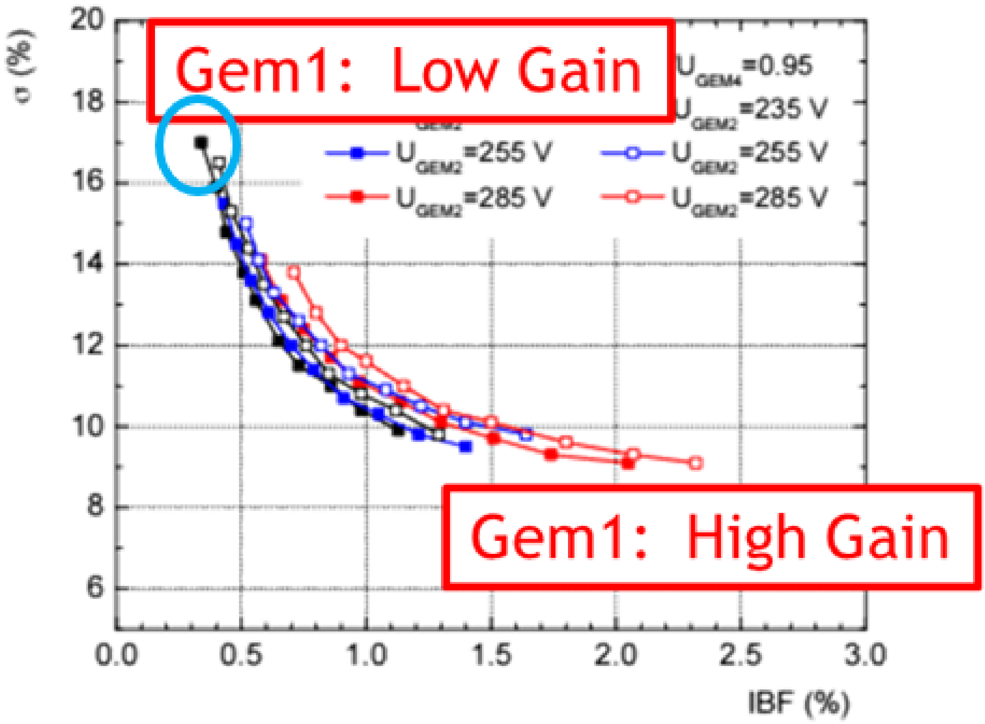

Figure 3.15: Results from R&D for the ALICE experiment indicate a ”universal” trend. Configurations with the lowest IBF suffer from poor energy resolution. The principle reason for this trend is the contribution of the first GEM to the overall gain.

and outer field cages where the space charge density has a discontinuity. Indeed, full calculations of space charge distortions for sPHENIX are shown in Figure 3.16. The blue curve indicates a calculation for a TPC spanning the radial range 30-80 cm. The maximum distortion is 2 cm found exactly at the inner radius. Notice, however, the red curve for a TPC spanning 20-80 cm. At the lowest radius, the distortion is indeed severe (3 cm, 50% worse than before), however the distortion of the track at 30 cm is drastically reduced to only 3 mm!. Thus, by modifying our TPC design from the originally-proposed version (30-80 cm) to a new version that spans (20-80 cm), can can easily and dramatically reduce space charge to under 1 cm.

3.5.2.4 Passive Mesh for IBF Reduction

Although our current proposal for IBF reduction (Ne gas; High E-field; Low IBF Op Point; Moved Inner Field Cage), makes our distortions manage-ably small, there is still significantly more that can be done to reduce IBF. Such a reduction would allow us to, for example, change the operation point of the GEMstack to regain much of the lost resolution. To understand the technique we must first gain insight on how IBF reduction in an MPGD detector works.

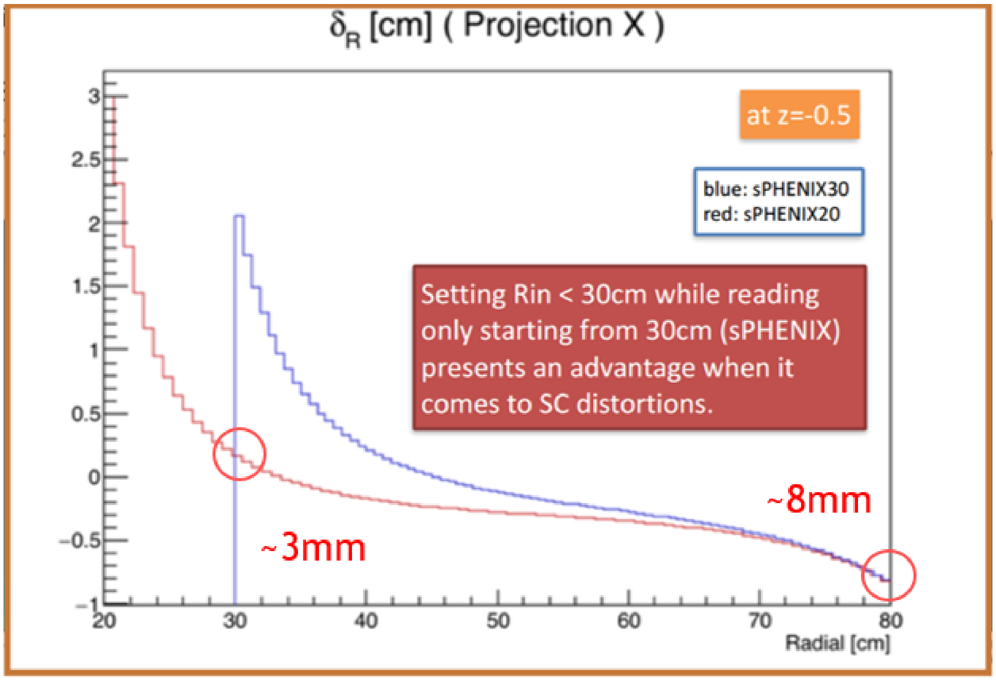

Figure 3.16: Electron paths are primarily influenced by the charge density closest to the electron. Necessarily, the greatest deflections from the ideal trajectory are found closest to the field cage. By moving the field cage entrance window from 30 cm to 20 cm, we are able to drastically reduce the deflection due to IBF to reasonably manageable levels.

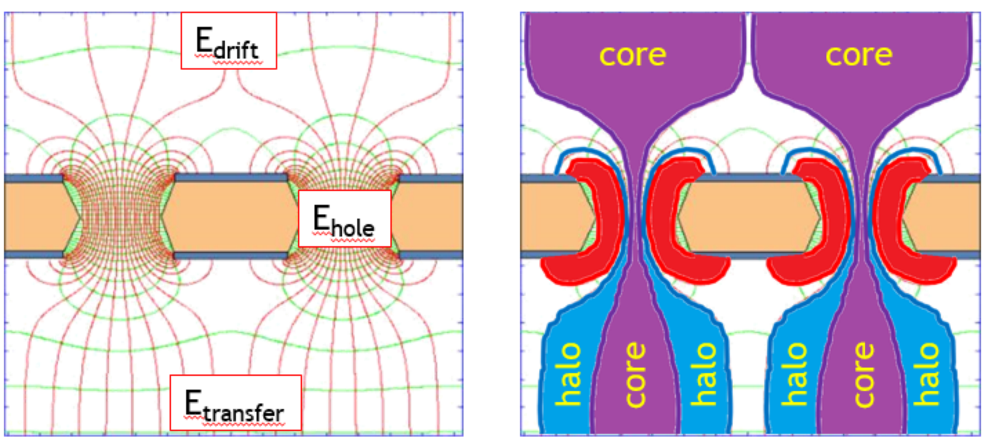

Figure 3.17: In the limit of zero diffusion, one can easily visualize the mechanism behind IBF suppression. When the exit field of a GEM significantly exceeds the entrance field, near 100 % electron transmission is achieved while many or most of the ions terminate instead on the GEM itself.

Figure 3.17 shows the electric field lines of a GEM under operation in the left panel. Notice that the density of field lines below the GEM is greater than above, indicating the the transfer field exceeds the drift field. The right hand panel shows the limit in which we ignore diffusion during transport. The violet region indicates the field lines passing from above the GEM to below. The blue "halo" region surrounds the "core". Electrons beginning above the GEM will all be transported through the holes. However, ions beginning below the GEM will distribute themselves among the core and halo, thereby having only a fractional transmission.

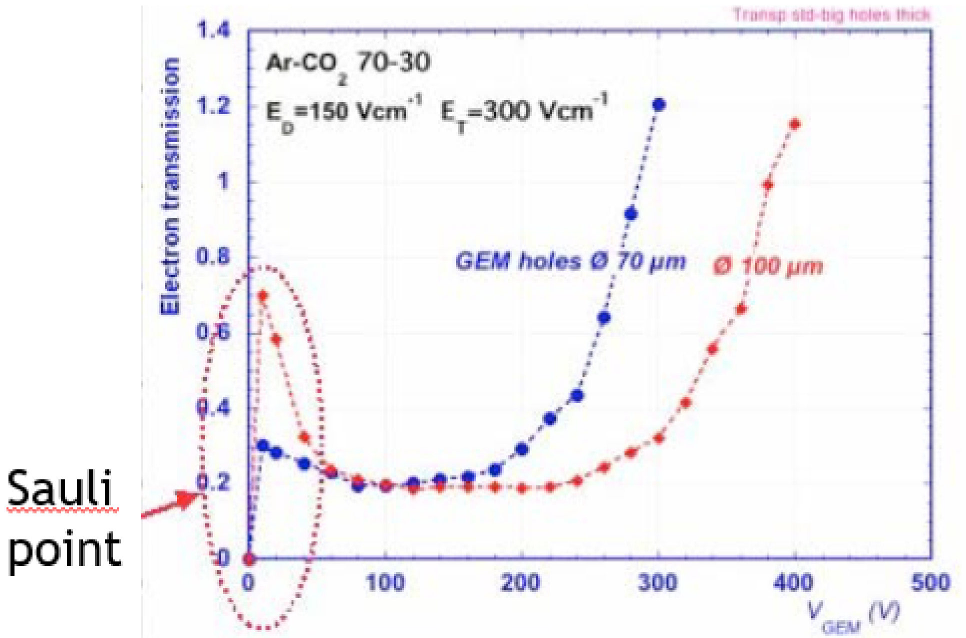

Figure 3.18: The so-called "Sauli Point" for a GEM is a spike in electron transmission at very low dV. sPHENIX has proposed and simulated using either a low ΔV GEM operating at the Sauli Point or even a simple mesh to create an electron-transparent but ion-blocking shield.

This effect is quite similar to that which induces the so-called "Sauli Point" (Figure 3.18) for GEM transparency at low avalanche field. Indeed, this phenomenon has served as the basis for design of the gating GEM anticipated for use the the ILC TPC. Inspired by that possibility and further encouraged by a private suggestion that the same might be accomplished by a passive mesh (H. Appelshäuser, ALICE), we began a second consideration of methods to combat IBF without compromising energy resolution.

Figure 3.19 summarizes the approach. The well understood degradation in energy resolution with decreasing IBF comes from fluctuations at low gain the the first GEM. Indeed, statistical distributions enforce this tendency, for example Poisson distributions have the variable equal to the mean. However, an avalanche is different. At the very least the primary electron in the avalanche will be present at small gain ∼1. For this reason, an avalanche stage with full transparency and no gain introduces no fluctuations. If such a structure were placed with asymmetric entrance and exist field, it is natural to assume that the electric fields would dictate high transparency and low IBF.

Full GARFIELD simulations indicate that this configuration should be viable. Many different mesh geometries have been modeled by sPHENIX, one of which is summarized

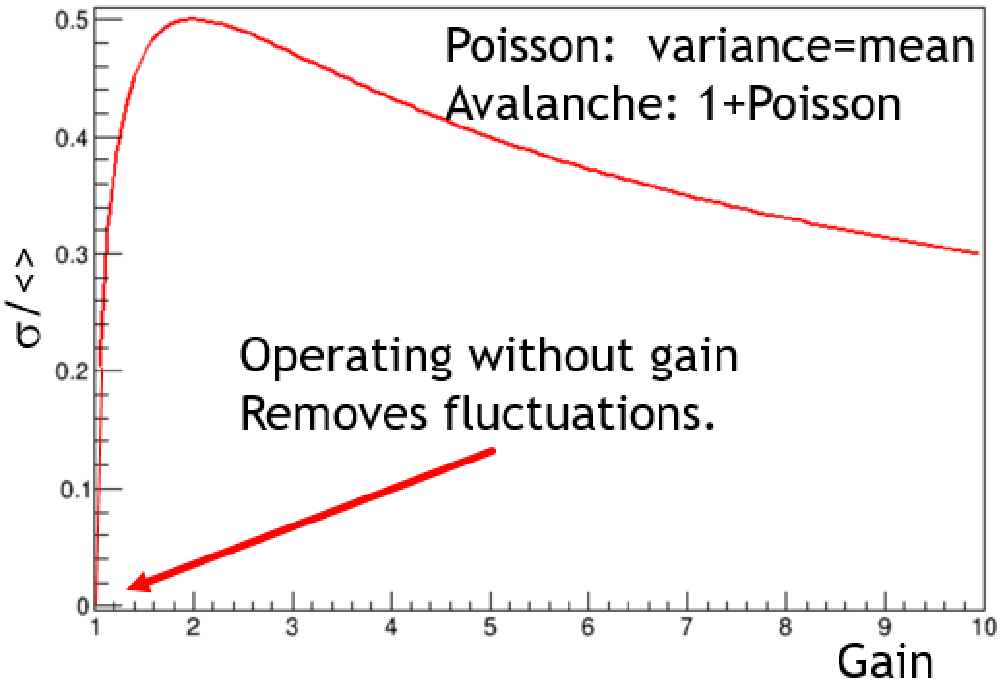

Figure 3.19: Electron gain differs from simple statistical calculations (*e.g.* Poisson) because even without gain, at the very least the electron that enters the avalanche exits as well. Therefore the fluctuations (measured as $\frac{\sigma}{mean}$) vanish in the low gain limit.

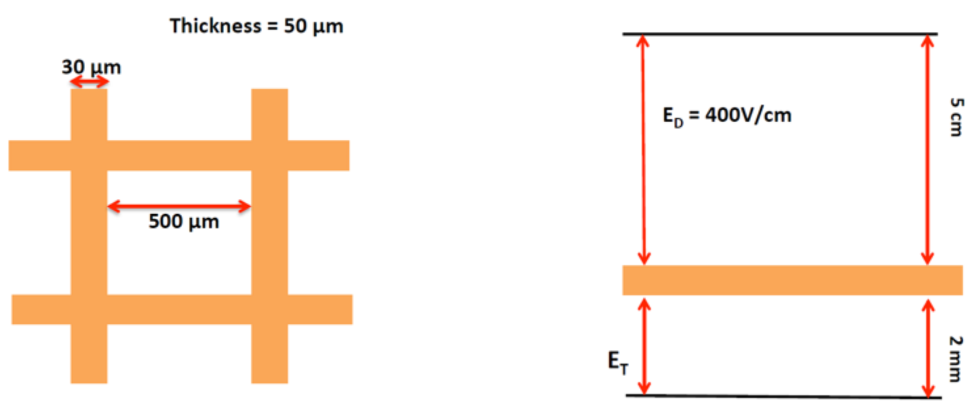

Figure 3.20: Full GARFIELD simulations including magnetic field in the idealized mesh shape shown here, square holes photographically etched into flat metal.

in Figures 3.20 and 3.21. Both the electron transmission (forward direction) and the ion blocking (backward direction) have been measured using GARFIELD in our operating gas and as a function of magnetic field in the TPC. Clearly, for quite reasonable ratios of drift and transfer fields, one can achieve nearly 100% electron transmission while blocking about 80% of the positive ions. This would, in principle allow for much more favorable operating points with very low IBF and good energy resolution. Future R&D will confirm these findings.

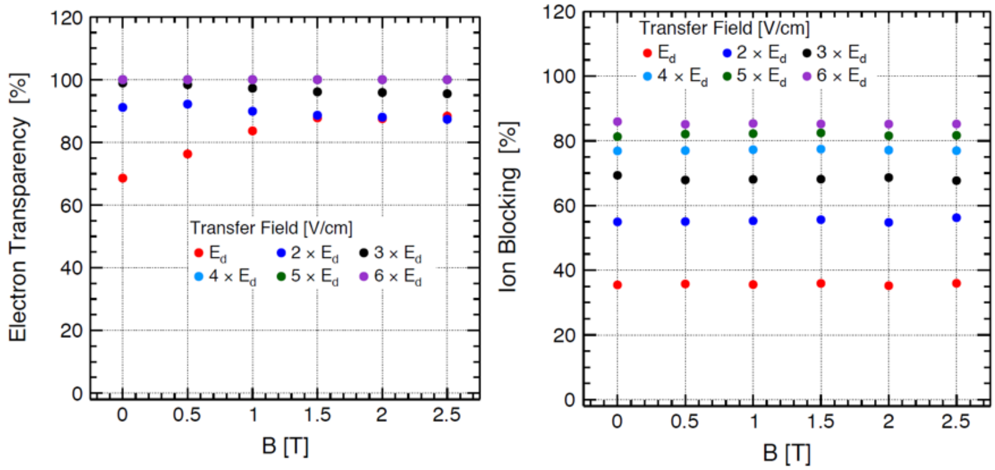

Figure 3.21: GARFIELD results indicate that for reasonable ratios of $\frac{E_{exit}}{E_{entrance}}$ near perfect electron transmission can be achieved while blocking 70-80% of the ions produced in the avalanche stage.

3.5.3 Diffusion and Resolution

The prior section justified our choices for minimization of IBF effects on the TPC:

- Use a low mass gas (Ne) to increase ion drift velocity.
- Use a high drift field to increase drift velocity.
- Select a GEM operating point for intrinsically low IBF.
- Move the inner field cage closer to the interaction point to counteract space charge.
- Adjust the field strengths on both sides of the field termination mesh to allow for passive IBF rejection.

These steps, will surely minimize the IBF distortions or a manageable level.This, our next consideration must be resolution.

The single point resolution of a gas chamber can be expressed as the quadrature sum of several terms:

$$\sigma_x^2 = \sigma_{pad}^2 + \frac{D_T^2 L}{N_{eff}} + \sigma_{sc}^2 \tag{3.4}$$

Here σ_x is the position resolution, σ_{pad} is the intrinsic resolution of the pad plane, D_T is the transverse diffusion constant, L is the drift length, N_{eff} is the effective number of electrons, and σ_{sc} is the uncertainty due to space charge distortion. The character of the diffusion constant reflects the random walk process. Clearly the lowest diffusion gas will give us the best precision so long as we achieve charge sharing among pads (so as to not ruin the pad term).

Although the N_{eff} term looks like simple counting statistics, it is somewhat more complicated. Two principle factors reduce the effective number of electrons as compared to the average number of ionization electrons. The first factor is only relevant when the number of electrons is very small on average. This one notes that:

$$\langle N \rangle \neq \left(\left\langle \frac{1}{N} \right\rangle \right)^{-1} \tag{3.5}$$

Although significant for numbers of primary electrons below 10, this correction is only a few % for our case. The second factor is more subtle and more significant. Since each electron's avalanche is of different strength, the error on the mean is larger than the error of a single measurement over $\sqrt{N}$. This calculated by Kobayashi for a Polya gain distribution with parameter θ as:

$$R = 1 + \frac{1}{1+\theta} \tag{3.6}$$

The the gases currently under consideration by sPHENIX this reduction in N_{eff} is between a factor of 1.5 and 2.

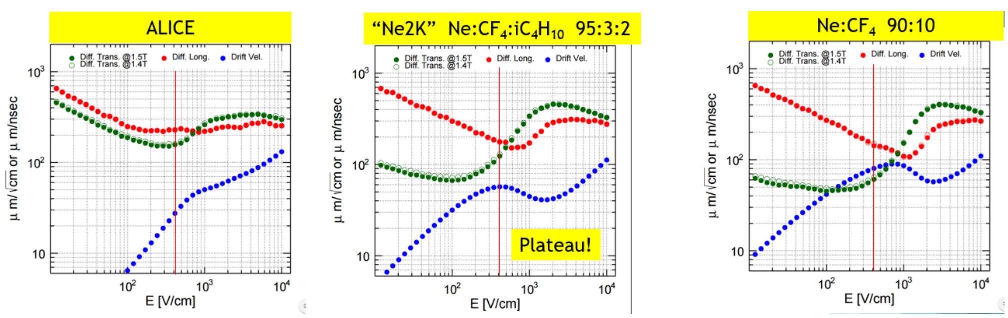

Figure 3.22: Three types of gases are analyzed for longitudinal diffusion (red), transverse diffusion (blue), and drift velocity (black). The left panel shows the original ALICE gas (Ar:CO_2), "Ne2K" (as described in the text), and our current leading choice (Ne:CF_4 90:10).

Figure 3.22 shows calculations of diffusion and drift velocity for several gas choices. The red curve is longitudinal diffusion, the green curve is transverse diffusion, and the blue curve (different scale) is drift velocity. Table 3.2 summarizes the diffusion-driven resolution.

Pure resolution considerations obviously favor the $Ne : CF_4$ gas mixture over Ne2K, however, the plateau at our exact drift velocity in Ne2K makes this remain an attractive choice. Both gases will be investigated moving forward.

Gas	N_{eff}	D_T	$\frac{D_T\sqrt{L}}{\sqrt{N_{eff}}}$	v_{drift}	T_{drift}	$\sigma_\tau(chr)$
Ne2K	31.4	$120\frac{\mu m}{\sqrt{cm}}$	214 μm	$56\frac{\mu m}{nsec}$	18 μsec	32$nsec$
Ne:CF_4 90:10	32.1	$60\frac{\mu m}{\sqrt{cm}}$	106 μm	$80\frac{\mu m}{nsec}$	12.5 μsec	17.5$nsec$

Table 3.2: Resolution comparison for Ne2K and Ne:CF_4 gases.

3.5.4 TPC Electronics

sPHENIX benefits tremendously from the developments in ALICE for their own TPC upgrade. In many ways, our detector is based upon theirs. It is therefore worthwhile to summarize their design before moving to the particulars of sPHENIX/

The ALICE TPC at the LHC is to read out continuously at 50 kHz in Pb+Pb collisions, a reasonable match to requirements at RHIC. Figure 3.23 shows the block diagram of signal processing based on the ALICE TPC upgrade electronics.

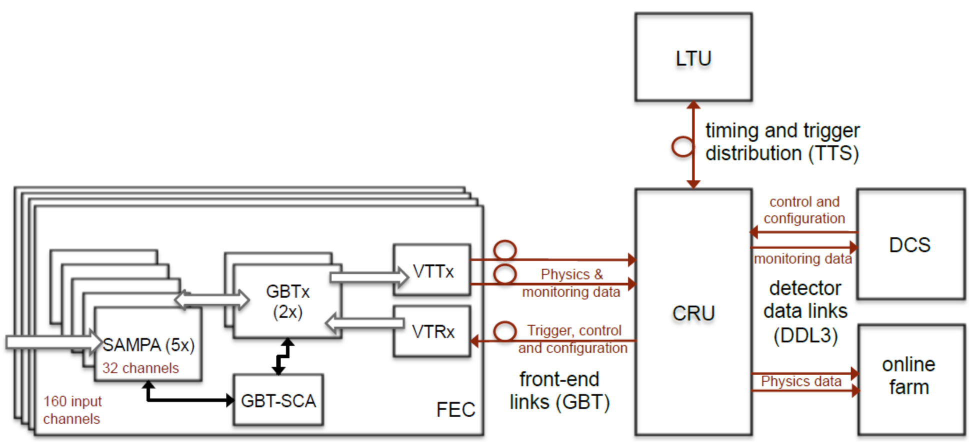

Figure 3.23: Block diagram of signal processing for ALICE TPC upgrade

Starting from the end of the signal processing chain, the Data Control System (DCS) and online farm is the computer system where the data are stored and processed for analysis. The LTU provides the timing and trigger signal to the Common Readout Unit (CRU), which is the post-processing system where some online calibrations and event reconstruction are performed.

The Front End Card (FEC) consists of SAMPA chips which amplify and shape the analog signals and digitize them. The DSP (data processing unit) is also on the chip. This formats the digital data into a data packet (it also performs baseline suppression, i.e., zero-suppression of the raw data). The packet is then sent to GBTx followed by VTTx. They convert the data packet into optical signals.

The block diagram of the SAMPA chips is shown in Figure 3.24. In the ALICE design, there

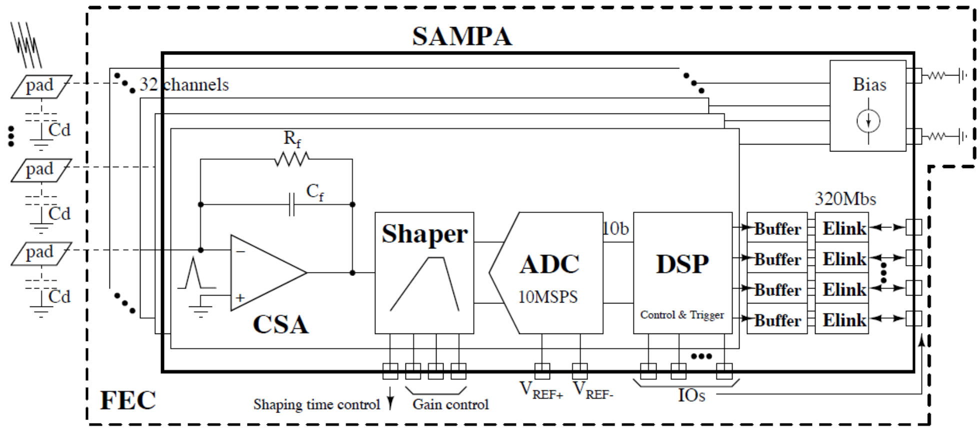

Figure 3.24: Block diagram of ALICE SAMPA chip

will be 5 SAMPA chips multiplexed by 2GBTx ASICs. One SAMPA chip accepts 32 inputs, therefore one FEC can process 160 inputs. The ALICE TPC will have 121 FECs per readout segment module. The TPC will be equipped with 18 segments in each side, 36 segments in total.

By contrast, the sPHENIX system is summarized in Figure 3.25. The sPHENIX FEE cards will each carry 8 SAMPA chips and thereby readout 256 channels on each FEE. Going outward in radius, the sPHENIX modules carry 5, 8, and 12 FEE cards respectively. This results in 153,600 active channels for the entire TPC system. Each sector of 25 FEE cards is serviced by a single PCI-express-based FPGA card, Data Aggregation Module (DAM), which is hosted on a server, Event Buffering and Data Compressor (EBDC). The DAM is responsible for event alignment and clustering. Furthermore, present calculations indicate that we can create false event boundaries from our continuous readout by copying ambiguous data into both triggered events. Then the result sub-event is compressed on EBDC and send to the sPHENIX event builder via Ethernet.

The SAMPA chip has reached a mature stage as evidenced by the waveform from the MPW2 test run. This waveform was obtained directly from the silicon in the ORNL laboratory of Chuck Britton. One should note that the SAMPA chip's rise time is on the slow side for sPHENIX. Our drive towards low diffusion to meet the resolution spec has necessitated the use of a ”cold” gas (namely CF_4) which has also increased the drift velocity. In principle, one should match the charge collection time to the time constant of the amplifier. With low diffusion and high drift velocity, there is a mis-match with the electronics time constant being longer than we would prefer. This increases the occupancy, but not to the point that the tracking efficiency is expected to suffer.

At the time of this writing we have received several SAMPA chips for testing. We have developed a utility test board that serves a list of important functions:

- The board opens multiple diagnostic channels to allow a complete evaluation of the

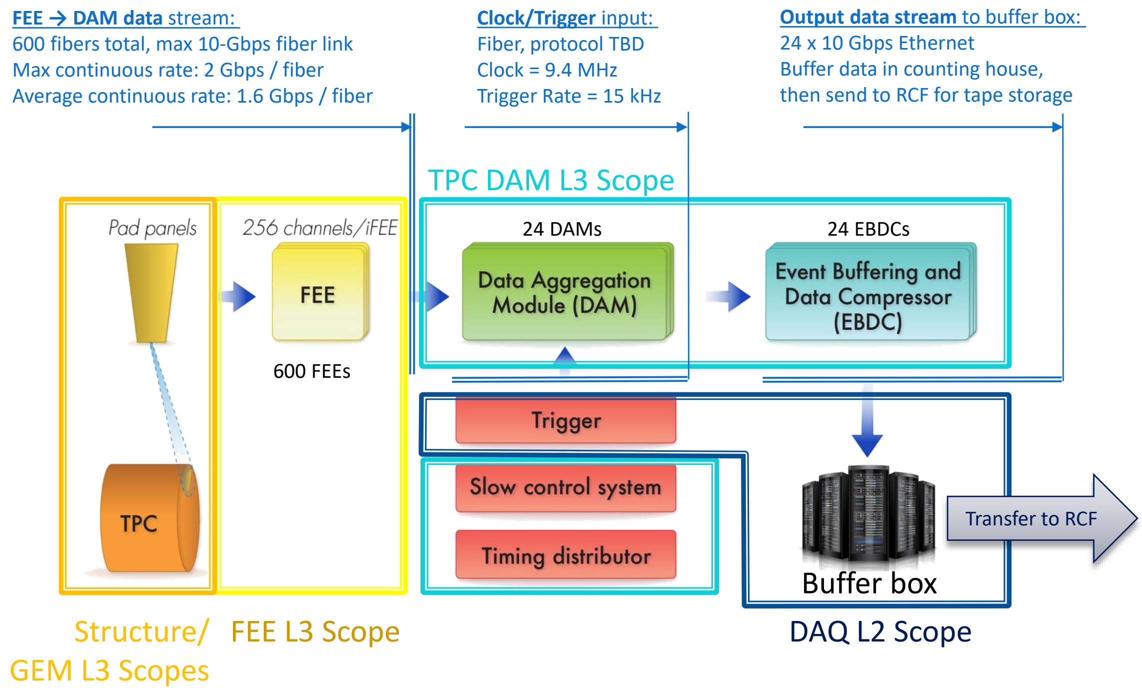

Figure 3.25: An overview of the TPC electronics chain. FEE cards housing SAMPA chips are located on board of the detector. Zero suppressed, untriggered data flows to Data Aggregation Modules (DAMs) hosted on Event Buffering and Data Compressors (EBDCs) located in the counting house. From there, the TPC data joins the main stream flow of the sPHENIX DAQ.

SAMPA chip.

- The board interfaces directly to existing GEM modules at BNL and Stony Brook so that physics signals (^{55}Fe, generated soft X-rays, cosmic rays) can be used to excite the GEMstack and read out through a SAMPA-based chain.

The experience of the test board should put us in an excellent position to develop the 8-SAMPA version of the board that will be compatible with modules on the main TPC.

Figure 3.26 shows the current leading implementation for the DAM device: using the ATLAS FELIX board. Because the DAM is a digital-in and digital-out board with on board programmable processing power, multiple already available options for implementation of the DAM exist. Figure 3.29 indicates a comparative study of the ALICE CRU module to the ATLAS FELIX module. Either of these devices fulfills the DAM throughput specification. While the CRU unit from ALICE can be paired with a SAMPA data stream, the FELIX board is being developed with the help of the BNL Instrumentation Division and ATLAS experiment since it appears likely to satisfy all the requirements, and local expertise will provide a stable platform for the DAM operations in the long term. Therefore, we determined the FELIX board as our first choice.

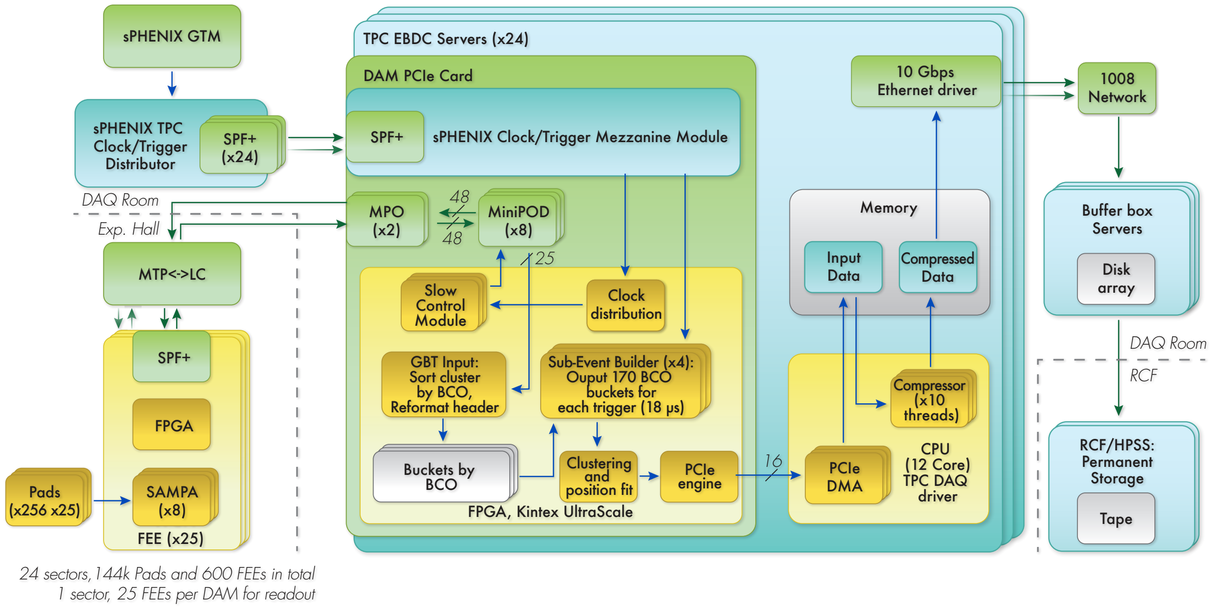

Figure 3.26: Block diagram for DAM and EBDC. Estimation of the DAM performance as realized using the FELIX board have been performed following this architecture assumption detailed in these diagrams. These studies indicate that not only can the FELIX card handle the desired throughput, but it can additionally assert "trigger coincidence" criteria by copying data from overlapping triggers into both events.

Data the DAM-EBDC system and at each processing stage is studied via a Monte-Carlo simulation of the collision and data stream. Part of the data stream from one of these simulation sets is shown in Figure 3.30. The result rate calculation is summarized in Table 3.4. We have also acquired via loan a FELIX version 1.5 card that is being used to study the throughput and verify the simulation results. This DAM and EBDC test stand has also been used as the DAQ in FEE prototype test stand.

3.5.5 TPC readout plane

One consequence of pushing resolution through low diffusion regards the size of the cloud that hits the pad plane. The advantages of a charge-division pad plane are entirely lost if the charge from a single avalanche is confined to 1 single pad. This this reason, "chevron" or "zig-zag" pads have been developed as a means of ensuring charge division for even narrow avalanches.

Figure 3.31 indicates the chevron segmentation style applied to our pad planes. Charge sharing is driven by the fine part of the zig-zag pattern, while channel count is driven by the macroscopic pad-to-pad spacing.

The radial pad size is ~1 cm. The transverse dimension of the pads varies with ~1 mm

Table 3.3: Raw data rate estimate for sPHENIX TPC and ALICE TPC cases

Parameters	sPHENIX (Au+Au 200 GeV)	ALICE (Pb+Pb 5.5 TeV)	Notes
dN/dy (Minbias)	180	500	
η coverage of TPC	2.2 ($\lvert\eta\rvert$ <1.1)	1.8 ($\lvert\eta\rvert$ <0.9)	
# of tracks in TPC	396	900	
Effective # of tracks in TPC (accounted for r-dep. η coverage change)	560	1690	note 1
Effective factor for track # increase for accounting albedo background	2	2	note 2
# of measurements in r	40	159	$\phi\times$time$\sim$20 bins for ALICE (from TDR)
# of samples in ϕ	3	2	
# of samples in timing	5	10	
# of bits of each sample	10	10	
Data volume increase factor by SAMPA header	1.4	1.4	Absolute maximum
Data volume/event (bits)	9.41×10^6	1.50×10^8	note 3
Data volume/event (bytes)	1.18×10^6	1.88×10^7	
Collision rate [kHz]	100	50	
Total data rate (bits/sec)	9.41×10^{11}	7.52×10^{12}	
Total data rate (bytes/sec)	1.18×10^{11}	9.41×10^{11}	

note 1: ALICE didn't estimate from first principle. We estimated for them.
note 2: We doubled the number of tracks to account for the background, based on STAR's experience.
note 3: Product of the previous seven rows. ALICE estimated the data volume as 160 Mbits/evt.

spacing of rectangular pads in the R1 module and ~2 mm spacing for the R2 and R3 modules.

The TPC amplification element is based on several layers of Gas Electron Multiplier (GEM) detectors. Traditional Muti-Wire Proportional Chamber (MWPC) technology is not considered because it a) cannot provide desired $r\phi$ resolution of 100 μm and b) the MWPC requires gating to stop ion back flow, and that significantly limits the data taking rate.

Four GEM layers are considered in the current scheme of the amplification element. Each GEM will provide gain in the range of typically a few thousand, suitable for the readout electronics considered for the TPC. The gain range is driven by two competing factors. Higher gains will improve the signal:noise and improve $\frac{dE}{dx}$ results, but will also increase the Ion Back Flow (IBF). ALICE intends to run at a gain of 2000 with SAMPA chip readout.

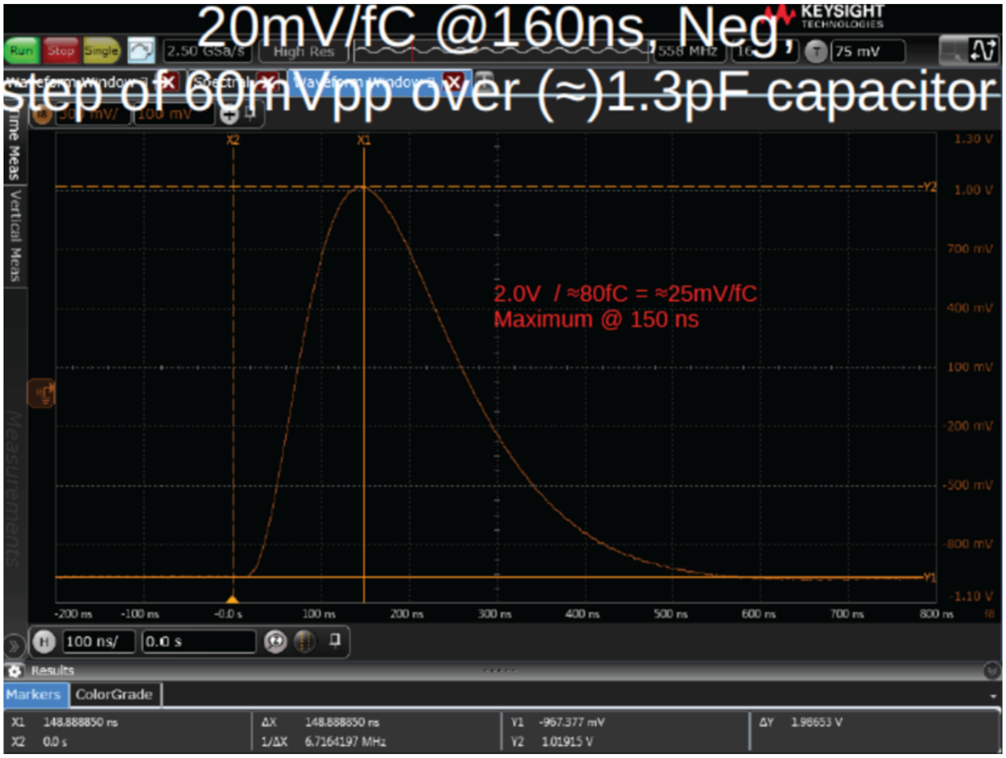

Figure 3.27: Wafer measurements at ORNL for ALICE capture the waveform coming from the SAMPA shaper in response to a delta-function excitation. The indicated peaking time of 150 nsec, while on the slow side for sPHENIX needs, is nonetheless OK for meeting our performance specifications.

ALICE results also demonstrate high stability of GEM operation in the environment of high energy heavy ion collisions.

The amplification element is shown in fig. 3.32.

The development of the sPHENIX TPC is greatly aided by the multi-year effort put into development of detector technologies for the EIC. In particular, this program has allowed studies of the complete suite of gas properties for all our candidate gases and many others that would be suitable for EIC, but not so much for RHIC.

Figure 3.33 shows the response of quad-GEM chambers to an X-ray source (^{55}Fe) in both the Ne2K and Ne:CF_4 gases current leading our choices. Experience in the lab showed excellent stability for both these gases over log running periods.

Furthermore, our R&D efforts have opened the door to BF measurements. Figure 3.34 shows an overlay of sPHENIX results on Ion Back Flow superimposed upon the iconic plot from ALICE, The agreement is excellent, opening the door to bench verification of some of the new ideas we have had for IBF suppression including the passive mesh concept. Currently we have **NOT** taken credit for this new effect in our simulations as a conservative measure to ensure that we do not over estimate the performance of our

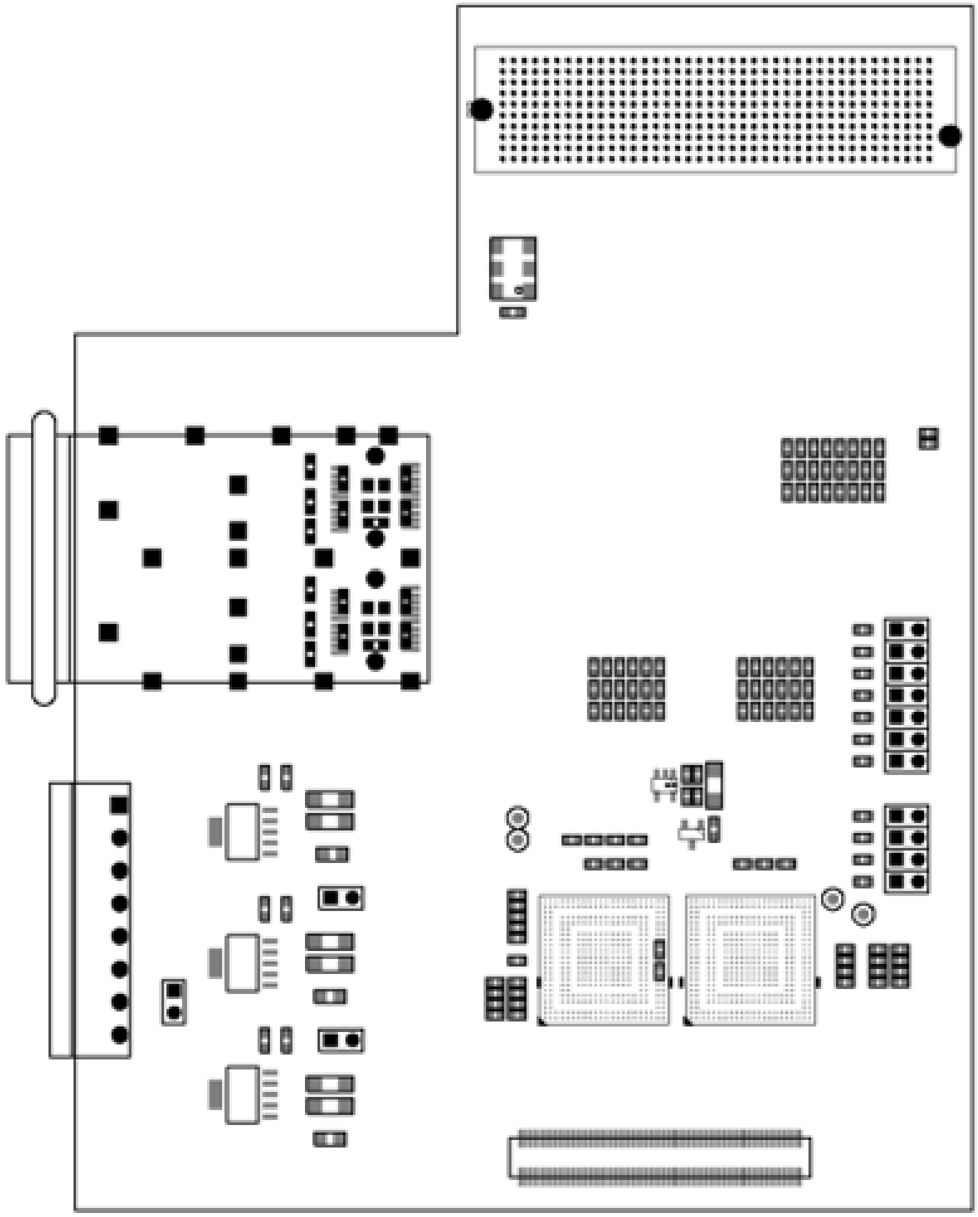

Figure 3.28: The first sPHENIX SAMPA prototype board is designed to house 2 SAMPA chips (similar to the iTPC for STAR) and a variety of diagnostic access points. The board is ordered. Delivery and firsts tests are anticipated for May 2017.

design.

One issue for all chevron pattern detectors is that of differential non-linearity. Typically the shape of the charge cloud folder with the segmentation of the pad plane does not produce a linear response with position. Indeed, as shown explicitly in Figure 3.35 the correlation between true position and measured position shows a saw-tooth pattern whose spatial period matches the pad spacing. Although our R&D shows that the troublesome response

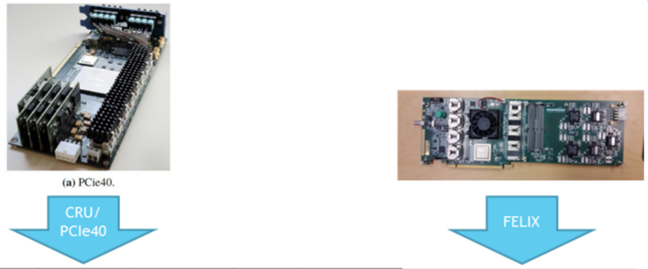

FPGA Family Name	Xilinx Virtex 6	Altera Stratix V GX	Xilinx Virtex 7	Altera Arria 10 GX **	Xilinx Virtex Ultrascale	Altera Stratix 10	CRU Requirements #	Xlinux Kintex Ultrascale
Status		available	available	ES available from Q2'15	available	end of 2017		Available
FPGA part number	XC6VLX240T	5SGXEA7	XC7VX690T	**10AX115**	XCVU190	10SG280		XCKU115
Used in	C-RORC	AMC40	MP7	**PCIe40**				FELIX v1.5 test boards
Logic Elements / Cells [M]	0.241	0.622	0.693	1.15	1.9	2.8		1.451
FFs [M]	0.3	0.939	0.866	1.7	2.14			1.3
LUTs [M]	0.15	0.235	0.433	0.425	1.07			0.66
18/20 Kb RAM Blocks	832	2560	2940	**2713**	7560	11721	**1920 / 2560**	4320
Total Block RAM (Mb)	15	50	53	**53**	133	229	**40 / 53**	75.9
≥ 10 Gb/s Transeivers	24	48	80	**96**	60	144	**48**	(48 input + 48 output fiber links in FELIX)
PLLs	12	28	20	32	60	48		48
PCIe x8, Gen3	2 (Gen2)	4	3	4	6	6		6

TPC Detector is the majority user (>70%) of CRU boards. CRU requirements is measured against TPC detector specific logic occupancy.

** Altough the maximum number of links of the Arria10 family is 96 links, the FPGA equiping the PCIe40 board has only 72 links

Figure 3.29: The DAM acts as a bridge from SAMPA data to the sPHENIX DAQ and simply applies digital horsepower to high speed digital input and output streams. As such, we can leverage developments of other experiments such as ALICE (left panel) and ATLAS (right panel). We currently favor the ATLAS-based solution using the so-called FELIX 2.0 card.

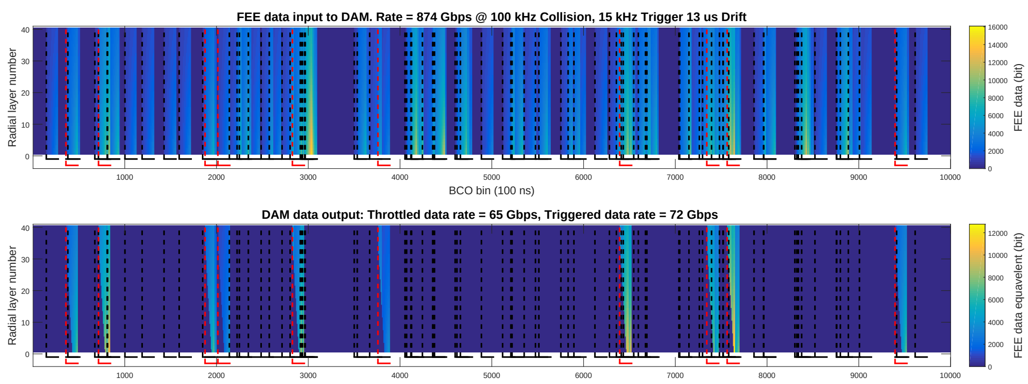

Figure 3.30: Example DAM data rate simulation under the configuration of 8 cm/μs drift and 100 kHz Au+Au collisions. Top panel is data transmission from FEE to DAM, and bottom panel for DAM data output. Both data streams are visualized as data bits (z-axis) histograms of TPC layers (y-axis) and Beam Collision Clock (BCO) time (x-axis). Black lines mark the the start and the extend of TPC hit stream from one Au+Au collision, and the red lines mark that of a triggered event, for which all TPC hits within $|\eta| < 1.1$ is recorded in the DAM event building stage. The result FEE to DAM average transmission rate is 900 Gbps, and EBDC output average average transmission rate is 70 Gbps, both of which are simulated over much longer running time (~ 1 s) than the time period being visualized in the figure.

can be removed from the data by simple and self-calibrating means, it is nonetheless quite desirable to design a pad plan that a priori would have little to no differential non-linearity.

Table 3.4: TPC DAM and EBDC average data rate for the default TPC configuration. For various design scenarios of drift speed and collision rate that are considered for TPC operation, the recorded data rate varies from 50–140 Gbps.

	Unit count	Rate per unit	Total rate	Assumptions and comments
Data on FEE Fibers	600 fibers	1.5 Gbps	880 Gbps	40-radial layer TPC and 100kHz Au+Au collision assumed. Rate is radial position dependent. The max data rate is 2 Gbps for the inner-radius FEEs.
BCO-buckets	24 DAMs	36 Gbps	900 Gbps	Unpack SAMPA data and add two 10-bit header per wavelet
After triggering	24 DAMs	10 Gbps	240 Gbps	On-DAM event builders collect 13 μs of hits after each trigger. This reduce data to 27%
After clustering	24 DAMs	5 Gbps	120 Gbps	Cluster finding and fitting on DAM FPGA. Expecting a reduction of total data volume to 50% based on STAR and ALICE experience.
After compression	24 EBDCs	3 Gbps	70 Gbps	Lossless compression on EBDC CPUs. Assuming the PHENIX experience of a reduction of total data volume to 60%
Buffer box logging	Buffer box system	70 Gbps	70 Gbps	Logging TPC data to disk in buffer box system in sPHENIX counting house.

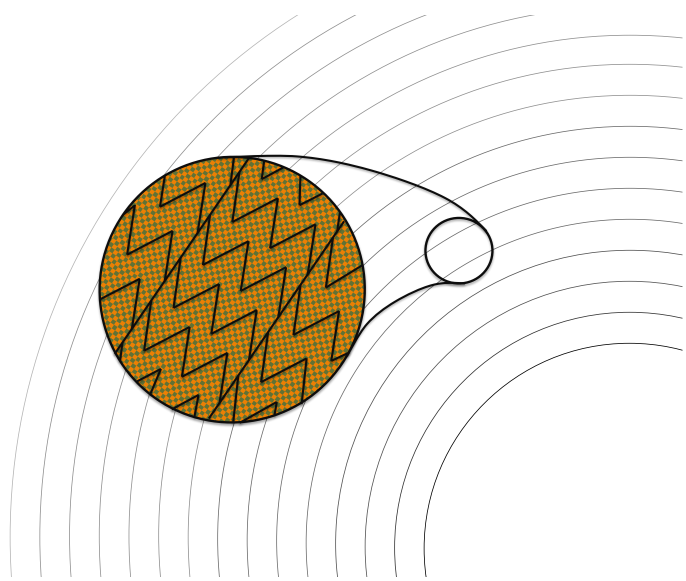

Figure 3.31: Schematic layout of the TPC pad rows and chevron pads.

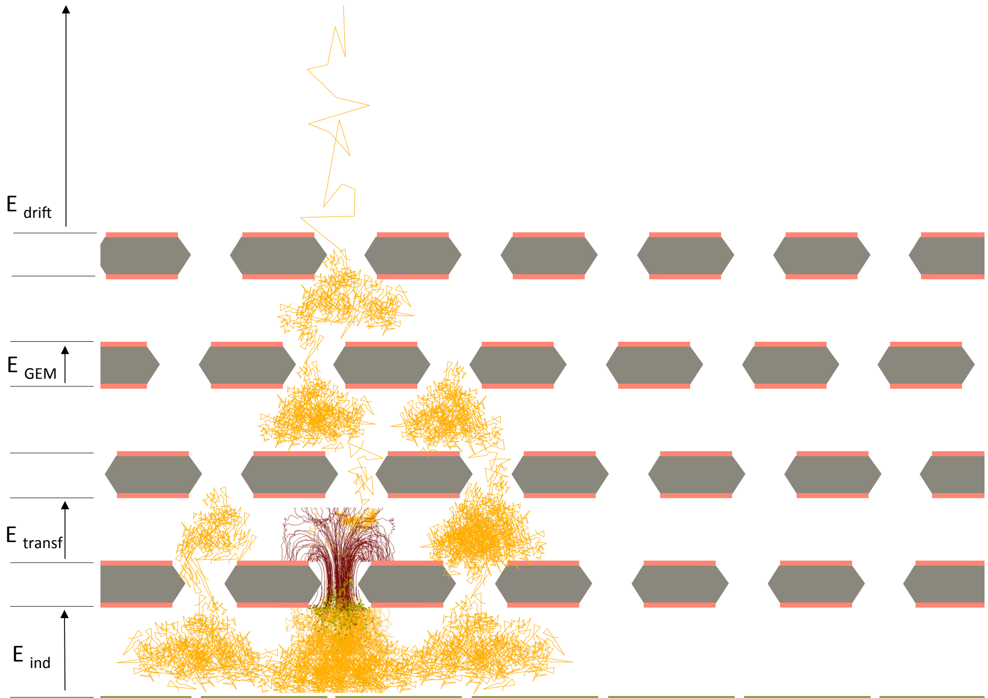

Figure 3.32: Schematic view not to scale of the readout element built with four layers of GEMs. Yellow lines show electron paths, brown lines show the ion paths for one single hole (simulation).

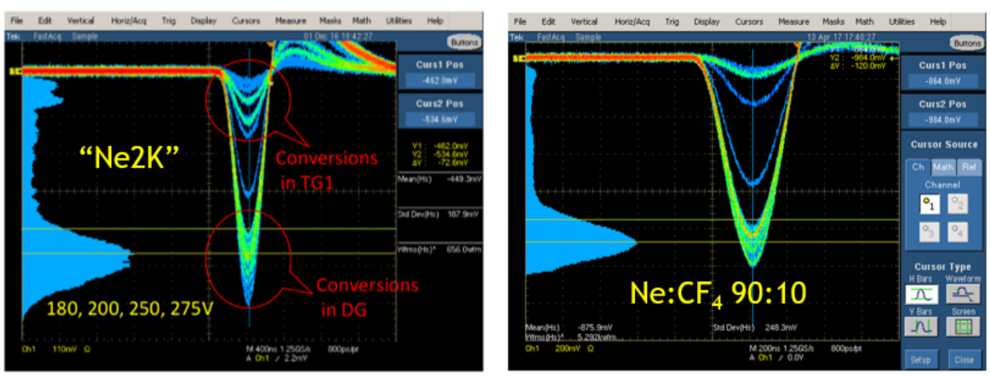

Figure 3.33: R&D results on our candidate gas mixtures (Ne:CF_4:iC_4H_{10} demonstrate good energy resolution and excellent stability when operated with a quad-GEMstack.

Again under the guise of EIC R&D we have studied at a theoretical level that issue of non-linearity as a function of pad shape. Figure 3.36 shows the anticipated response of our new design. Unfortunately the line spacings used in simulation are not possible in industry at the present time and so a compromise was made to the best that can be manufactured today. This new pad board in in house and expected to produce DNL results very soon.

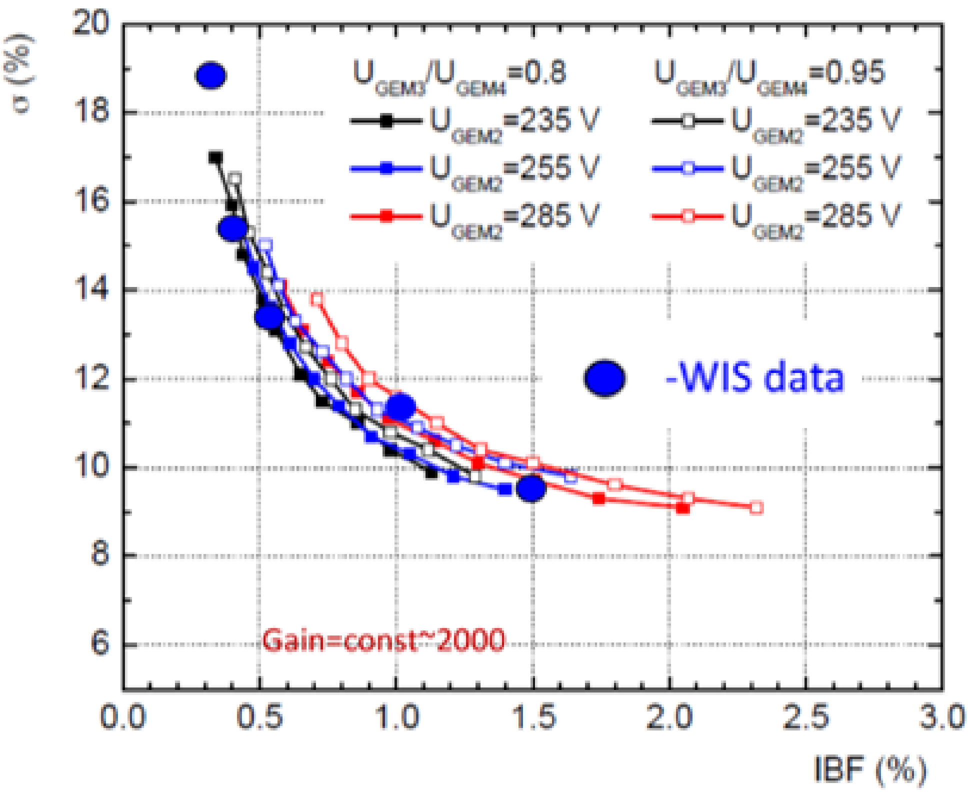

Figure 3.34: This figure shows results obtained on our labs (Weizmann Institute of Science) overlaid with the iconic ALICE results on IBF. These indicate that we are well positioned to experimentally investigate .

3.5.6 TPC field cage

The basic function of the TPC field cage is to provide a uniform drift field from the central membrane to the detector modules at each end. This field cage is traditionally defined by a series of conducting rings held at uniformly decreasing potential by a precision-matched chain of resistors. The field cage is then surrounded by a gas enclosure. Both for safety considerations and to avoid stray electric fields in neighboring detectors, the gas enclosure is usually grounded. Figure 3.37 shows the configuration found on the outer shell of the STAR TPC. Both the field cage and the gas enclosure are made structurally rigid using a hex cell honeycomb sandwich structure.

The field cage electrodes are made as a double-layer of staggered rings, one facing the operating gas and the other embedded in the field cage wall. The latter ring serves to shape the field and minimize nonuniformities in the drift volume. Dry nitrogen gas flows through the 5.7 cm gap, exceeding by slightly more than a factor of two the "rule of thumb" gap dielectric strength of $1\frac{kV}{mm}$ when operating at a central potential of 27 kV. Although in STAR the inner gas enclosure is skipped (exposing the field cage strips to outside air and stressing inner detectors with electric field) in the sPHENIX application we have more

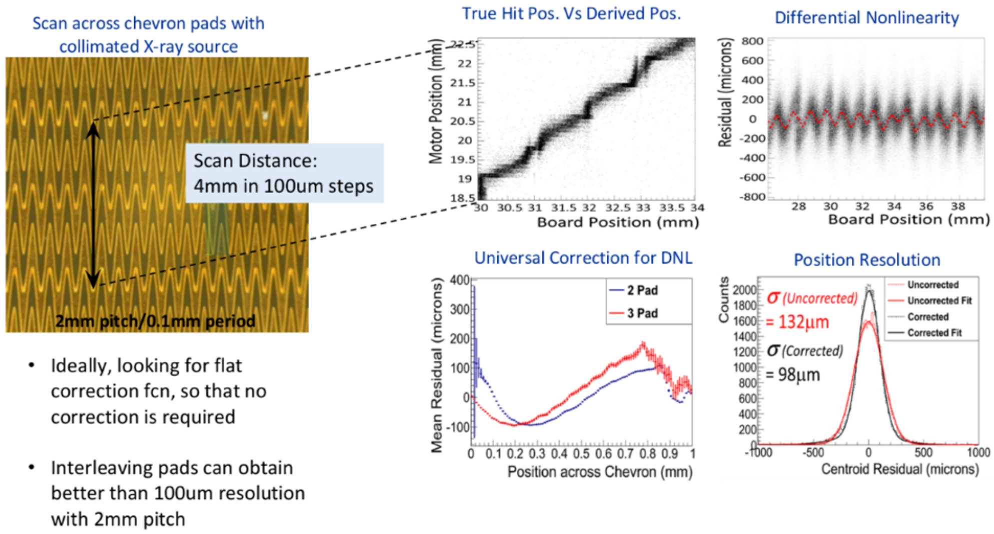

Figure 3.35: Extensive studies of various pad shapes have been performed to quantify and test reduction of differential non-linearity. These tests shows that after correction, resolution of the pad plane are easily achieved to better than 100 μm.

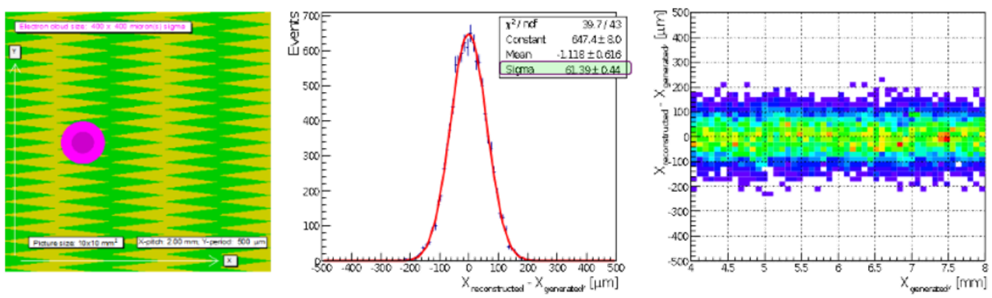

Figure 3.36: Theoretical studies of pad shape have been performed and indicate that significantly reduced non-linearity is achievable.

than enough room between the inner silicon pixels and the TPC active volume for an inner gas enclosure. Scaling to an identical safety factor as used by STAR, we would require a $5.7cm\frac{34kV}{27kV} = 7.2cm$ gap.

An "air" gap of this size would be undesirable for the outer TPC wall since it would limit the active volume and degrade the momentum resolution. Because the TPC is followed by the EMCAL, we can safely afford to solve the field issue using a solid of high dielectric strength. The concern over this solution is two-fold. First, the dielectric field strength of common materials is found to reduce with time in a variety of materials as shown in Figure 3.38. Much of this variation (*e.g.* FR4) is dominated by micro-gas bubbles within the material which can carbonize over time. Secondly, dependent upon material, solid material high voltage gaps, can be subject to permanent failure during a discharge event or over-time corona current.

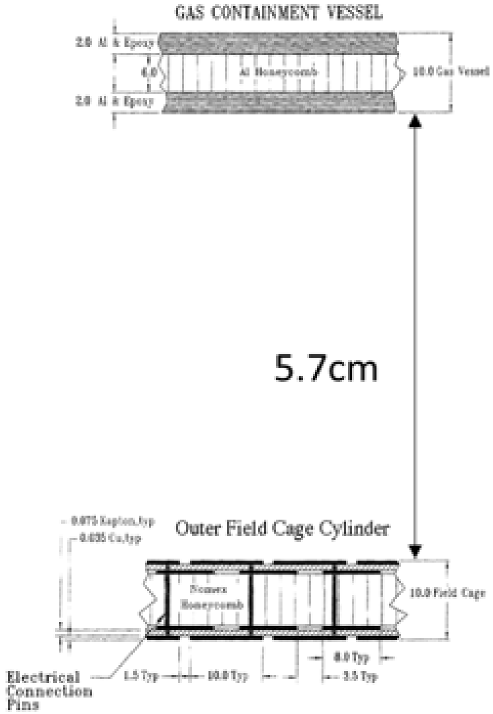

Figure 3.37: Scale drawing of the outer field cage and gas enclosure for the STAR TPC.

Material Type	Max. Operating Temperature (°C)	T/G °C	Voltage (V/mil) Note 1	Aged rating (V/mil)	W°C/m
FR4	**105-130**	**160**	**800**	**300/150**	**0.21**
FR4 Hi-Temp.	**130-150**	**170**	**800**	**300/150**	**0.22**
BT Epoxy	**140-160**	**180**	**1300**	**600/400**	**0.40**
Polyimide	**150-190**	**200**	**900**	**700/500**	**0.25**
HVPF*	**180-200**	**210**	**3000 to 7000**	**3000/2000**	**0.28**

***HVPF is a trademark of Sierra proto express.**

Figure 3.38: Dielectric strengths of various common circuit card materials, reproduced from figures by Sierra Proto Express, a Palo Alto-based circuitry company specializing in high voltage circuit card for both terrestrial and satellite applications.

sPHENIX is working with the Sierra Proto Express company to develop a robust solid core solution for the outer field cage that would maximize the reliability and longevity of the device. Although a multi-material, layered ultimate design is likely, the table below shows the required thicknesses for safety factors of 3X and 5X in the design assuming a single material type and neglecting contributions other than the insulator itself. Calculations here use the worst-case aging estimates from Sierra for each material type. These initial calculations seem promising, meaning that the ”air gap” solution is presently considered only as a fallback option. If the solid option realization has a sufficiently small radiation length, it can also be considered for the entrance window, thereby simplifying the design.

Material	χ_0 (cm)	Volt/mil	3X Safety	5X Safety
FR4	16.76	150	1.72 cm (10.3%χ_0)	2.88 cm(17.2%χ_0)
Kapton	28.58	500	0.52 cm (1.8%χ_0)	0.86 cm(3.0%χ_0)
HVPF	28.57	2000	0.13 cm (0.45%χ_0)	0.22 cm(0.75%χ_0)

After a complete suite of successful tests of the HVPF product we were disappointed to learn that Sierra could not expend their production process to pieces larger than 8″ x 8″ tiles. Fearing the worst for the many seams between these tiles we instead turned in the direction of lamination-in-place of multi-layer Kapton of the same base stock as is used for HVPF. Lab tests indicate that our design has a very large safety margin. We have designed a lamination tensioner system that will provide Kapton to the TPC shall at uniform tension to avoid trapper air pockets in the laminate.

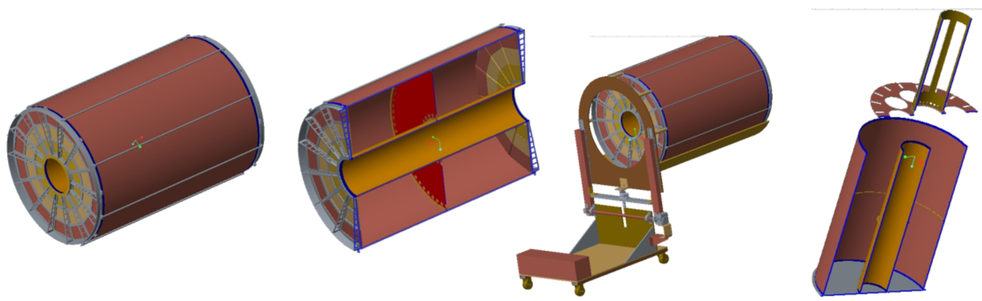

Figure 3.39: Mechanical modeling of the TPC is in an advanced stage including the device itself and also transportation/handling fixtures and assembly fixtures.

Mechanical designs for the TPC have reached an advanced stage. This advancement has been partly driven by our wise choice to prototype the TPC field cage at full size. Our budget allows for two complete field cage construction projects (prototypes v1 & v2), however, if the v1 device proves suitable for our needs the cost savings can be recovered. Figure 3.39 shows the advanced model concepts for the overall TPC including handling cart and central membrane installation tooling.

Figure 3.40 shows the plan for installation of the TPC into sPHENIX. Each wagon wheel has fittings for a rolling brace that will allow the TPC to roll in supported by a long cylindrical tube. The two ends of the tube will be held up by both the handling cart (delivery vehicle for the TPC and a second similar cart at the far end.The Handling cart falls within the scope and budget of the TPC, whereas the second cart is costed in the installation work package.

A conceptual holding fixture is also modeled for the TPC. We choose to hang the TPC from the HCal since the EMCAL walls are thinner material to reduce radiation length. Each side of the TPC accepts a ″1.4 top-hat″ shape. Two top-hats (east and west) are used to hang the TPC form the HCAL and thereby in the sPHENIX aperture.

Because our momentum resolution depends critically upon the lever arm of the TPC tracking we wish to track as close to the TPC field cage as possible. One realizes immediately,

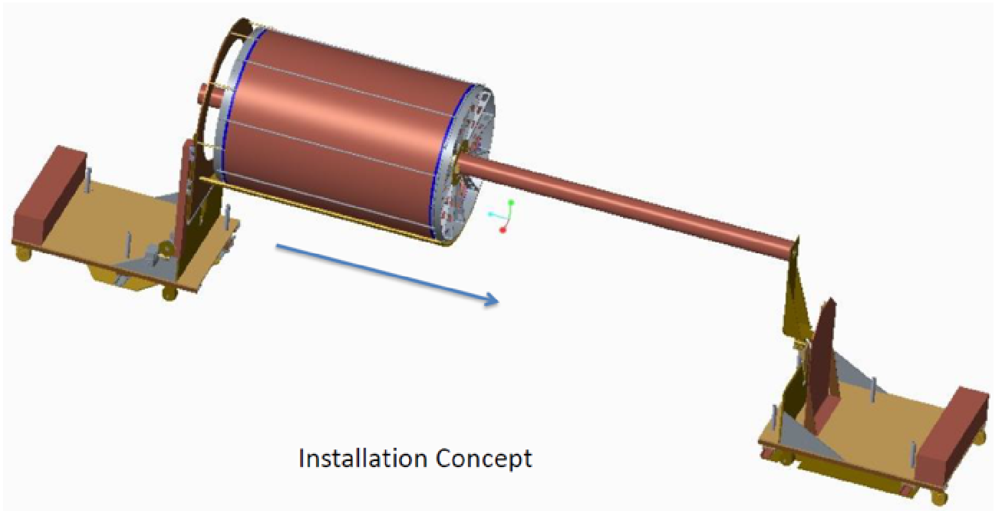

Figure 3.40: Installation of the TPC will include use of the handling cart and a second cart. The device will roll on temporary fixtures into place inside the already-assembled EMCAL.

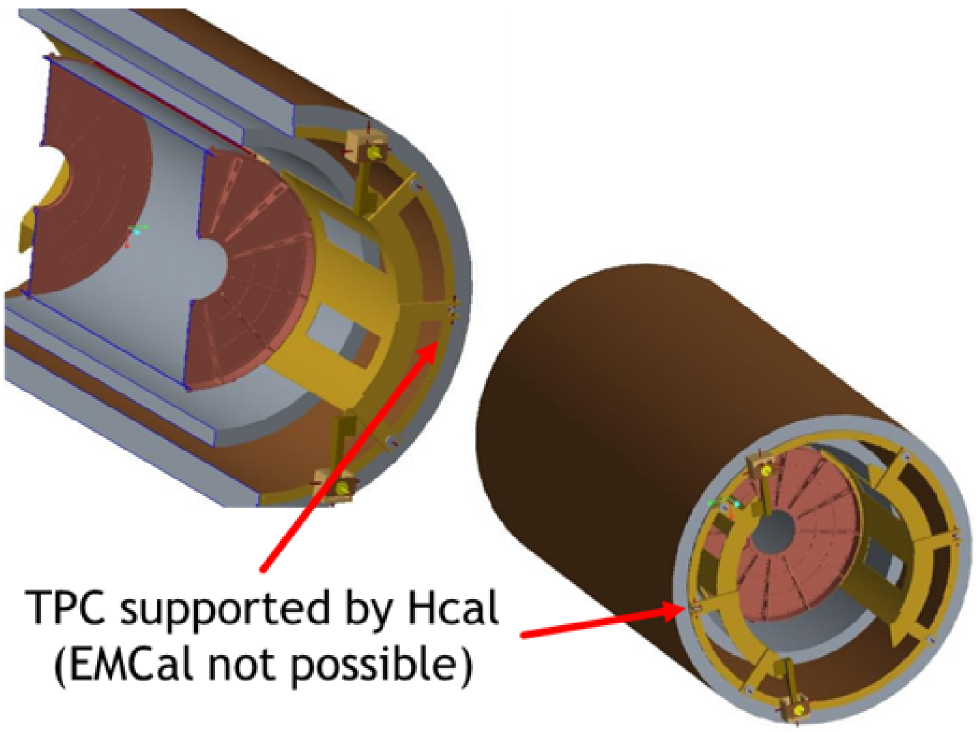

Figure 3.41: Because the EMCAL external structure does not provide sound support points for the TPC, we envision supporting the device from the inner HCAL.

however, that a step-function approximation to a uniformly decreasing potential creates non-uniformities in the electric field. These non-uniformities have a pitch that matches the segmentation of the electrode rings (colloquially called ”stripes”) and also a radial extent

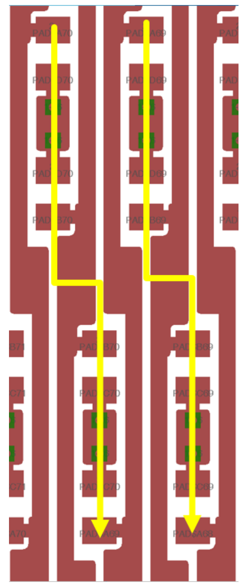

Figure 3.42: To improve field uniformity and bring the useful gas region as close as possible to the field cage, we have chosen a very fine field cage pitch (2.8 mm). This pitch is realized using SMD resistors of the HVPW (High Voltage Pulse Withstanding) variety. Current flow follows the yellow arrows.

that varies linearly with the pitch. It is therefore important to minimize the pitch of the striped electrodes.

Figure 3.42 shows the pattern we have chosen. Here a pitch of 2.8 mm is chosen and the resistive divider chains are made from surface mount components. Although physically small resistor packages are traditionally considered a failure risk, the resistors we have chosen are of a new type known as HVPW or High Voltage pulse Withstanding resistors. Each of the 1500 resistors in our multiple chains is rated to survive a 15 kV surge.

3.5.6.1 TPC Mechanical Tolerances

We have undertaken and completed an exhaustive simulation program to allow us to accurately specify the mechanical tolerances for the TPC field cage. For each variant of ”mis-construction” (see Figure 3.43, we have used Ansys to create a full field map. Two such variants include modules that are out of plane from their desired alignment and having the central membrane out-of-plane.

Once the electric field distortions are known, we use GARFIELD with the distorted electric field map and an ideal magnetic field map to measure the average position error from the pad plane by allowing the electric field distortions to go uncorrected. The net result of this lengthy procedure is that we are able to derive a complete suite of mechanical tolerances to which the field cage must conform in order to minimize tracking errors. Examples of these distortions for different electron launch points under the condition of 1 mm tilt of

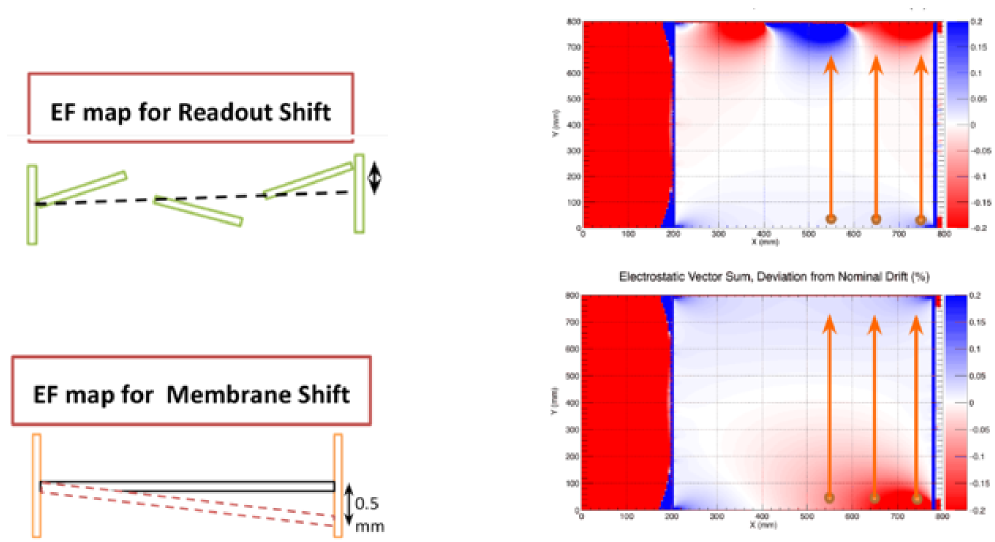

Figure 3.43: Ansys calculations have been performed to compare the electric field of an ideal TPC to that of a TPC build with manufacturing errors. These field calculations assist in defining the production tolerances.

the central membrane are shown in Figure 3.44. An interesting output from this study is the discovery of a local minimum in the field-induced distortions of the TPC us run under the conditions $v_{\vec{drift}} \times \vec{B} \sim E_{\vec{drift}}$. We are lucky at or very near this condition in both our candidate gases.

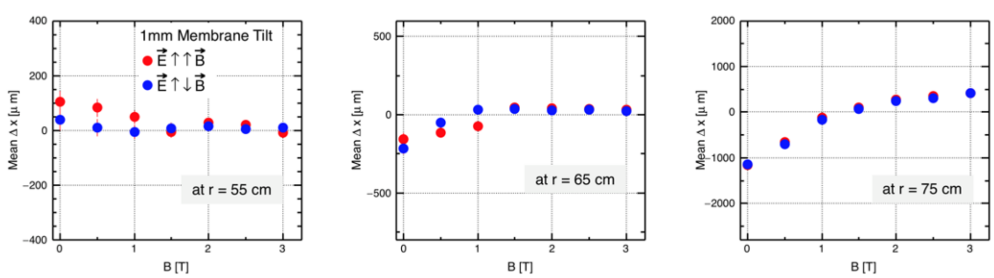

Figure 3.44: For each mechanical error calculated by Ansys, the distorted field us feed into GARFIELD so that position measurement errors can be deduced. Calculations not only yield a quantitative impact study of field cage errors, they also demonstrate a local minimum in tracking error when $v_{\vec{drift}} \times \vec{B} \sim E_{\vec{drift}}$, as is the case foe Ne2K gas.

Another substantive issue for the TPC is the size of the gas volume and maintaining cleanliness of the gas. Although it is true the PHENIX constructed an exceptional gas system for the old HBD detector (below 5 ppm and O_2 and H_2O at all times, the sPHENIX TPC i a much larger gas volume and will require special care in defining its fittings.

Our designs that are presently under construction for the full-scale prototype call out making both the wagon wheels and their mating pieces from solid Al block. Although this is by no means inexpensive, it allows for vacuum-quality seals at all places.

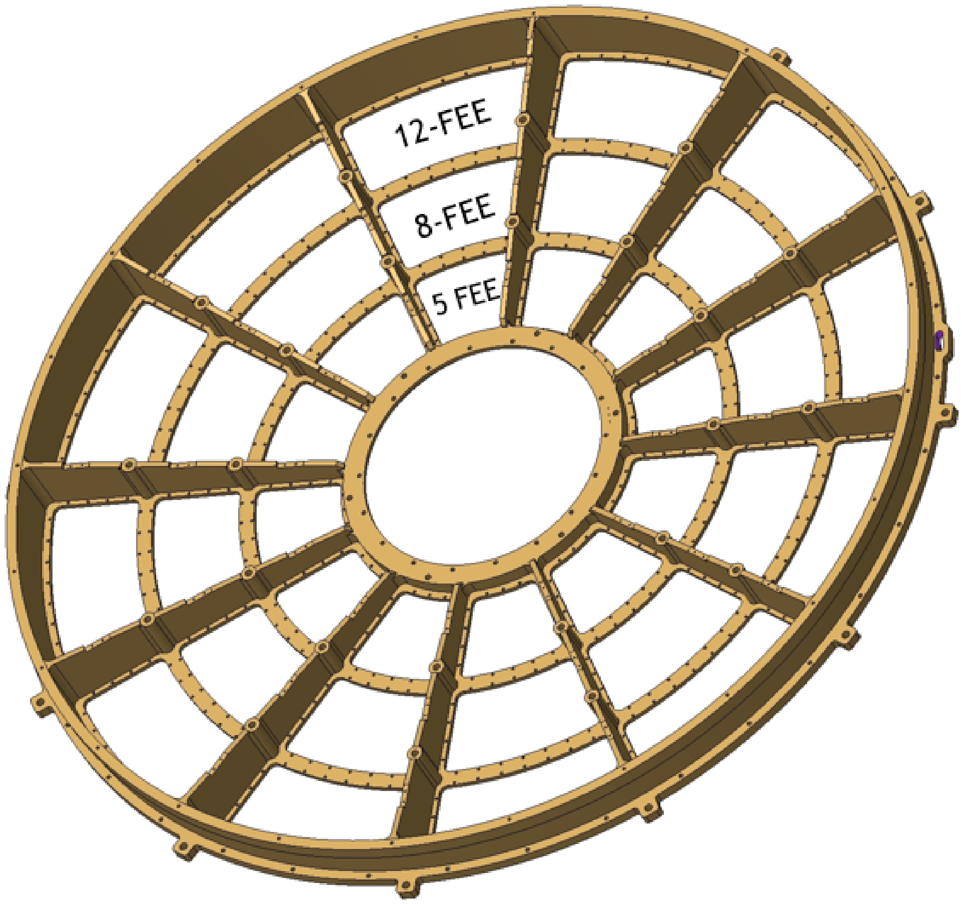

Figure 3.45: The TPC ”wagon wheel” shall be machined from single piece Al to eliminate cracks and minimize leaks.

Figures 3.45 and 3.46 show the details for completing the seals. The wagon wheels shall seal to the field cages using spring-energizes elastomer gland seals. These will proceed for simple insertion thereby eliminating the need to excessive force applies to the field cage cylinders during assembly. Furthermore, each TPC avalanche module will achieve an O-ring seal against the wagon wheel pieces.

3.5.6.2 TPC Fabrication

Because of the size of the TPC, the fabrication of all parts could, in principle, be accomplished at any of our collaborating institutions worldwide. That said, it would nonetheless be simplest if the field cage assembly was done locally, with smaller parts made around the world. This model proved quite effective in building the PHENIX Hadron Blind Detector, wherein the individual parts were manufactured at the Weizmann Institute of Science in Israel, and the assembly was accomplished at Stony Brook University.

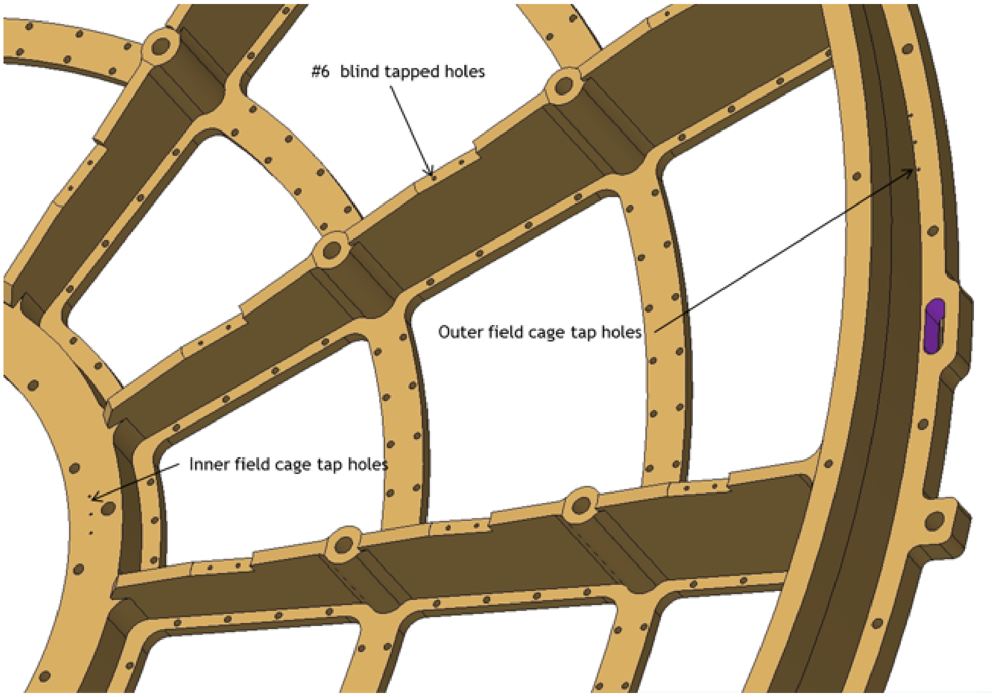

Figure 3.46: The "wagon wheel" includes allowances for all services, feedthroughs, installation fixtures, and support fixtures.

Because of the need to maintain active area to the largest radius, our designs for the TPC field cage and gas enclosure will be biased toward the thinnest of robust designs. Thus, the STAR and ILC field cage designs are the most appropriate as models for our work. Those devices were manufactured using large mandrels upon which layers of flexible circuit card and honeycomb were applied. Each mandrel is designed to release by "collapsing" to smaller radius after the TPC shell is cured, thereby releasing the shell. The completed shells are then outfitted with aluminum spoke-like end caps and a central membrane to form the completed field cage. We intend to design the field cage to safely hold the highest potential currently under investigation (ALICE gas $\sim 37\ kV$).

The open ports between the spokes of the end caps will be filled with "mechanical blank" modules to allow the field cage to become gas tight during the prototyping stage. This will allow full testing of the high voltage stability of the field cage without any of the gain stage modules in place.

During the prototyping stage, single items of the prototype gain stage module will be built. Because of the finite size of these units, there is a list of institutions that are capable of prototype construction, including Weizmann, Stony Brook, BNL, PNPI, Temple, and Vanderbilt. All of these institutions have past experience in the PHENIX HBD construction, or in the ongoing construction of the inner TPC layers for the ALICE upgrade. We envision two full sized prototypes whose design is driven by results from our ongoing TPC gain stage R&D, which has been funded by the EIC R&D program. As described below, we have already garnered extensive experience in multiple gain stage technologies, as well as a number of clever readout scheme applications.

The so-called ”pre-production prototype” will be the third and final stage of full sized prototype construction. Barring any discovered deficiencies, ”production” would involve the manufacture of the remaining gain stage modules as well as spare units. As with the prior work, it is likely that much of this effort will take place ”off site” from the location of the field cage itself, with working modules shipped via clean, dust-free packaging.

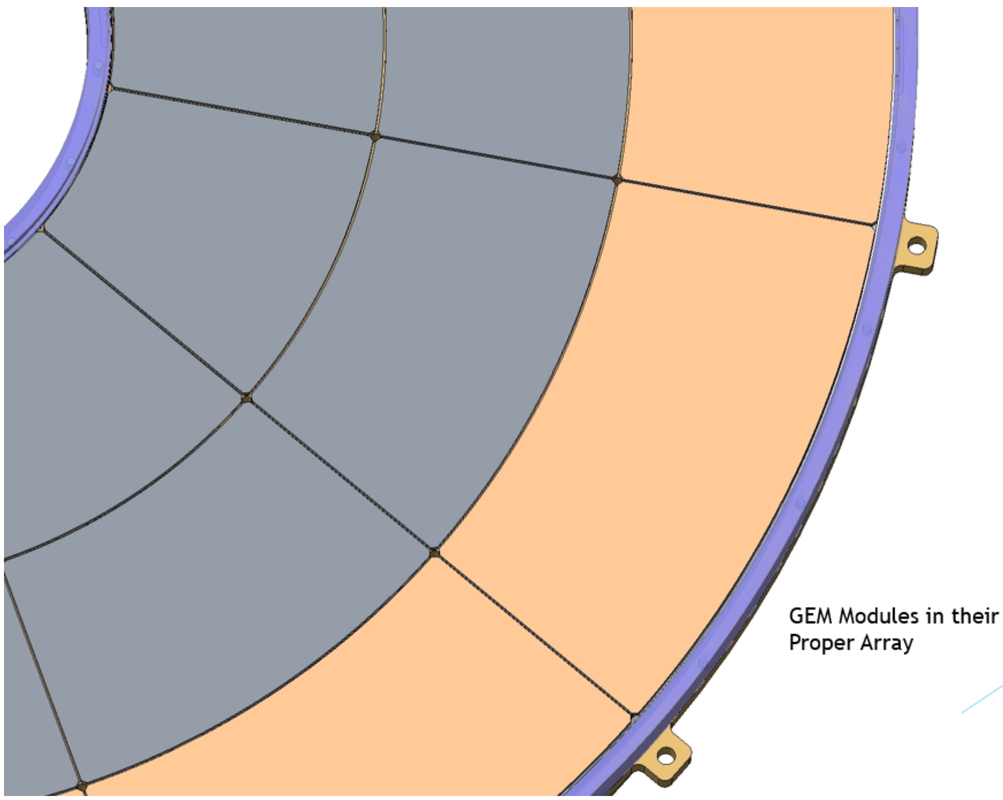

Figure 3.47: TPC modules have only $\frac{1}{16}$” gap and localize penetration services (gas, laser, temp, pressure, ...) at the ”corner points”.

Figure 3.47 shows the fit of the modules after assembly. a 1/6” gap is standard between all modules Furthermore at each corner junction, the modules allow for 1/4” feed-through allowing for gas in/out and laser signals.

Figures 3.48 and 3.49 highlight the gland seals.

3.5.7 TPC cooling and cabling

Our cooling requirements for the TPC electronics will be significant. Although we are only cooling $\frac{1}{2}$ as many channels as ALICE, these channels are distributed over only $\frac{1}{10}$ as much

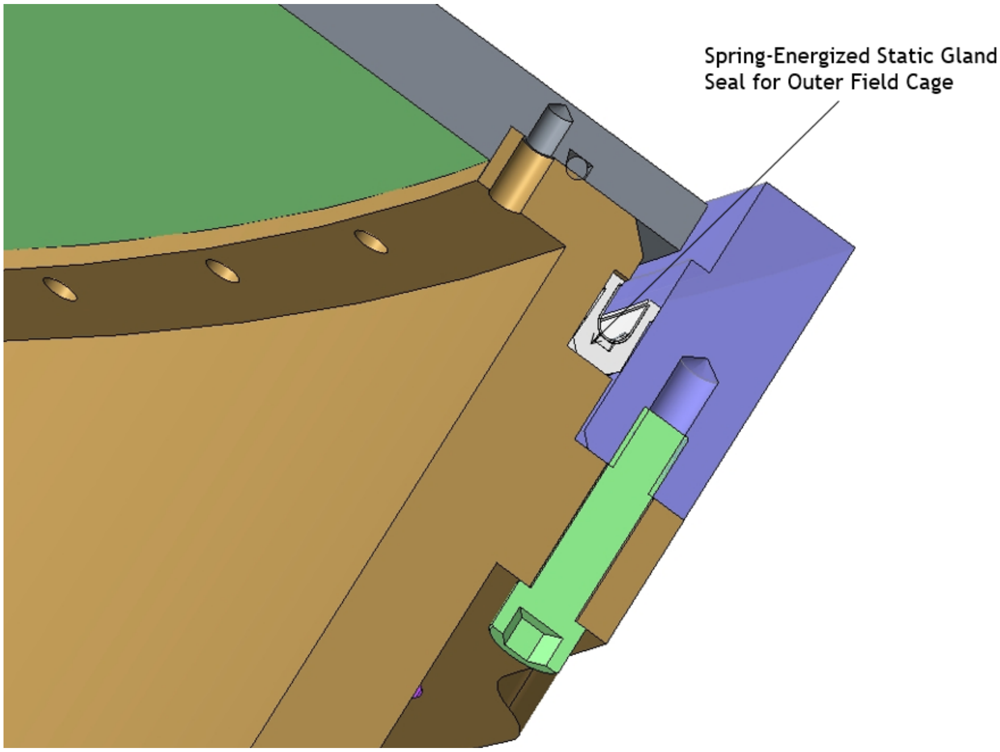

Figure 3.48: Both the inner and outer field cages avoid O-ring-induced distortions of the wagon wheel by making an annular seal. Stresses are further minimized using a spring-energized gland seal.

surface area. Therefore the power required from our cooling plant will be smaller overall, but we will need to design for very effective heat transfer to the cooling lines.

Figure 3.50 shows the configuration of the cooling plant currently in use by the ALICE experiment. The key feature of this cooling plant is that the coolant is delivered at pressures below one atmosphere so that in the event of a leak, gas is introduced into the coolant rather than coolant introduced into the gas. The ALICE resistor chains dissipate a significant amount of power (8W in each of 4 resistor bars). Higher power in the resistor chain is driven by the need for robust performance in the face of stray currents due to nearby ionization. Although the track density in sPHENIX and ALICE are very similar, the charge load onto the ALICE TPC frame is much higher. Among STAR, ALICE, and ILC, only ALICE water cools their resistor chain. Since our power dissipation will be the least of these three applications, we are safest to not water cool the resistor chain, and thereby preclude from the outset the risk of water leaking into the chamber. Our resistor chain design dissipates $\sim$1 Watt.

The cable plant for the TPC includes a pair of shielded coaxial high voltage leads whose diameter will be under $\frac{1}{2}''$ (*e.g.* Dielectric Sciences 2125: 100 kV; $\mathcal{O}$ 0.4″). Each sector will receive bias for the GEMstack as 8 independent voltages. The readout cards, will receive DC power input, optical connections for slow control and optical connections for data

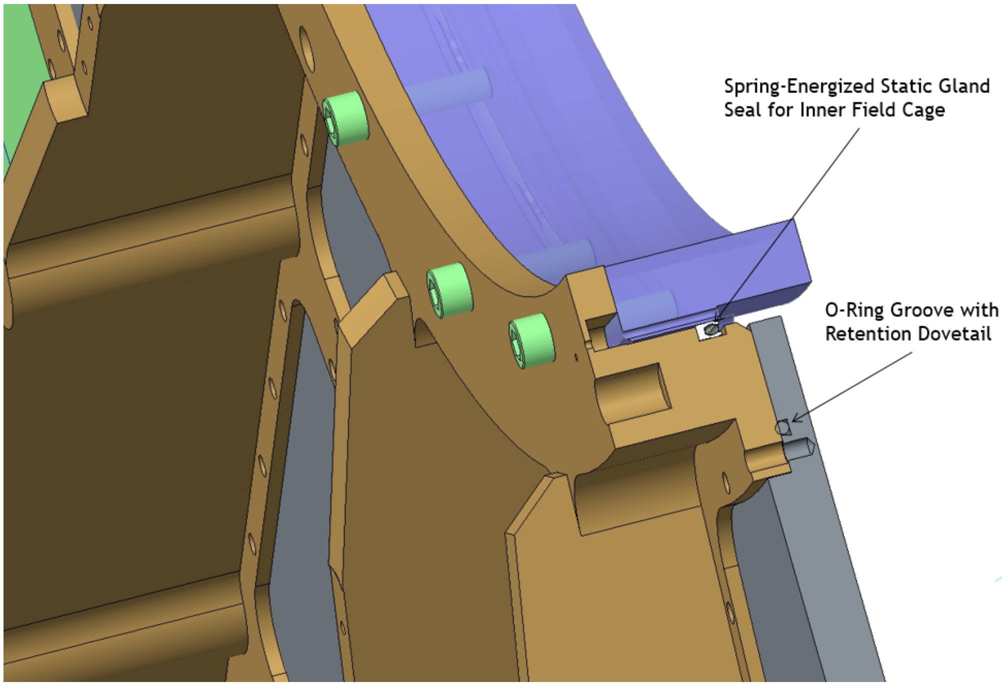

Figure 3.49: Schematic layout of TPC main elements.

output. To the extent possible, this significant cable plant will be localized so as to align with the end cap spokes, to minimize the radiation depth for the end cap detector systems.

3.6 TPC installation and calibration

The assembly order for sPHENIX specifies that the TPC will be inserted from the end after the calorimeters have already been installed onto the magnet.

TPC calibration will be achieved using a laser system, similar in philosophy to that used by STAR and prototypes for the ILC. Because the work function of aluminum is low, a UV flash will release electrons. Both the STAR TPC and the ILC TPC prototype used a pattern of aluminum applied to the central membrane to produce these reference tracks. The pattern used by STAR consists of lines shown in Figure 3.51, whereas that of the ILC was a pattern of dots. The laser system will not only provide an initial reference calibration, but can be fired at regular intervals (PHENIX fires their EMCAL laser at 1 Hz) during data collection to provide a continuous calibration of the drift velocity and space charge distortions. Gain calibrations can be roughly estimated using cosmic rays, but final calibration will use collision data. In addition to the central membrane pattern, we will shoot lasers directly through the gas at angles from the access points provides in the corner module meeting places.

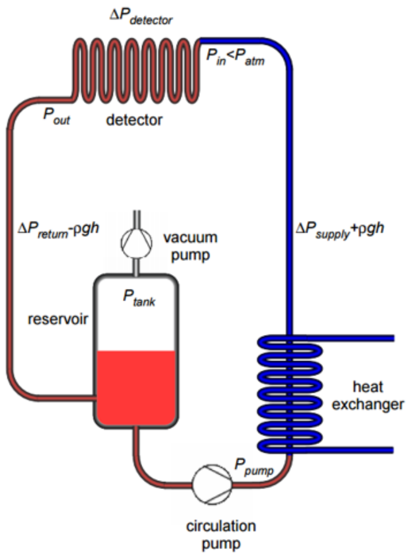

Figure 3.50: Diagram of the cooling plant in use the the ALICE TPC. The cooling plant is an under pressure system so that any leak results in gas bubbling into the coolant rather than coolant dripping into the detector.

Figure 3.51: Photograph of the central membrane of the STAR TPC. The pattern of Aluminum strips is used to release electrons via laser flash as a calibration signal.

3.7 Alternate TPC readout plane options

As discussed previously, we are currently investigating a list of possible alternate technologies for the readout plane. These alternatives include both the possibility of changing a classic gating grid to implement a prompt flush for positive ions (possibly resulting in a TPC with zero ion back flow, at the cost of adding a "duty cycle") and variations of the scheme for the MPGD-based gas amplification stage. Already discussed is the ongoing work to implement a hybrid μMEGA/GEM detector that would benefit from the superior ion back flow characteristics of the μMEGA and achieve remarkable stability by lowering the μMEGA gain requirements via the assistance of the GEMstack.

A unique suggestion has been tested at WIS. In this case, small self-supporting hexagonal GEM stacks were developed that could be used to populate any large surface. These devices would feature the robust performance of smaller GEMs while still maintaining a nearly hermetic acceptance. The first results with the prototypes show high mechanical rigidity of the elements, not affected by the transfer electric fields.

Besides providing nearly hermetic acceptance the modular solution requires a large number of small GEMs that allow one to reduce the overall cost of the readout plane, but more importantly such an approach benefits from a very stringent quality control at the production stage that insures high gain and residual ion backflow uniformity across the area of the reaction plane.

Chapter 4

Electromagnetic Calorimeter

4.1 Physics Requirements

The EMCal performance is central to the direct photon and upsilon measurements and it is also a key component, along with the hadronic calorimeter, of the calorimetric jet reconstruction. In this section the photon and upsilon requirements for the EMCal are discussed.

Direct photons and their correlation with jets are a unique probe of partonic interactions in the QGP. Photons can be the result of a hard scatter (for example $gq \to \gamma q$). The photon, not carrying color charge, does not interact strongly with the QGP and thus provides a direct measure of the momentum transfer of the hard scatter itself that is accessible in the final state. This is in contrast to dijet systems where both jets interact strongly with the QGP. Direct photon measurements in heavy ion collisions are limited by the rate of the photon production and the efficiency and purity with which the photon can be identified. Therefore, the main requirements on the EMCal from photon measurements are on the size of the acceptance and the contamination of the photon candidate cluster by energy deposited near the photon from the underlying event. As illustrated in Fig. 1.21, the photon/π^0 discrimination is not a driver of the calorimeter performance at the momenta of interest at RHIC.

For heavy ion collisions, one goal is that the detector resolution and segmentation not be a limitation on the electron cluster reconstruction compared to the underlying event background in a central heavy ion event. A typical cluster size (a 3x3 tower array) contains about 320 MeV of underlying event energy in the EMCal (see Fig. 4.23). For an Υ-electron cluster of 4 GeV, the underlying event blurring would produce a comparable contribution to the energy resolution with a detector resolution of $\Delta E/E \leq 16\%/\sqrt{E}$.

For the Υ, the EMCal requirements are driven by the need to reject hadrons by a matching condition between the track momentum and the EMCal energy. Hadrons misidentified as electrons will lead to an increased combinatoric background in the Υ mass distribution.

The design goal is to optimize the electron identification efficiency with respect to the pion rejection by the calorimeter energy matching condition. As in the photon case, central Au+Au collisions are the most challenging environment and drive the detector specifications. The physics requirement is to be able to have sufficient statistical precision to measure the suppression of the three Υ states separately.

4.2 Detector Design

4.2.1 Design Requirements

The design requirements for the sPHENIX electromagnetic calorimeter are based on the physics requirements described in the previous section. The calorimeter will play a major role in both the measurement of jets and single photons out to high p_T, as well as identifying and measuring the energies of the electrons from Υ decays. In addition, the calorimeter must fit inside the BaBar magnet and allow space for the tracking system that will reside inside the calorimeter. The calorimeter should also be as compact as possible in order to minimize the overall size and cost of the hadronic calorimeter. The basic detector design requirements can be summarized as follows:

- Large solid angle coverage ($\pm$ 1.1 in η, 2π in ϕ)
- Moderate energy resolution ($\leq 16\%/\sqrt{E} \oplus 5\%$)
- Fit inside BaBar magnet
- Occupy minimal radial space (short X_0, small R_M)
- High segmentation for heavy ion collisions
- Minimal cracks and dead regions
- Projective (approximately)
- Readout works in a magnetic field
- Low cost

The requirement for large solid angle coverage is driven by the need to accumulate high statistics for measuring jets and single photons out to the highest p_T possible in an unbiased way using full jet reconstruction over the entire central rapidity region. The requirement for the energy resolution is determined by achieving the best resolution possible consistent with the contribution to the energy resolution from the underlying event in central heavy ion collisions. The energy from the underlying event also requires the tower size to be small ($\sim$1 R_M^2) in order to minimize the background contribution for measuring the jet energy or the electron energy from Υ decays. This then also determines the minimum inner radius of the calorimeter and the required level of segmentation. The current design places the inner radius of the calorimeter at 90 cm and has a segmentation of 0.025 $\times$ 0.025 in $\Delta\eta \times \Delta\phi$, which leads to 96 $\times$ 256 = 24,596 towers over the full rapidity and ϕ range. Figure 4.1 shows the energy deposition in the sPHENIX calorimeter system as a function of the geometric position in the detector. In Figure 4.23, this is quantified in terms of the distribution of energy in single calorimeter towers and in 3x3 tower sums for central Au+Au HIJING events. The average energy for the tower sum is $\sim$320 MeV.

The requirement for minimal gaps and dead regions is driven by the need to measure jets over a large solid angle with good uniformity. Gaps are particularly undesirable since they can lead to missing energy for the electromagnetic component of the shower.

Projectivity in two dimensions (2-D proj.) is desired for the upsilon program. With a one dimensionally projective calorimeter (i.e., projective in ϕ only, or 1-D projective), the pion rejection at fixed electron efficiency degrades with increasing $|\eta|$, as electrons enter the calorimeter at increasing angles. The resulting shower is spread through a larger number of towers (Figure 4.20) and thus has higher contributions from the underlying event overlapping with the cluster, blurring the electron/hadron separation. At 70% electron efficiency the pion rejection degrades from a factor of 100 in the two dimensionally projective case to 60 for 0.7< $|\eta|$ <0.9 (see the discussion of Figure 4.27). This results in an increase in the combinatoric background and a corresponding decrease in the statistical power of the upsilon measurements from that shown in Figure 1.18

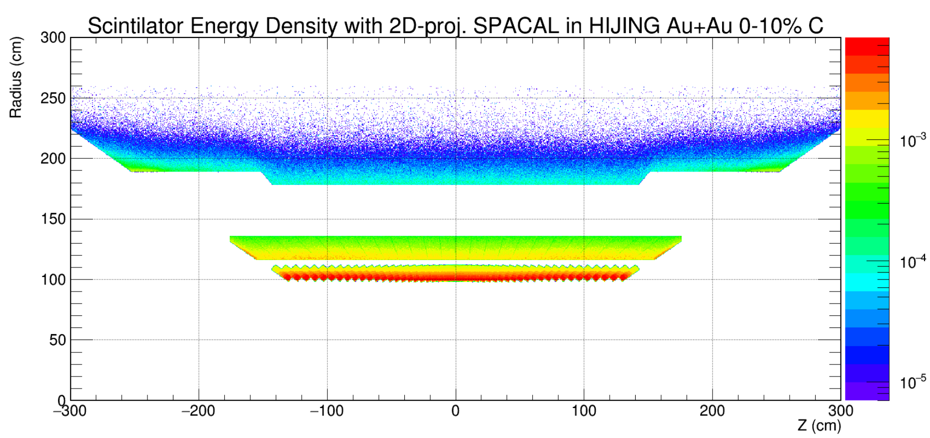

Figure 4.1: Visible energy density in the sPHENIX calorimeter systems in central Au+Au collisions. The electromagnetic calorimeter at radius of $\sim$100 cm observes a high amount of background energy density, which is quantified in Figure 4.23 in a later section. Each block of the EMCal consists of two towers in the z-direction.

The technology chosen for the EMCAL utilizes an absorber consisting of a matrix of tungsten powder and epoxy with embedded scintillating fibers (W/SciFi), similar to the SPACAL design that has been used in a number of other experiments [127, 128, 129, 130, 131]. In order to work inside the magnetic field, the readout will utilize silicon photomultipliers (SiPMs), which provide high gain and require minimal space. The readout will digitize the SiPM signals and also provide a trigger for high energy electrons and photons. The W/SciFi absorber matrix was developed at UCLA and has been tested several times in test beams at Fermilab [132, 133]. The matrix is formed by preparing an assembly of 0.47 mm diameter scintillating fibers, held in position by a set of metal meshes. The nominal center to center spacing of the fibers is 1.0 mm. The fiber assembly is encapsulated in a mixture of tungsten powder and epoxy, which is compacted by vibration to achieve a density $\sim$ 9-10 g/cm^3. This results in a sampling fraction $\sim$ 2.3% with a radiation length $X_0 \sim 7$ mm and a Molière radius $R_M \sim 2.3$ cm.

The design of the EMCal is being developed with the use of simulations, tests of individual calorimeter components, development of a complete mechanical design, and the construction and evaluation of several prototype calorimeters that are being studied along with the hadronic calorimeter in a series of beam tests. These various efforts of the EMCal design are described in the sections below.

4.2.2 Block Design and Construction

The full scope of the EMCal will require a total of 24576 towers, in 6144 blocks, each of which contains 2×2 towers. The manufacturing of such a large number of blocks is at an industrial scale. The Nuclear Physics Group at UIUC has significant production capabilities and expertise in producing detector components of this type. They have, in fact, built a similar tungsten-scintillating fiber calorimeter in the past in connection with the g-2 experiment [134]. Through our R&D program they have now developed extensive expertise and experience in producing the absorber blocks (see Section 4.4).

The procedure to fabricate the blocks is as follows. First the fibers are cut to the desired length. Then the fibers are filled into the screens (see Figure 4.2 for a drawing of a typical screen) as they are supported by a 3D printed holder placed at the top of a plastic cup which is used as a support structure (see Figure 4.3). Each block contains 2668 fibers. When the screens have been verified to be filled the fiber assembly is placed in a mold with machined slots to hold the screens in the proper place. The fibers are brought away from the edges of the mold near the read out end in order to make the area of the light collecting surface the same for all the block shapes (see Figure 4.4). This improvement allows for a single light guide size to be used for all block shapes. Additionally, it brings the fibers away from the edges of the light guides where the light collection efficiency is lower. The tungsten is then poured into the mold from the top. Vibration is used to ensure there are no voids in the tungsten filling. When the tungsten has been poured, the epoxy is poured over the top of the assembly and drawn through with a vacuum from the bottom of the mold. The block is left for at least 24 hours to allow the epoxy to dry. An example drawing of a block is shown in Figure 4.5. Table 4.1 lists some of the properties of the materials used in the fabrication.

When the epoxy is dry the block is removed from the mold. The edges of the screens are removed from the sides of the block and the top of the block is machined. The ends of the block are machined to expose the fibers. The quality of the end surfaces of the fibers is important for the performance of the calorimeter blocks since it directly affects the light output. A clean cut end with minimal fiber damage is required to maximize the scintillation light collection from the blocks. The ends are diamond-fly cut to provide such a surface. The blocks are then shipped to BNL for assembly into sectors.

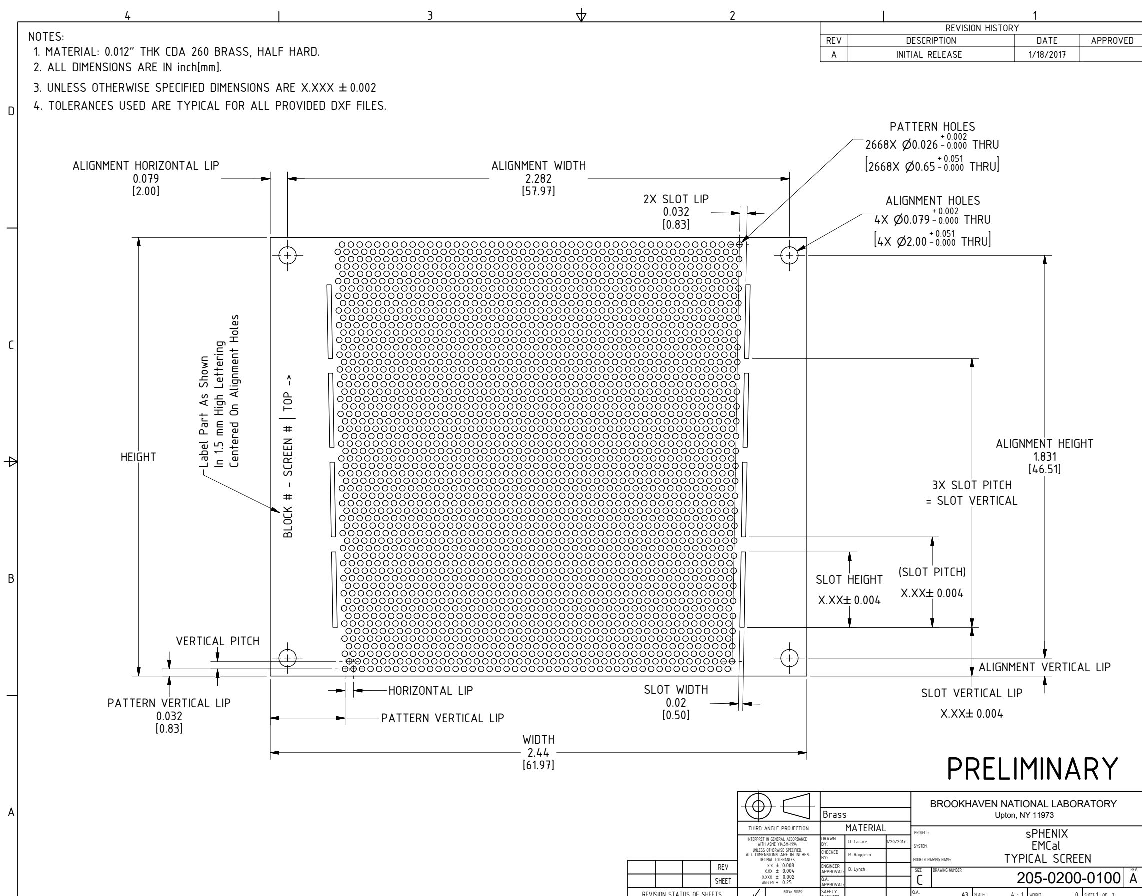

Figure 4.2: Drawing of a typical screen for the 2D projective EMCal modules.

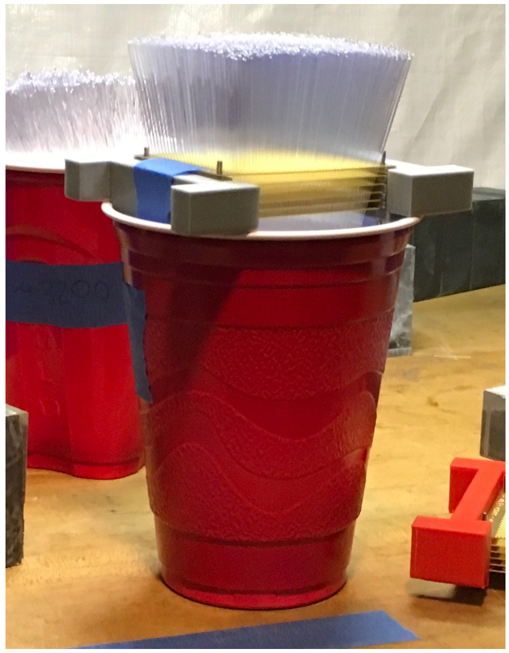

Figure 4.3: Photo of the fiber filling assembly.

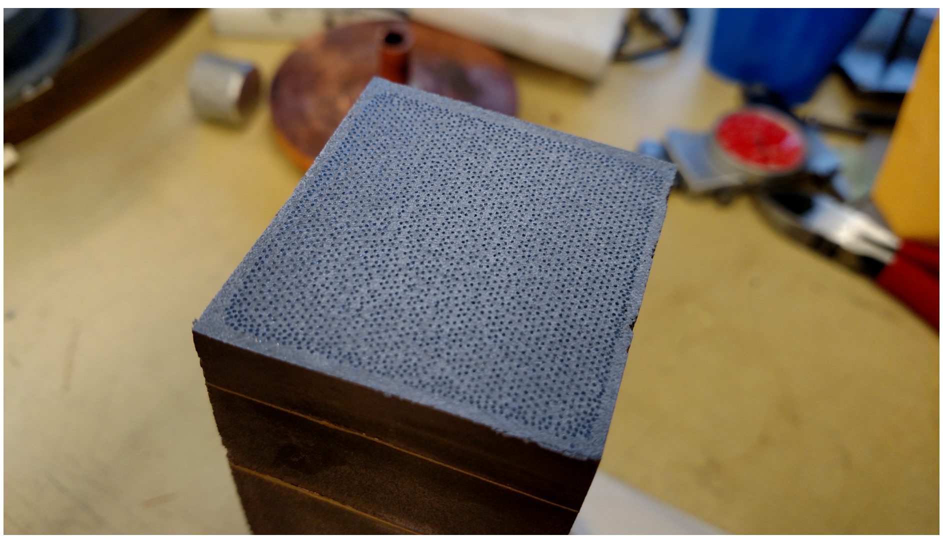

Figure 4.4: Photo of a cast block with the fibers on the read out end of the block moved away from the edge of the block to make the size of the light collection area the same for all block shapes.

4.2.3 Module and Sector Design

The EMCal will consist of 64 sectors (32 azimuthal $\times$ 2 longitudinal) that are supported by the inner HCal. Figure 4.7 shows the installation of an EMCAL sector on the Inner HCAL. Each sector will subtend 11.2 deg in ϕ and cover 1.1 units in η. They will be supported by

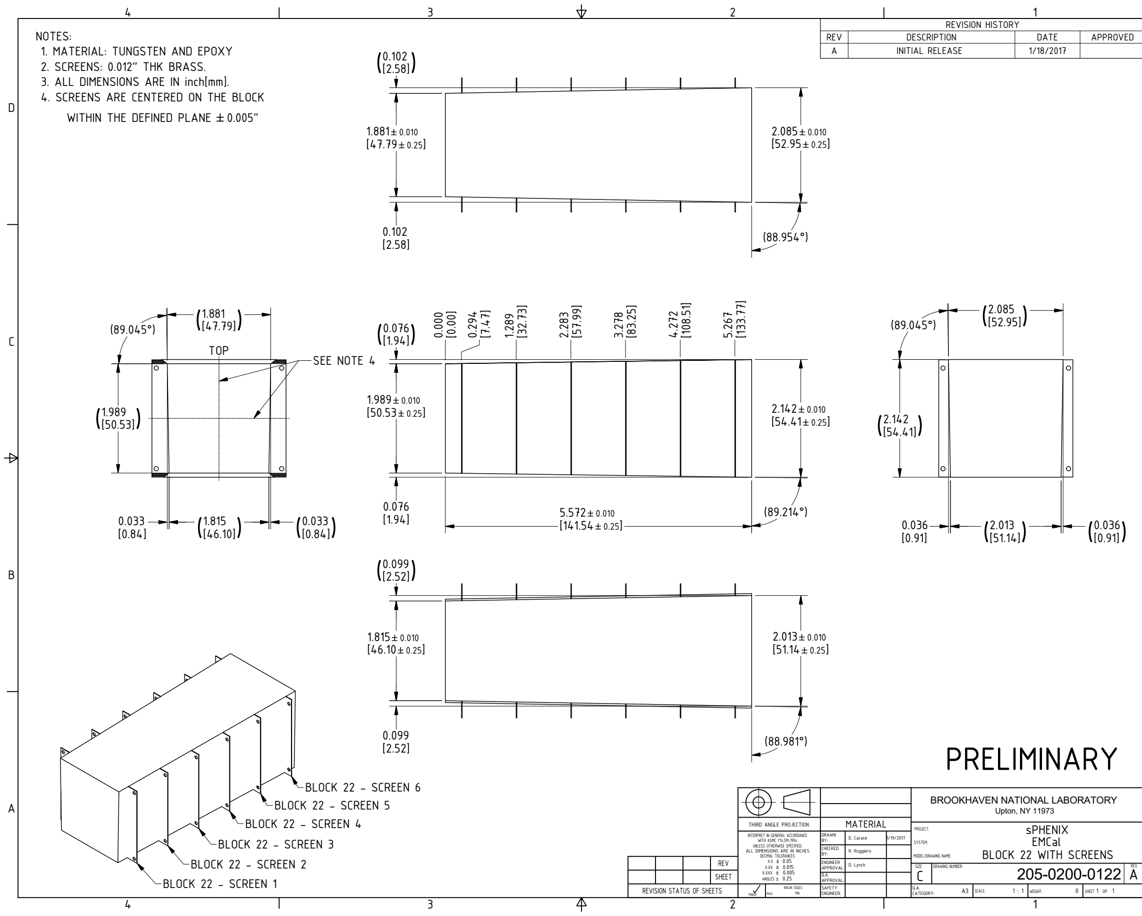

Figure 4.5: Technical drawing of a 2D projective block produced at UIUC.

rails that will be used for installing each sector one at a time and will allow removal of any sector for service or repair. Each sector will contain 384 towers that will be constructed from 96 blocks of 2×2 towers each. In the current design, four blocks will be joined together to form a module consisting of $2 \times 8 = 16$ towers. Twenty four of these modules will then be used to form a sector. The procedure for installing the blocks into the sector will be developed during the construction of the first pre-production prototype sector (Sector 0). Table 4.2 gives the key parameters for the EMCAL modules and sectors.

The EMCal towers are projective in both η and ϕ (i.e., 2D projective) but arranged so that they point slightly off the collision axis. This is done to minimize the effects of boundaries within the blocks and possible channeling of particles through these boundaries. In addition, since the collisions are distributed longitudinally with a $\sigma \sim \pm 10$ cm, the towers do not point directly to the interaction point. The pointing of the blocks back toward the interaction point is shown in Figure 4.8. This configuration ensures a minimal EMCal thickness of about 18 X_0 when viewed from the vertex region in the sPHENIX acceptance of $|\eta| < 1.1$. The average thickness of the active components of the EMCal is $20.1X_0$ and

Material	Property	Value
Tungsten powder	THP Technon 100 mesh	
	Particle size	$\leq 100\ \mu$m
	bulk density (solid)	$\geq 18.50\ g/cm^3$
	tap density (powder)	$\geq 11.25\ g/cm^3$
	purity	$\geq$ 99.9 percent W
	impurities ($\leq$ 0.1 percent)	Fe, Ni, O2 , Co, Cr, Cu, Mo
Scintillating fiber	Kuraray SCSF78 (blue)	
	fiber diameter	0.47 mm
	cladding	single
	core material	polystyrene
	cladding material	polymethylmethacrylate
	emission peak	450 nm
	decay time	2.8 ns
	attenuation length	$\geq$ 4.0 m
Epoxy	Epo-Tek 301	
	pot life	1-2 hours
	index of refraction	1.519 at 589 nm
	spectral transmission	$\geq$ 99 % at 382-980 nm

Table 4.1: EMCal module component materials

Figure 4.6: 2D projective block produced at Illinois.

$0.83\lambda_{int}$.

Figure 4.9 shows the layout of the absorber blocks inside an EMCAL sector along with the internal electronics and cooling. Each module forms a slice in ϕ that gradually tilts along the z axis in order to project back to a position near the vertex at larger rapidity. The 96 blocks for each sector are glued to a sawtooth support structure, shown in Fig. 4.10,

Parameter	Units	Value
Inner radius (envelope)	mm	900
Outer radius (envelope)	mm	1161
Length (envelope)	mm	$2 \times 1495 = 2990$
tower length (absorber)	mm	144
Number of towers in azimuth ($\Delta\phi$)		256
Number of towers in pseudorapidity ($\Delta\eta$)		$2 \times 48 = 96$
Number of electronic channels (towers)		$256 \times 96 = 24576$
Number of SiPMs per tower		4
Number of towers per module		$2 \times 8 = 16$
Number of modules per sector		24
Number of towers per sector		384
Number of sectors		$2 \times 32 = 64$
Sector weight (estimated)	kg	326
Total weight (estimated)	kg	20890
Average sampling fraction		2.3%

Table 4.2: Key parameters of the EMCal modules and sectors

that is attached to a metal plate (strong back) that is attached to the rail system which is mounted on the inner surface of the Inner HCal. The entire sector is enclosed in a thin walled stainless steel box that provides overall support and light tightness. Figure 4.11 shows a cross section of the sector showing the location of the absorber, the light guides, front end electronics and cabling. The towers are read out from the front at the inner radius of the detector. This allows access to the electronics from inside the magnet through a removable cover on the sector enclosure.

4.2.4 Light Guides

Light guides are used to optically couple the SiPMs to the readout surface of the calorimeter blocks. Each light guide will define a readout tower. The surface area of a single tower is roughly 19.8 mm x 19.8 mm = 392 mm^2, while the combined active area of the 4 SiPMs is 4x (3 mm x 3 mm) = 36 mm^2, so only 9 % of the active area is covered by the optical sensors. The severe space limitations inside the sector require the use of a very short light guide, and considerable effort was spent by using optical ray tracing simulations and actual measurements in the lab to optimize its design.In the end, it was found that a simple trapezoidal design gave the best overall light collection efficiency ($\sim$ 15 % for the 4 SiPMs) and was the simplest to construct. Figure 4.12 shows the final design of the light guide.

However, because we require $\sim$ 25K individual light guides for all the towers, and the cost for machining such a larger number was prohibitive, it was necessary to find a cost effective method for producing them. The solution in the end was to produce them by

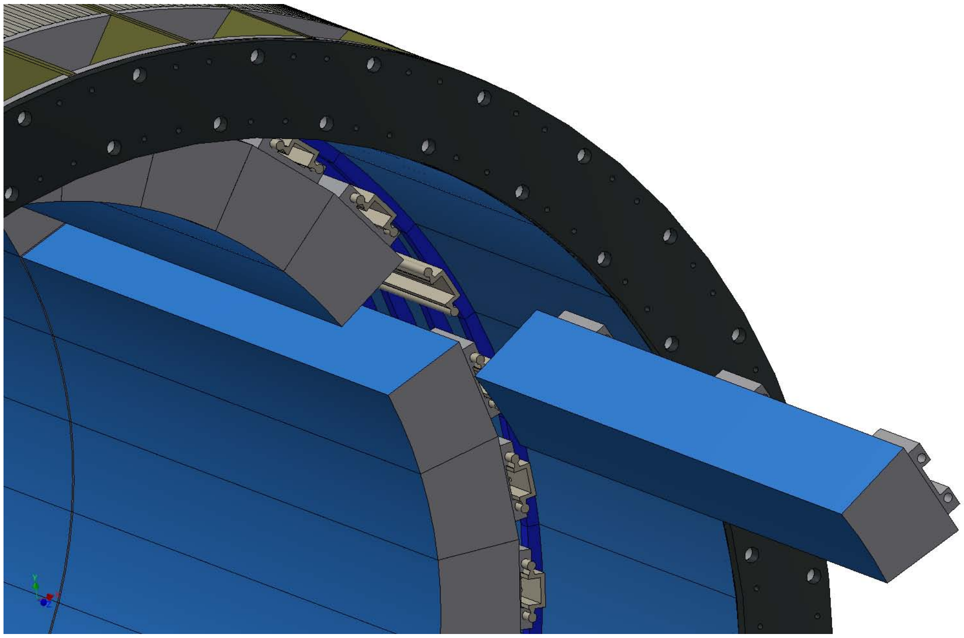

Figure 4.7: EMCal sector showing installation on the Inner HCal.

Figure 4.8: Drawings showing the projectivity of the EMCal blocks along the beam direction (left) and in ϕ (right).

injection molding using a UV transmitting acrylic, but it required a very specialized process to produce optical quality parts using this method. This process was finally successfully developed by a company that specializes in high precision injection molding (NN, Inc. in East Providence, RI). The result was very high quality light guides at a price of $\sim$ \$10 a piece. Figure 4.13 shows some samples of the light guides after they are produced with the injection molding sprue still attached, after machining and finally glued onto the absorber block. Silicone cookies are then used to optically couple the SiPMs to the light guides.

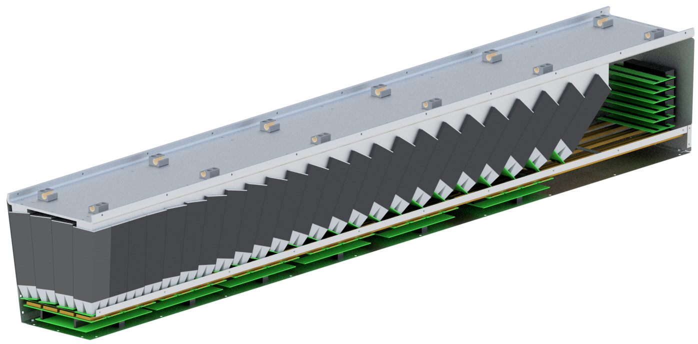

Figure 4.9: EMCAL sector showing internal block layout, electronics and cooling.

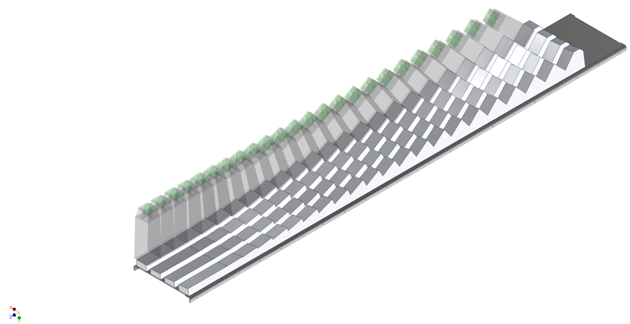

Figure 4.10: Sawtooth support structure used to support the blocks inside the EMCAL sector.

4.2.5 Sensors

The photosensor selected for the EMCal is the Hamamatsu S12572-015P SiPM, or Multi Pixel Photon Counter (MPPC), described in detail in the Electronics - 6.1 Optical Sensors section of this document. This device will be used for both the HCal and EMCal. The EMCal will use a 2x2 arrangement of 4 SiPMs per tower, passively summed into one preamp/electronics readout channel. Figure 4.14 The 4 SiPMs will be gain-matched (selected) and will share a common bias voltage.

4.2.6 Electronics

The readout electronics for the EMCal consists of the analog front end, slow controls, digitizers and power distribution system. The EMCal Preamp Board consists of an 8×2

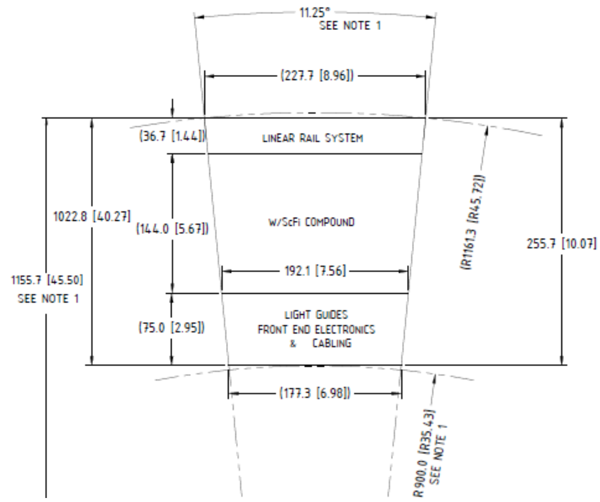

Figure 4.11: Cross sectional drawing of an EMCal sector.

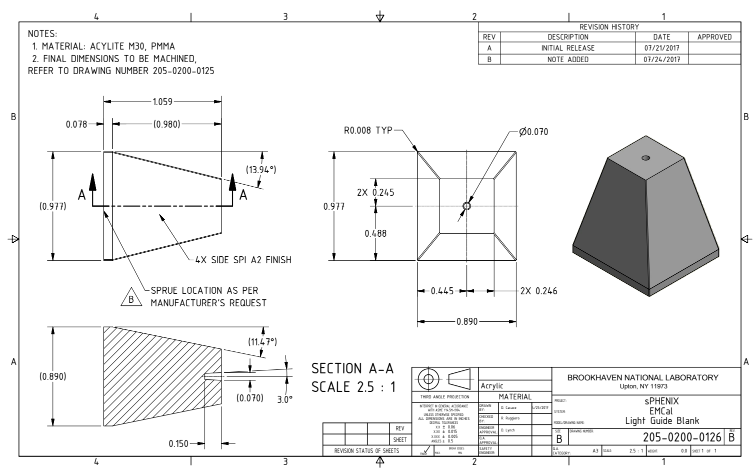

Figure 4.12: Final design for the EMCal light guides.

array of preamplifier circuits that are laid out to match the geometry of the light guides. The Preamp Boards are mounted directly to the light guides. The analog signals from each of the four SiPMs associated with an EMCal tower are passively summed into one readout channel. The analog sum signal is amplified with a common-base transistor amplifier, shaped with a 30 ns peaking time and driven differentially to digitizer electronics located near the detector. The analog signals are digitized with a Flash ADC operating at 6 times the beam crossing (BCO) frequency and stored in a digital pipeline with a 40 BCO latency. Upon receipt of a Level-1 (L1) trigger, the digital wave form is transferred to a readout buffer capable of buffering up to 5 events for readout to the data acquisition system via a

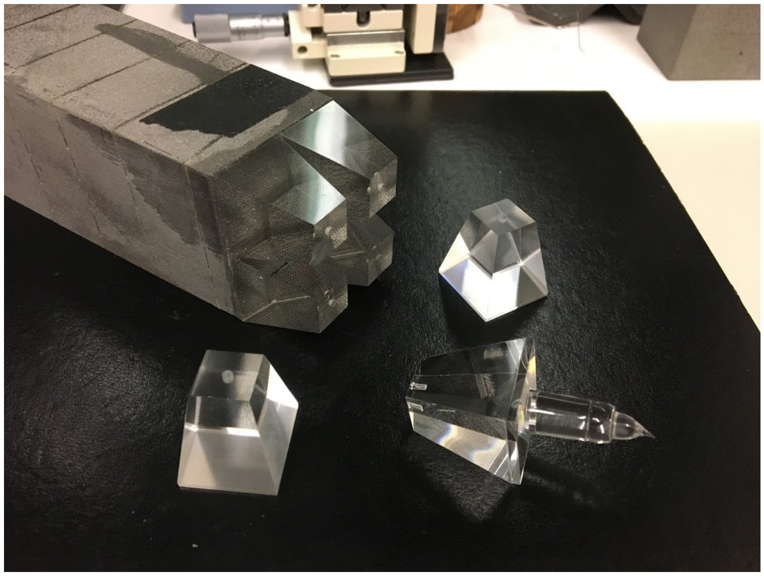

Figure 4.13: Light guides produced by injection molding showing parts after removal from the mold, after machining and finally glued onto absorber block.

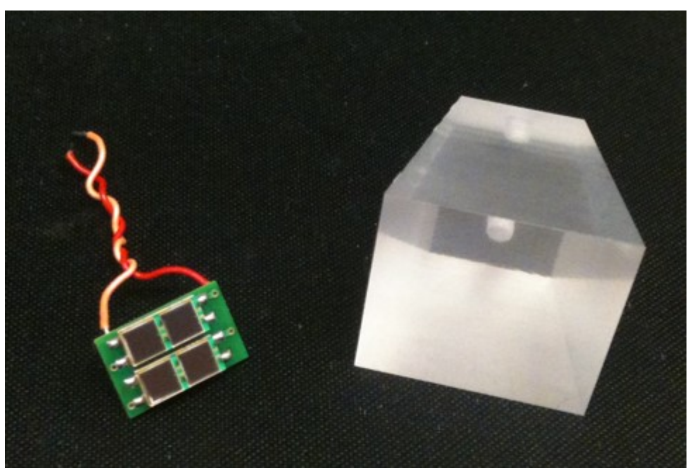

Figure 4.14: Four-SiPM PCB and lightguide. The SiPMs will be optically coupled to the narrow end of the light guide using a clear silione adhesive.

high speed optical link. The digitizer boards also compute trigger primitives which are transmitted to the Level-1 trigger system through independent optical fiber links. Full details of the calorimeter electronics can be found in Chapter 6.

4.2.7 LED Calibration

Pulsed LEDs (450 nm), mounted on the SiPM side of the preamp PCB, and projecting light into the lightguides, will be used to calibrate the detector channels and monitor gain drift.

4.2.8 Cooling

The gain of the SiPMs have a strong dependence on temperature and we therefore need to stabilize and monitor their temperature during operation. In addition, we expect the dark current in the SiPMs to increase significantly due to exposure to neutrons over the course of running for several years. From measurements done in the PHENIX experimental hall, we expect that the total neutron exposure in a year of running may reach $\sim 10^{11}$ n/cm^2 and the dark currents to reach up to several hundred μA per device. We therefore need to provide additional cooling to reduce the noise as it increases over time. A liquid cooling system is being designed that will cool both the preamps and the SiPMs themselves This system is integrated with the readout electronics and cabling scheme inside the sector and is designed to fit in the $\sim$ 7.5 cm of radial space, as shown in Fig 4.11. A prototype version of this cooling system has been designed and implemented in the V2.1 EMCAL prototype described below and will be tested along with the detector in the test beam.

4.3 Simulations

4.3.1 Introduction

Both the 2D and the 1D SPACAL designs have been implemented in detail using the sPHENIX analysis framework and GEANT4. The 1D implementation allows for verifying the simulation with existing test beam data. A large set of calorimeter simulations has been run with the aim of defining design goals and quantifying detector and physics performance. The basic features of the simulation setup are as follows:

- Both the 1D and 2D projective EMCal designs are implemented in a full detector simulation of sPHENIX. The structure of the SPACAL in simulation is detailed to each of the 20M fibers (including core and cladding) to properly study the shower sampling.

- The simulation is based on GEANT4 v4.10 [135] with the QGSP_BERT_HP physics list.tpref

- The default GEANT4 Birks correction model for scintillation light production [135] with Birks constant $k_B = 0.0794$ mm/MeV [136] is implemented.

- The mean number of photoelectrons per GeV of total energy deposit is assumed to be 500. The observed number of photoelectrons follows a Poisson distribution.
- The pedestal width is taken to be 8 photoelectrons with a zero-suppression of 16 photoelectrons per EMCal tower, based on the experience of the EIC eRD1 beam test with the SPACAL [132].
- The sPHENIX offline analysis framework is used to handle the conversion of the ADC value to measured energy, group towers into EMCal clusters, and match with tracks.

Example event displays for a single tower and the full EMCal are shown in Figure 4.15 and 4.16, respectively.

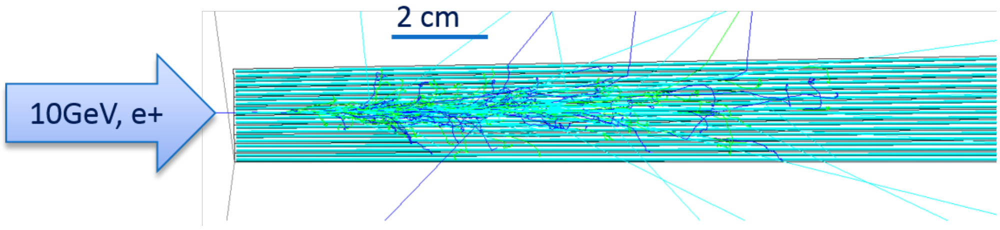

Figure 4.15: Event display of a 10 GeV positron shower in a single SPACAL tower. Scintillation fibers as embedded in the module are also shown, while the absorber material is not displayed.

4.3.2 Verification of Simulation

The simulation was initially verified with data from the EIC eRD1 beam test of the 1D projective SPACAL prototype [132]. As shown in Figure 4.17, the simulation and data agree quite well for three choices of beam energies:

- The measured energy resolution for electron showers is reproduced in simulation within 10%.
- A 10% contribution of muons is expected in the test beam with a "non-electron" Čerenkov cut. Likewise a small amount of electrons and other beam background are suggested by the data.
- The simulated hadronic shower response is consistent with data within a factor of 2 across all energy bins.

Even though good agreement has already been achieved with default tuning of the simulation, further improvements were made to improve the fidelity of measurements to simulation:

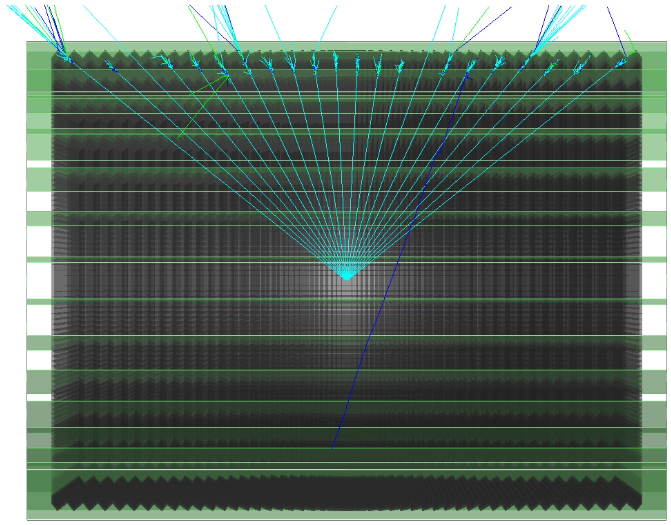

Figure 4.16: Simulation display of a half cut view of the 2D projective EMCal. The SPACAL modules (2x8 towers each) are display in gray; the stainless steel enclosure box is displayed in green.

- The Birks constant for the fiber core material has been tuned. Preliminary tests showed that a higher Birks constant than the one found by the CALICE experiment [137] can significantly improve the agreement for the hadronic shower component.

- Implementation of fiber-to-fiber light collection efficiency variations which account for measured variation in the response of the calorimeter as a function of the position of the incident particle.

An extensive beam test of a section of a prototype sPHENIX electromagnetic calorimeter around zero pseudorapidity has been carried out the Fermilab Test Beam Facility with a wide variety of incident particles, energies, and track position and angle. These results have been submitted for publication[138] and have shown excellent agreement between simulation and measurements. A beam test of a higher pseudorapidity slice of the EMCAL was carried out in February 2017 and also showed good agreement with simulation in spite of the fact that the absorber blocks were th first 2D projective blocks ever produced. A second beam test of a higher pseudorapidity prototype with improved 2D projective blocks was carried out in 2018 and the data from this test is currently being analyzed.

4.3.3 Sampling Fraction

In the W-epoxy and scintillator fiber structure, only energy deposition in the core of fiber is visible via detection of scintillation light, which represents a small fraction of the total shower energy. The sampling fraction is around 2.4% as shown in Figure 4.18 with two choices of typical showers: 4 GeV electrons as typical Υ decay products; and 24 GeV photons as typical for γ-jet measurements. The higher energy showers are sampled with lower sampling fraction as the shower moves deeper into the calorimeter, where the fibers have larger spacing due to the projectivity.

4.3.4 Lateral Shape of Showers

To study the properties of the EM shower in the W-epoxy and scintillator fiber structure, the lateral extension of the EM shower is quantified in Figure 4.19 by histogramming all scintillator GEANT4 hits with their distance to the projection of the incoming 4 GeV electrons (as typical Υ decay products in the central pseudorapidity). The Molière radius is about 2 cm in order to contain 90% of the EM shower. A 3×3 EMCal tower-cluster contains about 95% of the EM shower. For pion showers in the EMCal, which the calorimeter system is designed to reject, the same 3×3 EMCal tower-cluster contains about 50% of the shower energy, which helps to improve the efficiency of the E/p cut. The inner hadron calorimeter (HCal) immediately behind the EMCal is used to catch the tails of the pion shower in order to veto hadrons. A 3×3 inner HCal tower-cluster can contain 60% of the energy of the pion shower tail. These simulations serve as a guideline for the choice of tower size for both EMCal and inner HCal, as the choice of tower segmentation is optimized for the shower containment in 3×3 tower-clusters, and a finer towering structure would not significantly improve the clustering.

The shower size is also quantified using 1-D and 2-D SPACAL towers as shown in Figure 4.20. For a 2-D projective SPACAL, despite the fact that the towers are shifted along the longitudinal direction, a circular distribution of towers for the EM shower is observed around the track projection for both central and forward pseudorapidity. This leads to a round-shaped cluster with a minimal number of towers necessary to contain an EM shower. In comparison, a shower in the 1-D projective SPACAL is spread into multiple towers along the polar direction, which leads to an elongated cluster covering more towers as quantified in the right panel of Figure 4.20.

4.3.5 Single EM Shower Performance

The linearity and energy resolution for photon clusters as simulated through the full sPHENIX detector and analysis chain are presented in Figure 4.21 and 4.22.

For sPHENIX γ-jet measurements, the photon clusters were simulated with the full sPHENIX detector, which produces an energy resolution better than $14\%/\sqrt{E}$ as shown on the left side of Figure 4.21.

Single electrons are also simulated with the full sPHENIX simulation implementation, and the resolution is shown in the right panel of Fig. 4.21. The electron energy resolution is comparable to the $\sim 16\%/\sqrt{E}$ stochastic term requirement, and has a less than 3% constant term.

As shown in Figure 4.22, the linearity for the 2D SPACAL towers is better than 3.5%, as defined as the relative deviation from $E_{\mathrm{reco}}/E = 1$ at the maximum photon energy of $E = 32$ GeV. The linearity is improved to better than 2.0% when photons are in the forward rapidity direction, where the SPACAL becomes thicker along the path of the photon and therefore smaller back-leakage occurs. The single electron linearity is very similar to the single photon linearity as shown in the right panel of Fig. 4.22. In both cases the simulation demonstrates less than 3% linearity.

4.3.6 Occupancy

The occupancy in central Au+Au collisions (the highest background event) is illustrated in Figure 4.1 and quantified in Figure 4.23. For a typical 3×3 EMCal tower-cluster in the 2-D projective SPACAL, the mean background energy is approximately 322 MeV. For the 1-D projective SPACAL at forward rapidity, a significantly larger underlying event (about 550 MeV) would be included in a cluster since electron showers would spread into more towers (as illustrated in the right panel of Figure 4.20). Meanwhile, this background presents a large tail extending to higher energy, which leads to a challenge of rejecting hadron showers for electron-ID as the logarithmically dropping hadron shower tail is shifted up in energy by this background.

Simulations were also performed with single photons and electrons embedded in $\sqrt{s} = 200$ GeV Au+Au 0-4 fm HIJING backgrounds. These embedded simulations quantify the expected background for the most central Au+Au events, which are events with the largest backgrounds. The linearity and resolution of the embedded single photons and electrons simulated with the full sPHENIX detector are shown in Figs. 4.24 and 4.25, respectively. The Au+Au background causes the linearity to degrade at small energies, however at large photon energies the linearity remains less than 3% similarly to the single particle simulations. The resolution is also degraded, within the limited statistical precision of this simulation, due to the inclusion of the underlying event in the cluster energy, which adds an additional term to the resolution that goes as 1/E.

4.3.7 Electron Identification

One key function of the EMCal is to identify the electron/positron tracks within the hadronic background for the Υ measurement. The energy of the electron/positron from the Υ decay range from 2-10 GeV, with averages of 4.8 GeV in the central pseudorapidity to 5.7 GeV in the forward direction $(0.7 < \eta < 0.9)$. The primary method of electron-identification (eID) is to match the measured track momentum with the measured cluster energy in the EMCal. Furthermore, the inner hadron calorimeter can improve the eID by vetoing track candidates with a large leakage behind the EMCal. For each track, cluster energy information from both the EMCal and inner HCal is analyzed using a likelihood method, by comparing the observed cluster energy with the EMCal-HCal two-dimensional probability distributions extracted from template samples of pure electrons and hadrons. By selecting tighter or looser cuts, the hadron rejection versus electron efficiency curves can be mapped out for each combination of track rapidity, track momentum, and SPACAL configurations.

The reference electron identification performance is shown in Figure 4.26 in single particle simulations (expected performance in $p+p$ collisions) and 4.27 in the most central Au+Au collisions (top 0-10% in centrality). These reference eID performance curves are simulated with a 1-D projective SPACAL fiber structure. The hits in GEANT4 can be grouped around the track projection into clusters in order to estimate the performance for the 2-D projective SPACAL, or grouped radially in order to estimate the performance for the 1-D projective SPACAL. The cluster energy is summed over all energy deposited in the fiber core (prior to the Birks correction model for scintillation light production [135]), which is then scaled to the measured energy in the calorimeter with a scaling constant of 1/(sampling fraction).

In these reference studies, the 2-D projective SPACAL provided better than 100:1 pion rejection at 95% efficiency for 4 GeV electrons in $p+p$ collisions (Figure 4.26), and better than 90:1 pion rejection at 70% efficiency for 4 GeV electrons in the most-central Au+Au collisions (left panel of Figure 4.27). These pion rejection and electron efficiency values have been used for the estimates of the Υ in our reference design. We also estimate that if a 1-D projective SPACAL is used, the pion rejection at large pseudorapidities will be reduced due to the larger cluster size necessary to contain the EM-shower, as shown in the right side of Figure 4.27.

Significant simulation effort has also been invested into updating these projections with a realistic setup of the SPACAL as shown in Figure 4.16, including incorporating the support/enclosure structures and the longitudinal offsets of the modules, and improved shower simulation (including the Birks scintillation model [135], photon fluctuations, and pedestal widths, which are cross-checked with test beam results as shown in Figure 4.17. When compared with the reference performance, preliminary results show improved eID performance with the suppressed hadron response in the default GEANT4 Birks scintillation model.

4.3.8 Dynamic range

The dynamic range required for the ADC system is studied by comparing the maximum energy deposition in a tower to the pedestal width. For a simulated 50 GeV photon shower, a maximum of 22k photoelectrons were observed in a single tower as shown in Figure 4.28 (assuming a high pixel count SiPM). To encode this maximum photoelectron count down to the pedestal noise of 8 photoelectrons, a 12-bit ADC is required. The EMCal electronics, which provides a 14-bit ADC, will satisfy this requirement.

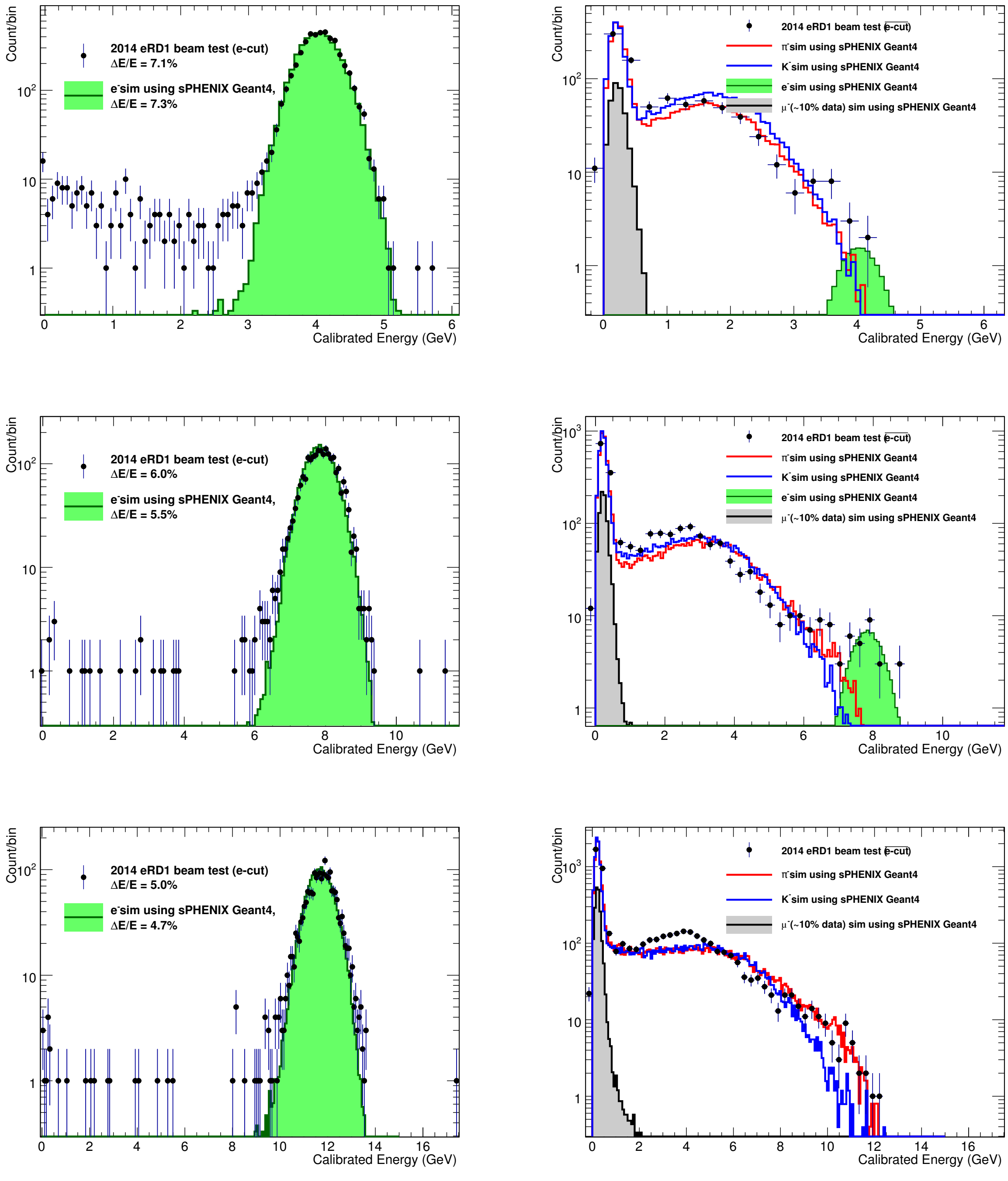

Figure 4.17: Comparison of the eRD1 beam test data and sPHENIX GEANT4 simulation for three choices of beam energies: 4.12 GeV (top), 8.0 GeV (middle) and 12.0 GeV (bottom). The left column data (black points) are with an electron requirement based on a beam Cherenkov detector, and the right column with a non-electron requirement. Curves represent simulated electrons (green), pions (red), kaons (blue) and muons (black).

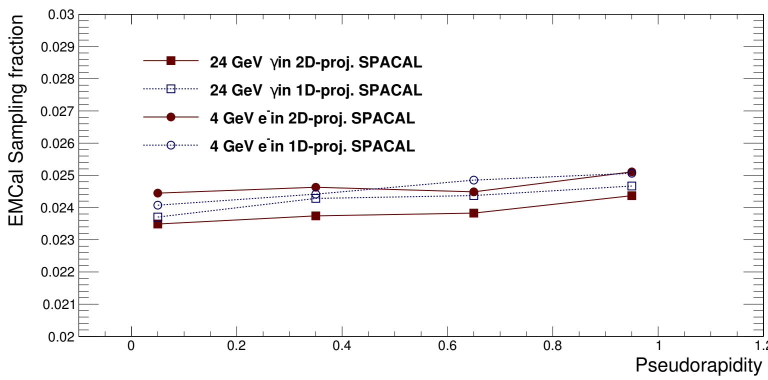

Figure 4.18: The sampling fraction of the 1D and 2D projective SPACAL as a function of pseudorapidity. Two energy ranges were chosen: the circles represent electron showers at 4 GeV, which is a typical energy for Υ measurements; the squares represent photon showers at 24 GeV, which is a typical energy for γ-Jet measurements.

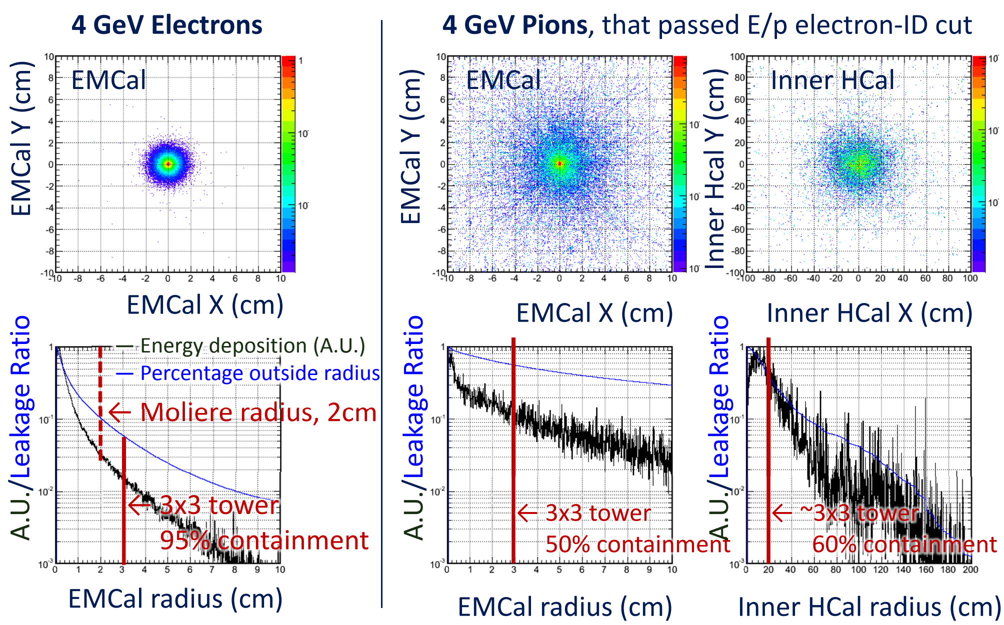

Figure 4.19: The lateral expansion of 4 GeV electron showers in the EMCal (left column), which is compared with 4 GeV negatively charged pion showers in the EMCal (middle column) and in the inner HCal (right column). The center, $(X, Y) = (0, 0)$ cm, denotes the projection of the electron track. Then the energy deposition of all scintillator hits in GEANT4 is histogrammed versus the lateral distance from the track projection. The top row shows the energy deposition density in the 2-D lateral dimension, and the bottom row shows the energy density (black) and the shower leakage ratio (blue) vs. lateral radial distance.

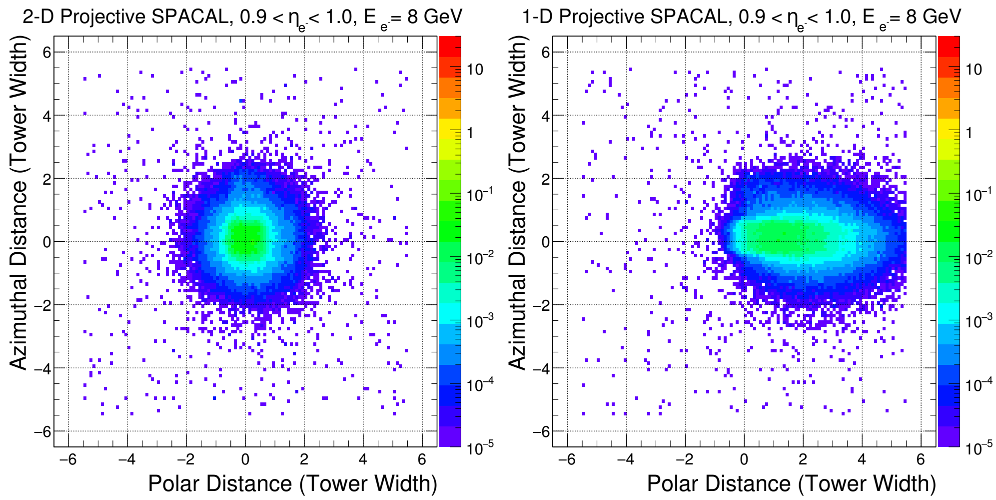

Figure 4.20: For very forward pseudorapidity, the lateral distribution of 8 GeV electron showers as observed in the 2-D projective (left) and 1-D projective (right) SPACAL towers. The polar (X-axis) and azimuthal (Y-axis) distances are defined as the distance between the tower and the electron track projection, in the unit of tower width.

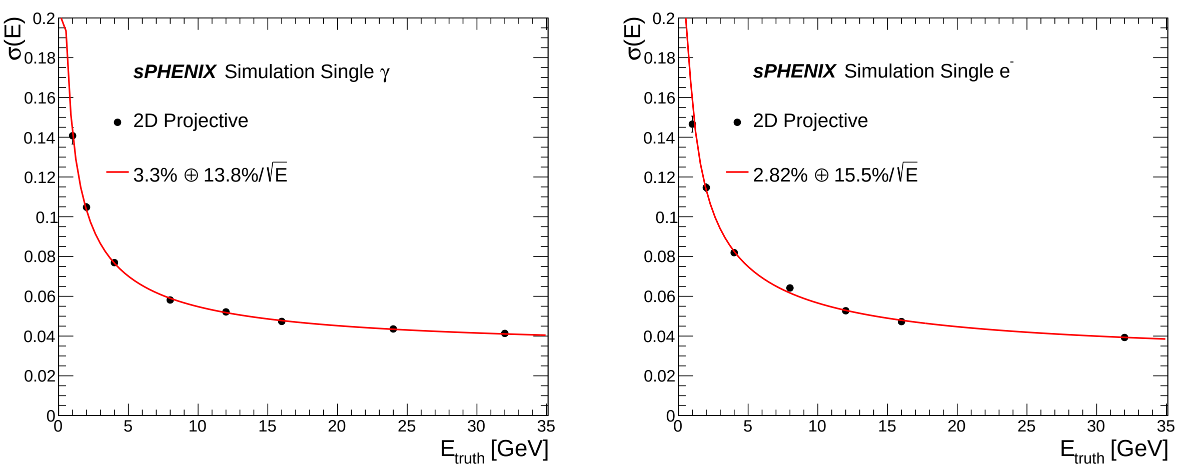

Figure 4.21: Left: the energy resolution for single photon clusters as reconstructed with the fully simulated sPHENIX detector, right: the energy resolution for single electron clusters as reconstructed with the fully simulated sPHENIX detector. Fits are performed as a quadratic sum of linear and statistical terms to show the resolution 2D projective towers.

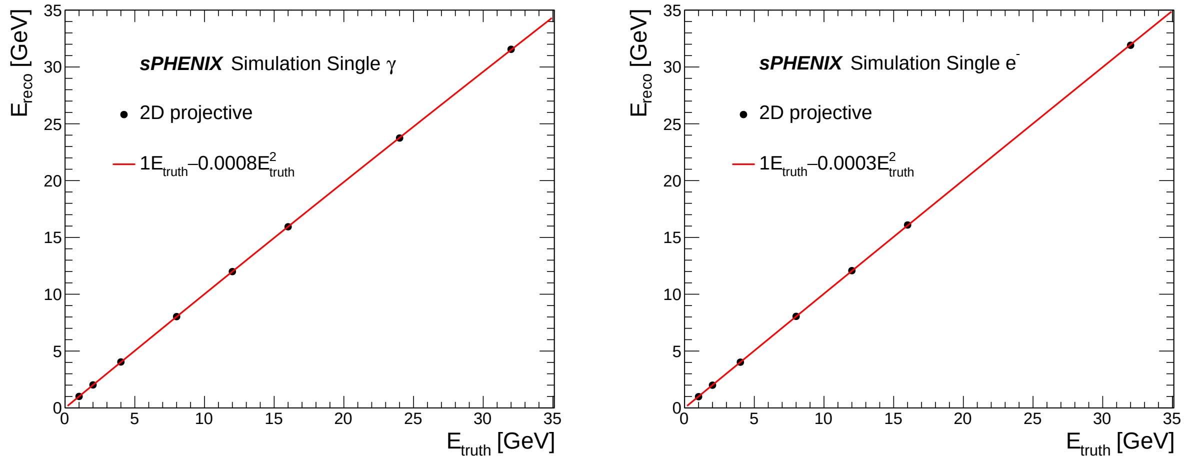

Figure 4.22: Linearity for single photon clusters (left) and single electron clusters (right) as reconstructed with the full sPHENIX detector simulation and analysis chain. The linearity is calibrated for each pseudorapidity region to 1 at the low energy end, while the non-linearity towards the high energy end is quantified via a quadratic fit.

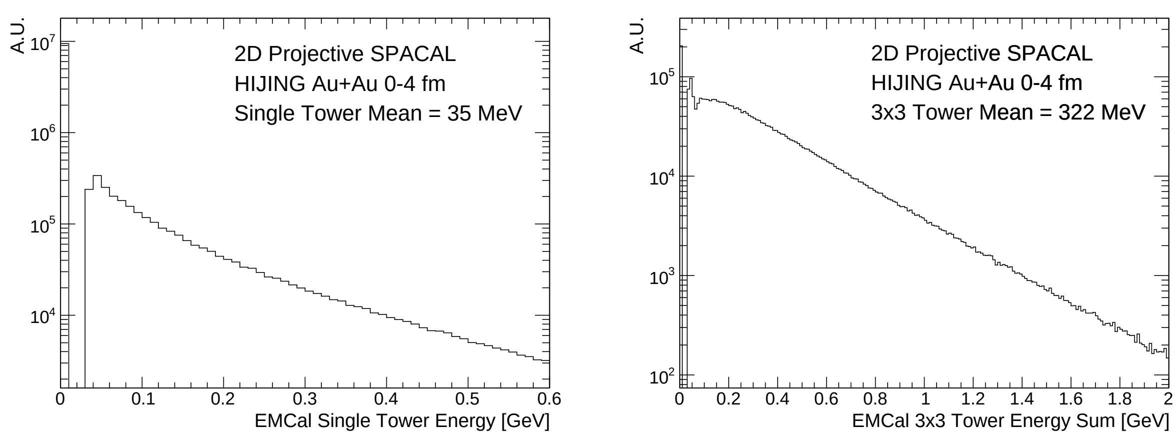

Figure 4.23: (left) Energy per tower ($\sim 1R_M^2$) for central Au+Au HIJING events, (right) Mean energy for a 3×3 EMCal tower-cluster. The 2-D projective SPACAL configuration is shown here.

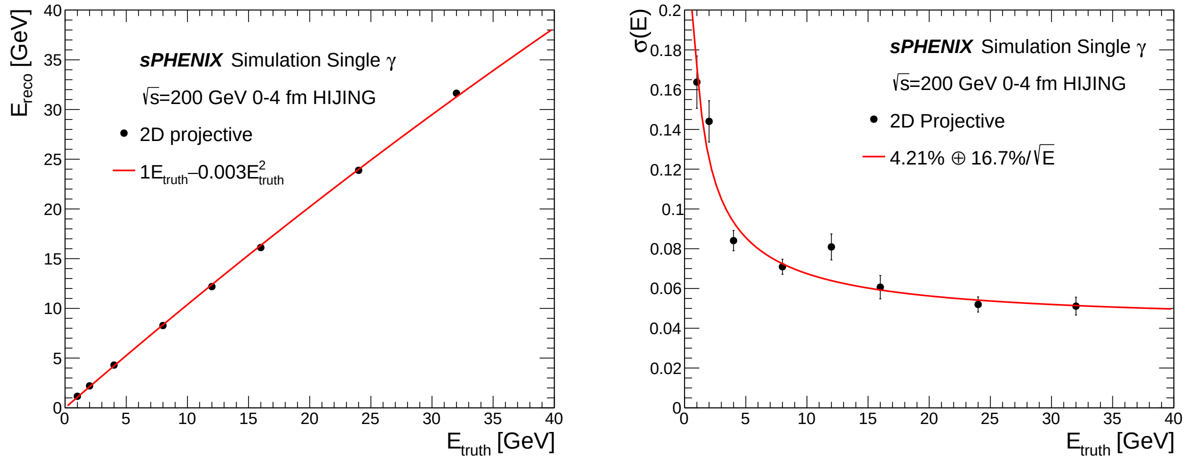

Figure 4.24: The linearity (left) and resolution (right) for single photons embedded in $\sqrt{s} =$ 200 GeV 0-4 fm HIJING Au+Au backgrounds is shown.

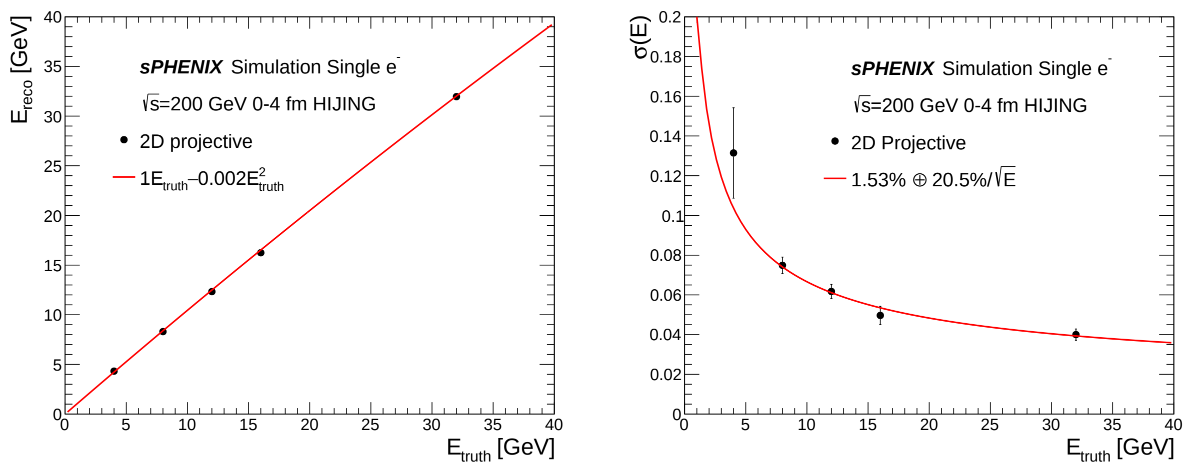

Figure 4.25: The linearity (left) and resolution (right) for single electrons embedded in $\sqrt{s}$ = 200 GeV 0-4 fm HIJING Au+Au backgrounds is shown. The $1/\sqrt{E}$ term in the resolution is largely unconstrained due to the poor statistical precision of this simulation.

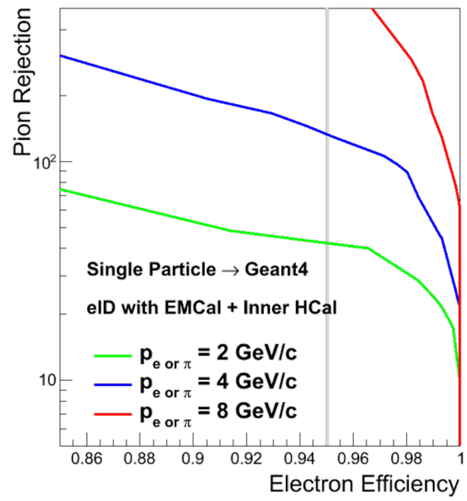

Figure 4.26: Pion rejection vs. electron identification efficiency for a single particle simulation for the 2-D projective SPACAL, which represents the performance for p+p and EIC collisions.

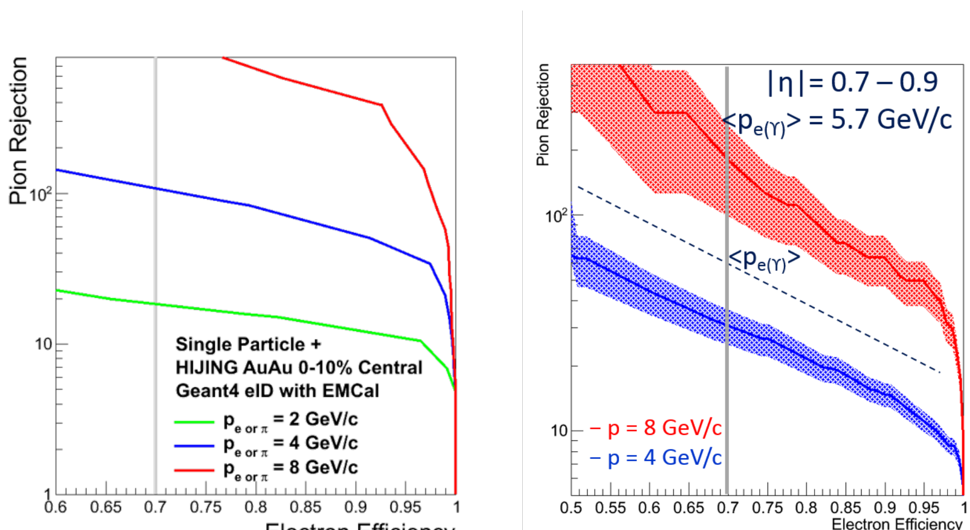

Figure 4.27: The pion rejection vs electron identification efficiency for the 2-D projective (left) and 1D-projective (right) SPACAL in central Au+Au collisions (0-10% central).

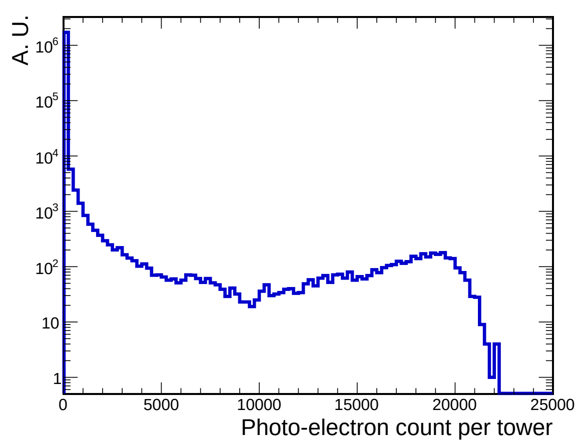

Figure 4.28: Number of photoelectrons per tower for 50 GeV photons as the maximum energy shower targeted by this calorimeter system. To encode the maximum photoelectron count down to the pedestal noise level, a 12-bit ADC is required.

4.4 Prototyping and Testing

Over the past 3 years, several prototypes of the EMCAL have been built and tested in order to study its design and improve its performance. These prototypes have evolved from the original 1D projective UCLA design to the 2D projective design that is in the current design of the sPHENIX detector. Each of these prototypes was tested in the beam at the Fermilab Test Beam Facility (FTBF) in order to measure their energy resolution, linearity and other key performance parameters. They each were tested in a stand alone configuration where the EMCAL prototype was studied in detail by itself, and also in combination with prototypes of the Inner and Outer HCALs to simulate the final sPHENIX configuration. The sections below give a brief summary of the results from these tests.

4.4.1 1D Projective Prototype (V1)

The first EMCAL prototype (V1) consisted of 1D projective blocks similar to the blocks that will be used in the detector for the most central rapidity range. The blocks were essentially copied from the original UCLA design and consisted of a combination of blocks produced at UIUC and by the company that supplied the tungsten powder for all of the blocks we produced so far (Tungsten Heavy Powder). The prototype consisted of an 8×8 array of 64 towers made up of 2×2 tower 1D projective blocks. The detector was tested at the FTFB in the winter of 2016 and the results have been summarized and submitted for publication [138]. As an overall summary of the results, Figure 4.29 shows the energy resolution measured for this prototype for the beam centered on a single tower. For the UIUC blocks at an incident beam angle of 10°, the measured energy resolution was $12.7\%/\sqrt{E} \oplus 1.6\%$ after unfolding a 2% momentum spread of the beam, which agrees well with tests done by the UCLA group with similar prototypes of their design [132, 133].

An additional important test in the 2016 test beam results is shown in Fig. 4.30, which shows the hadron rejection of the EMCal as tested and described in Ref. [138]. The measured rejection factor compares well to three different GEANT4 simulation configurations as shown in the bottom panel of Fig. 4.30. For electrons in the range of 4-5 GeV, where electron and positron pairs from Υ decays are expected to be measured in the sPHENIX acceptance, the hadron rejection as measured with the 1D projective prototype will provide the required discriminatory power for electron identification.

4.4.2 2D Projective Prototypes (V2 and V2.1)

The second EMCAL prototype (V2) consisted of 2D projective blocks that represented the large rapidity region ($\eta \sim 1$) of the sPHENIX calorimeter. It consisted again of an 8×8 array of 64 towers which was made up of 16 2D projective blocks, each having 2×2 towers. These were the first 2D projective blocks ever produced and allowed us to develop the numerous

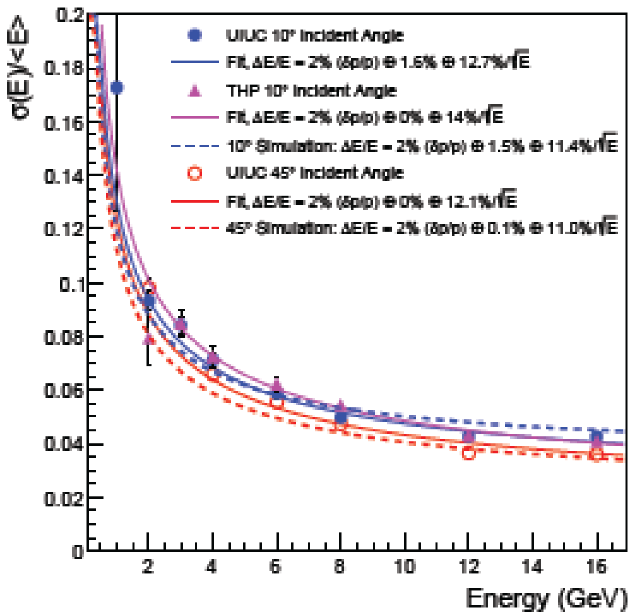

Figure 4.29: Energy resolution measured for the first EMCAL prototype (V1) consisting of 1D projective with the beam centered on a single tower.

new procedures required to produce these blocks. The prototype was tested at Fermilab in 2017, again in stand alone mode to measure its detailed performance parameters, and also in combination with prototypes of the Inner and Outer HCAL. These results have been presented at various conferences and appear in the proceedings [139].

We observed a strong position dependence to the shower response due to non-uniformities in the light collection and dead material near the block boundaries. We corrected for this using two methods. One was using a scintillation hodoscope in the beam to measure the beam position and the other was to use the measured shower position from the calorimeter itself. Both methods gave similar results and are shown in Fig.4.31 The energy resolution measured over a 4×4 cm region of one of the blocks, which included the boundaries between 4 light guides but not the boundaries between different blocks, was $\sim 13.0\%/\sqrt{E}$ $\oplus$ 1.5% after unfolding a 2% momentum spread of the beam at an incident beam angle of 10°, which is well within the sPHENIX specs. However, when the beam spread was expanded and block boundaries were included, the energy resolution degraded slightly as shown in Fig. 4.32. In this figure, the simulation does not exactly reproduce the test beam measurements since the poor non-uniformities have not been implemented into the simulation. We believe this degradation in the resolution was mainly due to initial problems in producing the first 2D projective blocks that have now been corrected, and we have also implemented additional improvements in the light collection as well. A new version of the 2D projective prototype (V2.1) with the improved blocks has been tested in

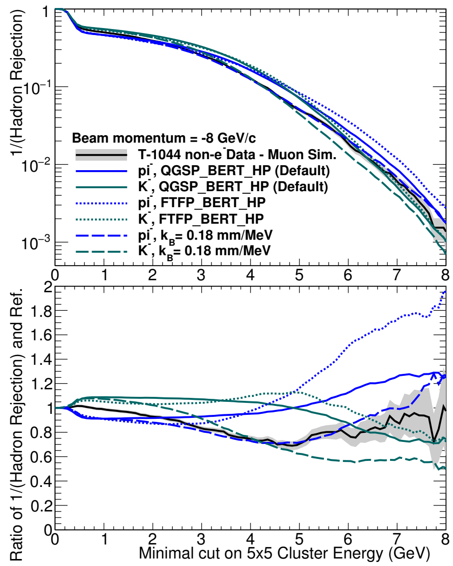

Figure 4.30: The hadron rejection is shown as a function of the minimal energy cut for a 5x5 tower cluster for a negatively charged beam of momentum 8 GeV/c. The test beam data are shown as a black curve, with uncertainties in grey, and are compared with several pi^- and K^- simulation configuration curves.

the test beam at Fermilab in early 2018, and preliminary results show improvements in the overall light collection around the block boundaries.

4.5 DOE MIE Scope

Anticipated DOE funding is not sufficient to support construction of the full electromagnetic calorimeter covering $-1.1 < \eta < 1.1$, which, as has been described, has a total of 256 towers in ϕ and 96 towers in η. The physics consequences of permanently reducing the acceptance of the EMCAL has been explored by the collaboration in a cost reduction document, which concludes that the main physics goals can still be largely achieved with the acceptance reduced to $-0.85 < \eta < 0.85$, if no other sources of funding for the restoration of the full acceptance becomes available. Due to the modular design of the EMCAL, it is possible to construct EMCAL sectors with reduced pseudorapidity coverage without any changes to the overall design of the sector or the blocks.

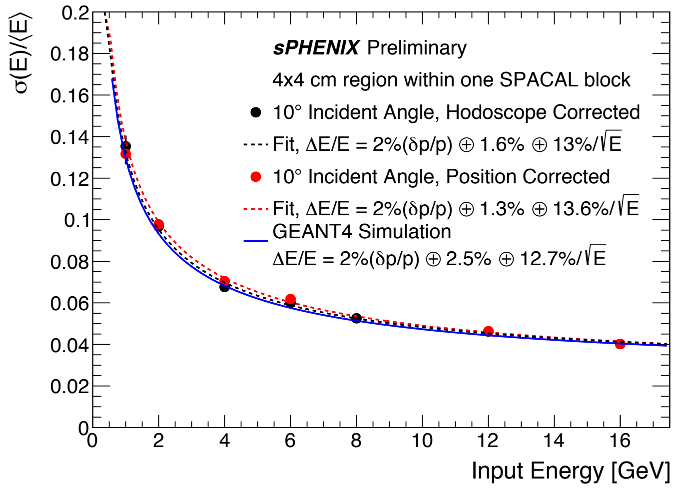

Figure 4.31: Energy resolution measured for the second EMCAL prototype (V2) consisting of 2D projective towers with the beam centered on a region containing several towers but excluding block boundaries. Curves show two methods used for position dependent corrections

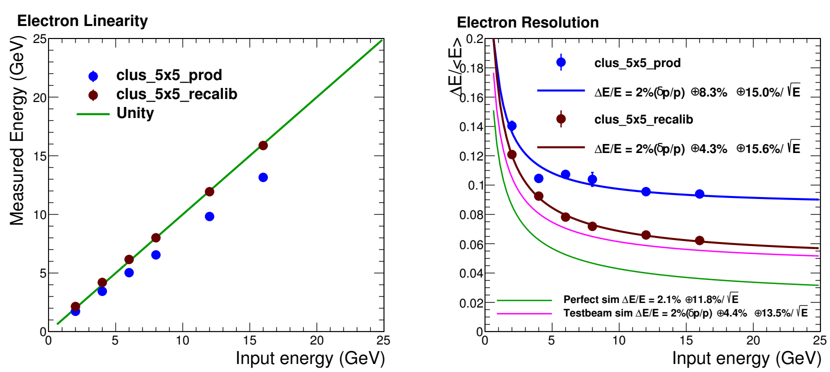

Figure 4.32: The linearity (left) and energy resolution (right) of the 2D SPACAL prototype including the block boundaries as measured in the 2017 test beam. The blue points show the energy before the hodoscope position calibration, and the brown points show the energy after the hodoscope position calibration. The resolution degrades slightly due to the inclusion of the block boundaries, which contain non-uniformities.

Chapter 5

Hadronic Calorimeter

The hadronic calorimeter (HCal), essential for the measurement of jets, is a steel-scintillator sampling calorimeter with two longitudinal segments, one inside and one outside the magnet. As the result of a recent descoping effort, however, the current baseline replaces the inner longitudinal segment (called the Inner HCal) with an uninstrumented aluminum frame. The collaboration is actively pursuing different options to restore the Inner HCal. The outer longitudinal segment (called the Outer HCal) also serves as the flux return of the solenoid and provides mechanical support for the solenoid and the detector components inside the solenoid. This chapter describes the reference design of the HCal detectors, prototypes of these detectors, test beam performance, simulation results, and progress toward the development of a complete detector design. As the descoping exercise only concluded in December 2017, most performance plots presently at hand—and shown here in the document—are with the configuration that has the Inner HCal. Since the Inner HCal only comprises 0.55 λ (compared to 3.8 λ in the Outer HCal), those plots serve as reasonable proxies for the descoped version of the detector. Studies on the impact of the uninstrumented aluminum frame are presented in Section 5.3 (Simulations).

5.1 HCal Requirements and Overview

The performance requirements for the sPHENIX HCal are driven by the physics requirements related to measuring jets in relativistic heavy ion collisions and the need to realize the HCal in an efficient, cost-effective manner.

A uniform, hermetic acceptance is required between $-1.1 < \eta < 1.1$ and $0 < \phi < 2\pi$ to minimize the systematic errors associated with energy that is not measured by the detector. For similar reasons, the calorimeter system is required to absorb >95% of the incident hadronic energy, which sets the required depth of the calorimeter system to 4.9 nuclear interaction lengths[1]. The modest single hadron energy resolution requirement of $\frac{\sigma}{E} \sim \frac{100\%}{\sqrt{E}}$ for the HCal is adequate in heavy ion collisions since, for low energy jets, the jet energy resolution is dominated by the subtraction of the underlying event and not the energy resolution of the HCal.

Key design aspects of the HCal are determined by the mechanical and practical limitations. To limit civil construction in the 1008 interaction region at RHIC, it is highly desirable that the sPHENIX detector fit through the existing shield wall opening. In addition, the engineering challenge of supporting the HCal increases with the radius of the detector, which drives a design that makes use of the Outer HCal as the magnet flux return and places the Inner HCal segment or replacement aluminum frame inside the solenoid magnet where it also supports the EMCal. For these reasons we have chosen a novel tilted plate calorimeter design, which is described more fully in the following sections.

5.2 Detector Design

The design of the hadronic calorimeter has been developed by a program of simulation and prototyping which is continuing to optimize the design. The reference design consists of two longitudinal compartments. As the result of a descoping process at the end of 2017, the Inner HCal, located inside the solenoid, is replaced an uninstrumented 0.25 λ aluminum frame, the design of which is taken from the Inner HCal. Engineering finite element analysis has shown that an Al version of the Inner HCAL design is capable of supporting the EMCal within safety margins. The collaboration is actively pursuing different options to restore the Inner HCal, which comprises 0.55 nuclear interaction lengths (as originally designed in stainless steel). This would provide more information on the longitudinal development of electromagnetic showers, thus providing additional discrimination between electrons and hadrons beyond determination of E/p in the electromagnetic shower. The larger Outer HCal provides the remaining interaction lengths (3.8 λ) needed to achieve the required energy resolution and serves as flux return for the solenoid magnet. In order to keep cost low, the Inner HCal uses a very similar design as the outer one.

The basic calorimeter concept is a sampling calorimeter with absorber plates tilted from the radial direction. This design provides more uniform sampling in azimuth and gives some information on the longitudinal shower development. The current design uses tapered plates for the Outer HCal. The Inner HCal would not require tapered plates as studies showed that tapering the shorter Inner HCal plates was not necessary, and tapering them increased the machining cost. Extruded tiles of plastic scintillator with an embedded wavelength shifting fiber are interspersed between the absorber plates and read out at the outer radius with silicon photomultipliers (SiPMs). The tilt angle is chosen so that a radial track from the center of the interaction region traverses at least four scintillator tiles. Each tile has a single SiPM, and the analog signal from each tile in a tower (five for

[1] for a typical 30 GeV jet where the leading particle carries 2/3 of the jet energy

the Outer HCal, four for the Inner HCal) are ganged to a single preamplifier channel to form a calorimeter tower. Tiles are divided in slices of pseudorapidity so that the overall segmentation is $\Delta\eta \times \Delta\phi \sim 0.1 \times 0.1$.

5.2.1 Scintillator

Property	
Plastic	Extruded polystyrene
Scintillation dopant	1.5% PTP and 0.01% POPOP
Reflective coating	Proprietary coating by surface exposure to aromatic solvents
Reflective layer thickness	50μ
Wrapping	one layer of 100 μ Al foil, one layer of 30 μ cling-wrap, one 100 μ layer of black Tyvek
Attenuation length in lateral (with respect to extrusion) direction	$\sim$2-2.5 m
Wavelength shifting fiber	Single clad Kuraray Y11
Fiber size	1 mm round
Fiber core attenuation length	> 2 m
Optical cement	EPO-TEK 3015

Table 5.1: Properties of HCal scintillating tiles.

The scintillating tiles are similar to the design of scintillators for the T2K experiment by the INR group (Troitzk, Russia) who designed and built 875 mm long scintillation tiles with a serpentine wavelength shifting fiber readout [140]. The MINOS experiment developed similar extruded scintillator tiles. The properties of the HCal scintillating tiles are listed in Table 5.1.

We have considered two wavelength shifting (WLS) fiber manufacturers: Saint-Gobain (formerly BICRON), product brand name BCF91A [141], and Kuraray, product name Y11 [142]. Both vendors offer single and double clad fibers. The Kuraray single clad fiber was chosen due to its flexibility and longevity, which are critical in the geometry with multiple fiber bends. The properties of the HCal wavelength shifting fibers are listed in Table 5.2.

The scintillator emission spectrum and the fiber absorption spectrum are shown in Figure 5.1. The fiber routing was designed so that all energy deposited in the scintillator is within 2.5 cm of a WLS fiber, and the bend radius of any turn in the fiber has been limited to 35 mm based on T2K and our own empirical experience with test tiles. The two ends of a fiber are brought to the outer radius of a tile where a small plastic holder carries a 3×3 mm SiPM at 0.75 mm from the end of the polished fibers. Both the Inner and Outer

Property	
Fiber diameter	1.0 mm
Formulation	200, K-27, S-Type
Cladding	single
Cladding thickness	2 percent of d (0.02 mm)
Numerical Aperture (NA)	0.55
Emission angle	33.7 $^\circ$
Trapping Efficiency	3.1 percent
Core material	polystyrene (PS)
Core density	1.05 g/cc
Core refractive index	1.59
Cladding material	Polymethylmethacrylate (PMMA)
Cladding density	1.19 g/cc
Cladding refractive index	1.49
Color	green
Emission peak	476 nm
Absorption Peak	430 nm
Attenuation length	$>$ 3.5 m
Minimum bending radius	100 mm

Table 5.2: Properties of Kuraray Y-11 (200) wavelength shifting fibers.

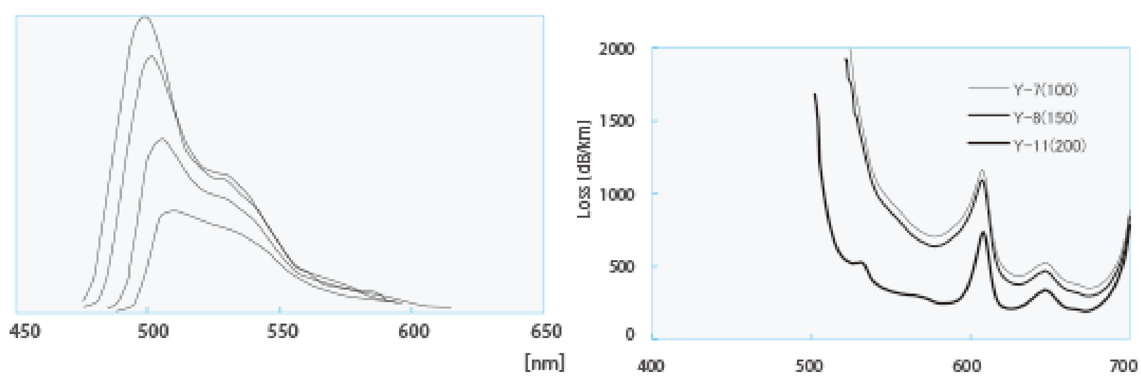

Figure 5.1: Y-11 (200) WLS fiber emission spectrum for various fiber lengths (10, 30, 100, 300 cm, from top to bottom) (left) and transmission loss (right).

HCal are north-south symmetric and require 24 tiles along the η direction. The design requires 12 different shapes for tiles for each longitudinal segment. As an example, Fig. 5.2 shows the tile and embedded fiber pattern for the Outer HCal.

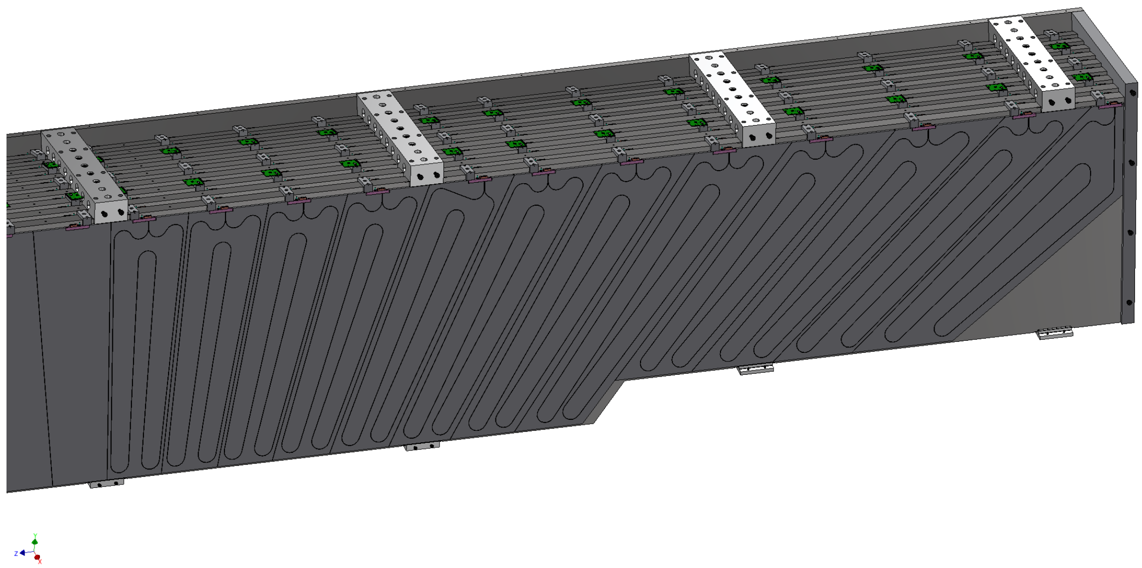

Figure 5.2: Scintillator tiles in a layer of the Outer HCal.

5.2.2 Outer HCal

The major components of the Outer HCal are tapered steel absorber plates and 7680 scintillating tiles which are read out with SiPMs along the outer radius of the detector. The detector consists of 32 modules, which are wedge-shaped sectors containing 2 towers in ϕ and 24 towers in η equipped with SiPM sensors, preamplifiers, and cables carrying the differential output of the preamplifiers to the digitizer system on the floor and upper platform of the detector. Each module comprises 9 full-thickness absorber plates and 2 half-thickness absorber plates, so that as the modules are stacked, adjoining half-thickness absorber plates have the same thickness as the full-thickness absorber plates. The tilt angle is chosen to be 12 degrees relative to the radius, corresponding to the geometry required for a ray from the vertex to cross four scintillator tiles. Table 5.3 summarizes the major design parameters of the Outer HCal, which is illustrated in Figure 5.3.

Since the Outer HCal will serve as the flux return of the solenoid, the absorber plates are single, long plates running along the field direction. The Outer HCal SiPM sensors and electronics are arranged on the outer circumference of the detector.

5.2.3 Inner HCal

The Inner HCal (or the replacement aluminum frame) occupies a radial envelope bounded by a 50 mm clearance inside the solenoid cryostat and the outer radius of the electromag-

Parameter	Units	Value
Inner radius (envelope)	mm	1820
Outer radius (envelope)	mm	2700
Length (envelope)	mm	6316
Material		1020 low carbon steel
Number of towers in azimuth ($\Delta\phi$)		64
Number of tiles per tower		5
Number of towers in pseudorapidity ($\Delta\eta$)		24
Number of electronic channels (towers)		$64 \times 24 = 1536$
Number of optical devices (SiPMs)		5 × 1536 = 7680
Number of modules (azimuthal slices)		32
Number of towers per module		$2 \times 24 = 48$
Total number of absorber plates		$5 \times 64 = 320$
Tilt angle (relative to radius)	°	12
Absorber plate thickness at inner radius	mm	10.2
Absorber plate thickness at outer radius	mm	14.7
Gap thickness	mm	8.5
Scintillator thickness	mm	7
Module weight	kg	12247
Sampling fraction at inner radius		0.037
Sampling fraction at outer radius		0.028
Calorimeter depth	λ	3.8

Table 5.3: Design parameters for the Outer Hadronic Calorimeter.

netic calorimeter. The skin on the inner radius provides support for the electromagnetic calorimeter and the HCal, while steel rings at either end carry the load to the Outer HCal.

Table 5.4 shows the basic mechanical parameters of the Inner HCal reference design. The detector would be built in 32 modules, which would be wedge-shaped sectors comprising 8 gaps with 7 full-thickness plates and 2 half-thickness plates (so that as the modules are stacked, adjoining half-thickness plates have the same thickness as the full-thickness plates). The modules contain 2 towers in ϕ and 24 towers in η equipped with SiPM sensors, preamplifiers, and cables carrying the differential output of the preamplifiers to the digitizer system on the floor and upper platform of the detector. The instrumentation consists of 6144 scintillating tiles and optical devices, 1536 preamps, and cabling. Figure 5.4 shows the arrangement of absorber plates in a sector with scintillator tiles sandwiched between stainless steel absorber plates. To preserve the "four crossing" geometry, the tilt angle is chosen to be 32 degrees relative to the radius.

In the current baseline, the Inner HCal is replaced with a design that clones the steel frame of the Inner HCal design and uses a hardened aluminum alloy for the material. Studies have demonstrated that this frame provides the mechanical support necessary for the inner

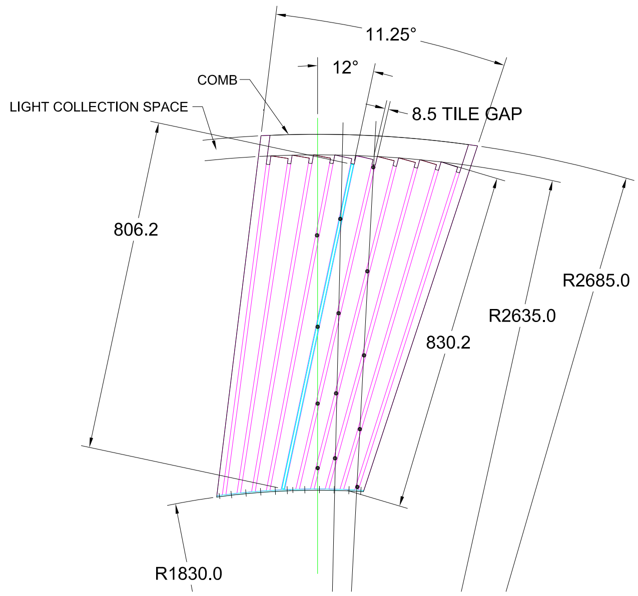

Figure 5.3: Transverse cutaway view of an Outer HCal module, showing the tilted tapered absorber plates. Light collection and cabling is on the outer radius at the top of the drawing.

Parameter	Units	Value
Inner radius (envelope)	mm	1157
Outer radius (envelope)	mm	1370
Length (envelope)	mm	4350
Material		310 stainless steel
Number of towers in azimuth ($\Delta\phi$)		64
Number of towers per module		$2 \times 24 = 48$
Number of tiles per tower		4
Number of towers in pseudorapidity ($\Delta\eta$)		24
Number of electronic channels (towers)		$64 \times 24 = 1536$
Number of optical devices (SiPMs)		$4 \times 1536 = 6144$
Total number of absorber plates		$4 \times 64 = 256$
Tilt angle (relative to radius)	$^\circ$	32
Absorber plate thickness	mm	13
Gap thickness	mm	8.5
Scintillator thickness	mm	7
Number of modules (azimuthal slices)		32
Module weight (SS310)	kg	907.19
Sampling fraction		0.076
Calorimeter depth	λ	0.55

Table 5.4: Design parameters for the Inner Hadronic Calorimeter.

detectors. As discussed above, the collaboration is actively pursuing options to restore the Inner HCal.

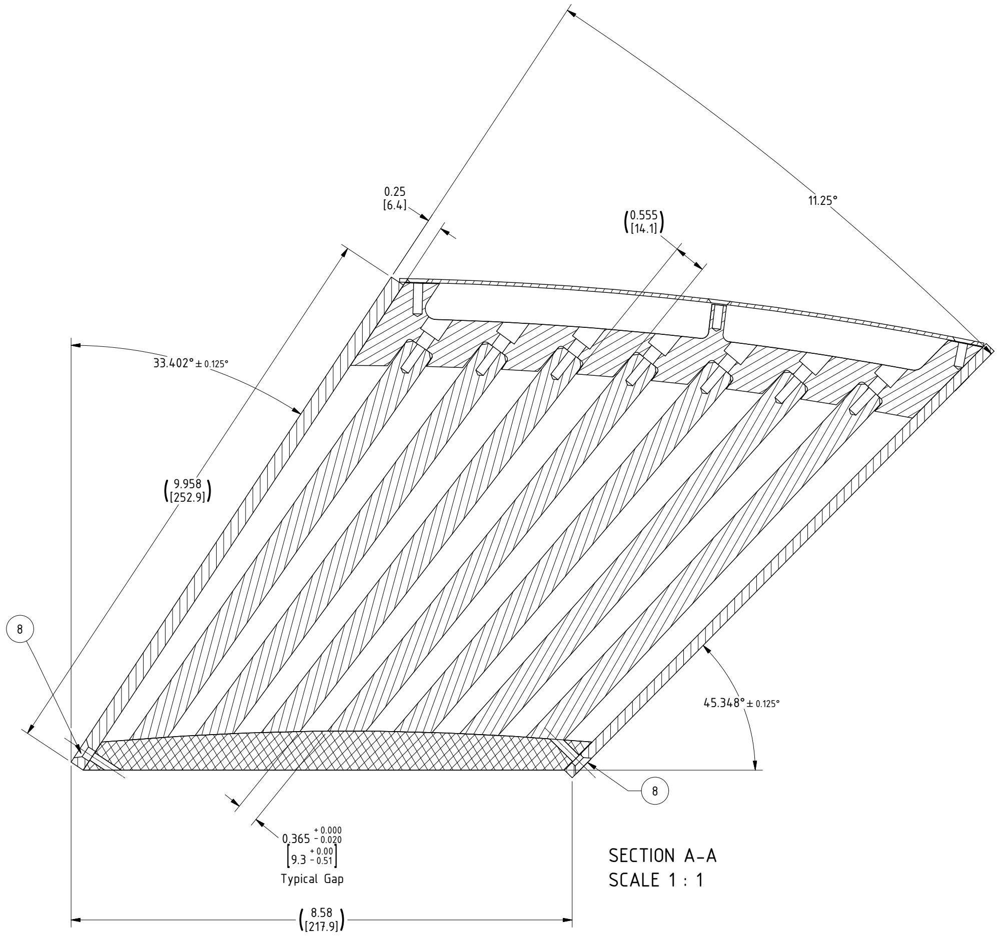

Figure 5.4: Transverse cut of an Inner HCal module, showing the tilted tapered absorber plates. Light collection and cabling is on the outer radius at the top of the drawing.

The Inner HCal (or aluminum frame) modules are to be bolted together with spacers maintaining the 8.5 mm gap between plates for inserting the scintillator tiles. The plates would be assembled into mechanically complete modules at the raw material (steel or aluminum) vendor, at BNL, or at a collaborating institution. In parallel, scintillating tiles would be prepared with their SiPMs and LED flashers, and tested with cosmic rays before installation into the Inner HCal modules. A potential assembly sequence for the Inner HCal modules is shown in Figure 5.5.

The SiPMs attached to the tiles in a given tower must be gain matched, because we plan to provide the same bias voltage on all five of the SiPMs in a tower. This should be possible by sorting the SiPMs according to the manufacturer's measurements. The SiPM sensors, preamplifiers, and cables are arranged on the outer circumference of the Inner HCal, with

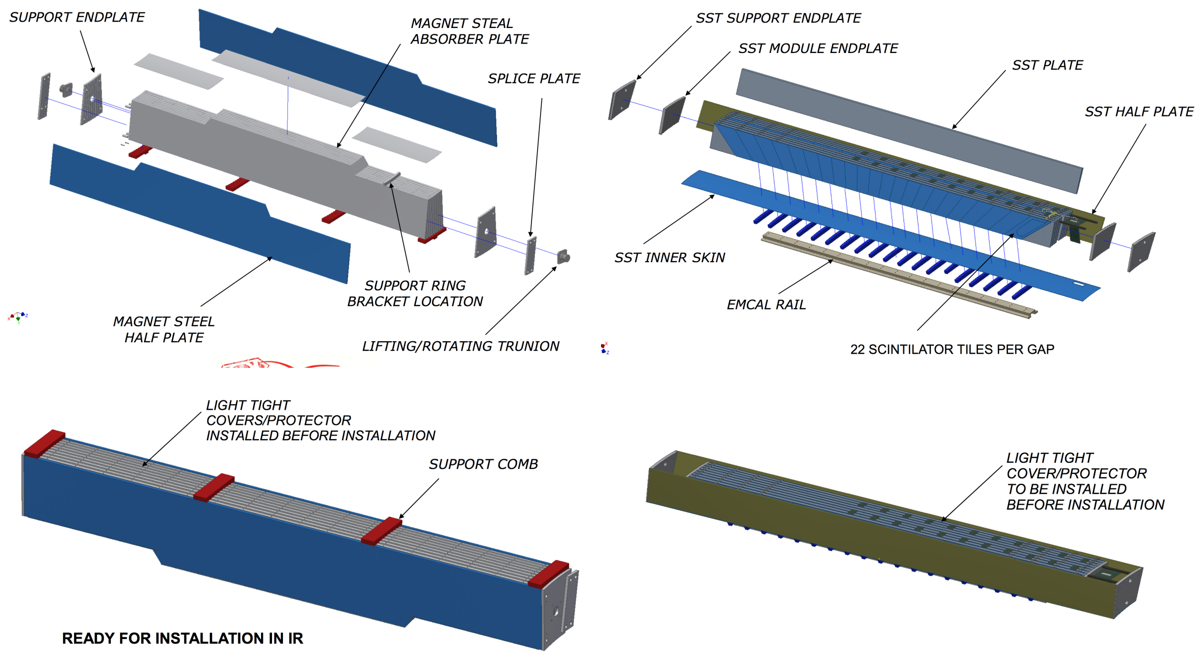

Figure 5.5: Assembly of Inner HCal modules.

cables exiting the two ends of the modules. Interface boards mounted at the ends of the modules monitor the local temperatures and leakage currents, distribute the necessary voltages, and provide bias corrections for changes in temperature and leakage current. As part of the production QA, we have a requirement that tile plus SiPM pairs in each tower must have a response within 10% of each other. The current design plan is shown in Figure 5.6.

The Inner HCal is designed to be inserted as a complete unit into the solenoid cryostat, and access to the on-detector electronics and cables would require both the EMCal and Inner HCal to be removed from their positions inside the solenoid cryostat. Therefore, it is important that any Inner HCal on-detector electronics be thoroughly tested and burned in before completing the assembly of the detector in the magnet.

5.2.4 Mechanical Design

The current mechanical design concept for the outer and inner hadronic calorimeter subsystems relies on a load transfer scheme where the tilted steel plates in the Inner and Outer HCal form the primary structural members for transferring loads. The concept further requires the Inner HCal to support the EMCal, and the Outer HCal must support the inner HCal and the superconducting solenoid magnet independently. The Inner HCal comprises 32 independent sectors joined at its longitudinal ends by stainless steel rings

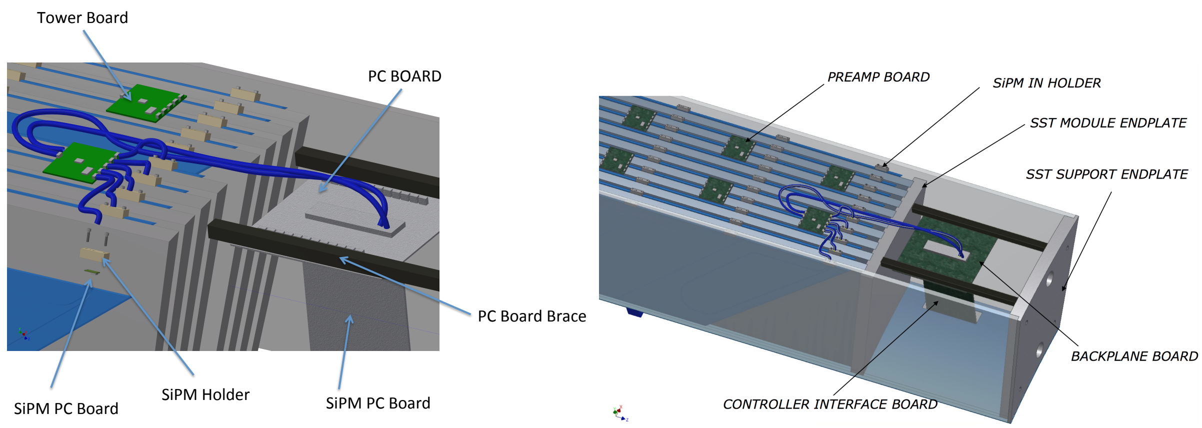

Figure 5.6: The design for electronics and cable routing from an Inner HCal sector. The SiPM holders are mounted directly on the end of the tile with a single preamplifier/shaper/driver board mounted nearby. An Interface Board at the end of the sector, provides power and bias voltage distribution and local monitoring.

to integrate the sectors into a single entity, which in turn is installed inside and through the solenoid magnet and mounted to the Outer HCal by mounting rings on either end. The outer HCal sectors are joined at their longitudinal ends by steel splice plates between adjacent sectors into a single unit, which is mounted on the Central Platform. The reference design for the Inner and Outer HCal support structure is shown in Figure 5.7.

Validation of this mounting scheme has been demonstrated using finite element modeling and analysis to calculate the stresses and displacements of the design concept. Analyses of the Inner HCal structure with and without the EMCal load has been performed and an example of the results is shown in Figure 5.8, showing that the final assembly deformation is within the tolerance necessary ensure that scintillator tiles are not compressed. Similarly, analyses of the Outer HCal structure and multiple Inner HCal installation procedures have been performed to validate the concepts.

5.3 Simulation

The GEANT4 simulation toolkit [135] is employed for simulation studies of the HCal system. The GEANT4 QGSP_BERT_HP was selected as the default physics processes list, which is recommended for high energy detector simulations like the LHC experiments [143]. Figure 5.9 shows an example event display of a 10 GeV pion shower in the GEANT4 Monte Carlo.

After the GEANT4 simulation stage, digitization was implemented with the following four steps:

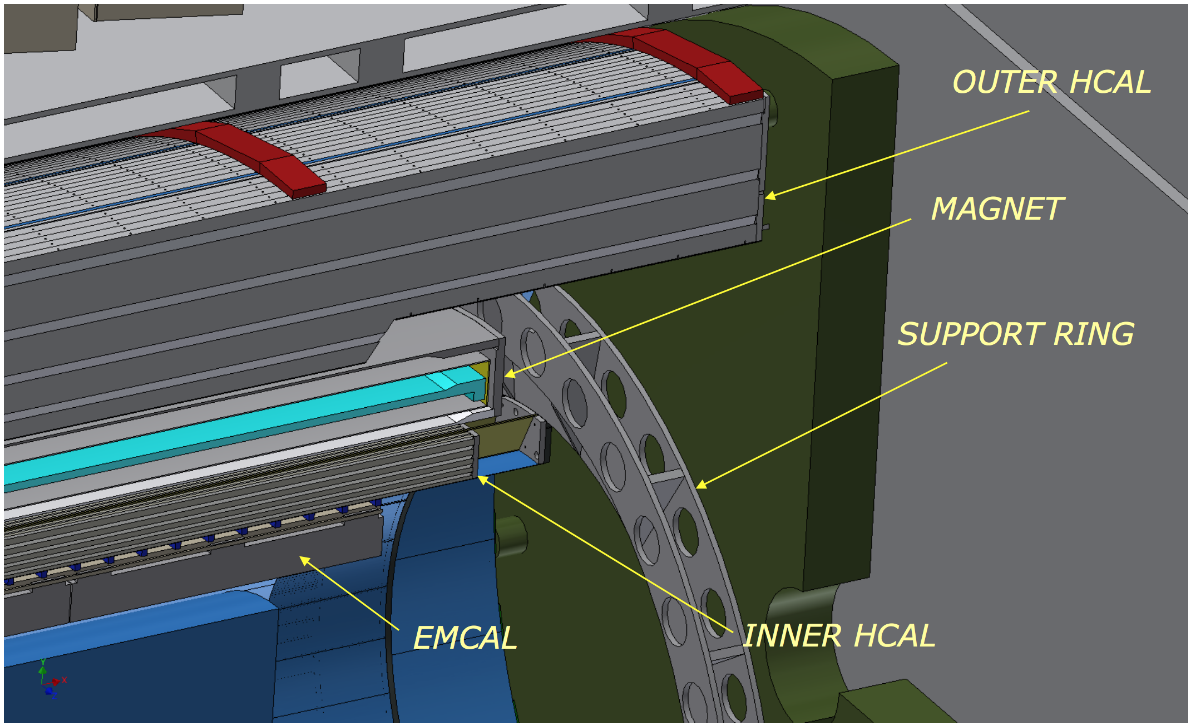

Figure 5.7: Inner and Outer HCal with support structure.

1. Energy depositions for each GEANT4 tracklet in the scintillation volume are collected in the sPHENIX analysis framework.

2. The Birks' law of scintillator non-linearity [144] with a default Birks' constant of $k_B = 0.0794$ mm/MeV [136] is implemented to convert ionizing energy deposition to visible energy that is proportional to the expected number of photons produced in the scintillator.

3. The visible energy in each calorimeter tower is summed in a timing window of 0-60 ns to calculate the mean number of active pixels in the SiPM readout. The scale of the mean number of active pixels is set by the mean active pixel count as measured in cosmic tests of the HCal. The actual active pixel number is a random number following a Poisson distribution using the mean number of active pixels as a parameter.

4. In the last step, the ADC for each readout channel is proportional to the sum of the actual active pixel number and a random number following the pedestal distribution. The sum is scaled to an ADC value using measured pixel/ADC value from cosmic tests and discretized to integer ADC value.

The sPHENIX simulations have been integrated with the sPHENIX software framework [145], enabling the same analysis software setup to be used to analyze the full

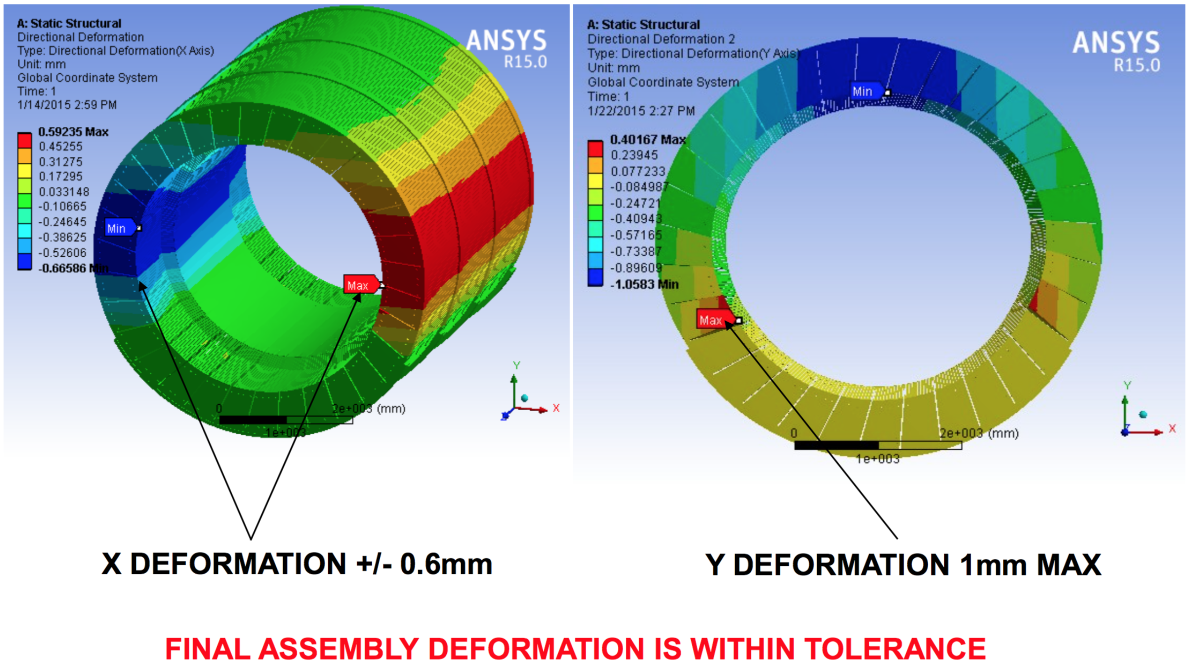

Figure 5.8: Results of finite element analysis of Outer HCal after final assembly, showing the maximum deformation of the structure.

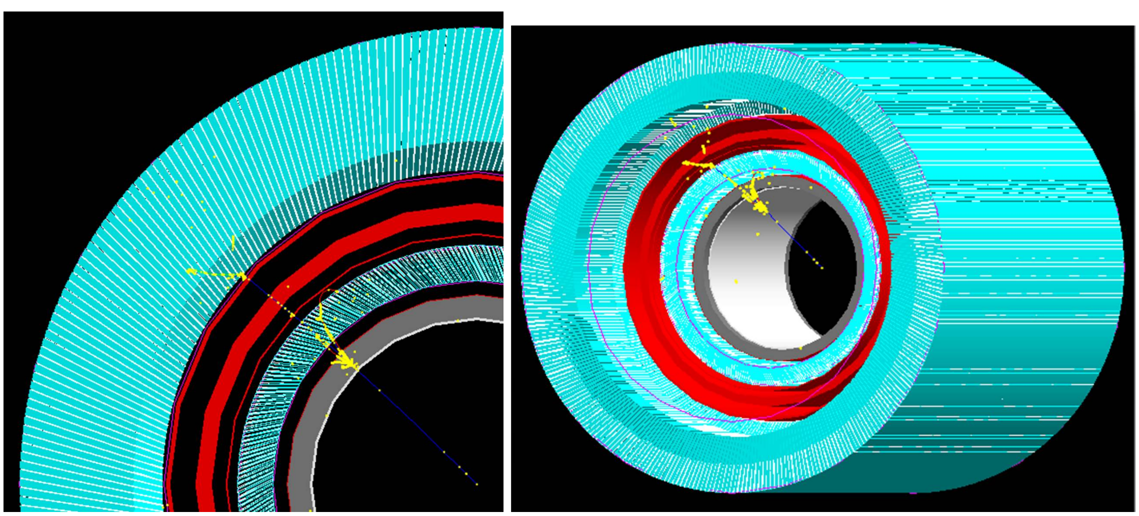

Figure 5.9: GEANT4 event display of a 10GeV π shower in the sPHENIX calorimeter system.

simulations with all the other detector subsystems. Magnetic field maps for the BaBar magnet have been imported from OPERA calculations. The magnetic field map in the region of the Outer HCal takes its geometry into account with the field concentrated in the steel plates and the scintillators in a field free region.

The implementation of the hadronic calorimeters is highly configurable. This allows for the investigation of different design choices (inner and outer radius, plate tilt angle, gap size for scintillator, scintillator thickness, pseudo rapidity coverage, etc.) The superconducting magnet is simulated with the proper location and material of the cryostat. All simulated tracks which reach a layer 10 cm outside the outer HCal are aborted and their energy recorded to yield an estimate of the leakage from the back of the Outer HCal.

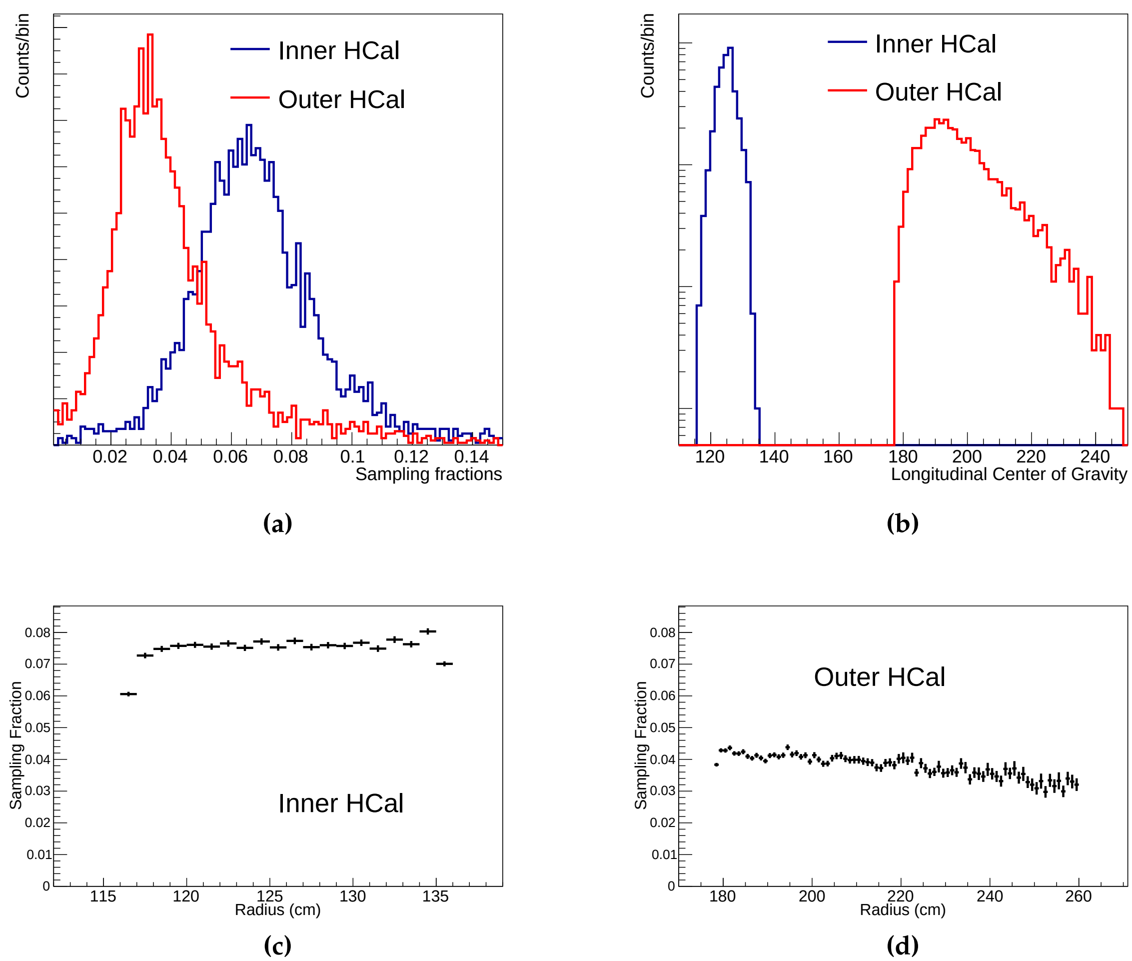

Figure 5.10: GEANT4 simulations of (a) HCal sampling fractions and (b) longitudinal center of gravity for the inner and outer sections. The longitudinal center of gravity shows where the hadronic shower begins to develop in the calorimeter. Also shown are GEANT4 simulations of (c) sampling fraction in the Inner and (d) Outer HCal as a function of depth along the radius, showing it is uniform for inner but decreases for the outer as expected from the tapered plate design.

To elucidate the effect of design choices, single particle simulations were performed using fixed momenta with random pseudorapidity $0 < \eta < 0.1$ and random azimuthal angle

$0 < \phi < 2\pi$. The vertex was randomized along the beam axis within $\pm$10cm. A reference configuration of the HCal as described in the previous section was chosen. In particular, the Inner HCal tilt angle is 32 degrees and the Outer HCal tilt angle is 12 degrees. The energy deposited in the scintillator and absorber are recorded. This information is used to calculate the sampling fraction. Figure 5.10 (a) shows the pion sampling fractions in both inner and outer sections of the HCal. The average sampling fractions were estimated to be 6.7% for the inner and 3.5% for the Outer HCal. Using the average sampling fractions, the summed energy in each compartment was corrected and combined to yield the calorimeter response. The longitudinal center of gravity (LCG) is a good measure of the depth of the hadronic showers inside a calorimeter. The LCG is defined as

$$\mathrm{LCG} = \frac{\Sigma^{G4Hits} E_{dep} \frac{(r_{in}+r_{out})}{2}}{\Sigma^{G4Hits} E_{dep}}, \tag{5.1}$$

where E_{dep} is the GEANT4 hit energy deposited in the scintillators, and r_{in} and r_{out} are the inner and outer radius of the hits, respectively. Figure 5.10 (b) shows the LCG for the pion showers inside Inner and Outer HCal.

We examined the effect of the sampling fraction variation as a function of depth in the Inner and Outer HCal compartments. As noted previously, while the steel plates in the Inner HCal are have a uniform thickness, the steel plates in the Outer HCal widen with the radius, which causes the sampling fraction for the Outer HCal to be reduced as a function of radius, since the scintillator tiles maintain a constant thickness. This effect is demonstrated in Figure 5.10 (c), (d) which shows the sampling fraction for the Inner HCal is constant as a function of depth along the radius while it decreases for the Outer HCal. An extensive study was performed to investigate its impact on the energy resolution. A correction factor was applied to the scintillator tiles modifying the light response in order to even out decreasing sampling fraction as a function of depth. This step was applied at the GEANT4 step level. Only a very modest improvement was seen in the energy resolution. The small improvement would likely be lost in a realistic device when towering and clustering are included. Therefore, from this study we conclude that the variation in the Outer HCal sampling fraction as a function of depth is not a significant contributor to the HCal energy resolution.

Finally, the energy response of the combined HCal is calculated by adding the energy deposited in the scintillators and corrected by the sampling fractions. Figure 5.11 shows the energy reconstruction for pions in the HCal. An event selection was applied to select showers that pass through the EMCal with minimum ionizing energy loss. Deposited energy from showers are shared between the Inner and Outer HCal. As seen from the figure most of the energy is deposited in the Outer HCal. The combined energy response from the two sections shows the peak for the fully reconstructed 12 GeV pions.

The physics performance specification requires the jet energy resolution of the combined calorimetry to be smaller than the fluctuations due to the subtraction of the underlying event in heavy-ion collisions, or an energy resolution better than 20% for a 25 GeV jet. In order to establish the capabilities of the full sPHENIX calorimetry system, a full GEANT4

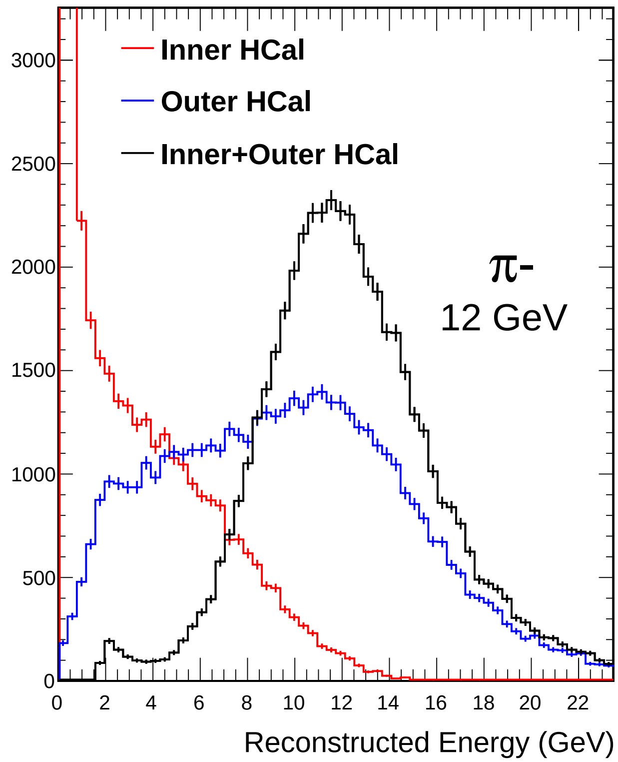

Figure 5.11: Pion reconstruction in the HCal. The energy deposited by 12 GeV $\pi-$ showers in two compartments of HCal. Energy deposited in the scintillators are corrected by the sampling fractions and added together for total energy.

set of simulations were performed to establish the energy resolution performance in the context of a realistic energy calibration scheme. Jets are generated using PYTHIA 8 to simulate the proton-proton collisions at 200 GeV and reconstructed by clustering calorimeter towers with the anti-k_T jet finding algorithm in the FastJet package, with the resolution parameter $R = 0.4$. Generated particles are put through the same package to determine the truth jet. Truth jets are selected to be in the central region of $|\eta| < 0.45$. The z position of the vertex (along the beam axis) is randomized following a Gaussian distribution with $\sigma = 10$ cm.

Jets typically deposit energy in all calorimetry segments, and the energies reconstructed in calorimeters need to be properly calibrated to get an estimate of the truth jet energy. The EMCal calibration is set for pure electromagnetic (EM) energy, but the EMCal has a different response to EM and hadronic showers. Also, the response of calorimeters to a jet depends on the longitudinal center of gravity, the position at which shower begins to develop inside the calorimeter. The response also varies with jet energy. Therefore, the EM and hadronic energy deposit in different calorimeters needs to be calibrated separately, taking the energy dependence into account. Such a calibration procedure is similar to the method developed in the analysis of single-hadron showers in test beam data (see Section 5.5).

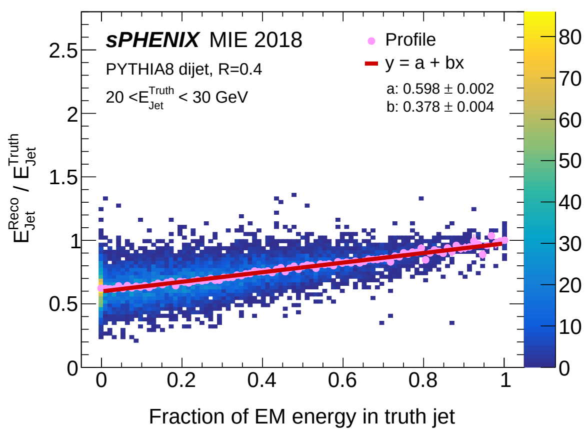

Figure 5.12: The ratio of reconstructed to truth jet energy distributions as a function of electromagnetic energy fraction in a truth jet from simulated proton-proton events. The closed circles represent the profile along the x-axis, and the solid line is the linear fit to the profile.

Figure 5.12 shows the jet energy response, the ratio of reconstructed to truth jet energy, $E_{\text{Jet}}^{\text{Reco}}/E_{\text{Jet}}^{\text{Truth}}$, as a function of the EM energy fraction in a truth jet. The truth EM energy is obtained by summing the energy of EM particles; γ, π^0, $e^{\pm}$, and η. If a jet is mostly composed of electromagnetic energy, the response is close to unity as expected by the fact that the EMCal is already well calibrated for EM energy. As jet energy is more hadronic, however, the response decreases down to ~ 0.6. Such a dependence of the response on the EM energy fraction might result in worse energy resolution, and the relative energy scales of calorimetry compartments are thereby needed to correct it.

To reduce the use of truth information from Monte Carlo simulation, a data-based calibration technique utilizing photon+jet events in p+p collisions has been developed, assuming the reconstructed photon energy provides good access to the parent parton energy of the associated jet. The photon is reconstructed using the jet reconstruction algorithm for simplicity, but only the energy deposit in the EMCal is treated as the reconstructed energy of a photon and the energy deposit in the HCal is ignored. Events containing only two reconstructed objects, one photon candidate and one jet candidate, are selected to remove split jets and minimize the difference between the reconstructed photon energy and the truth jet energy. Reconstructed photon and jet candidates are required to be found in the opposite hemisphere ($\Delta\phi(\gamma - \text{jet}) > \pi/2$). For photon candidates, the leading particle with the highest z (the fraction of jet momentum carried by the particle) is required to be a photon, and the fraction of energy deposit in the HCal to the EMCal be smaller than 0.1.

For jets, due to the different EMCal response to EM and hadronic showers, EMCal clusters with hadronic energy needs to be separated from those with EM energy and be calibrated individually. First, based on the fact that photon does not leave a track, matching between the EMCal clusters and the tracker tracks is performed. After track information is extrapolated to the calorimeter plane, each track is matched to the nearest cluster and the distributions of $d\eta$(track-cluster) and $d\phi$(track-cluster) are fitted by a Gaussian function. The cluster is considered to have an associated track if $|d\eta|$ and $|d\phi|$ are both within 3σ of the fit. Single particle simulations were performed to validate the track-cluster matching; approximately 95% of photons and 89% of neutral pions have no associated tracks while 98% of electrons and 97% of charged pions have a single track. Second, the clusters passed the track-cluster matching are sorted by the cut on the $E_{\mathrm{EMCAL}}/p_{\mathrm{track}}$ ratio to distinguish charged-hadrons contribution from electrons contribution. If the track momentum is higher than 1 GeV, clusters with an E/p ratio within 3σ from unity are considered electromagnetic, and the rest are considered hadronic. If the track momentum is lower than 1 GeV, all clusters are considered hadronic because the E/p distributions of electrons are relatively wide in this p_T region.

The reconstructed jet energy after the calibration can be expressed as:

$$E_{\mathrm{Jet}}^{\mathrm{reco}} = E_{\mathrm{EMCal}}^{\mathrm{em}} + A(E) \cdot E_{\mathrm{EMCal}}^{\mathrm{had}} + B(E) \cdot E_{\mathrm{InnerHCal}} + C(E) \cdot E_{\mathrm{OuterHCal}}\,, \tag{5.2}$$

where $E_{\mathrm{EMCal}}^{\mathrm{em}}$ and $E_{\mathrm{EMCal}}^{\mathrm{had}}$ are the deposited energy in the EMCal classified as electromagnetic and hadronic, respectively. Similarly, $E_{\mathrm{InnerHCal}}$ and $E_{\mathrm{OuterHCal}}$ are the deposit energy in the Inner HCal and the Outer HCal, respectively. The coefficients A, B, and C are scale factors. For the CD-1 configuration (the uninstrumented aluminum frame), the 3rd term related to the Inner HCal is zero by definition. The scale factors are determined by minimizing the quantity,

$$\Sigma_{i=1}^{N} (E_{\mathrm{Jet},i}^{\mathrm{reco}} - E_{\gamma,i}^{\mathrm{reco}})^2 / (E_{\gamma,i}^{\mathrm{reco}})^2\,, \tag{5.3}$$

using the numerical minimization computer program, MINUIT2 [146]. All of the three scale factors are set as free parameters and determined at the same time.

According to the sPHENIX run plan, it is expected to collect data with an integrated luminosity of $\mathcal{L}_{\mathrm{int}} \approx 48\ \mathrm{pb}^{-1}$ during the first p+p run. Thirty sets of photon+jet events, each corresponding to $\mathcal{L}_{\mathrm{int}} \approx 45\ \mathrm{pb}^{-1}$, were generated and each set was independently analyzed to study the statistical fluctuations that might be present in the process of generating the calibrations using the statistics expected in real data. Due to the limited statistics at higher energy, the reconstructed photon energy in the range of $20 < E_{\gamma}^{\mathrm{Reco}} < 30$ GeV has been studied. Calibrations at higher energy will require a combination of Monte Carlo and additional measurements to establish, but the low-energy photon+jet calibration will establish a baseline.

Figure 5.13 shows the distributions of scale factors obtained from the thirty sets of simu-

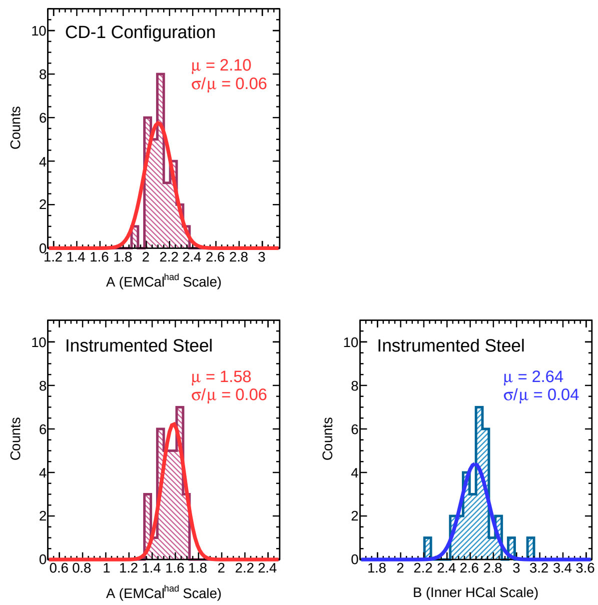

Figure 5.13: Distributions of scale factors A for EMCal with hadronic energy (left), B for the Inner HCal (middle), and C for the Outer HCal (right) with the CD-1 configuration (upper) and the instrumented steel configuration (lower). Thirty sets of photon-jet events with $\mathcal{L}_{\text{int}} \approx 45\ \text{pb}^{-1}$ are generated in proton-proton simulation to calculate the scale factors.

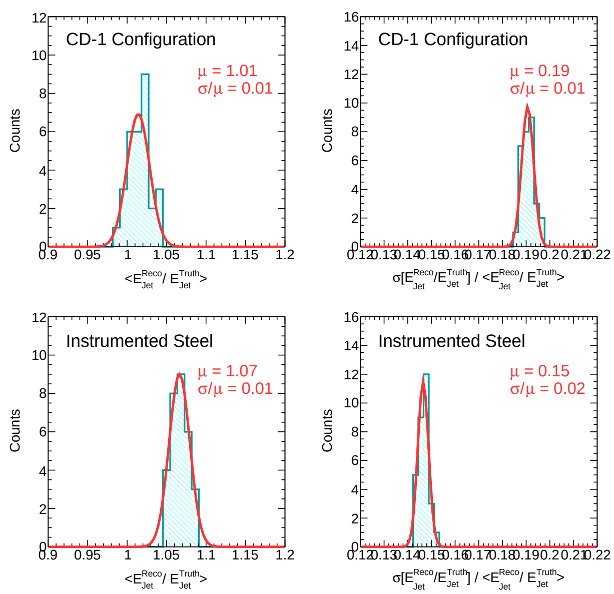

Figure 5.14: Distributions of Jet Energy Scale (JES, left) and Jet Energy Resolution (JES, right) with the CD-1 configuration (upper) and the instrumented steel configuration (lower), after the jet energy is calibrated by thirty sets of scale factors shown in Fig. 5.13.

lated photon-jet events. Upper plots are for the CD-1 configuration, and bottom plots are for the configuration with the instrumented steel which has the additional scale factor B. The relative standard deviations of 3–6% have been observed. Next, these scale factors have been applied to independently-produced samples of dijet events. Figure 5.14 shows the distributions of Jet Energy Scale (JES) and Jet Energy Resolution (JER) after the jet energy is calibrated using thirty different sets of scale factors. For each set, the JES is obtained by the mean of the Gaussian fit to reconstructed to truth jet energy distributions, $< E^{\mathrm{Reco}}_{\mathrm{Jet}} / E^{\mathrm{Truth}}_{\mathrm{Jet}} >$, and the JER is defined by the standard deviation divided by the mean $\sigma[E^{\mathrm{Reco}}_{\mathrm{Jet}} / E^{\mathrm{Truth}}_{\mathrm{Jet}}] / < E^{\mathrm{Reco}}_{\mathrm{Jet}} / E^{\mathrm{Truth}}_{\mathrm{Jet}} >$. Compared to the scale factors, JES and JER show sharper distributions with the relative standard deviation less than 2%, indicating they are less affected by the lack of statistics.

Figure 5.15 shows the ratio of reconstructed to truth jet energy distributions as a function of electromagnetic energy fraction in a truth jet, similar to Fig. 5.12, but after the scale factors (the mean values of Fig 5.13) are applied. The slope parameter b is changed from (0.378 ± 0.004) to (-0.002 ± 0.008), which means the response after the calibration is fairly constant regardless of whether jet energy is electromagnetic or hadronic. The intercept a is slightly higher than unity, possibly due to the fundamental discrepancy between the reconstructed gamma energy and truth jet energy. Such an over-correction can be adjusted using the MC truth information at the later level and does not affect the resolution. It is worth noting that although jets in photon+jet events are mainly initiated by quarks, the scale factors obtained from photon+jet samples well flatten the EM dependence of jet response in QCD dijet samples that are more gluon-dominated. This indicates that similar calibration factors are applicable to both quark and gluon jets.

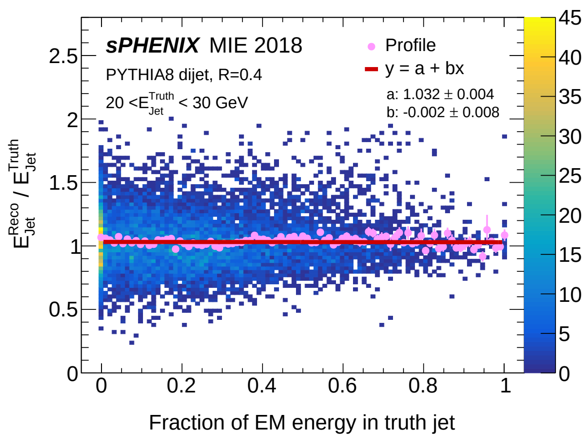

Figure 5.15: The ratio of reconstructed to truth jet energy distributions as a function of electromagnetic energy fraction in a truth jet from simulated proton-proton events, similar to Fig. 5.12, but after the calibration. The closed circles represent the profile along the x-axis and the solid line is the linear fit to the profile.

To study the energy dependence of scale factors, more samples of dijet and photon-jet events are generated in different bins of truth energy, $E_{\mathrm{Jet}}^{\mathrm{Truth}}$ = [20, 30, 40, 50, 60] GeV. Each bin contains 50k events, which are expected to be enough to reduce statistical fluctuations. Figure 5.16 shows the ratio of reconstructed to truth jet energy distributions in dijet samples with different truth jet energies for the CD-1 configuration (closed circles) and the configuration with the instrumented steel (open squares). The CD-1 configuration is centered at the lower value than the configuration with instrumented steel, as the energy deposit in the frame cannot be reconstructed and combined into the total jet energy.

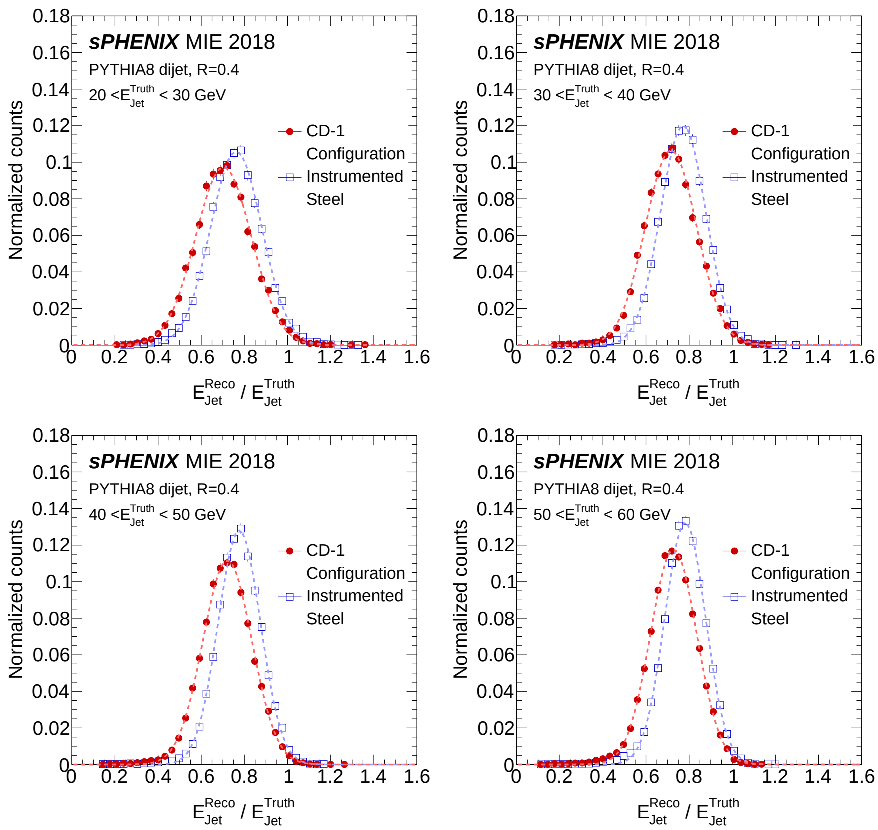

Figure 5.16: The ratio of reconstructed to truth jet energy distributions from simulated proton-proton events with the CD-1 configuration (closed circles) and the instrumented steel configuration (open squares). The total area under each histogram is normalized to unity. Each plot shows the result of different truth jet energy, $E_{\mathrm{Jet}}^{\mathrm{Truth}}$ = [20, 30, 40, 50, 60] GeV.

Figure 5.17 shows the scale factors as a function of reconstructed photon energy for CD-1 configuration (left) and the configuration with the instrumented steel (right). Red, blue, and green points are scale factors for $E_{\mathrm{EMCal}}^{\mathrm{had}}$, $E_{\mathrm{InnerHCal}}$, and $E_{\mathrm{OuterHCal}}$, respectively. For the cross points with the realistic statistics ($\mathcal{L}_{\mathrm{int}} \approx 45\ \mathrm{pb}^{-1}$), the mean and the standard deviation in Fig 5.13 are taken as the central value and the statistical uncertainty, respectively. The results with the realistic statistics are compared to the ones with the enough statisis (50k events) in the lowest $E_{\gamma}^{\mathrm{Reco}}$=[20, 30] GeV bin and in a good agreement within uncertainties. It implies that the scale factors for the lowest $E_{\gamma}^{\mathrm{Reco}}$ bin can be obtained by analyzing real data and be extrapolated to the higher energy region based on the Monte Carlo simulation.

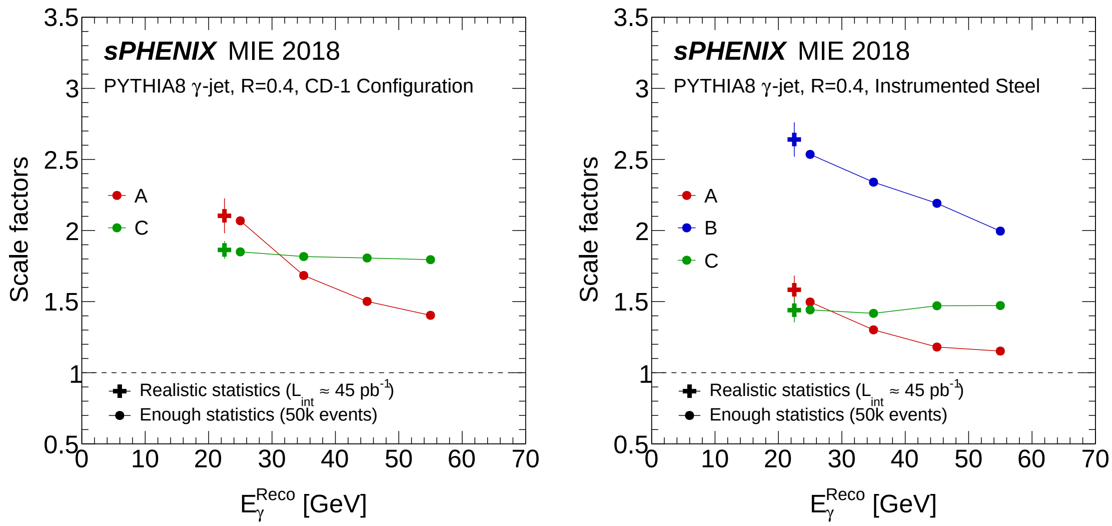

Figure 5.17: Scale factors for the EMCal with hadronic energy (red), InnerHCal (blue), and Outer HCal (green) as a function of reconstructed photon energy with the CD-1 configuration (left) and the instrumented steel configuration (right). Cross points represents simulations with realistic statistics ($\mathcal{L}_{\mathrm{int}} \approx 45\ \mathrm{pb}^{-1}$) and circular points are ones with enough statistics (50k events).

Figure 5.18 summarizes the truth jet energy dependence of JES (left) and JER (right) before (open circles) and after (closed circles) the calibration. Similar to the scale factor, the central value and the statistical uncertainty of cross points are obtained by the mean and the standard deviation of Fig. 5.14, respectively. The results with realistic statistics and larger statistics match well each other in the lowest $E_{\mathrm{Jet}}^{\mathrm{Truth}}$=[20, 30] GeV bin. After the calibration, the JES is closer to unity both for the CD-1 configuration (red) and the instrumented steel configuration (black). The JER is improved over the whole energy range for the instrumented steel configuration, and remains almost the same for the CD-1 configuration. This is likely because in addition to a better overall energy measurement, an energy measurement in three compartments allows the calibrations to better correct the dependence of the longitudinal center of gravity in the hadronic calorimetry segments.

In addition, the inner HCal with the instrumented aluminum (blue) is simulated in the same way as the CD-1 configuration (red) and inner HCal with the instrumented steel (black), and compared in Fig. 5.19. Once instrumented, the resolution of aluminum inner HCal can be improved to be comparable as that of the steel inner HCal through the calibration procedure. It confirms that the energy measurement in all three segments, EMCal, Inner HCal, and Outer HCal, would improve the calibration performance and result in better energy resolution.

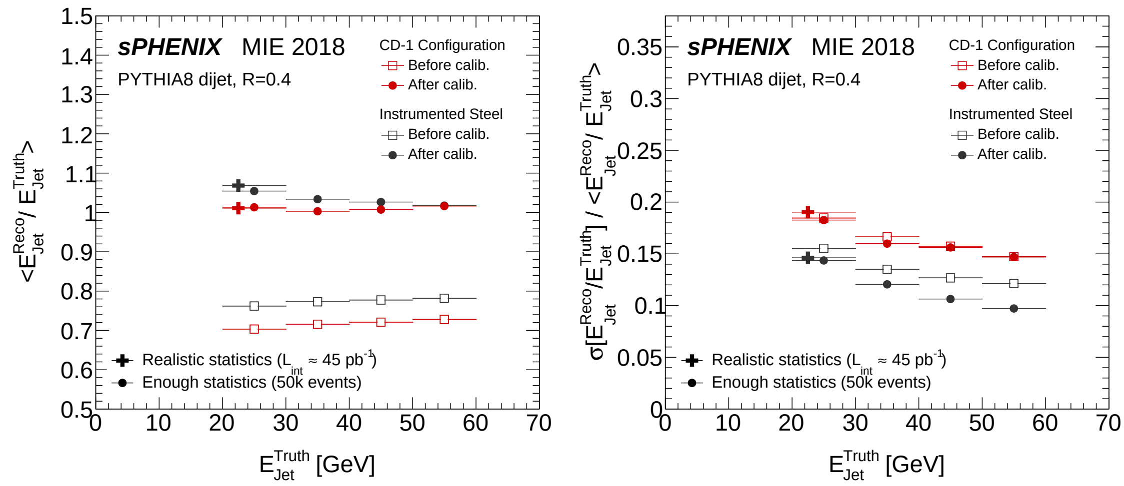

Figure 5.18: Jet energy scale (left) and resolution (right) as a function of truth jet energy in simulated proton-proton events with the CD-1 configuration (red) and the instrumented steel configuration (black). Open and closed markers indicate before and after the calibration, respectively. Cross points represents simulations with realistic statistics ($\mathcal{L}_{\text{int}} \approx 45\ \text{pb}^{-1}$) and circular points are ones with enough statistics (50k events).

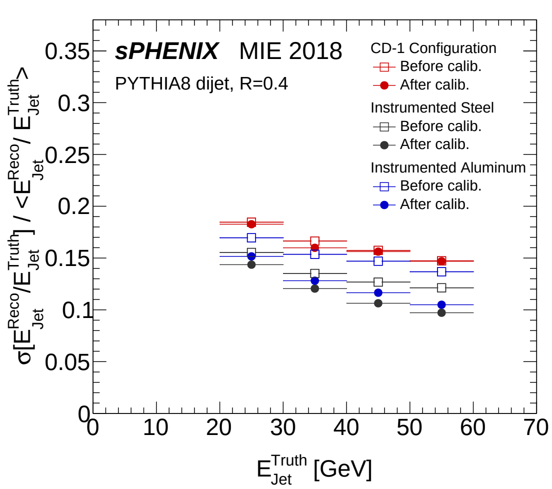

Figure 5.19: Jet energy resolution as a function of truth jet energy in simulated proton-proton events with the CD-1 configuration (red), the instrumented aluminum (blue), and the instrumented steel (black) configuration. Open squares and closed circles indicate before and after the calibration, respectively.

5.4 Prototype construction

To verify the design performance, HCal prototypes have been assembled at Brookhaven National Laboratory and tested at the Fermilab Test Beam Facility (FTBF) as experiment T-1044.

- The first beam test was performed in February of 2014. It was during the preliminary stage of the detector development. The goals included characterization of the light yield of the full detector for hadronic showers, as well as an investigation of the energy response and calibration procedures. This prototype reflects an earlier iteration of the design, where both the Inner and Outer HCal were located outside of the solenoid magnet. In addition, fiber routing from this earlier design has since been further optimized.
- The second beam test was performed in April of 2016. The prototype configuration was intended for mid-rapidity configuration in the sPHENIX detector and reflects the current positions of the Inner and Outer HCal.
- The third beam test was performed in January 2017. The calorimeter was configured in a manner that mimics the high-rapidity configuration of sPHENIX. The same steel was used as in the 2016 test. The main goal for this phase was to understand the performance in the high-rapidity configuration.

This section will focus on the set-up and results from the 2016 and 2017 prototype tests. The T-1044 test beam configurations include both sections of Inner and Outer HCal prototypes as well as an EMCal prototype. The Inner and Outer HCal prototypes are constructed as a small pseudorapidity and azimuthal segment ($\Delta\eta \times \Delta\phi = 0.4 \times 0.4$) of the full scale sPHENIX design. A mock cryostat, comprising three vertical plates of aluminum, was placed between the Inner and Outer HCal to provide as many radiation lengths of material as a particle would encounter traversing the sPHENIX solenoid (approximately 1.4 X_0).

5.4.1 Tile Construction

Figure 5.20 (a) shows the tile production steps for the Inner HCal. The design of the Outer HCal tiles are similar, but the Outer HCal tiles are larger to accomodate the larger radius of the Outer HCal. The scintillation light produced in the tiles by ionization from charged particles is contained within the tile and reflected diffusely by a reflective coating and reflective tile wrapping. The light is absorbed by the fiber embedded in the scintillator. Figure 5.20 (b) shows the fiber routing patterns for the tiles used in the 2016 study. As shown in Figure 5.20 (c), the two ends of the fiber are brought together at the outer radius of the tile where a small plastic mount supports a 3×3 mm^2 SiPM at the fiber exit. The fiber exit is orthogonal to the tile edge and glued at a depth in the tile that allows for

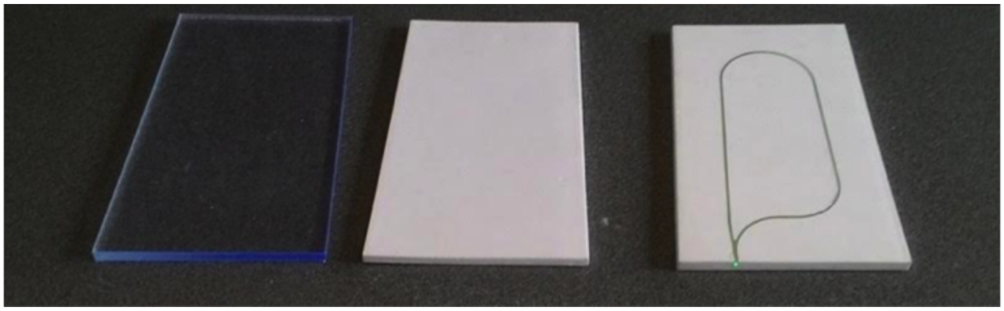

(a) Inner HCal scintillator tiles at different stages of production. The tiles shown are after the extruded scintillator is cut to size (left), after application of the reflective coating (middle) and after the groove for the fiber is cut.

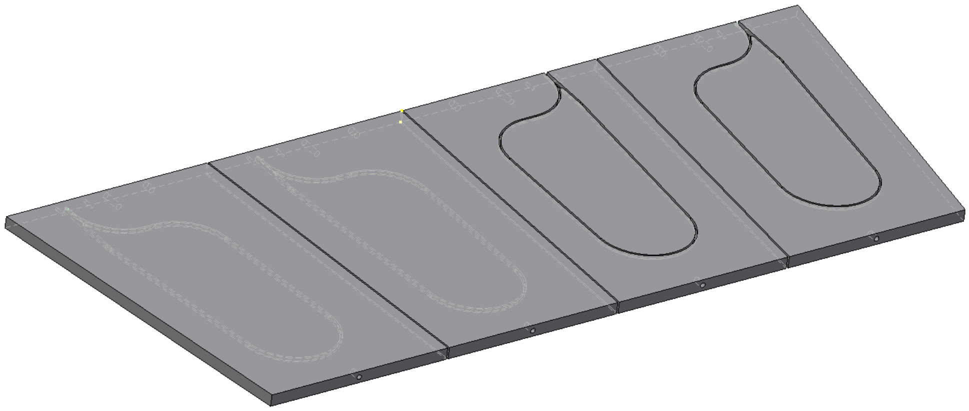

(b) Inner HCal tile design patterns

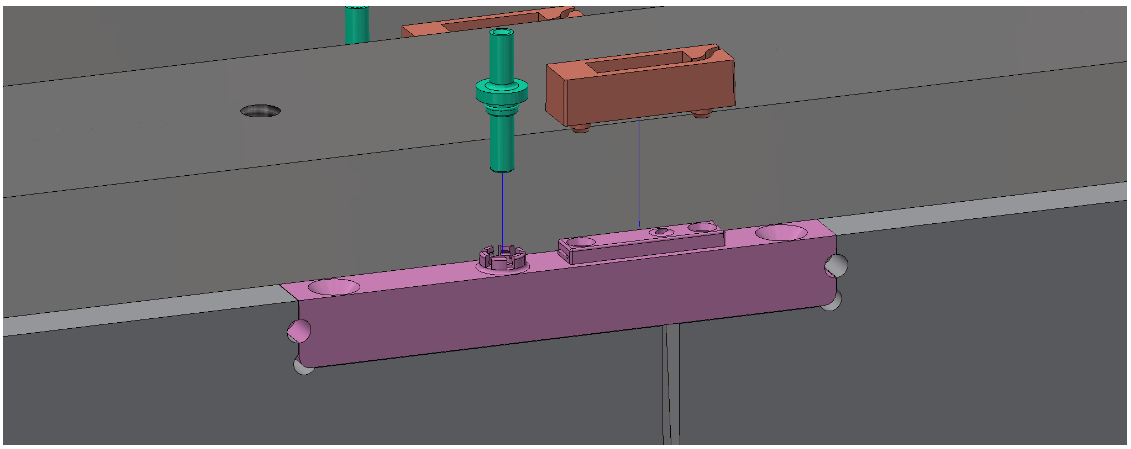

(c) Plastic coupler to attach the SiPM at the fiber exit

Figure 5.20: HCal tile production. (a) Inner HCal scintillating tiles in several stages of production. From left to right tiles are machined, then coated and embedded with WLS fiber. (b) 4 scintillating tiles arranged symmetrically around $\eta = 0$ to be inserted between the steel absorber plates. (c) SiPM installation at the fiber exit using a plastic coupler.

installation of the SiPM centered around the fiber exits. The air gap between the fiber ends and the face of the SiPM allows the emitted light to spread over the face of the SiPM, reducing the probability of optical saturation resulting from the two or more photons impinging on the same pixel. A gap of 0.75 mm satisfies the following two requirements: (1) there be no more than a 5% variation in the SiPM response when fibers and SiPM are misaligned by 0.2 mm; (2) no more than 20% loss of light outside of SiPM sensitive area.

Scintillating tiles for the calorimeter are manufactured by the Uniplast Company in Vladimir, Russia. A dry mix of polystyrene granules, PTP, and POPOP is melted and extruded, producing a continuous band of hot scintillating plastic 25 cm wide. The scintillator is then cut into 2 m long pieces. After passing inspection for defects and discolorations, these pieces are mechanically machined into the tiles according to the specified dimensions. The tiles are then placed in a bath of aromatic solvents resulting in the development of a white diffuse reflective coating over the whole tile surface with an average thickness of 50 μm. This process also removes microscopic non-uniformities normally present on the surface of extruded plastic, which decreases aging and improves the ability of the tile to withstand pressure without crazing. It also enhances the efficiency of light collection in tiles with embedded fibers. The coated tiles are then grooved and WLS fibers are embedded. The fibers are glued using optical epoxy (EPO-TEK 301) with special care given to the fiber position at the exit from the tile. The fibers are cut at the tile edge and polished by hand.

5.4.2 Tile Testing

To determine the light response across the tiles, various studies have been performed. In one study, an LED with a collimator is attached to a mount on a two-dimensional rail system with very accurate stepper motors. This allows an automated analysis with very high positional precision. The LED scans of the Outer HCal tiles consist of 174 points in the long direction (X) and 54 points in the short direction (Y) for a total of 9,396 points. The scan positions are 0.5 cm (approximately the LED spot size) apart in each direction. The principal disadvantage of an LED scan is that light is inserted into the tile directly rather than being induced by ionizing radiation. During the FTBF test beam running, a "tile mapper" was constructed and placed on a two-dimensional motion table. The motion table moves up/down and left/right, keeping the position along the beam direction fixed. The tile mapper included four Outer HCal tiles placed perpendicular to the beam direction, so that movement on the motion table corresponds to different positions on the tile face. Each tile is read out individually, which enables a detailed study of the light response as a function of position. The scan consists of 20 total positions, 10 positions focused on the inner part of the tile and 10 focused on the outer part of the tile. A few of the outer scan positions fall near the edge and are excluded from the analysis. This study was performed with a 16 GeV negative pion beam.

Figure 5.21 shows the LED scan of an Outer HCal tile using a 405 nm UV LED. Additional scans were performed using 375 and 361 nm UV LEDs with similar results. The overlaid black circles indicate the positions on the tiles used in beam scan described in the previous paragraph. The relative positional accuracy of the points is 0.2-0.3 cm. The numbers show the ratio of the average ADC value of the 16 GeV pion data to the average ADC value of the LED scan for that position. Note that the same tile was not used the two studies and the normalization is arbitrarily chosen so that the numerical values are near unity.

Most of the points have ratio values close to unity, indicating good agreement between the 16 GeV pion data and the LED data. The points close to the SiPM, which can be seen as the red region in the upper left, show a downward trend in the ratio values, suggesting that the intense bright spot in the LED data is not as significant in the 16 GeV pion data. Additionally, the set of five points near 150 mm in the Y position and less than 200 mm in the X position, are systematically lower than the LED data and their positions appear to overlap the embedded WLS fiber. This is most likely due to the fact that, in the LED scan, some of the light from the LED is captured directly by the fiber, so there is a modest enhancement at the fiber that is not present in the 16 GeV pion data. Both sets of five inner points, however, show a decreasing trend as the points get close to the SiPM.

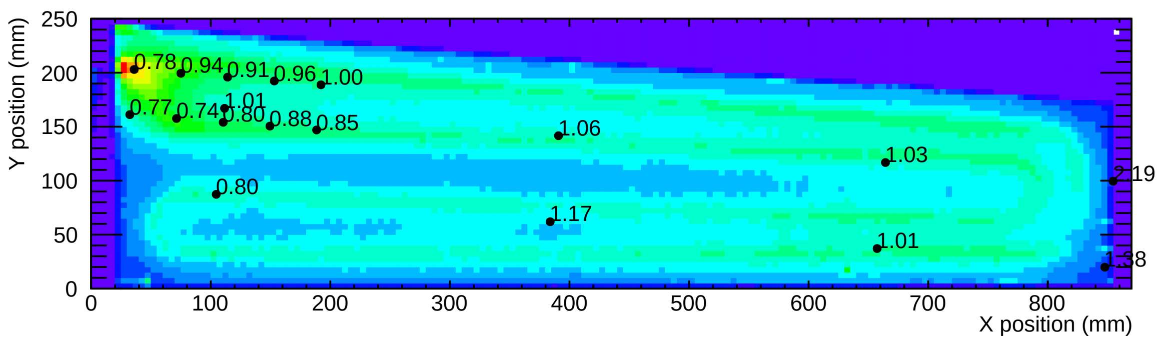

Figure 5.21: LED response of a scintillation Outer HCal tile with tile mapper scan data overlaid as black points. The numerical value shown at each point is the normalized ratio of the LED response to the tile mapper response.

Figure 5.22 shows the average ADC value for each scan position as a function of the distance from the SiPM. While the 16 GeV pion data do not show as much of an enhancement near the SiPM as the LED scan, it can be seen that for points less than 15 cm away from the SiPM that there is a strong rise in the average ADC as the distance to the SiPM decreases. This is most likely due to the fact that some of the light in the fiber is carried in the cladding, which has a very short attenuation length, and is therefore lost for most positions in the tile. Studies of small double-ended scintillating tiles have indicated that up to 50% of the light is carried in the cladding, though this is with LED light rather than scintillation light. Here the results indicate that about 33% of the light is carried in the cladding. The area in which more light is collected due to light being present in the cladding is of order 5 cm^2 right around the SiPM mounting, which is at the back of the calorimeter. The spatial density of shower particles is lowest at the back of the calorimeter and therefore this small amount of additional light has a negligible effect on the determination of the shower energy.

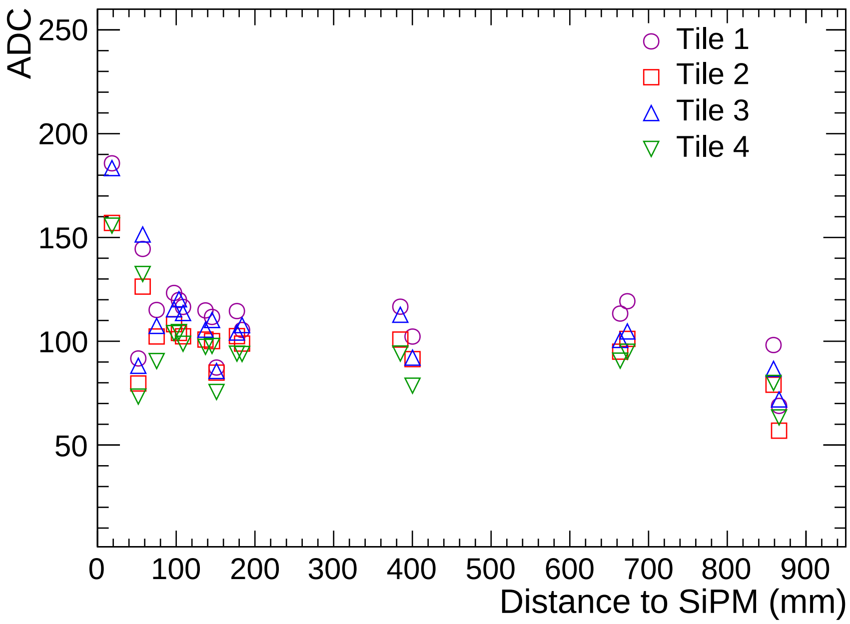

Figure 5.22: Outer HCal tile scan using 16 GeV pion beam. Average ADC value in the tile plotted as a function of distance from the SiPM. The points below 150 mm indicate an enhancement close to the SiPM.

5.4.3 Assembly

Figure 5.23 (a), (b) shows the fully assembled Inner and Outer HCal prototypes. The major components are 20 steel absorber plates and 80 scintillating tiles which are read out with SiPMs along the outer radius of the detector. The 2016 and 2017 prototype Inner HCal was based on an earlier design with tapered plates and five tiles per tower. The 2018 prototype will test the final design for the Inner HCal with flat plates and four tiles per tower. The Outer HCal prototype is unchanged.

The SiPMs from five tiles are connected passively to a preamplifier channel. This resulted in a total of 16 towers, 4 in ϕ by 4 in η, equipped with SiPM sensors, preamplifiers, and cables carrying the differential output of the preamplifiers to the digitizer system. Sixteen preamplifier boards corresponding to the 16 towers are visible. In order to make the whole system light tight, the front and back sides were covered with electrically conductive ABS/PVC plastic. This material quickly diverts damaging static charges if there is a

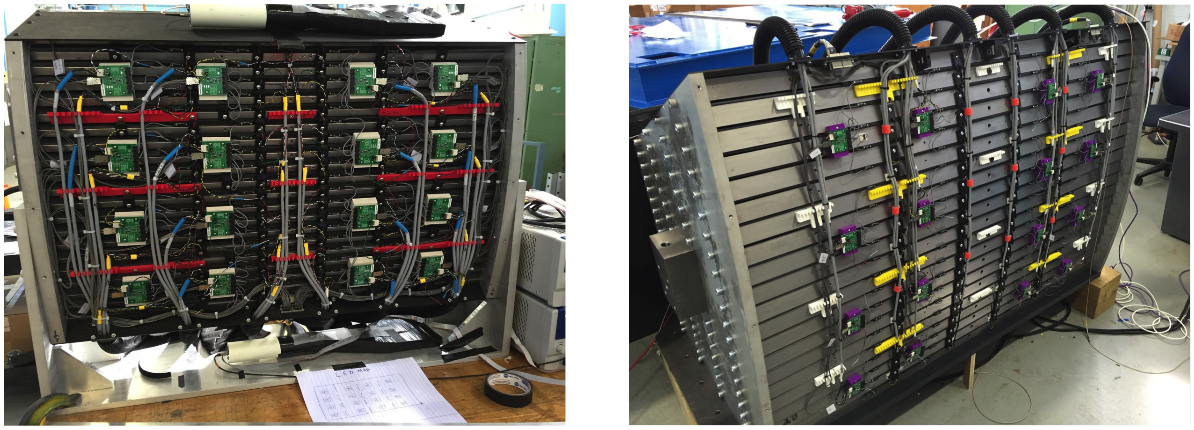

(a) (b)

Figure 5.23: Fully assembled (a) Inner and (b) Outer HCal test beam prototypes. Each section has 20 steel absorber plates stacked together and 80 scintillating tiles are inserted between them. SiPM read out from five tiles are ganged together as a tower. This results in a total of 16 towers equipped with SiPM sensors, preamplifiers, and cables carrying the differential output of the preamplifiers to the digitizer system.

buildup. Corners were sealed with light tight black tape. No light leaks were observed during the entire data taking period.

Since the same bias voltage is supplied to all five SiPMs in a given tower, the SiPMs must be gain matched so that their responses are the same. The SiPMs are sorted and grouped to towers according to the manufacturer's measurements. The SiPM sensors, preamplifiers, and cables are arranged on the outer radius of the Inner HCal. The interface boards mounted on the side of the modules monitor the local temperatures and leakage currents, distribute the necessary voltages, and can provide bias corrections for changes in temperature and leakage current.

5.4.4 Prototype Calibration

The initial HCal calibration was performed using cosmic MIP events in order to equalize the response of each tower. A set of cosmic MIP events was recorded prior to the test beam data taking in order to calibrate the detector. The cosmic MIP events were triggered with scintillator paddles positioned at the top and bottom of the HCal (in the ϕ direction as seen from the interaction point). In each run, four vertical towers are scanned from top to bottom (e.g. Tower 0-3 in Figure 5.24). This yields eight individual runs in order to fully calibrate both the Inner and Outer HCal sections. Figure 5.24 (a) shows the ADC distributions in the 4×4 Inner HCal towers. Each spectrum is fit with a function that is the sum of an exponential and a Landau distribution, where the exponential function corresponds to the background and the Landau function represents the MIP events. As seen in Figure 5.24, the background component is relatively small. Clear cosmic MIP peaks are observed in all towers.

The corresponding simulation of cosmic muons is performed with 4 GeV muons (the mean muon energy at sea level) moving from the top to bottom of the HCal prototype with the standard GEANT4 setup discussed in Section 5.3. Figure 5.24 (b) shows energy deposition in only one column of towers. The mean energy deposited by the cosmic muons in each tower is approximately 8 MeV for the Inner HCal. Because of the tilted plate design, towers at the bottom of the Inner HCal have more deposited energy than the top ones. This feature was first observed in data and then confirmed by the simulations. This simulation was used to calibrate the ADC signal in each tower to the corresponding energy loss in the test beam. Once the ADC signal height, $I(ch)$, is determined by a functional fit to the ADC timing samples, the energy deposited is calculated by:

$$E(ch) = I(ch)\frac{E_{dep}^{cosmic}(ch)}{E_{dep}^{ADC}(ch) \times SF(muon)}, \tag{5.4}$$

where $E_{dep}^{cosmic}(ch)$ is the total deposited energy extracted from the GEANT4 simulations, $E_{dep}^{ADC}(ch)$ is the ADC signal height measured from cosmic data, and $SF(muon)$ is the muon sampling fraction.

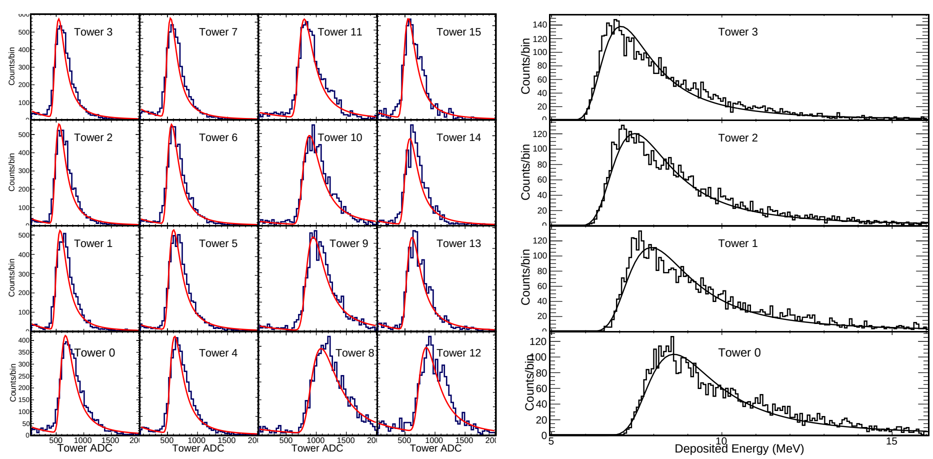

(a) **(b)**

Figure 5.24: Tower to tower calibration for the Inner and Outer HCal was done with cosmic muons. (a) Measured raw ADC spectra of cosmic ray muon events in the Inner HCal. (b) Inner HCal cosmic muon energy deposition in simulation in one column. Muons were simulated at 4 GeV moving from the top to bottom. Energy depositions in the bottom towers are higher due to the tilted plate design where muons have to go through a longer path through the scintillating tiles.

5.5 Prototype performance

5.5.1 HCal Standalone Measurements

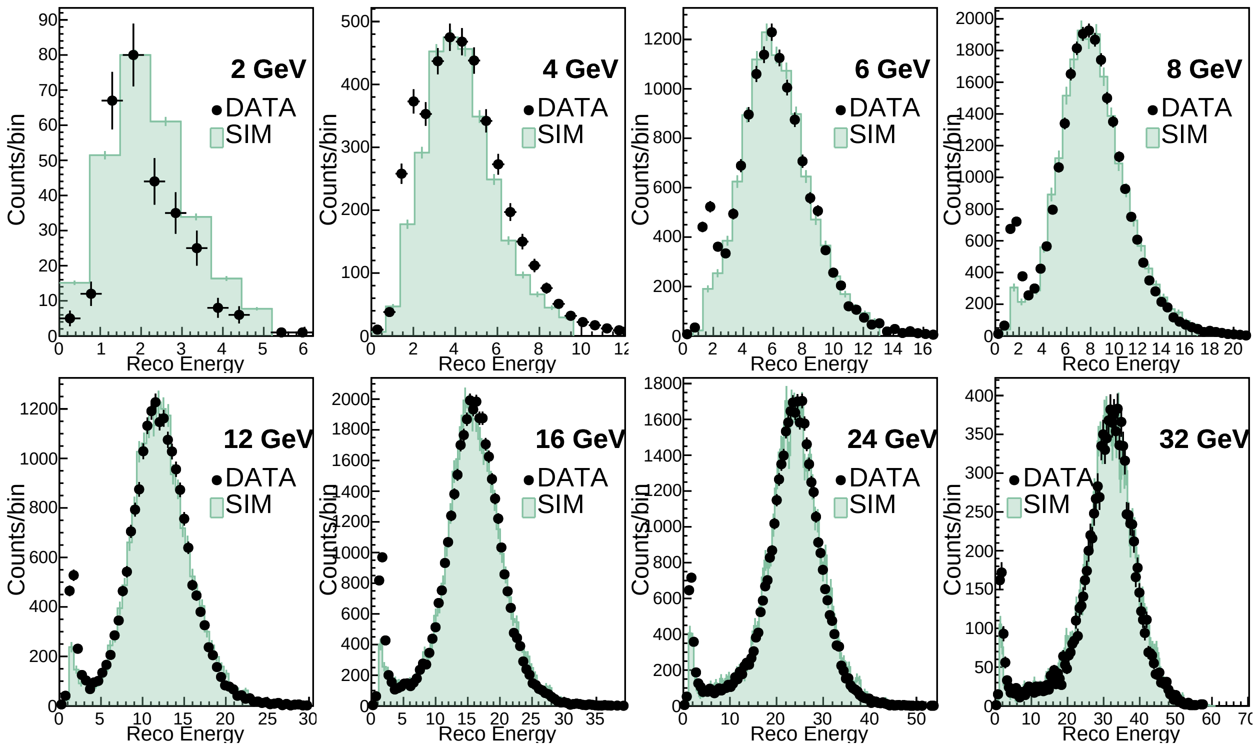

Figure 5.25: Hadron reconstruction in the standalone HCal setup. Calibrated 4 × 4 tower energies were added together from the inner and the Outer HCal. The simulation is shown by the filled histogram and the solid points are the data. Both are in good agreement. The peak at the lower energies in the data corresponds to the small fraction of muon events that pass through the HCal leaving only the minimum ionizing energy, which were not simulated.

The HCal standalone data are collected with only the inner and outer sections of the HCal in the beam line and no EMCal in front. In this configuration, electromagnetic showers generally start earlier in the calorimeter and deposit most of their energy in the Inner HCal. The hadronic showers, however, are typically deeper than the electromagnetic showers and deposit most of their energy in the Outer HCal. The beam is adjusted to be in the middle of the prototypes in order to maximize the hadron shower containment in the 4 × 4 Inner and Outer HCal towers. Data were collected with negatively charged particle beams with energies between 2 GeV and 32 GeV, which contain an admixture of mainly electrons and pions. Electron and pion events were tagged using the two beamline Cherenkov counters. Hodoscope and veto cuts based on the beam location were applied but no significant effect on the energy resolution due to the beam position was found. Both high and low gain signals from the HCal towers were collected but only low gain channels are used for analysis.

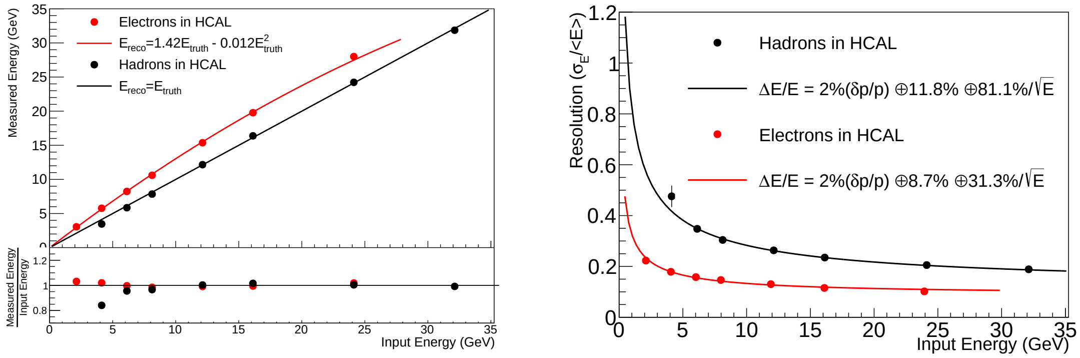

(a) **(b)**

Figure 5.26: HCal standalone measurements without the EMCal in front. (a) HCal linearity for electrons and hadrons. The lower panel shows the ratio of reconstructed energy and the fits. (b) Corresponding HCal resolution for hadrons and electrons. The beam momentum spread ($\delta p/p \approx 2\%$) is unfolded and included in the resolution calculation.

The energy from all of the towers of both the Inner and Outer HCal are summed to determine the reconstructed energy:

$$E_{HCAL} = Gain_{inner}E_{inner} + Gain_{outer}E_{outer}, \tag{5.5}$$

where E_{inner} and E_{outer} are the sum of the calibrated tower energy ($\Sigma_{ch}E(ch)$) of the Inner and Outer HCal, respectively. The asymmetry between the two sections is defined as

$$A_{HCAL} = \frac{E_{inner} - E_{outer}}{E_{inner} + E_{outer}}. \tag{5.6}$$

The gain calibration constants, $Gain_{inner}$ and $Gain_{outer}$, are determined in order to minimize the dependence of E_{HCAL} on A_{HCAL} and the deviation of E_{HCAL} from the beam energy. The same gain calibration constants are used in analysis of all beam energies.

Figure 5.25 shows a comparison of the reconstruction hadron energy between data and simulation. The simulation (filled histogram) and data (solid points) are in excellent agreement for 6-32 GeV beam energies. The data has a beam momentum spread of 2% which has been included in the simulations as well. At lower energies, hadron measurements are poor due to lower fractions of hadrons in the beam as well as the increased beam size. The peak at the lower energies in the data corresponds to the small fraction of muons events that pass through the HCal leaving only the minimum ionizing energy. The corresponding energy resolution and linearity for hadrons are shown in Figure 5.26. The data are fit with the function, $\Delta E/E = \sqrt{(\delta p/p)^2 + a^2 + b^2/E}$, as labeled on the plot. A beam momentum spread ($\delta p/p \approx 2\%$) is unfolded and included in the resolution calculation. The hadron energy resolution is $11.8 \oplus 81.1\%/\sqrt{E}$, which matches the expected resolution from simulations very well. The HCal was calibrated for hadronic showers and then used to measure electron showers. The electron resolution for the standalone HCal is $8.1 \oplus 31.3\%/\sqrt{E}$. This demonstrates that the HCal can assist the EMCal by measuring the electron energy leaking from the EMCal into the HCal.

As seen in Figure 5.26 (a), the hadron energy response is well described by a linear fit where the reconstructed energy is the same as the input energy. The bottom panel shows the ratio between the reconstructed energy and the fit. The 4 GeV hadron measurement is poor because the hadron peak is difficult to distinguish from the muon MIP peak due to their proximity, as seen in Figure 5.25. The response of the electrons is described well with a second order polynomial due to non-linear e/h response.

5.5.2 Hadron Measurement With The Full Calorimeter System (sPHENIX Configuration)

The full hadron measurement is done with the sPHENIX configuration, which includes all three segments of calorimeters including the EMCal in front of the HCal. In this configuration the total energy will be reconstructed by summing up the digitized data from both the EMCal and the HCal. The development of hadronic showers is a complicated process with significant fluctuations in the reconstructed energy compared to electromagnetic showers. Determining the shower starting position helps to understand the longitudinal shower development fluctuations. Therefore, in this analysis, the events are sorted into three categories depending on their longitudinal shower profile:

- HCALOUT: Events where hadrons pass through the EMCal and Inner HCal and primarily shower in the Outer HCal alone or pass through the full calorimeter system without showering. These events are shown as the blue points in Figure 5.27.
- HCAL: Events where hadrons pass through the EMCal. In these events, hadron showers start in the Inner HCal, or the Outer HCal, or pass through all three calorimeters. These events are shown as red points in Figure 5.27.
- FULL: This represents all hadrons irrespective of when they start showering. They are shown as black points in Figure 5.27. These include hadron showers that start in the EMCal, Inner HCal, Outer HCal, or pass through all three calorimeter systems.

These event categories help diagnose each calorimeter independently as well as improve our understanding of the leakage variations, shower containment, and longitudinal fluctuations of particle showers depending on their starting position. The EMCal energy was balanced with respect to the HCal in a similar way, by changing the gain factors described in the previous section. As expected, Figure 5.27 shows the fraction of HCAL or HCALOUT events increases as a function of beam energy. The peaks at the lower measured energy correspond to the small fractions of muon events that pass through the calorimeters leaving only the minimum ionizing energy.

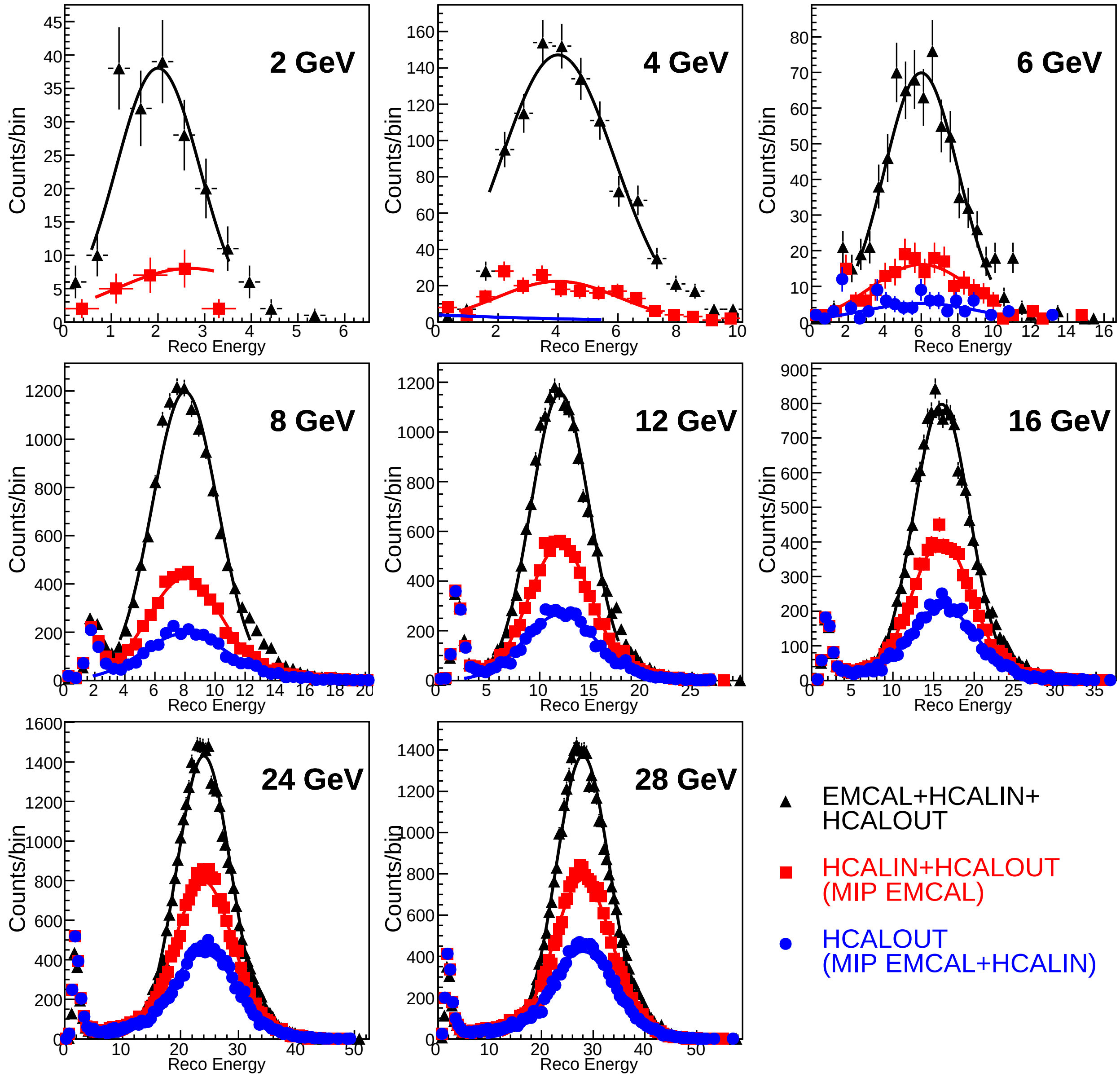

Figure 5.27: Hadron energy measurements with combined EMCal+HCal detector. Events were sorted into three categories: 1) HCALOUT where particles pass through the EMCal and Inner HCal and then shower in the Outer HCal; 2) HCALIN+HCALOUT where particles pass through the EMCal and then shower in either HCal; 3) EMCAL+HCALIN+HCALOUT which includes all showers irrespective of their starting position.

The corresponding hadron resolution is shown in Figure 5.28 (b). Data are fit in a similar manner with $\Delta E/E = \sqrt{(\delta p/p)^2 + a^2 + b^2/E}$, i.e. with a fixed beam momentum spread term of $\delta p/p \approx 2\%$ subtracted from the constant term in quadrature. HCALOUT showers that pass through the EMCal and Inner HCal have a resolution of $17.1 \oplus 75.5\%/\sqrt{E}$. HCAL showers that pass through through the EMCal have a resolution of $14.5 \oplus 74.9\%/\sqrt{E}$.

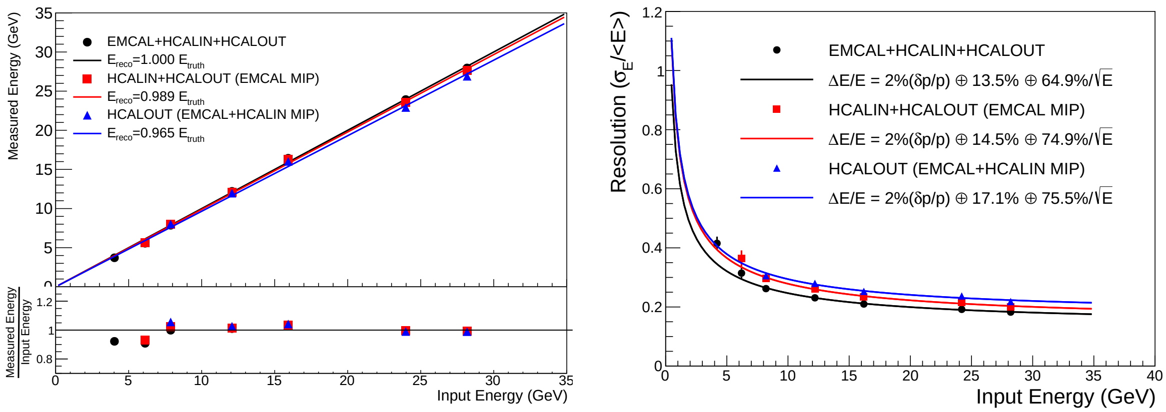

(a) **(b)**

Figure 5.28: Hadron (a) linearity and (b) resolution measured with the combined EMCal+HCal (sPHENIX configuration) detector setup. Three sets of data points corresponds to the event categories shown in Figure 5.27. The bottom panel of (a) shows the ratio of the measured energy and corresponding fits.

A combined resolution of all the showers irrespective of their starting position (FULL) is 13.5 $\oplus$ 64.9%/$\sqrt{E}$. The hadron resolution improves without the MIP cuts because it reduces the overall shower fluctuations and leakages.

The linearity is shown in Figure 5.28 (a). The bottom panel shows the ratio of the measured energy and the corresponding fits. The FULL reconstructed showers are normalized to the input energy. This results in the HCAL and HCALOUT reconstructed showers linearity slightly below the input energies, due to higher leakage in those event categories. In all cases the single hadron energy response is exceeds the sPHENIX performance specifications.

5.6 Ongoing developments

5.6.1 Test Beam in 2018

Building on the success of the three HCal prototypes, we plan to construct a fourth prototype for testing in the FNAL test beam in 2018. In addition to a new EMCal prototype and the same Outer HCal reused from the 2017 beam test, the 2018 prototype will consist of two prototype Inner HCal sectors with the flat plate design, one with hardened aluminum alloy and the other with steel. Previous beam tests used the tapered plates for the Inner HCal prototype, as it was designed and built prior to the design change to flat plates and four tiles per tower. Simulations studies have demonstrated the change from tapered to flat plates has little effect on the performance; nevertheless, such a change in design warrants confirmation with a beam test. The 2018 beam test will test the final designs for all components of the calorimeter system and is expected to be the final beam test.

5.6.2 Self Trigger

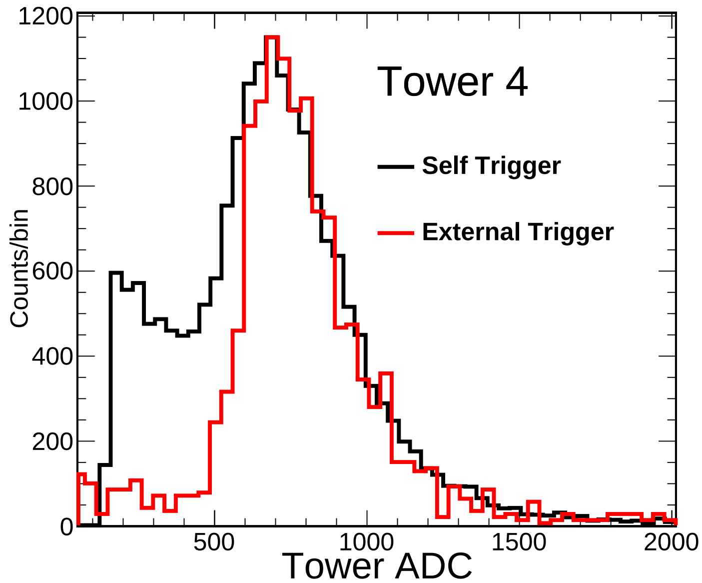

Figure 5.29: ADC distribution in a inner HCAL tower for cosmic muons. Two trigger configurations are compared: the two scintillator paddle cosmic trigger and the self trigger.

The prototype was calibrated with cosmic muon events triggered with external scintillator paddles positioned at the top and bottom of the HCal. As noted in the previous section, this procedure successfully equalized the response of each tower. The calibrated energy sum agrees with the simulation very well. However, because of the cylindrical geometry of the completed sPHENIX and the time required for collecting enough cosmic ray events, this triggering method can not easily be scaled to the full geometry, which includes 1536 towers (64 in $\phi \times 24$ in η) for each HCal.

A self trigger configuration has been tested with the HCal prototype. This trigger configuration removes the single tower backgrounds, improving the rejection factor. The algorithm is based on requiring at least N towers with signal greater than some threshold, thus removing a lot of single tower noise events. The trigger algorithm is executed by the FPGA on the data buffer. The steps of the algorithm is follows:

- Get an 8 bit signal amplitude. For each tower in the HCal, take the 12 bit post sample minus the pre sample to get a signal amplitude. The separation of the post and pre samples is user definable, but was set to be 5 samples. If the amplitude is below 0, it is set to 0. If the amplitude is above 2040, it is set to 255. Otherwise, the bottom 3 bits are dropped from the amplitude to produce a 8 bit amplitude value. Note that since we use a bipolar ADC, the 12 bits is effectively only 11 bits. The above 0 and 2040 limits are to check for over and underflow of those 11 bits, which can happen since we operate on 12 bits.

- Get the number of towers above single tower threshold. Sum up the number of towers above the single channel threshold.

- Scale by the gain factors. Scale the 8 bit amplitude for each tower by the gain scale factors. The gain factor allows one to gain-balance the towers at the trigger level. After the scaling, the amplitude is a 16 bit value. To return to an 8 bit value, the top 2 bits and bottom 6 bits are dropped, i.e. the amplitude is divided by 64.

- Sum tower amplitudes. Sum up all the tower amplitudes to get the total sum in a HCal module. Since the sum is a 8 bit number, if the sum is above 255 it gets set to 255.

The above algorithm is run for Inner and Outer HCal independently. We require at least three out of the sixteen towers to be higher than a common threshold to define a self trigger. Figure 5.29 shows a comparison of the energy deposited in a tower when triggered with self trigger and external trigger. A clear Landau distribution is seen in both setups. The self trigger configuration contains a small number of noise events which can be further cleaned with appropriate geometry cuts. This method also confirmed our calibrations for both sections of the HCal prototypes. While this is still in a developmental phase, the self trigger can be very useful calibrating the full HCal detector.

5.6.3 LED System

A LED pulser system has been developed for tracking short term gain changes caused by temperature compensation of the SiPMs and effects of increased leakage current caused by radiation damage. The system has been integrated into the Slow Controls system to eliminate additional cabling and circuitry on the detector. In the HCal prototype from January 2017, five UV LEDs were located on the controller. Since each tower has five individual tiles, each tile was connected to distinct LEDs via optical fibers. The tower response was measured when each tile was illuminated separately or in some combination. It helps to quickly identify the dead channels and stability of their light outputs during data taking.

5.6.4 Tile testing setup

Since the first prototype productions of tiles, the need for additional quality control tests at Uniplast was realized. The final thickness of each tile produced for the 2017 prototype was measured and recorded at several locations along the tile to ensure they satisfied the tolerance requirements to fit cleanly between the steel plates. Additional quality control tests to ensure fibers where not damaged and could provide light output were also performed. The results of each test were provided to BNL along with the tiles.

In addition, a tile tester is being prepared by collaborators at Georgia State University and Debrecen which will further test the light output by the fibers at Uniplast prior to shipping. The tester will measure the signal output by a particular set of SiPMs when cosmic rays pass through a stack of tiles. This will allow Uniplast to confirm that the tiles and fibers are emitting a consistent amount of light throughout the final production.

Chapter 6

Calorimeter Electronics

The sPHENIX reference design for electronics is based on a common electronics design for both the EMCal and HCal detectors using off the shelf components. This approach will reduce the overall cost and minimize the design time for the electronics. A block diagram of the calorimeter readout chain is shown in Fig. 6.1. The technical specifications for the calorimeter electronics are set by physics requirements and are summarized in Table 6.1. For the EMCal, the expected energy range for photons is expected to be 1 GeV to 50 GeV. For a 1 GeV photon incident on the center of an EMCal tower, 80% of the energy will be deposited in the central tower with 20% of the energy shared among the 8 surrounding towers. This implies a minimum energy of 25 MeV and a dynamic range of 10^3 to cover the range of expected energy deposition in a single tower of the EMCal.

Table 6.1: Technical Specifications for the Calorimeter Electronics.

Component	Requirement	Specification
Optical Sensor	Pixel Size	$15 \times 15 \mu m^2$
	Dynamic Range	10^4
	PDE	25%
	Gain	10^4
	Pixels/GeV: EMCal	1600
	Pixels/GeV: HCal	
Amplifier/Shaper	Gain	100 mV/pC
	Signal-to-Noise	10:1
	Peaking time	30nSec
Digitizer	Resolution	14 Bit (13 Bit effective)
	Maximum Sampling Frequency	65 MHz
	Latency	40 BCO
	Multi-event Buffering	5 Events

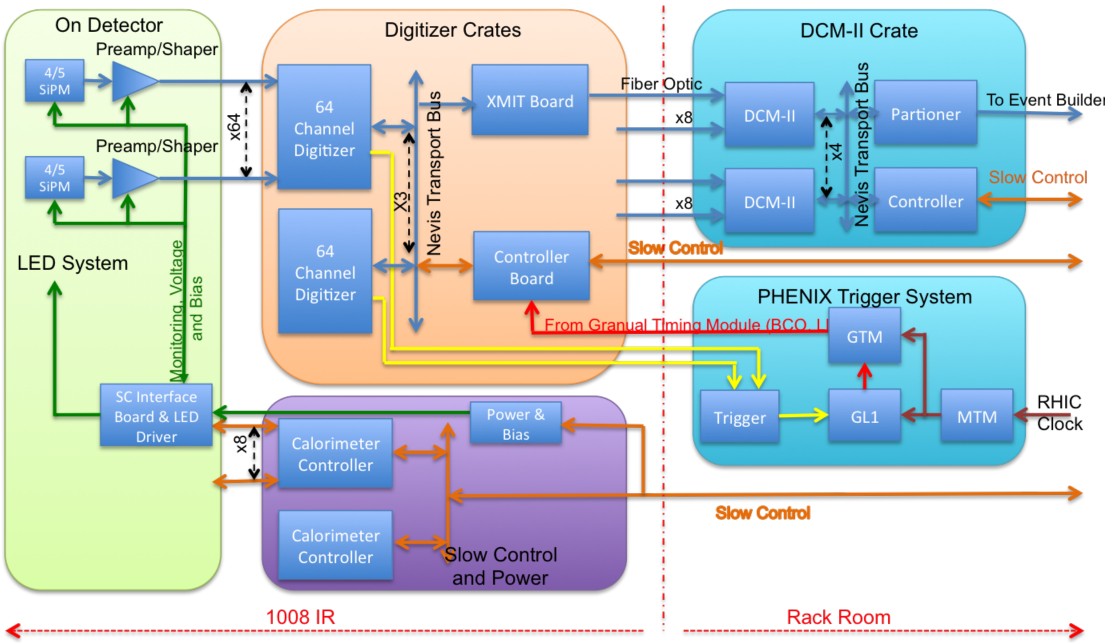

Figure 6.1: Block diagram of the calorimeter readout chain. The optical signals are amplified locally and driven as differential analog signals to the digitizers located near the detector. Upon receipt of a level one trigger, the digital data for triggered event is transmitted via optical fiber to the sPHENIX data acquisition system. for recording.

The reference design uses multiple Silicon Photomultipliers (SiPMs) as the optical sensors for the calorimeters. The Analog signals from the SiPMs associated with a single tower in the calorimeters are passively summed, amplified, shaped and differentially driven to digitizer boards located in racks near the detector. The differential analog signals are received by 64 channel digitizer boards and digitized by a 14 bit ADC operating at a sampling rate 6 times the beam crossing frequency. Upon receipt of a Level-1 (L1) trigger signal, the digitized data is optically transmitted to the PHENIX DAQ.

The EMCal front end electronics for an EMCal sector module consists of 2x2 SiPM Daughter Boards which mount directly on the EMCal light guides for 4 towers, 2×8 Preamplifier Boards which connect to 4 SiPM Daughter Boards via flex cable, and an Interface Board which plugs into 4 Preamplifier Boards. Located in a crate near the detector are the Calorimeter Controllers, capable of controlling 8 Interface Boards. The amplified differential analog signals are driven directly to the nearby digitizers. There are a total of 384 EMCal front end channels in a EMCal 1/2 sector module.

The HCal front end electronics for an HCal module consists of SiPM Daughter Boards with a single SiPM which couples directly to a an HCal tile fiber and an HCal single channel Preamplifier Board mounted next to the tower. Mounted on each end of an HCal module are Interface and Backplane boards which provides the voltage distribution, monitoring and gain corrections, and an LED Driver board that distributes a calibration/monitoring light pulse via optical fiber to each of the tiles in an HCal module. The differential analog signals are brought directly to connectors located on the ends of the HCal module

The analog analog signals from both the EMCal and HCal are waveform digitized using identical electronics. The digitizer system consists of a 64 channel digitizer board with 14 bit ADCs running at 6 times the beam crossing frequency (BCO), a crate controller which provides slow control for the crate, and an XMIT module which transmits the triggered data from the digitizer boards to the sPHENIX Data Acquisition System. The system is designed to read an event out in 40μSec and operate at a level 1 trigger rate up to 15kHz. In addition to digitizing all the channels, the digitizer board is capable of producing trigger primitives which are transmitted over dedicated optical links to the sPHENIX trigger system.

Detailed descriptions of each of the modules for the EMCal and HCal front end electronics and digitizer system are given in the following sections. A summary of the number of boards for the full detector is given in Table 6.2.

Table 6.2: Electronics Component Count.

	SiPMs	98304
	SiPM Daughter Boards	6144
	Preamp Boards	1536
EMCal Front End Electronics	Interface Boards	384
	Controller Boards	64
	Controller Crates	4
	SiPMs	13824
	Preamp Daughter Boards	3072
	Interface Boards	128
HCal Front End Electronics	LED Driver Boards	128
	Controller Boards	16
	Controller Crates	2
	Signal Cables	1728
	Digitizer Boards	432
Digitizer Electronics Electronics	XMIT Modules	144
	Controller Boards	36
	Clock Master	36
	Crates	36

6.1 Optical Sensors

The compact nature of the EMCal and HCal detectors and the location of the EMCal and Inner HCal being inside the 1.5T solenodial field require that the optical sensors be both physically small and immune to magnetic effects. A device with large gain is also desirable in order to reduce the demands on the performance specifications of the front end analog electronics. For both the EMCal and HCal detectors, silicon photo-multipliers (SiPMs) from Hamamatsu have been chosen as the reference design optical sensor. SiPMs have the advantage that they are immune to magnetic fields, have large gain and are small in size.

6.1.1 Device Characteristics

SiPMs are inherently limited in their dynamic range by the number of micro-pixels in the device, as shown in Figure 6.2. Due to the digital nature of the SiPM, the usable dynamic range is significantly less than the the total number of micro-pixels. Each micro-pixel fires once per event regardless of how many photons hit it. Distributing the incident light uniformly across the active area maximizes the useful range, but for large signals it is still limited by optical saturation, that is more than one photon hitting the same micro-pixel. While increasing the number of micro-pixels would increase the dynamic range, there are trade-offs in that more micro-pixels typically means lower gain and lower photon detection efficiency, PDE.

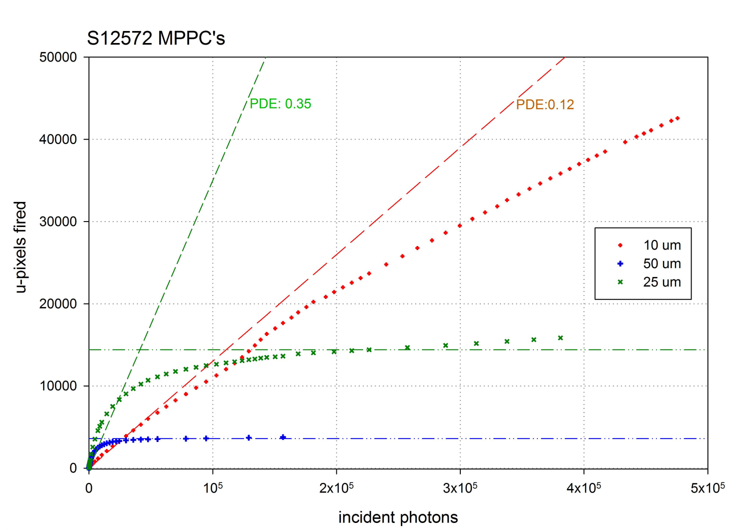

Figure 6.2: Optical saturation in Hamamatsu S12572 MPPCs. 10μm, 25μm, and 50μm micro-pixels

In order to achieve the required dynamic range, a device with a large number of micro-cells is required, which limits the number of devices that meet the technical specifications for the optical sensors. Hamamatsu has a number of devices with high pixel counts, high gain, and good PDE which meet the sPHENIX technical requirements. For both the EMCal and HCal detectors, the reference design is based on the Hamamatsu S12572-33-015P MultiPixel Photon Counters (MPPC). The device is a $3 \times 3\,\text{mm}^2$ device with 40K pixels each $15 \times 15\,\mu\text{m}^2$ in size. A photograph of the device is shown in Figure 6.3 and a technical drawing is shown in Figure 6.4. The properties of this device are summarized in Table 6.3.

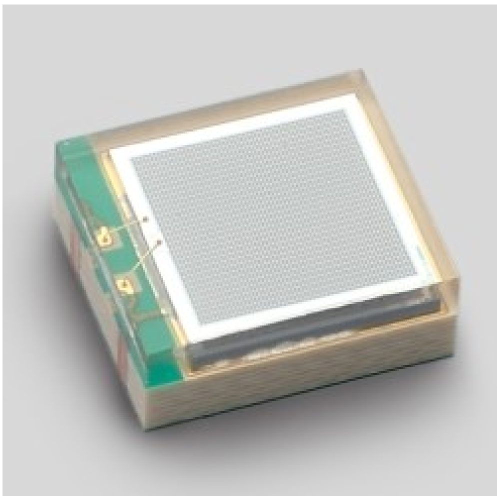

Figure 6.3: Hamamatsu S12572 MPPC (SiPM). The device is $3 \times 3\,\text{mm}^2$ with 40,000 pixels $15\mu\text{m}^2$.

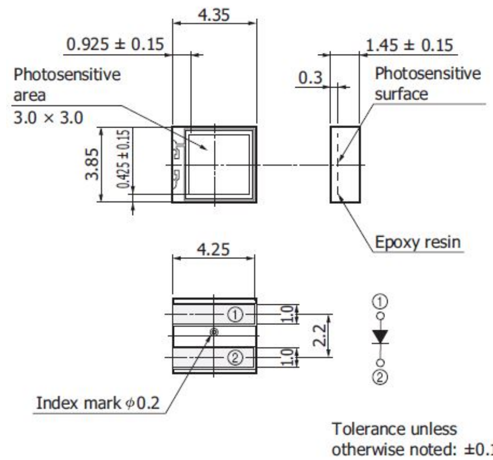

Figure 6.4: Hamamatsu S12572 MPPC surface mount package dimensions.

The 40K pixels of the Hamamatsu S12572-15P device limit the dynamic range of device to be $\sim 10^4$. However, the optical saturation at the upper end of the range is difficult to correct for as the device response deviates from linearity as the number of activated pixels approaches the total number of pixels in the device, so the effective pixel count is significantly less than 40K. With a PDE of $\sim$ 25% it should therefore be possible to adjust the light level to the SiPM using a mixer to place the full energy range for each tower ($\sim$ 25 MeV–50 GeV) in its useful operating range. For example, if the light levels were adjusted to give 10,000 photoelectrons for 50 GeV, this would require only 200 photoelectrons/GeV, which should be easily achieved given the light level from the fibers entering the mixer.

The performance of a SiPM is affected by the temperature of the device. SiPMs show an increasing dark current and a diminishing gain with increasing temperature. Figure 6.5 shows the dependence of gain on temperature for different SiPMs and the dependence of device leakage current on temperature for Hamamatsu S12572 SiPMs of different pixel sizes. Devices with larger pixel sizes typically have higher gain, but also higher leakage current. The leakage current increases rapidly above 30 °C, suggesting the benefit of operating in 5-20 °C range. While in principle cooling could be used to mitigate the increased dark current due to radiation damage, the scale of the increase (orders of magnitude) greatly exceeds the potential benefits of cooling (factors of 2) over the temperature range 0-40 °C. Figure 6.6 shows the leakage current, signal amplitude, and signal noise performance of a S12572-015P SiPM and an sPHENIX preamp as a function of temperature.

Property	
active area	3mm x 3mm
number of micro-pixels	40,000
micro-pixel pitch	15 μm
geometric fill factor	0.53
package	surface mount
window	epoxy resin
window refractive index	1.55
operating temperature	0-40 deg C
spectral response range	320-900 nm
peak sensitivity wavelength	460 nm
photon detection efficiency (PDE)	0.25
Dark Count Rate (typ)	1 Mcps
Terminal capacitance	320 pF
Gain	230,000
Gain temp coefficient	3500 / °C
Breakdown voltage (V_{br})	65 ± 10 V
Recommended Operating Voltage	V_{br} + 4V
Temp coeffic at V_{op}	60 mV / °C

Table 6.3: Properties of Hamamatsu S12572-015P MPPC.

6.2 Readout Electronics

The EMCal and HCal readout electronics consist of the analog front end electronics mounted directly on the detectors, and the digital back end system mounted in racks near the detector in the sPHENIX Interaction Region. The analog front end system consists of the SiPM daughter boards, Preamplifier boards, calibration and monitoring systems, and power distribution. The analog front end electronics is functionally the same for both the EMCal and HCal detectors with different packaging to account for differences in the mechanical design of the 2 detector subsystems. The digitizer and power systems are common to both subsystems

6.2.1 HCal Electronics

An HCal module consists of 2×24 towers covering the full range in η and 2 ϕ slices with 2×12 towers readout on each end of the module. Each of the tiles that form a tower (4 for the Inner HCal and 5 for the Outer HCal) have single SiPM mounted on the SiPM Daughter Board that is attached to the edge of the tile where the wave shifting fiber ends are. The SiPMs for a tower are connected to a Preamplifier Board located on the outer radius, in the center of the tower with a shielded cable. The signals are received on the Preamplifier

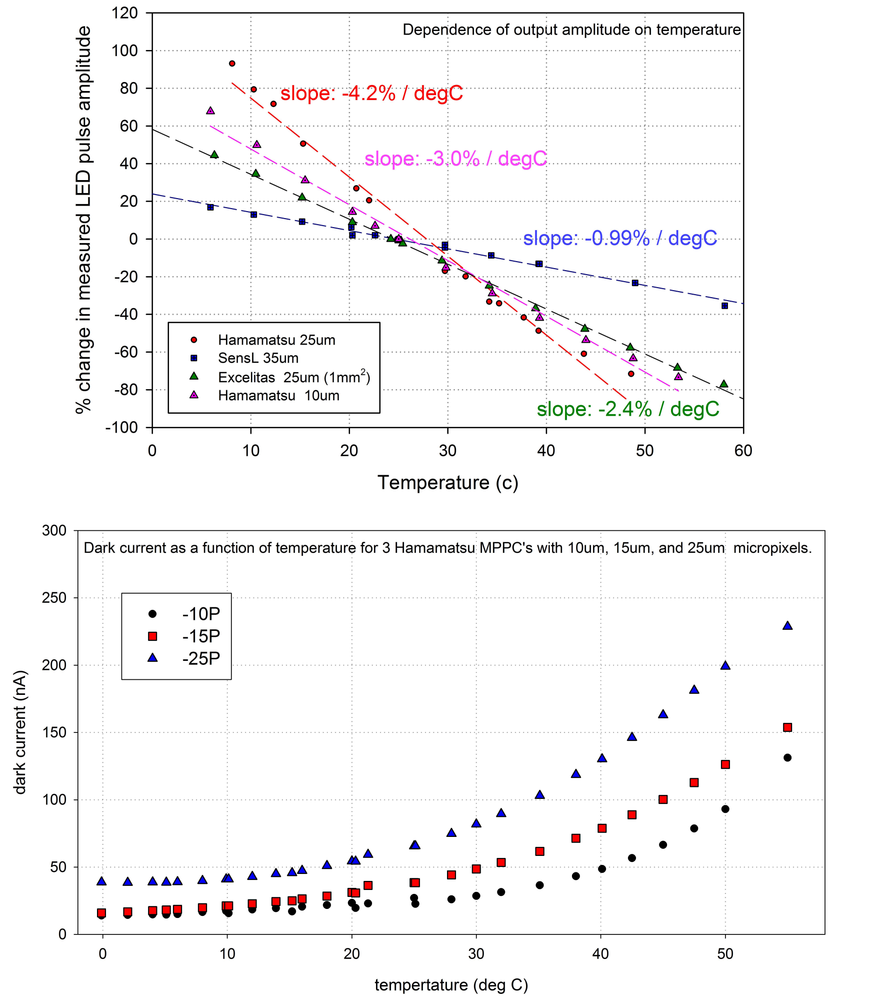

Figure 6.5: Percent change in LED signal amplitude vs temperature for Various SiPMs. (top) and Dependence of leakage current on Temperature in Hamamatsu S12572 MPPCs with 10μm, 15μm, and 25μm micro-pixels (bottom).

Board where they are passively summed, amplified, shaped and driven differentially to the digitizer system. Located on each end of the HCal module are the HCal Backplanes, Interface Boards and LED Driver Boards. The Interface Board distributes the SiPM bias voltage and low voltage to the Preamp Boards for 24 of the towers in an HCal module. The HCal Interface Board also has ADCs for monitoring the SiPM temperatures, bias currents and voltages. The HCal Interface Board also has 24 DAC channels, 1 per tower, that is used to provide a voltage adjustment to the SiPM bias voltage to compensate for temperature variations and changes in the bias current due to increased leakage current as a result of neutron damage to the SiPM. The Interface Board plugs directly into an HCal Backplane Board, which is a passive board containing the cable connections for 24 towers. This arrangement allows for an HCal Interface Board to be replaced with minimal disturbance to the preamp power cables. Also connected to the HCal Interface Board is an LED Driver

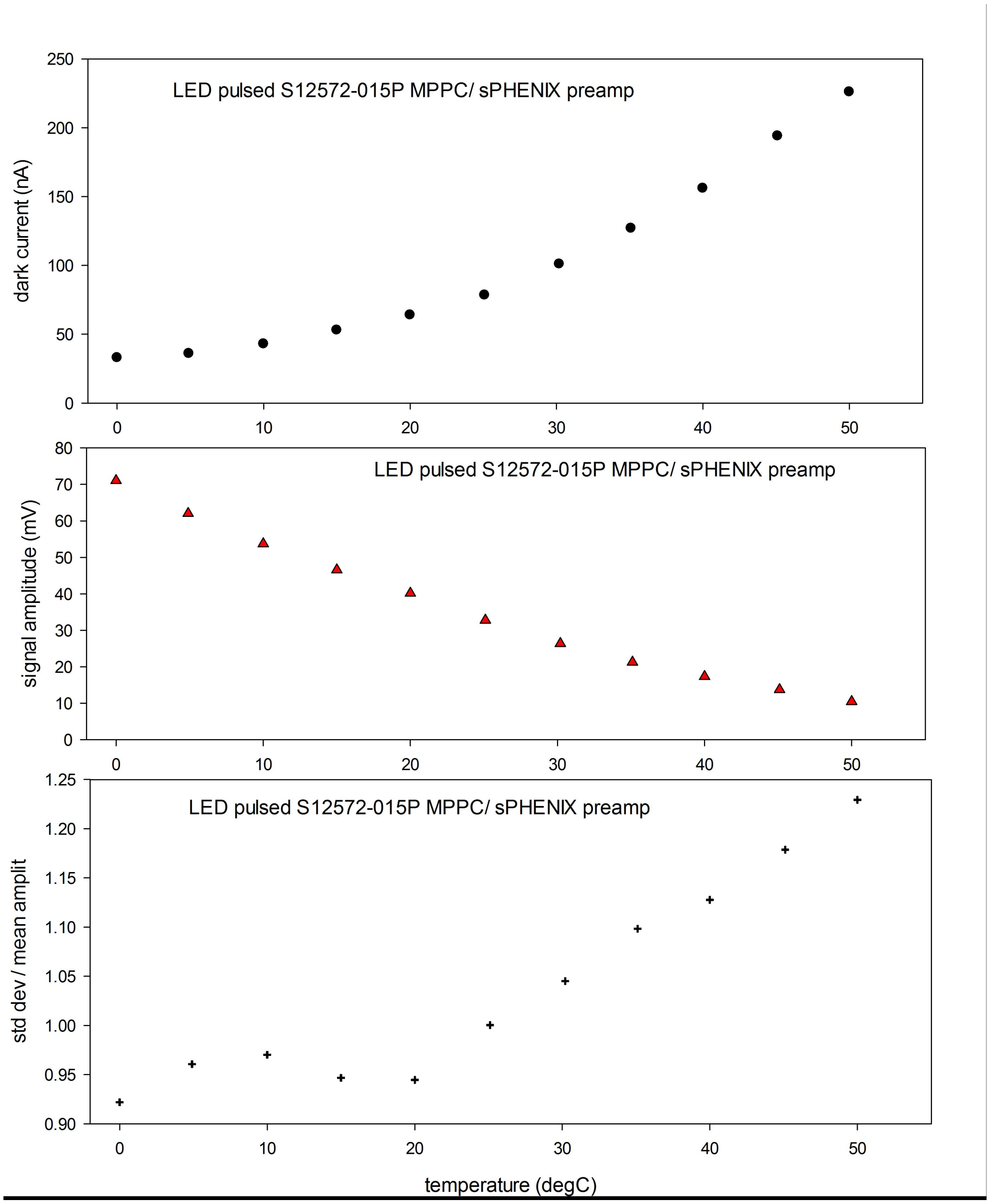

Figure 6.6: Performance as a function of temperature - Hamamatsu S12572-015P MPPCs with an sPHENIX preamp. Dark current as a function of temperature (top), signal (LED pulse) amplitude vs temperature (center), and for the LED signal, stddev/mean vs temperature (bottom)

Board. The LED Driver Board consists of an LED driver circuits, 5 LEDs, and light mixing blocks. Twenty-four light fibers, one per tile per tower are connected to a light mixing block. Digital circuitry allows selection of which LED is pulsed and the pulse amplitude. This arrangement allows for a single tile in each of 24 towers to be illuminated independent of the other tiles in a tower for testing and calibration purposes. A bi-directional serial link connects the HCal Interface Board to a Calorimeter Controller board in a nearby crate.

The Controller board transmits to the Interface Board the parameters for the temperature compensation and gain control, LED enables, pulse amplitudes and pulse triggers, and reads back the monitoring information from the Interface Board. Each Controller is capable of controlling 8 HCal Interface Boards. Each Controller board has an Ethernet connection for communications with the sPHENIX Slow Control computer. A block diagram of the HCal electronics chain is shown in Figure 6.7.

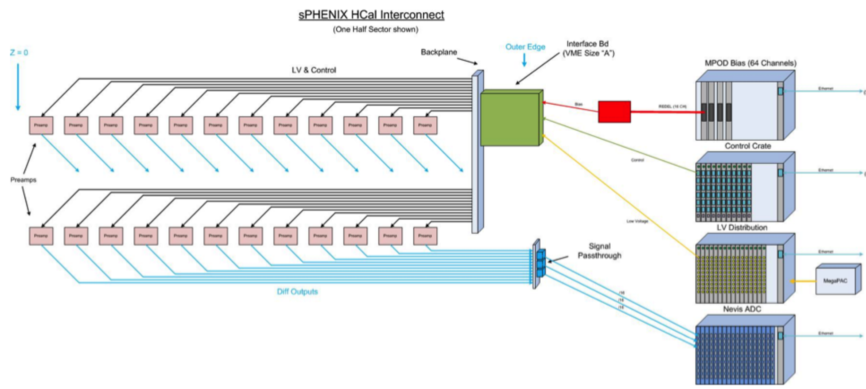

Figure 6.7: A block diagram showing the overall design of the HCal electronics for one half sector of the HCal. There are a total of 128 half sectors for the inner and outer HCal combined. Not shown are the connections for the LED monitoring system.

6.2.2 EMCal Electronics

A half sector of the EMCal consists of 384 towers in a 8×48 ($\phi \times z$) configuration. To match the mechanical layout of the EMCal towers, the EMCal analog channels are arranged in a 8×2 array on a Preamp Board matching the EMCal tower geometry. The 16 SiPMs (4 per tower) for a 2×2 array of towers are surfaced mounted on a small daughter board that also has an LED mounted in the center of the 4 towers and a thermistor for monitoring the local temperature. Four SiPM daughter boards are connected to a Preamp Board by a short flex cable. The signals from the 4 SiPMs associated with an EMCal tower are passively summed, amplified, shaped and differentially driven over shielded cable to the digitizer system located in nearby racks. Four EMCal Preamp Boards plug into an EMCal Interface Board which distributes the bias voltage and preamp low voltage. The EMCal Interface board also provides monitoring for the voltages, currents, and temperatures, alone with 64 DAC channels for bias gain adjustment and programmable LED drivers. The six EMCal Interface boards in a half sector are connected with a bi-directional serial connection to a Calorimeter Controller board. The EMCal control system is identical to the HCal control system described earlier. A block diagram of the front end electronics for one EMCal half sector is shown in Figure 6.8.

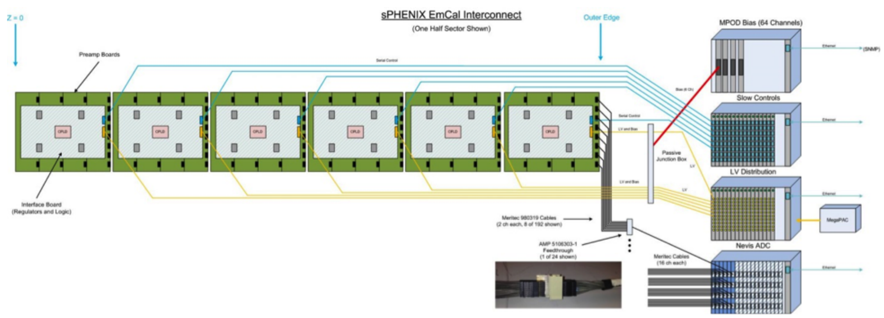

Figure 6.8: A block diagram showing the overall design for the EMCal electronics for one half sectors for the EMCal. There are a total of 384 towers per half sector and 32 half sectors for the EMCal.

6.2.3 Amplifier, Shaper Driver Circuit

To improve light collection, four SiPMs will be used in parallel for the EMCal and the Inner HCal, and five for the Outer HCal. This paralleling of devices also leads to a total input capacitance into the Preamplifier that can exceed 1.5nF. Preamp circuits that use feedback to obtain linearity are prone to oscillation due to the significant input pole presented by this source capacitance. Other approaches which amplify signal voltage developed across a source resistor produce nonlinearity due to the inherent dynamic source impedance of SiPMs and an excessively long wave shape. A common-base transistor amplifier (CBA) was chosen to address these concerns. The CBA acts as a transresistance amplifier or current to voltage transformer without the need for feedback. The result is a stable circuit with an input impedance of less than 4 ohms.

A differential output amplifier is required to drive the signals through 10 meter Meritec cables to the inputs of the Digitizer Boards which are located in rack mounted crates near the detector. The shaper/driver is a differential driver amplifier configured as a multiple-pole feedback filter with a corner frequency of 5 MHz which provides a peaking time of 30 nS for ADC sampling at 65 MHz. In order to observe signals from Minimum Ionizing Particles for calibration of the EMCal and HCal detectors, a second high gain output stage is provided. This stage is identical to the normal gain output stage with the exception of the stage gain. Selection of which output stage is used, is determined through the slow control system at the time the readout is initialized for readout, providing control on a run-by-run basis. A schematic diagram of the front end amplifier/driver circuit is shown in Figure 6.9.

The SiPM delivers nominally 37 fC for a single micro-cell fired and the CBA produces an Equivalent Noise Charge of about 43 fC, as shown in Figure 6.10, so the signal to noise ratio is approximately 0.86 at the single micro-cell level. A Minimum Ionizing Particle is expected to produce approximately 35 photoelectrons which would yield 9 micro-cells fired given a PDE of $\sim 25\%$.

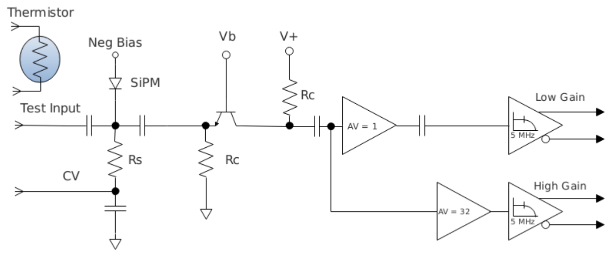

Figure 6.9: Schematic diagram of the EMCal and HCal Preamplifier/shaper/driver circuit. Selection of the normal gain or high gain output is made through the slow control system (not shown) at the time the system is configured for data taking. For standard data taking, the normal gain is used.

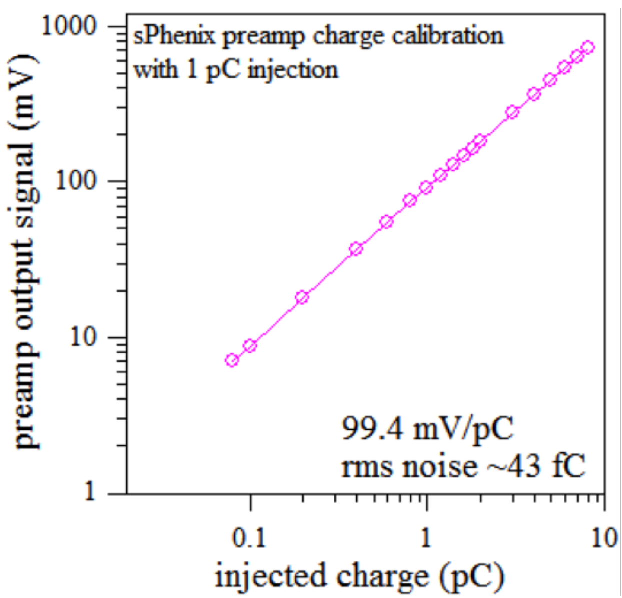

Figure 6.10: The response of the common-base transistor amplifier as a function of the injected charge as measured in the lab. The measured RMS noise is $\sim$ 43 fC which is matches the charge injected by a single micro-cell of the SiPM firing.

6.2.4 Gain Stabilization

The SiPM reverse breakdown voltage, V_{br}, is proportional to temperature and increases nominally by 60mV/°C. As the SiPM bias increases over V_{br}, the SiPM begins to operate in Geiger mode with a gain up to 2.75×10^5 and is linearly proportional to the bias over-voltage, V_{ov}. The range of this over-voltage is typically 4 Volts and represents the useful gain range of the device. In order to compensate for temperature variations and maintain a stable gain, a closed feedback loop consisting of a thermistor, ADC, logic and a DAC will be used to adjust V_{ov} and stabilize the voltage as shown in Figure 6.11. The thermistor is located near the SiPMs and is measured by 16 bit ADC located on the Interface Board. The digitized where a local processor computes an offset for the bias voltage to correct for temperature variations. The 12 bit correction is transmitted back to the Interface Board where a 12 bit DAC provides an offset voltage to adjust the SiPM bias voltage for the desired gain.

One effect of the increase in leakage current resulting from neutron damage is that voltage drop across the current limiting resistor for the bias supply changes as function of time. In order to compensate for this changing voltage, the bias current for SiPMs in an EMCal or HCal tower is monitored. The measured bias current, combined with the known value of the limiting resistors is used to compute an additional correction to the bias that is added to the bias correction required for temperature variations in order to maintain a stable gain.

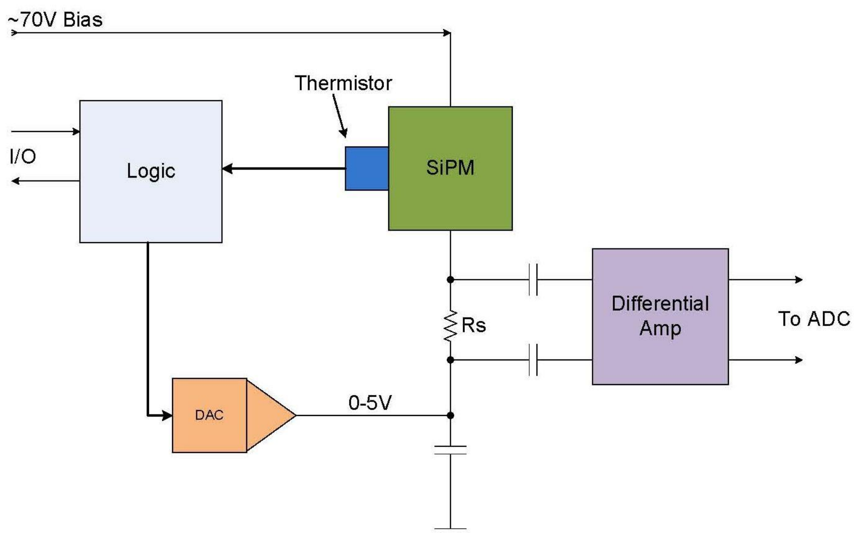

Figure 6.11: Block diagram of a temperature compensating circuit for SiPMs

6.2.5 Slow Control and Monitoring

The slow control and monitoring for the EMCal and HCal electronics consists of the Interface Board and Controller Board. The Interface Board mounts directly on the detector, with the Controller located in a rack mounted crate nearby. A block diagram of the slow control and monitoring system for the EMCal and HCal detectors is shown in Figure 6.12. The Interface Board contains a Xilinx®CoolRunner-II™ CPLD, 16 bit ADC and multiplexers to monitor voltages, leakage currents and temperatures. The CPLD runs a state machine that selects each of the analog channels to be monitored, reads out the associated ADC information and updates the bias DACs when new settings are transmitted to it from the Controller Board. A single Interface Board is capable of monitoring 24 towers for the HCal and 64 Towers for the EMCal. The data is transmitted serially to the Controller Board which is capable of controlling up to 8 Interface boards. A processor on the Controller Board uses the temperatures measured by the thermistors next to the SiPMs to determine the individual DAC settings to correct the bias voltage to compensate for temperature variations and maintain a stable gain. The DAC settings are transmitted back to the CPLD on the interface board and loaded into the appropriate DACs. All digital data is transmitted to the slow control monitoring system via the crate back plane and crate controller.

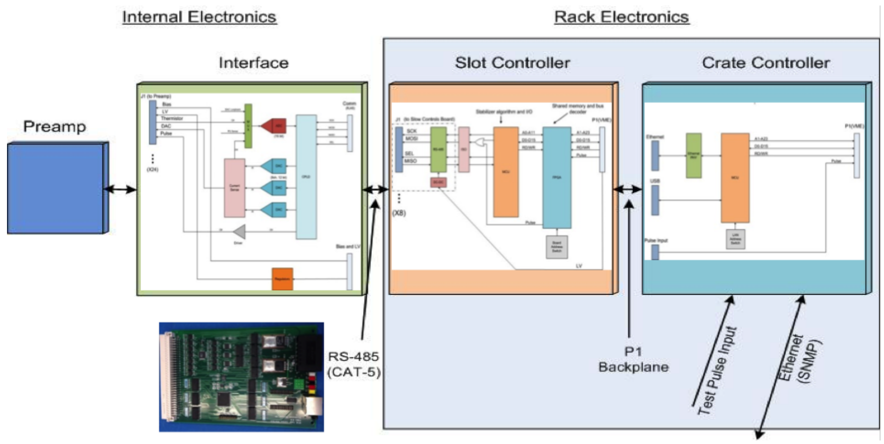

Figure 6.12: Block diagram of the slow controls for the calorimeter front end electronics. The inset picture shows a prototype module of the HCal Interface board that will be used on the HCal Beam Test prototype.

6.3 Digitizers Electronics

The reference design digitizer electronics for sPHENIX is based on the digitizer system built for the PHENIX Hadron Blind Detector (HBD) [147] and modified for the PHENIX Muon Piston Calorimeter (MPC) detector. A block diagram of the Digitizer Board is shown in Figure 6.13. Differential signals from the preamplifiers are received over a 10 meter Hard Metric cable by an Analog Device AD8132 differential receiver which also serves as the ADC driver. The signals for 8 towers are digitized by an Analog Device AD9257 8 channel, 14 bit ADC operating at 6x the Beam Crossing Clock (BCO). The serialized data from the ADC is received by an Altera Arria V GX FPGA which provides digital pipeline that is 85 BCOs deep to provide a trigger latency of up to $\sim 85\ \mu$s. Upon receipt of a Local Level 1 (LL1) trigger, up to 31 time samples (set during system configuration) for each channel is buffered in an event buffer for readout. The ADC board is capable of buffering up to 5 events.

The LL1 data from Digitizer Boards are received by an XMIT Board using token passing to control the readout from the Digitizer Boards over the back plane. The data is formatted into a standard sPHENIX data packet. Formatted data is sent by 1.6 GBit optical links using 8Bit/10Bit encoding to the sPHENIX second generation Data Collection Modules (DCM-IIs). In order to meet the sPHENIX readout requirement of $\leq 40\mu$s 3 Digitizer boards will be readout by a single XMIT board. In this configuration, a digitizer crate will house 4 XMIT groups, capable of reading out 768 channels of SiPMs.

The Crate Controller interfaces to the PHENIX Granule Timing Module (GTM) via the Clock Master and fans out the 6x BCO and LL1 triggers to the Digitizer and XMIT modules. The Crate Controller also has dedicated bi-directional serial optical link to the sPHENIX Slow Control system for run-time configuration of the Digitizer system. The Crate Controller is also capable of a slow read out of Digitizer Boards through the back plane for testing and debugging purposes.

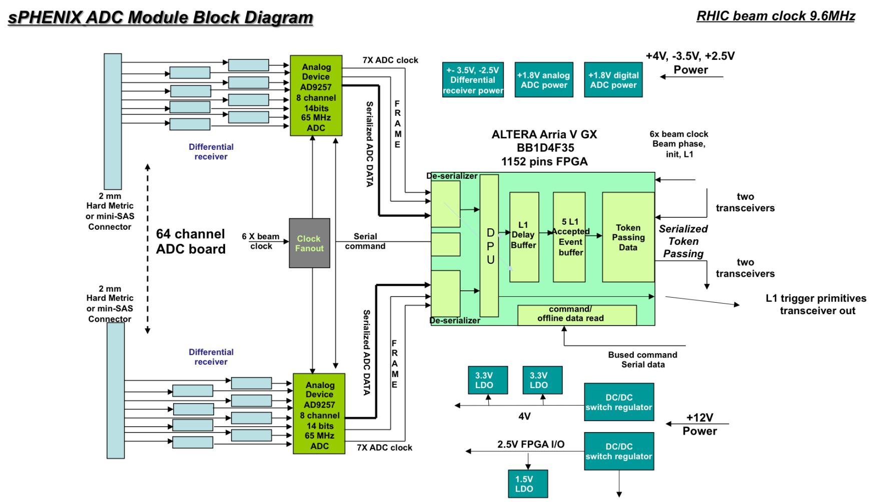

Figure 6.13: Block diagram of the Digitizer Module electronics.

In addition to processing the data for 64 channels, the Digitizer Board also produces the LL1 trigger primitives. For each tower, the 6 samples corresponding to a beam crossing are summed and pedestal subtracted to form an integrated pulse amplitude for the tower. Additional corrections for gain or pedestal shifts can be applied to the integrated signal. The sums from 4 towers forming a 2×2 tower array are then summed together to form an 8 bit 2×2 patch sum trigger primitive. A total of 16 2×2 trigger primitives are formed on each digitizer board every beam crossing. These 16 trigger primitives along with a framing word and header word are transmitted optically using 8b/10b encoding to a trigger processing system located off detector. For a 10 MHz beam crossing frequency, this results in a 1.8GBit/sec data rate per digitizer board.

6.4 Power Systems and Ground

Low voltage power for the analog front end electronics will be provided using bulk supplies and distributed through the second generation PHENIX LV distribution system. The PHENIX LV system is a crate based system which fans out up to 200 low voltage channels which are individually switched and monitored. Control of the system is provided via MODBUS/TCP and client software such as Iconics Graphworx. All low voltage will be locally regulated on the detector. For the digitizers, low voltage power will be supplied by local bulk supplies and DC-to-DC converters located in the crates. Local monitoring of the digitizer voltages will be done using a monitoring system similar to PHENIX monitoring system based on ADAMS modules by Advantech using a MODBUS/TCP interface.

Bias power for the SiPMs will be provided by commercial power supplies such as the WEINER-ISEG system proposed for Hall-D at Jefferson Lab. Bias voltage from single channel of the WEINER-ISEG system is fanned out multiple SiPMs with all the SiPMs for a tower receiving a common bias voltage that has been adjusted for temperature variations and leakage current effects.

The estimated power consumption for the different components of the EMCal and HCal readout electronics is summarized in Table 6.4.

Table 6.4: Summary of the estimated power consumption for the EMCal and HCal readout electronics. For the SiPM Daughter Boards, power is after radiation damage.

Board	Board	Sector	Total Power
EMCal On Detector Front End Electronics			
SiPM Daughter Boards	280 mW	26.7 W	1.71 kW
Preamp Boards	5 W	120.0 W	7.68 kW
Interface Boards	4.5 W	27.0 W	1.75 kW
Total On-Detector Power		173.7 W	11.2 kW
HCal On-Detector Front End Electronics			
SiPM Daughter Boards (Inner)	17 mW	3.4 W	108.8 W
SiPM Daughter Boards (Outer)	17 mW	4.2 W	134.4 W
Preamp Boards	020 mW	14.4 W	921.6 W
Interface/LED Boards	3.5 W	3.5 W	224.0 W
Total On-Detector Power		21.7 W	1.39 kW

Critical to minimizing the noise and maintaining the requirements for the signal-to-noise is a well developed grounding plan. Preliminary work has started on defining such a plan. It is a star grounding plan with the reference point defined near the front end electronics. All electronics will be electrically isolated from the mechanical components of the detector which are separately connected to the experimental ground. All power supplies will have isolated returns decoupling them from the AC power ground. A preliminary grounding plan is shown in Figure 6.14.

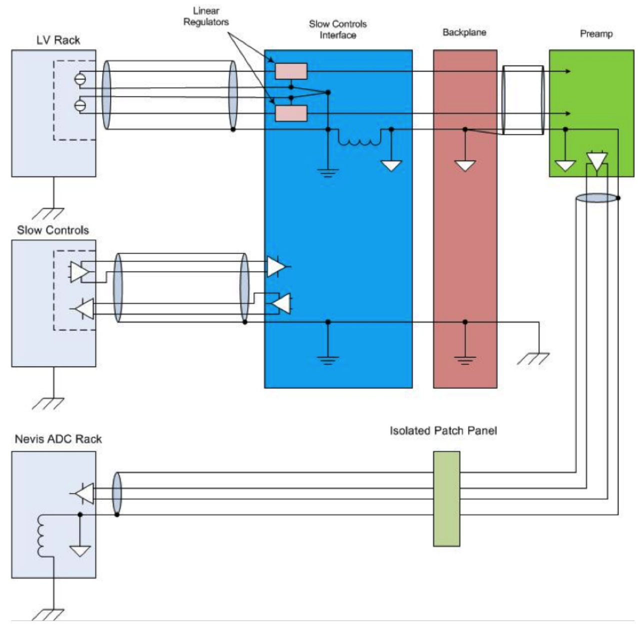

Figure 6.14: Preliminary grounding plan for calorimeter electronics which is based on a star grounding configuration. Not shown is the grounding of the mechanical parts of the calorimeters.

6.5 Electronics Cooling

The power requirements for the front end electronics is summarized in Table 6.4. For the Inner and Outer HCal detectors the resulting heat load is not anticipated to be a problem; however, for the EMCal sectors the heat generated by the SiPms and EMCal front end electronics must be removed. As a whole, the subsystem can eventually generate 11 kW of heat while operating. The plan is to use a water or water/glycol mixture to provide cooling for the system and maintain its temperature to slightly below ambient (20°C). The cooling concept is shown in the cooling circuit layout in Figure 6.15. Since the detector will be inaccessible while running, the filling, bleeding and draining operations must be able to be done from remote areas. Because of the location of the system, it must be monitored remotely for performance and failures. In addition, redundancy must be built into it provide continuous uninterrupted service throughout the run. The number of active components installed inside the active area in these areas must be reduced to a minimum to reduce failure rates. If the fluid used is water, the consequences of leaks is damage to the detectors electronics, while if fluorocarbons are used, the cost of leaks can quickly become prohibitive. In order to minimize the risk of leaks, the number internal connections needs to be minimized, type of connection optimized to reduce the probability of leaks occurring.

To remove heat from the EMCal Preamplifier Boards, a custom cold plate will be designed that will be coupled to each Preamplifier Board with a Gap Pad thermal interface. Multiple

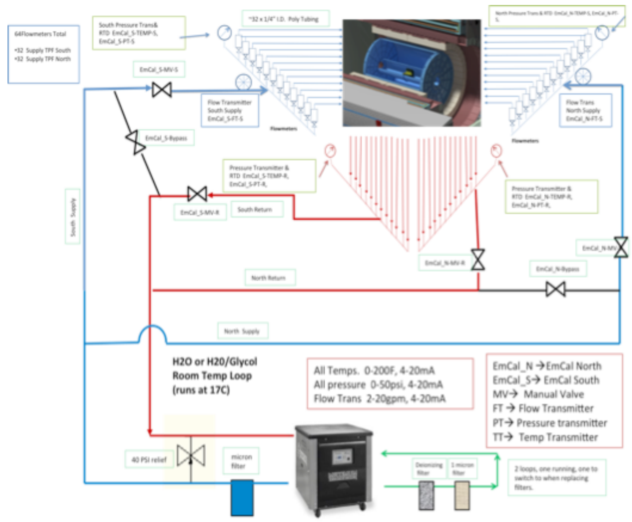

Figure 6.15: Conceptual design of the the cooling system for the EMCal front end electronics.

3074 cooling loops connect the cold plates and will also provide the mechanical support for
3075 the Preamplifier Boards. A conceptual design of the preamplifier cold plates and cooling
3076 for an EMCal Sector is show in Figure 6.16. The cold plate will also have four copper
3077 thermal straps to transfer the heat from the associated SiPM Daughter Boards to the same
3078 cold plate. Prototypes of cold plates being tested are shown in Figure 6.17. Fluid for each
3079 EMCal sector is provided from a multi channel manifold control box outside the solenoid.
3080 The control box will have the capability of balancing flowers to each of the sectors as well
3081 as monitor the pressure, temperature and flows to each side of the EMCal. A total of 64
3082 cooling loops will be used to insure proper balancing for the removal of heat in throughout
3083 the system.

3084 ### 6.5.1 Cooling Plant

3085 The chillers for the EMCal will be located some 125 feet away from the detector. Indepen-
3086 dent lines and chillers will be installed for both manifold control boxes (North and South).
3087 This will be run to allow either side of the EMCal to be operated independently of the
3088 other. In addition, a third chiller will be plumbed into the system to be used as a back-up
3089 and ready to be switched over in a moments notice. Since the detector will be located in
3090 an area with limited accessibility, active components inside the interaction area must be
3091 reduced. In addition, the filling, bleeding and draining operations must be performed
3092 remotely.

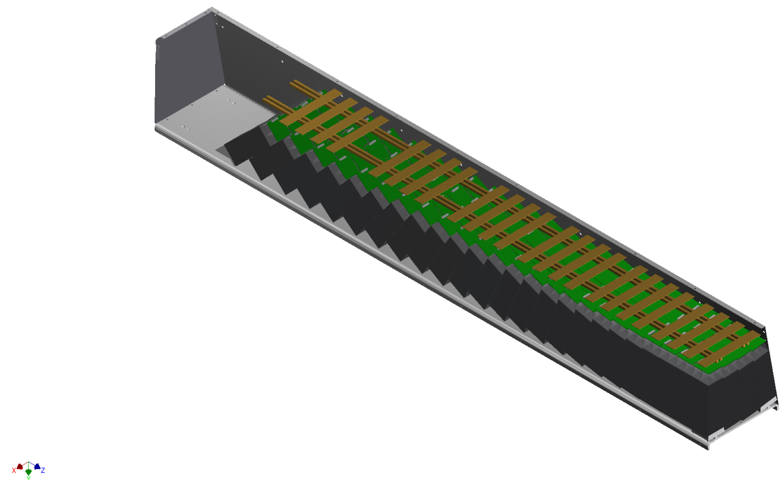

Figure 6.16: Conceptual design of the cooling plates and channels for an EMCal Sector. Connections to the cooling supply lines are made at the high η end of the EMCal Sector.

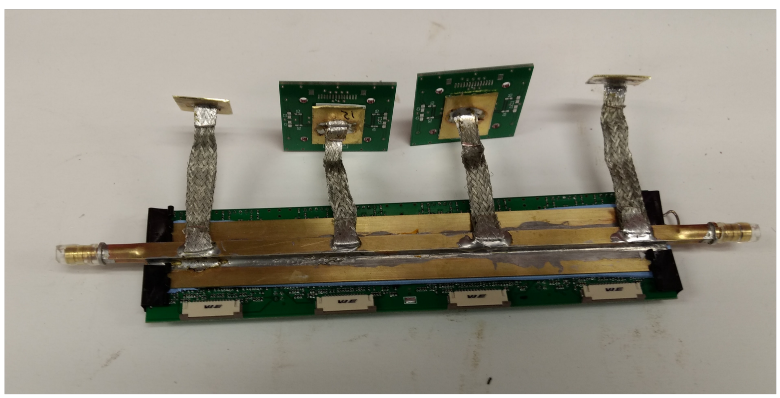

Figure 6.17: Prototype cooling plates for the EMCal SiPM Daughter Boards used for proof of principle. Design concept is to use a thermal connector to simplify installation.

6.5.2 Monitoring and Safety System

Each cooling loop will have remote sensors installed so that health of the system can be monitored. The flow, temperature and pressure of the supply and return of each control box will be recorded and alarmed in case of change for normal operation parameters. The low voltage and bias voltage of the EMCal will be interlocked to this monitoring to prevent equipment damage in case of cooling system failure. Active components in the interaction area must be kept to a minimum for reduce the risk of failure. In addition, only robust industrial components should be selected for inaccessible components. Water trace monitors should be installed in several locations to monitor for potential leaks during times of inaccessibility.

6.6 Radiation Tolerance

6.6.1 Neutron Radiation Effects

Silicon photo-multipliers have been found to be susceptible to damage from neutron radiation. Matsumura et.al. as part of the T2K collaboration found that exposure to protons resulted in an increase in the device leakage current, increased noise, and reduced single photoelectron resolution [148]. Qiang et.al. of the GlueX experiment has also measured increased leakage current after neutron irradiation [149]. Musienko et.al. of the CMS HB/HE Calorimeter Upgrade also studied radiation damage and worked with manufacturers to develop more radiation-hard SiPMs [150]. Simulations to estimate neutron fluences in the sPHENIX IR based on studies of the current STAR and PHENIX IRs at RHIC [151] suggest that the expected neutron fluence is approximately 2×10^{10} n/cm^2 per Run year. Based on the measurements of increase in leakage current due to neutron damage and the expected neutron rates in the sPHENIX interaction region and number of studies on the impact to SiPM performance in context of the sPHENIX calorimeter requirements have been carried out.

Studies of SiPMs were conducted in the current PHENIX IR during Run 14 and Run 15 to observe the effects of neutron radiation on a sample SiPMs of various pixel size, in the approximate sPHENIX environment. Figure 6.18 shows leakage currents measured from different Hamamatsu devices during Run 15 as a function of fluence. Part of this study done in the PHENIX IR during Run 15 was to investigate whether thermal neutrons were causing some of the damage to the SiPMs. Two groups of identical devices, positioned at the same location in the IR, were compared; 2 SiPMs were placed inside a Gadolinium-shielded box to eliminate thermal neutrons, the other 2 SiPMs were left un-shielded. Both groups of SiPMs showed a similar increase in leakage current. There was no obvious difference in the damage to the 2 groups based on the leakage current measurements, suggesting that the observed damage was not caused by thermal neutrons. The data for these devices is included in Figure 6.18.

As a follow-up to the PHENIX IR measurements, with a more controlled, neutron source, we irradiated additional SiPMs at the BNL Solid State Physics Irradiation Facility. A deuterium-tritium neutron source was used to generate 14 MeV neutrons. We exposed

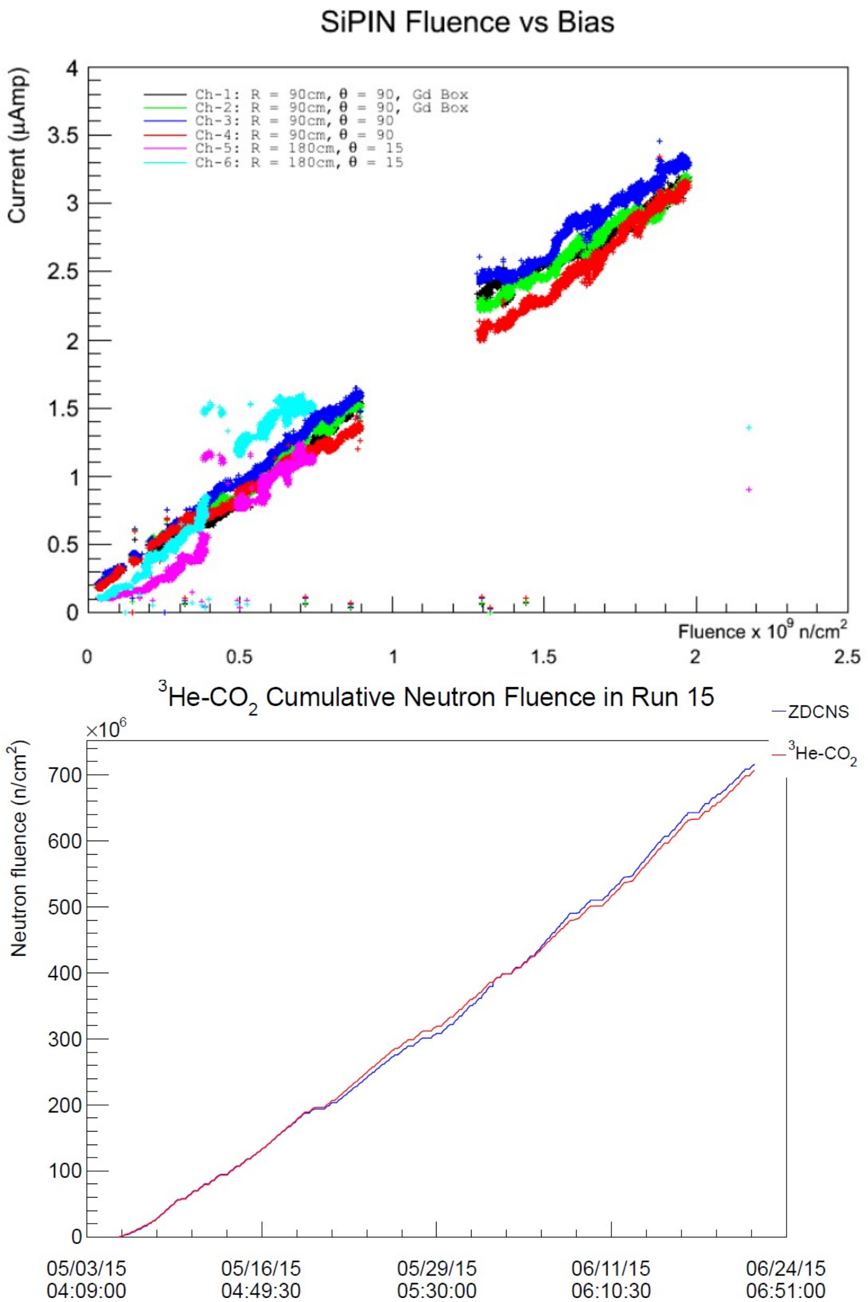

Figure 6.18: SiPMs in the PHENIX IR during Run 15 p-p running. The devices – Hamamatsu S12572-025P, -015P, and -010P all showed a steady increase in leakage current with cumulative neutron fluence during Run 15.

the devices to neutrons at a flux rate of $10^5 \mathrm{n/cm^2}$. The SiPMs were characterized before and after irradiation. Figure 6.19 shows a plot of the increasing leakage current versus exposure time for the SiPMs tested.

Two additional studies have been done to understand the effects of neutron irradiation

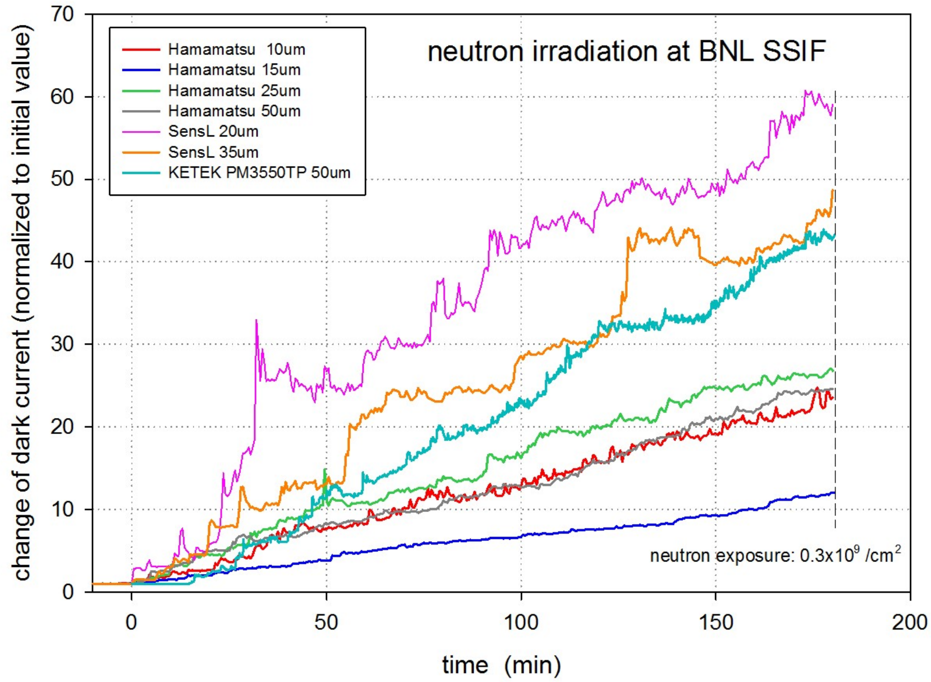

Figure 6.19: Various SiPMs studied at BNL SSGRIF facility. Increasing leakage current vs time during neutron exposure.

on SiPM devices using neutron sources at National Laboratories. In the first, SiPMs were exposed to neutron fluences at the University of Indiana Low Energy Neutron Source (LENS) facility, equivalent to about 2 orders of magnitude higher than what is anticipate over their sPHENIX lifetime at RHIC. These results are shown in Figure 6.20. In the second test, Hamamatsu SiPMs were irradiated at the Los Alamos LANSCE facility to the approximate fluences expected over the expected lifetime in sPHENIX (about $7 \times 10^{10}\,\mathrm{n/cm^2}$). The leakage current verses V_{bias} curves for the devices before and after irradiation are shown in Figure 6.21. The S12572-015P shows an increase from 50nA to 250μA at its operating voltage.

In summary the following radiation damage studies of SiPMs have been done:

- PHENIX IR RUN14 (200 GeV Au-Au, h-Au), 2 Hamamatsu -025P SIPMs-about 3 weeks of beam running time.
- PHENIX IR RUN15 (200 GeV p-p, p-Au, p-Al) 30 Hamamatsu -010P, -015P, -025P SIPMs - about 8 weeks of beam running time.
- Neutron generator irradiation studies at BNL SSGRIF SiPMs from Hamamatsu, SensL, AdvanSiD, Excelitas, and KETEK of various μ-pixel sizes cumulative exposures to $10^9\,\mathrm{n/cm^2}$.

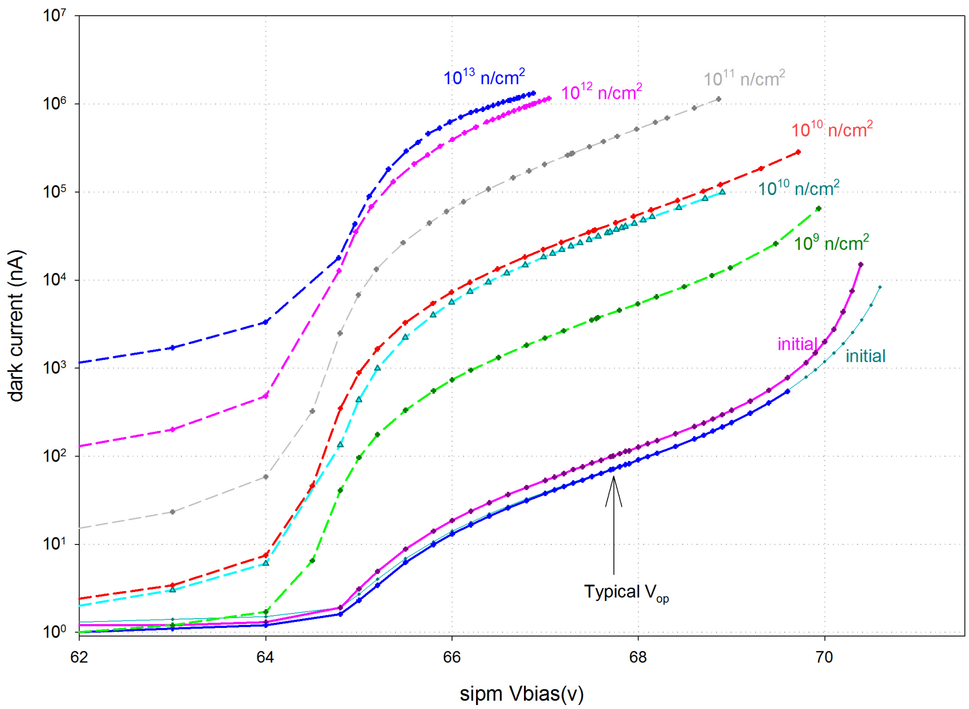

Figure 6.20: Neutron damage in Hamamatsu MPPCs exposed at Indiana Univ LENS facility

- Neutron Irradiation studies at Indiana University LENS Facility Hamamatsu -025P MPPCs cumulative exposures up to 10^{13} n/cm^2.

- Neutron Irradiation studies at Los Alamos (LANSCE) - Hamamatsu MPPCs of various μ-pixel size -Cumulative exposures to about $7x10^{10}$ n/cm^2.

The increase in leakage current due to neutron damage poses a technical challenge for maintaining a constant gain, however, the gain stabilization circuit as described in Section 6.2.4 is designed to compensate for the increased leakage current. While the increase in the leakage current will limit the ability to observe single photo-electron peaks, the leakage current increases that are expected in 3 years of sPHENIX running will not significantly impact the signals that are of interest for sPHENIX, As part of the on going R&D effort, studies will continue to understand the impact of the neutron damage in context of the sPHENIX requirements.

In addition to the effects of neutron damage to the SiPMs, there the also the possibility of damage to the electronics components due to ionizing radiation. During the past several runs of PHENIX, the radiation levels at several locations in PHENIX interaction region that correspond the approximate locations of where the front end electronics will be located has been measured. The total ionizing dosage (TID) measured per run is dependent on the beam species and energies, but typical values range from 2 kRad to 10 kRad per run with the highest dosage coming during the 510 GeV p+p running periods. While

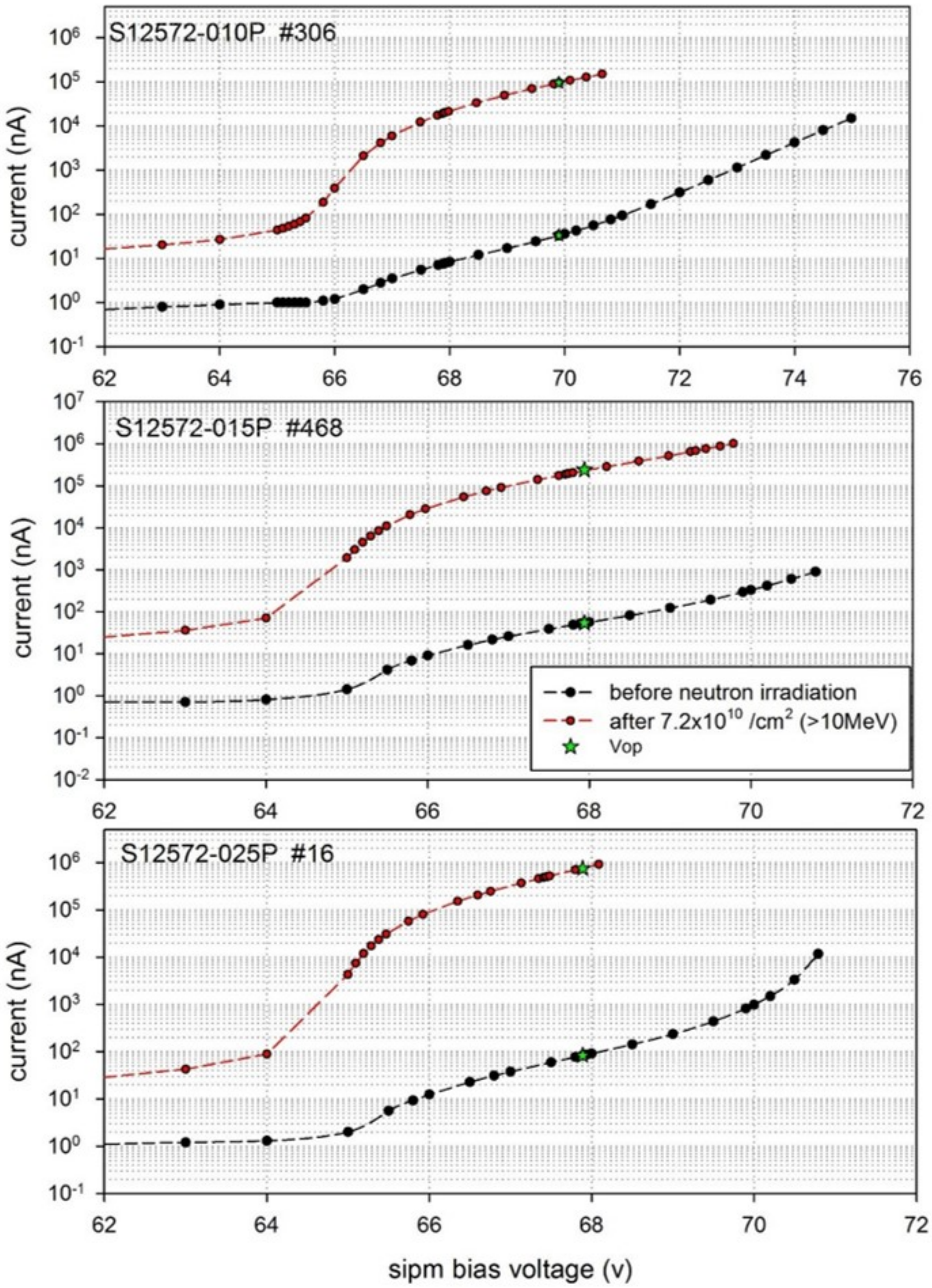

Figure 6.21: Neutron damage in Hamamatsu MPPCs exposed at Los Alamos LANSCE facility

3173 these dosages are several orders of magnitude lower then what is experienced at the LHC
3174 experiments, it is still necessary to consider the effects of radiation damage on the front
3175 end components. The three areas of concern are the analog devices (amplifiers, DACs and
3176 ADCs), the voltage regulators and the CPLD used for temperature compensation, gain

corrections and monitoring. For the analog components and regulators, when possible, devices certified as radiation tolerant for CERN LHC applications will be chosen. In cases where devices can not be identified that have been LHC certified, testing will be done to evaluate their radiation tolerance and the impact of failure due to irradiation.

In the reference design, the Xilinx®CoolRunner-II™ CPLD technology has been chosen. This device has been tested for radiation effects up to an integrated TID of 22 kRad [152]. There were no Single Event Errors (SEE) observed in the flash memory, allowing the device to be recovered at any time by powering device off and back on. The SRAM cells are sensitive to protons with energies greater then 15 MeV with a MTBF of 11 days in the worst case. The actual MTBF in real applications will be higher since only a small fraction of the Single Event Upsets (SEU) will generate a functional error.

Chapter 7

Minimum Bias Trigger Detector

The sPHENIX Minimum Bias Trigger Detector (MBD) is responsible for providing the primary Level-1 trigger for heavy-ion collisions. The trigger should have good efficiency for hadronic collisions and a z-vertex resolution of a few cm, while minimizing background triggers. The z-vertex measurement is necessary to select for collisions within $|z| < \pm 10$ cm, which is the nominal region which the sPHENIX silicon tracking system is designed to cover. The PHENIX Beam-beam Counters (BBC) served very successfully as the MBD for PHENIX, and sPHENIX plans to pursue reusing the BBC detector. The BBCs operated very successfully for 16 years in PHENIX, and with the long experience of its operation, and extensive understanding of its maintenance, cooling, and calibration needs, it serves as an ideal detector for the MBD in sPHENIX.

7.1 Reuse of the PHENIX BBC in sPHENIX

The PHENIX BBCs consists of two identical sets of 64 counters installed on both sides of the collision point along the beam axis, one on the North side and the other on the South side [153, 154]. Each counter is composed of one-inch diameter mesh-dynode photomultiplier tubes (Hamamatsu R6178) equipped with 3 cm thick quartz on the head of the PMT as a Cherenkov radiator (see fig. 7.1). Quartz is chosen as the radiator since a radiation hard design is needed for the BBC, which sits close to the beam-pipe in the forward regions where radiations levels are among the highest in PHENIX. Since the PMTs are inherently tolerant to radiation, the BBC system is radiation hard. Over 16 years of running, no significant degradation of the BBC performance has been noticed.

In PHENIX the BBCs were placed 144 cm from the center of the interaction diamond, just around the beam pipe, where the magnetic field was about 0.3T. The inner and outer edges of the BBC are at radii of 5 and 15 cm, respectively, and corresponds to a pseudorapidity range from 3.0 to 3.9, with coverage over the full azimuth. While the mesh-dynode PMTs are designed to operate in moderate magnetic fields, the field strength in sPHENIX will

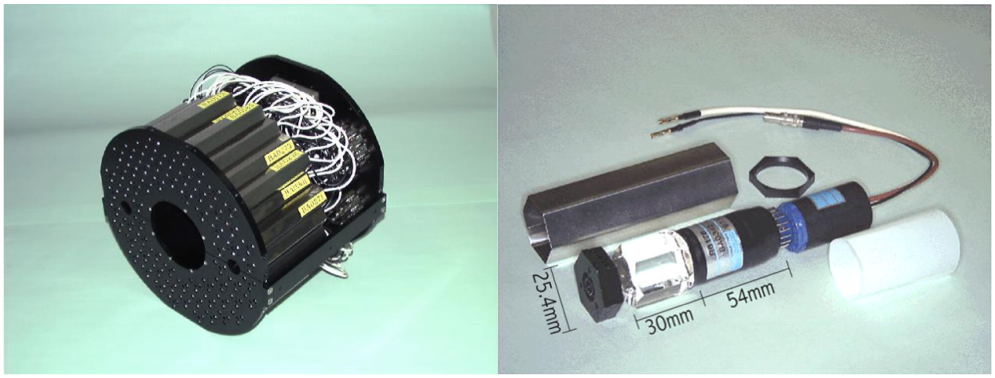

Figure 7.1: (left) The BBC array mounted on the BBC mechanical frame. (right) The individual bbc counter module.

be much higher at $|z| = 144$ cm than it was in PHENIX. Thus, the BBC's will have to be moved in sPHENIX to a z location where the effect on the magnetic field will be tolerable to the BBC PMTs.

Table 7.1 shows the pseudorapidity coverage and longitudinal magnetic fields for different z-positions in sPHENIX. The min-bias efficiencies in the table were evaluated from PYTHIA6 and Hijing Monte Carlo studies. At $z = 144$ cm, the field is 1.11T, which would result in 2 orders of magnitude lower gain in the PMT. Thus, the BBCs can only reliably operate at $|z| > 250$ cm, where the fields are roughly similar to what it operated under in PHENIX. Here, the PMT gains are reduced by less than a factor of 2, which can be compensated by running at voltages of 100-200 V higher. Note that since the BBCs already were designed to operate in moderate magnetic fields, the mechanical frame and everything connected to the BBC are already made of non-magnetic materials, so the BBC housing can be re-used.

z (cm)	η_{min}	η_{max}	B_Z (T)	PMT Rel. Gain	Au+Au MB Eff (%)	p+p MB Eff (%)
144	3.0	3.9	1.11	0.01	90	39
200	3.33	4.23	0.75	0.15	89	36
250	3.56	4.45	0.50	0.5	88	34
300	3.74	4.63	0.32	0.9	87	32

Table 7.1: Parameters for the MBD at different z-vertex locations. The gains are taken from the Hamamatsu R5505 datasheet (and verified in the lab). The trigger efficiency is determined from HIJING and PYTHIA6 Monte Carlo for 200 GeV Au+Au and p+p events.

The PMT gain as a function of magnetic field is taken from the Hamamatsu R5505 datasheet, which is a similar PMT to the R6178 used in the BBCs. The R6178 was never widely adopted and the datasheet is not publicly available. Howver, the BBC PMTs were tested in fields of 0.3T before installation in PHENIX and the results are consistent with the datasheet for the R5505. Also, a spare BBC PMT was tested in the dipole magnet facility in BNL's

Instrumentation Dept., and a gain curve was mapped out up to 0.5T. The gain curve was found to be consistent with the R5505 datasheet.

Estimates for the efficiencies for triggering are given in the last two columns of table 7.1. The efficiencies were estimated from Hijing events for 200 GeV Au+Au, and Pythia 6.4.28 events for 200 GeV p+p. A trigger is accepted when at least two charged particles are in the acceptance of both BBCs for Au+Au collisions, while in p+p the requirement is one charged particle in each arm. The efficiency percentages for the $z = 144$ cm case are consistent within a few percent of what has been observed in PHENIX, with the difference due to the fact that conversions of photons in the beam-pipe and other upstream material can boost the efficiency slightly. The efficiency for Au+Au collisions drops by only 3% relative to what has been seen in PHENIX even if moving the BBCs out to $z = 300$ cm. This is expected since the multiplicity drop is not very large when going to the more forward pseudorapidity, and also because in Au+Au collisions the efficiency is largely determined by the multiplicity fluctuations in only the most peripheral events. Starting from mid-peripheral collisions enough particles are created that the efficiency is 100%.

The situation for p+p collisions is a bit worse, since the multiplicities are much lower. Here the BBC efficiency will be $\sim$20% lower than the PHENIX case. However, in p+p the MB efficiency is much less important since a minimum bias p+p event are dominated by largely uninteresting soft collision events. The trigger rates for min-bias p+p events were often prescaled by a factor of 10^4 or more in PHENIX. Thus, the location that optimizes min-bias efficiency while still allowing for operation of the BBC in sPHENIX is at $|z| = 250$ cm.

The BBCs are designed to handle the maximum expected multiplicity in PHENIX, which is about 30 particles, and thus there are no questions about it's performance in this regard to sPHENIX. This is important when using the BBC as a reaction-plane detector, which uses the multiplicity of particles as a function of position to determine the event-plane of the heavy ion collision.

7.2 MBD FEE Upgrade

While the existing BBC FEMs are available and could work for the MBD readout in sPHENIX, it would be far preferable to upgrade to modern electronics. The BBC FEMs rely on many legacy Trigger and DAQ systems, such as the Arcnet slow control system, the FE2 DCM, the JSEB-I, and the BBC Local Level1 trigger system, which are now 18 years old and would require extra manpower to maintain.

Fortunately, the BBCs can be read out with one modification to the proposed sPHENIX Front-End Electronics system for the calorimeters. A discriminator/shaper (D/S) board needs to be developed, as shown in Fig. 7.2. The discriminator/shaper board is needed to shape the 2 ns wide signals from the BBC PMTs so that it can be digitized at the 16.7 ns sampling time of the sPHENIX digitizers. In addition, the raw signal will be split, with the split signal being used to provide a fast time measurement of better than 120 ps that is needed to make the vertex measurement for the minimum bias trigger.

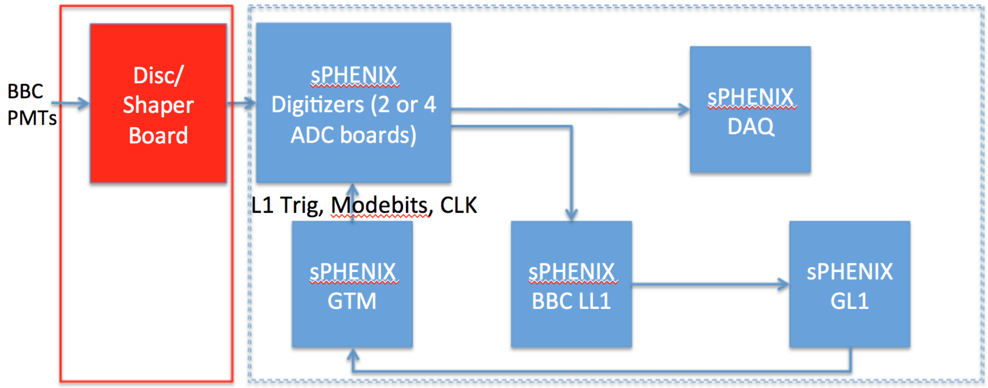

Figure 7.2: Readout diagram for the sPHENIX MBD. The items in the right box are common to the rest of the sPHENIX Calorimeter FEE and DAQ.

To accomplish the timing measurement, the D/S board will discriminate the BBC signal, and generate a 1 volt square pulse (less than one RHIC clock wide) to the sPHENIX digitizers. The time of arrival can be extracted from this discriminator pulse. The time resolution of the sPHENIX digitizers have been measured to be better than 13 ps by using a passively split signal similar to the discriminator pulse, and then comparing the time measurement between the two split pulses. The D/S board is under development and will be tested for its contribution to the overall time resolution.

As a backup solution, a time-to-analog converter (TAC) could be used to generate a linearly rising analog voltage until it is stopped by discrimination from a signal. This amplitude is then digitized by the sPHENIX digitizer ADC and represents the time of arrival. The TAC is reset every RHIC clock to provide a time measurement every crossing. At 12 ENOB, the sPHENIX digitizers should be capable of 26 ps/bin.

Whichever scheme is chosen for the discriminator, the sPHENIX digitizers will be able to determine the time of hit on each channel, the amplitude, and whether there was a hit or not using the on-board FPGA. This information, which form the basis of the trigger primitives from the MBD, will be sent each crossing to the MB Level-1 trigger board for further processing, as detailed in section 8.3.1.2.

Chapter 8

Data Acquisition and Trigger

8.1 The Data Acquisition

In this section we detail the architecture of the sPHENIX data acquisition and how to satisfy the requirements to achieve a 15 kHz data accept rate with a livetime greater than 90% in a high-multiplicity environment. The estimates are based on the the RHIC Collider Projections as documented in Ref. [116]. Compared to the luminosity achieved in 2014, we expect an increase of up to about a factor of two of the rates of interaction which take place within a z-vertex range $|z| < 10$ cm for Au+Au collisions at 200 GeV. The $|z| < 10$ cm vertex is inside the coverage of the sPHENIX tracking system. In the case of Au+Au collisions, we expect to record minimum bias triggers mostly (i.e. a simple interaction trigger), and expect to collect in the order of 100 billion events in a typical 22-week running period. There are also selective jet and photon triggers that can sample additional physics from the entire accessible vertex range $|z| < 30$ cm. In p+p and p+A collisions, more selective triggers utilize the EmCal, the HCal, and the tracking system. Select results from simulation studies are given in the sPHENIX proposal [1].

The operation of the DAQ system is governed by the *Global Level-1 Trigger* (GL1) and the *Timing System*, which instructs the front-end electronics to “select” (or accept) the data from a given collision, or not. If accepted, the data are sent up from the front-end and are eventually stored on disk and tape. This operation is commonly referred to as “triggering”.

The GL1 decision to accept the data from a given collision is based on the input from a number of *Local Level-1* systems (LL1), which examine the data from various detector systems and communicate a number of key properties to the GL1. A good example of such a property is the aforementioned collision vertex. We will select collisions that take place very close ($\pm$10 cm) to the center of the sPHENIX detector, and discard most of the others. After taking the various LL1 inputs, the overall “busy” state of the DAQ system, and several other factors into account, the GL1 either accepts or rejects the data of the collision in question. It takes this decision for every beam crossing.

Once a collision is accepted, the GL1 instructs the Timing System to inform the Front-end of this fact. The Timing Systems then sends this information in a detector-specific way and format (which varies from system to system), and the front-end then sends the data.

The front-end electronics operates in lockstep with the RHIC accelerator clock. The current design sets the basic clock frequency to 6 times the beam crossing rate, at about 55MHz. The Timing System gets its name from the fact that it distributes this clock to the various Front-End Modules (FEMs) and other components of the DAQ. The detector-specific aspects will include the adjustment of the clock phases to compensate for different propagation times, and the selection of the right beam crossing. As an example, the calorimeter electronics digitizes the data from each beam crossing and retains 64 such data sets. The timing system then instructs the front-end to go back a certain number of crossings and select the data from the right collision. The required information can vary from system to system.

This chapter is structured in the following way. We will first detail the the core Data Acquisition system, the Local Level 1 system, and then the GL1 and Timing System.

8.2 The Core DAQ System

Table 8.1 shows a breakdown of the expected data sizes per subsystem. The estimate for the readout of the calorimeters is based on 16 samples from each channel, and assumes an occupancy of 25% for the EmCal (estimated from HIJING Monte Carlo and plausible expectations for pedestal noise), and 100% for the HCal and the BBC. The estimate for the VTX-pixels, the only detector that has been used previously, is derived from data from the PHENIX Run 14, where the pixel configuration consisted of two layers at 25 and 50 mm radius, respectively, with 10 and 20 ladders. In sPHENIX, the pixel layers will be at 24 and 44 mm, with a total number of 36 ladders. The average data size of approximately 42 kbytes per minimum bias event in Run 14 200 GeV Au+Au is scaled by 36/30 to account for the increased number of ladders to achieve full azimuthal coverage, and then by 1.1 to account for the smaller radial positions of the layers.

Table 8.1: Counts of channels, fibers, and readout components for select subsystems from the reference design. The last column is the estimated data size from that subsystem per event in Au+Au collision at 200 GeV. In the case of the VTX, the only subsystem that has been in use previously, the data are from the Au+Au part of the PHENIX Run 14, scaled for full azimuthal coverage and smaller radial positions.

subsystem	channels	occupancy	data size (kbytes)
EmCal	24,576	25%	150
HCal inner	1,536	100%	100
MBD	512	100%	3.5

The architecture is a fully pipelined design, which allows the next event to be triggered without waiting for the previous event to be fully processed. The design allows for a depth of 4 such events to be buffered in front end modules before transmission. This multi-event buffering is the key concept to achieve the design event rate of 15 kHz while preserving livetime.

The different detector systems use two conceptually very different readout strategies. The calorimeters, the minimum bias detector, and the Intermediate Tracker use existing DAQ hardware. Those system are read out in a "triggered" fashion, that is, the front-end electronics generates data only when it receives a trigger. The readout of these systems closely follows the design of the PHENIX DAQ [155].

Conversely, the front-end electronics for the TPC and the future MAPS detector will read data in a *continuous*, or *streaming* mode. It will sample and send up the sampled waveform data continuously. Subsequent processing will select the parts of the waveform that correlate with triggered events.

The two readout modes differ in the way the data are read in the front-end. In the case of the triggered detector systems, the Front-End Module (FEM) digitizes the data from the connected detector channels. The data selected by the triggered system flow from the FEMs to Data Collection Modules (DCM's). The second generation of DCMs, the DCM2, was developed for the PHENIX silicon vertex detectors and runs detector-specific FPGA code to zero-suppress and package the data. This provides the freedom to change the data format as necessary by loading a new version of the FPGA code. A DCM2 has inputs for 8 data fibers.

A group of DCM2s interface with commodity computers called Sub-Event Buffers (SEBs) via 1.6 GBit/s serial optical links through a custom PCIe interface card, the JSEB-II. Due to overhead in the data encoding, the effective bandwidth through the fiber is 1.28 GBit/s. This 4-lane PCIe card is capable of sustaining 500 MB/s input into the SEB. This bandwidth is needed to achieve the envisioned event rate of about 15 kHz.

The TPC data are sampled by front-end cards that interface to a high-end FPGA PCI-Express card, the *Data Aggregation Module* (DAM), which provides up to 48 fiber inputs. The processing of the streaming data will be performed by a combination of the FPGAs and the CPUs of the servers that host these readout cards. Those *Event Buffering and Data Compressor* machines (EBDC) have functionality similar to the Sub-Event Buffers of the triggered systems in that they hold the data from the respective subset of connected readout channels. This is shown in the top part of Fig. 8.2, which shows the samples waveform of a given TPC channel. In the second part of Fig. 8.2 we show regions of interest derived from samples above a threshold. Those regions are then correlated with events that have been triggered for readout with the other detectors, and only those regions are kept.

In both cases, those *sub-events* still need to be combined into a full event that contains all the data from one collision collected from the SEBs and EBDCs.

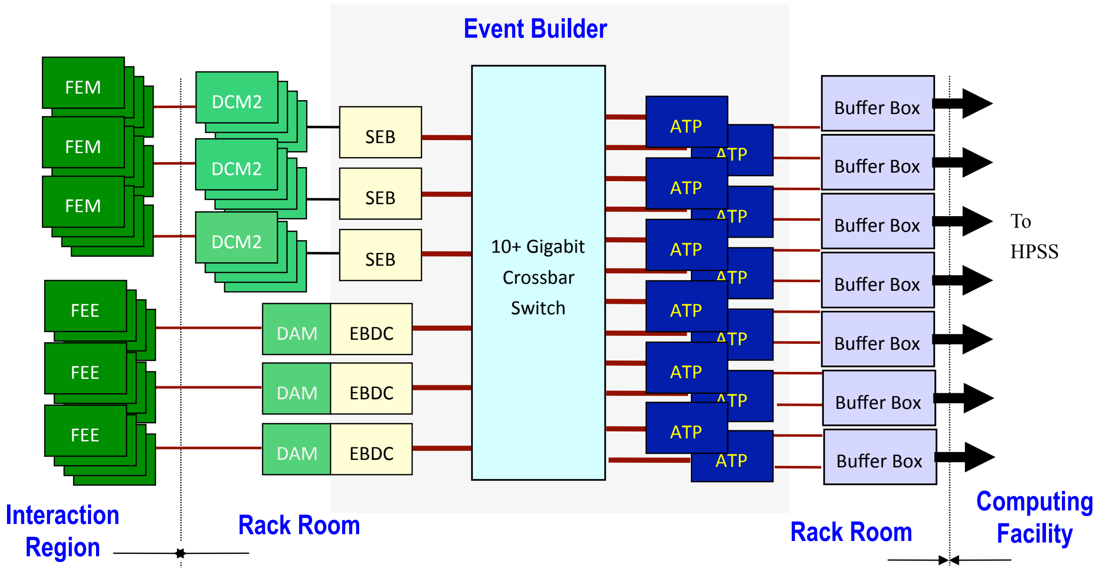

Figure 8.1: Overview of the event builder design. The data are digitized in the Front-End Modules and zero-suppressed and packaged in the Data Collection Modules. The data from a given collision are initially distributed over many SEBs and EBDCs. The data from one collision are collected in the ATP's, which sees the full complement of data of that collision for the first time. The ATP compresses the data before transmitting them to the *Buffer Boxes*, from where the data are transferred to a long-term storage system.

This task is performed by the Event Builder, which consists entirely of commodity PCs running Linux. The SEBs and EBDCs are connected to a high-end network switch, which is central to the Event Builder. It must be able to sustain the aggregated bandwidth in a non-blocking fashion. Non-blocking means that data can flow at line speeds between two arbitrary ports, while at the same time line-speed data is being transferred between any other two ports. Network equipment is subject to rapid improvements and price drops. While viable options do currently exist, we expect that a wide selection of commodity-priced network switches will be available at commissioning time.

Also connected to the switch are a number of *Assembly and Trigger Processors* (ATPs). Through the network switch, each ATP receives the sub-events from a given collision and combines them into a fully assembled event.

8.2.1 TPC Readout

The front-end electronics of the TPC is detailed in chapter 3. The DAQ obtains the data and meta-information from about 20 EBDC machines (fig. 8.1. Those provide the TPC data event-by-event to the Event Builder. The streaming-mode readout relies on a significant data reduction in the DAM and the EBDC by correlating the TPC waveforms with triggered

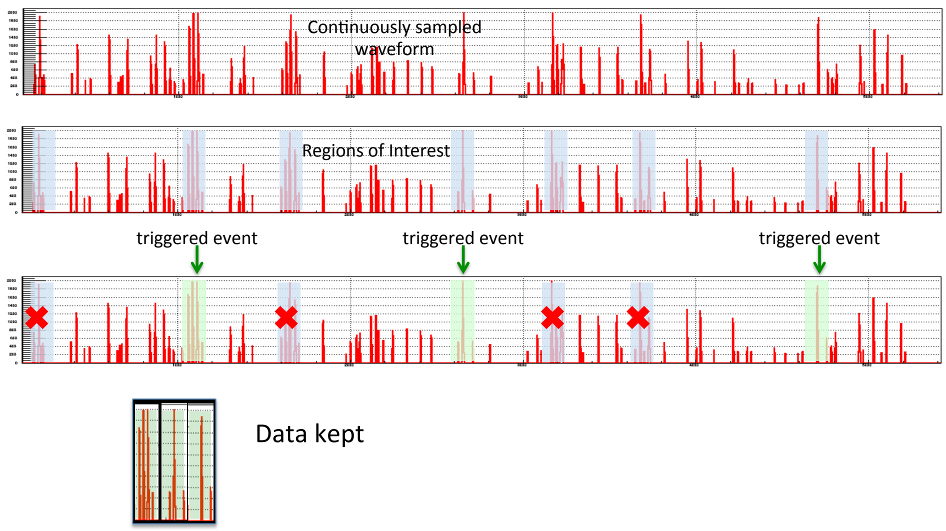

Figure 8.2: A conceptual overview of the TPC "streaming" readout. The front-end electronics continuously samples the waveforms. A processing system selects "regions of interest", indicated in this example as amplitudes above a threshold. Further processing selects those regions that correlate with triggered events.

events and subsequent clustering. However, the clustering under full load has not yet been demonstrated, and we are budgeting the data volume from the TPC to be up to 80 Gbit/s. We expect the clustering to reduce the data volume by a factor of two.

8.2.2 Calorimeter Readout

The current layout for the EmCal, the largest source of calorimeter data, is to read out 3 digitizers (3×64 channels) through one data fiber, resulting in a total number of 128 data fibers. With 8 inputs per DCM2 we need 16 DCM2s. These 16 DCM2s would connect in groups of 4 (a *DCM group*) to 4 SEBs. This is similar in scope to the PHENIX silicon detectors.

Table 8.2 breaks down the counts of the various components by subsystem.

There is freedom to configure the mapping of DCM2s to SEBs differently, and vary the number of DCM2s that send their data to a given SEB. In this way, we could obtain more bandwidth by using more SEBs which connect to fewer DCM2s each, or save SEBs by

Table 8.2: Counts of channels, fibers, and readout components for the subsystems from the reference design.

subsystem	channels	fibers	DCM2s	SEBs
EmCal	24,576	128	16	4
HCal inner	1,536	12	2	2
HCal outer	1,536	12	2	2
MBD	256	2	1/2	1

connecting more DCM2s to fewer SEBs.

8.2.3 Data Compression

While the number of SEBs and EBDCs is determined by the topology of the front-end and fixed for a given configuration, the number of ATPs is not fixed and can be adjusted to match the load. We use the ATPs to perform a late-stage, distributed compression of the data before they are sent to the so-called *Buffer Boxes* that receive the data from the ATPs and provide local storage capacity. The compression has traditionally yielded savings of 45% – 100GB of data shrink, on average, to 65GB.

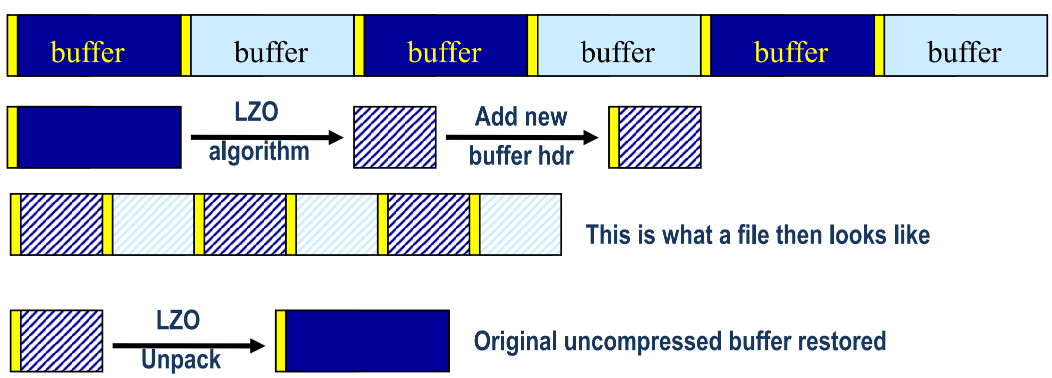

Figure 8.3: The principle of the raw data compression. The event data are organized in so-called buffers typically holding 50-100 events. Instead of sending this buffer to storage, the ATP compresses the entire buffer, and adds a new buffer header to the binary blob of compressed data, which is then sent to storage. On readback, the compressed payload is restored into the original buffer, which is passed on to the next software layer as if it had been read from storage this way. The compression functionality is entirely confined to the lowest I/O layers of the software.

Fig. 8.3 shows the principle of the late-stage compression. Naively one would think that we use existing tools (such as *gzip*) to compress a file on disk. However, this would require an uncompressed file to be written in the first place, thereby negating most of the speed advances in both the network and storage system. In addition, this file would need to be unpacked in its uncompressed state to disk on readback, again negating most benefits of the compression. What is needed is a compressed data format that can be generated in-memory and be written out, and be read back directly. This is accomplished through the concept of a *buffer structure*, which is strictly a storage-technology feature and generally invisible to the other software layers. A *PHENIX Raw Data File* (PRDF) is simply a concatenation of such self-contained buffer structures. At its core, the buffer structure is a means to improve the data throughput through network links, which are generally more efficient for larger data quantities due to the lower ratio of network overhead to payload. While a buffer with data from just one event is valid, the sizes are chosen such that a buffer contains about 50 to 100 events. This buffer structure also facilitates the compression through the concept of a compressed buffer.

The ATP creates a buffer that could be sent to the Buffer Boxes and written out as-is. The header of such a buffer, indicated in yellow in fig. 8.3, holds the length of the buffer and other meta-information, and in addition indicates that the payload contains actual event data. Rather than sending this buffer to the buffer boxes, the ATP uses the LZO [156] algorithm to compress the entire buffer in a loss-less manner. The resulting binary blob of data receives a new buffer header, this time indicating that the payload is an entire compressed buffer. Due to the presence of the header, the result is again a legitimate buffer structure that can be sent to the buffer boxes and written to disk just like the original, uncompressed buffer.

On readback, the I/O software layer examines the buffer header and learns that the payload is a compressed buffer. It reverses the compression and so restores the original buffer, which is then passed on to the next software layer as if this buffer had been read from disk in this form. In this way, the entire compression functionality is confined to the lowest I/O layer and transparent to user code.

The Buffer Boxes are designed to limit the number of concurrently written output files to a reasonably small value by receiving the compressed buffers from the ATPs and writing them to disk. They provide about 80 hours of local storage capacity, which will help us to ride out short-term outages of the tape storage system without the need to stop taking data. In addition, the local buffering levels the changing data rates of the experiment and allows us to transfer the *average*, rather than the peak, data rate of the experiment to the long-term HPSS tape storage system located at the RHIC computing facility. This improves the utilization of the tape drives, and in general reduces the load on the network fibers and switches. The already transferred files can stay on disk for 2 or 3 days and are available to a local computing cluster for online monitoring and calibration purposes. Especially the calibration processes typically require access to all files of a given run, and we take advantage of the availability of the files on the buffer boxes. By the time the oldest data files need to be deleted from the local storage system, the calibration constants required for reconstruction will be available.

8.2.4 Data Acquisition Performance

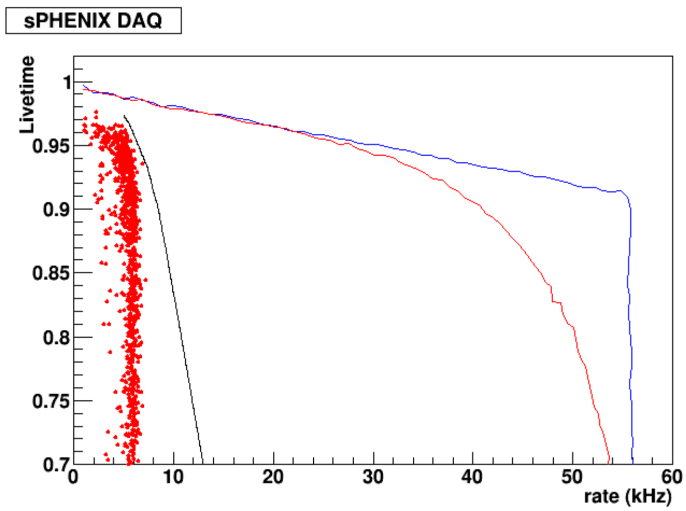

Figure 8.4: Livetime as a function of DAQ accepted event rate. The points are measurements from Run 14 Au+Au running in PHENIX, the black line is the measured performance from one older PHENIX system, the red line shows the simulated performance with 4 event buffering with the sPHENIX calorimeter ADC system, and the blue line shows the expected behavior with 100 events buffered in the front end.

The sPHENIX data acquisition system eliminates the slower DCM I modules, and also uses the TI TLK2501 optical links to transmit data from the front end modules to the DCM II at 1.28 Gbps. These changes, along with 4 event buffering in the front end modules, result in a predicted livetime as a function of DAQ rate following the solid red line in Figure 8.4 showing good livetime at 15 kHz.

8.3 Trigger

The goal of the sPHENIX trigger system is to sample the key physics from the delivered luminosity and reduce the selected event rate below the specified 15 kHz sPHENIX data acquisition bandwidth. This goal is achieved with a Level-1 trigger system providing decisions within a specified 4-5 microsecond latency during which detectors are able to buffer data output.

Tables 8.3, 8.4 and 8.5 show the Collider-Accelerator Detector group's projections for luminosities delivered and peak collision rates for Au+Au, p+p, and p+Au at 200 GeV, respectively. The sPHENIX schedule includes five years of physics running labeled Year-1 through Year-5. The Level-1 triggers need to be able to handle the highest projected rates and so we show the maximum projected values at the peak (beginning) of the store. These quantities are shown for all collisions and for the fraction of collisions – denoted f_{z10} – which lie within the restricted $|z| < 10$ cm range over which sPHENIX has optimal tracking coverage for pseudorapidity $|\eta| < 1.0$.

Table 8.3: Summary of C-AD key values for Au+Au at 200 GeV running.

Mode	nb^{-1}/wk [min]	nb^{-1}/wk [max]	f_{z10} [min]	f_{z10} [max]	ave/peak	peak rate [max]	peak rate $\times f_{z10}$ [max]
Au+Au (Year-1)	3	4.75	0.19	0.3	0.6	1.5E5	4.5E4
Au+Au (Year-3)	3	7.02	0.3	0.3	0.6	2.2E5	6.6E4
Au+Au (Year-5)	3	7.51	0.3	0.3	0.6	2.4E5	7.1E4

Table 8.4: Summary of C-AD key values for $p+p$ at 200 GeV running.

Mode	pb^{-1}/wk [min]	pb^{-1}/wk [max]	f_{z10} [min]	f_{z10} [max]	ave/peak	peak rate [max]	peak rate $\times f_{z10}$ [max]
p+p (Year-2)	25	64	0.16	0.19	0.6	1.2E7	2.4E6
p+p (Year-4)	25	64	0.19	0.19	0.6	1.2E7	2.4E6

Table 8.5: Summary of C-AD key values for p+Au at 200 GeV running.

Mode	pb^{-1}/wk [min]	pb^{-1}/wk [max]	f_{z10} [min]	f_{z10} [max]	ave/peak	peak rate [max]	peak rate $\times f_{z10}$ [max]
p+Au (Year-2)	0.14	0.35	0.17	0.25	0.6	2.8E6	6.9E5

8.3.1 Physics Driven Trigger Requirements

This section details the various physics based trigger requirements. We discuss five types of triggers below: (1) minimum bias trigger, (2) photon trigger, (3) jet trigger, (4) hadron trigger, and (5) Upsilon trigger.

(1) Minimum bias trigger. In the case of Au+Au collisions at 200 GeV, most of the physics is delivered by simply triggering on inelastic collisions - a minimum bias trigger (MBT). We expect to utilize the majority of the 15 kHz bandwidth for recording minimum bias Level-1 triggered events. The key requirements of this MBT are to fire on a large fraction of the 7.2 barn Au+Au inelastic cross section and to provide a selection on collisions with vertex $|z| < 10$ cm. The minimum bias detector (MBD) described in Chapter 7.1, and based on the existing PHENIX Beam-Beam Counter modules, meets these specifications.

In the case of $p+p$ and p+Au at 200 GeV, it is critical to sample the luminosity via more selective Level-1 triggers to ensure high statistics for single high p_T jets, high p_T hadrons, high p_T photons, and Upsilons decaying to dielectrons. From the rates shown in the Tables above, rejection factors of order 5,000-10,000 are needed in $p+p$ collisions at 200 GeV in order for individual Level-1 triggers to be allocated 1-2 kHz of bandwidth. All such Level-1 triggers are based on information from the Electromagnetic and Hadronic calorimeters.

We briefly recap the requirements for calorimetric-based triggering on single jet, single hadron, photon, and Upsilons in $p+p$ and $p+$Au collisions (where they are crucial to complete the scientific mission of sPHENIX). Expected trigger efficiencies and rejection factors are presented below using GEANT4 simulations of $p+p$ collisions in sPHENIX. For the case of $p+$Au collisions, it is expected that achievable trigger efficiencies will be similar to those in $p+p$ collisions. Additionally, the mean number of binary collisions in $p+$Au collisions is $\langle 4.6 \rangle$, thus somewhat lowering the rejection factors at a fixed window energy threshold. However, this decreased rejection is expected to match the data acquisition bandwidth since the peak rate in $p+$Au running is projected to be a factor of 3–5 lower than that in $p+p$ running (see Tables 8.4 and 8.5 above). Full simulations of the expected trigger performance in $p+$Au collisions are expected to confirm this. Furthermore, it is notable that in Au+Au at 200 GeV collisions, a subset of these triggers may still be useful to enhance the minimum bias data sample described above.

(2) Photon trigger. Collision events with a high-p_T photon can be selected by requiring that some amount of energy is deposited into a small set of EMCal towers above threshold. Due to the precise nature of the experimental signature (large amount of electromagnetic energy deposited in a small region), this trigger is likely to achieve large rejections for even modest p_T thresholds while maintaining an excellent efficiency. In $p+p$ collisions, an unprescaled trigger which is efficient for $p_T^\gamma > 10$ GeV photons will be crucial for enabling sPHENIX to collect the necessary comparison data for photon-tagged measurements of (jet and hadron) energy loss in Au+Au collisions, as well as for high-p_T photon production measurements which will serve as a reference for tests of binary-collision scaling in Au+Au collisions. Similarly, a $p_T^\gamma > 10$ GeV photon trigger in $p+$Au collisions would enable measurements of cold nuclear effects on hard process rates and on photon–hadron correlations. In both cases, the trigger could be configured with multiple thresholds, such that auxiliary lower-threshold triggers operated with a prescale could be used to determine the efficiency of the higher-threshold trigger with good efficiency.

Figure 8.5 demonstrates the simulated trigger efficiency curves and rejection factors for such a photon trigger, based on requiring some minimum energy in overlapping 4×4 EMCal tower windows, in GEANT4-simulated $p+p$ events. The simulations show that even a 5 GeV window trigger threshold will achieve a rejection factor of over 10^4.

For potential high-luminosity Au+Au running, a trigger which is efficient for $p_T^\gamma > 10$ GeV photons would utilize the full luminosity which can be delivered by RHIC. In particular, this would have the largest benefit for measurements which do not require the vertex to lie within the narrow 10 cm range, such as photon spectra or photon-jet balance (where the jet is measured purely calorimetrically). Since the effect of the underlying event in Au+Au collisions is small in small-sized windows of EMCal towers, it is likely the trigger could avoid the need for a subtraction or estimation of this background.

(3) Jet trigger. Collision events with a high-p_T jet can be selected by requiring that some amount of energy is deposited into a moderate-sized patch of the EMCal and HCal (a "jet patch" or FullCalo trigger). By using information from both the EMCal and HCal, the

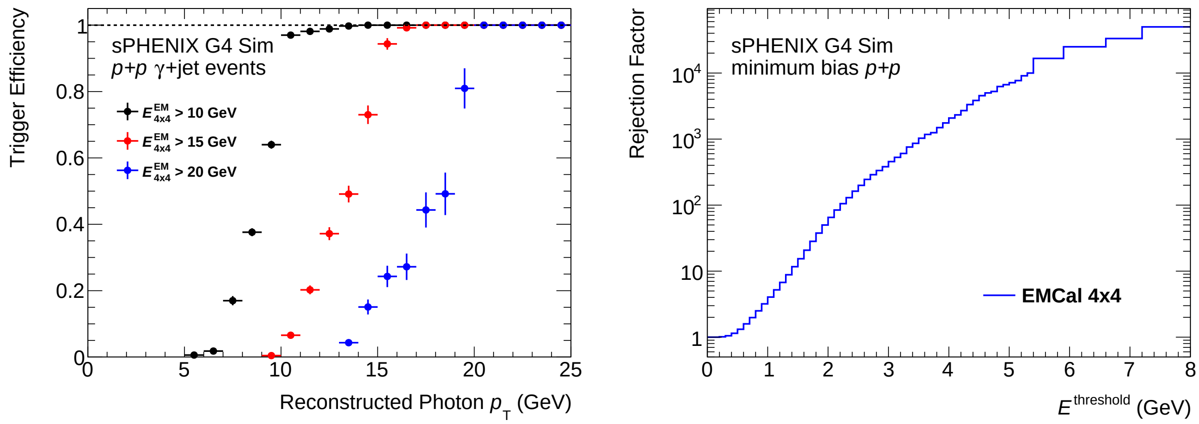

Figure 8.5: *Left:* Trigger efficiency for photons with respect to the reconstructed photon p_T. For this plot, PYTHIA 8 events with the prompt photon switch turned on and $\hat{p}_T > 8$ GeV were used. The efficiency is shown for three different energy thresholds using the EMCal 4x4 trigger. *Right:* Rejection factors in minimum bias p+p collisions for EMCal 4x4 energy thresholds.

trigger can avoid being biased by the fragmentation pattern or flavor of the jet and can operate with a high efficiency. In addition, the trigger could be configured to examine the total energy in different-sized patches (for example square patches which enclose circular jets with radius $R = 0.3$ and $R = 0.4$).

In p+p collisions, a jet patch trigger which is efficient for $p_T > 20$ GeV jets will allow sPHENIX to collect necessary comparison data for inclusive jet, dijet, jet structure, and other jet-based measurements of energy loss in Au+Au collisions. In p+Au collisions, such a trigger would enable the benchmarking of cold nuclear matter effects on jet and hadron production, especially at moderate and large p_T. Given the large collision rates projected for p+p and p+Au data-taking, the jet trigger must be configured to achieve a sufficiently large rejection for minimum bias events, setting a lower limit on the minimum p_T at which the trigger could record events unprescaled. Additionally, the trigger could also be configured with lower p_T thresholds and a finite prescale to provide events which are used to determine the efficiency turn-on curve for the unprescaled, high threshold-p_T jet trigger. The segmentation of the calorimeter available at Level-1 is shown in Figure 8.6.

Figure 8.7 demonstrates the simulated trigger efficiency curves and rejection factors for the FullCalo Jet trigger in GEANT4-simulated p+p events. The simulations show that a 12 GeV window trigger threshold will achieve a rejection factor of over 10^4.

In Au+Au data-taking at high luminosity, a jet trigger could complement the number of high-p_T jet events recorded for offline analysis. This would have a particularly large impact for measurements which do not require a narrow selection on the collision vertex and would, for example, allow sPHENIX to explore the quenching of jets near the kinematic limit and at very large initial virtuality ($\gtrsim$ 60 GeV). However, the presence of the

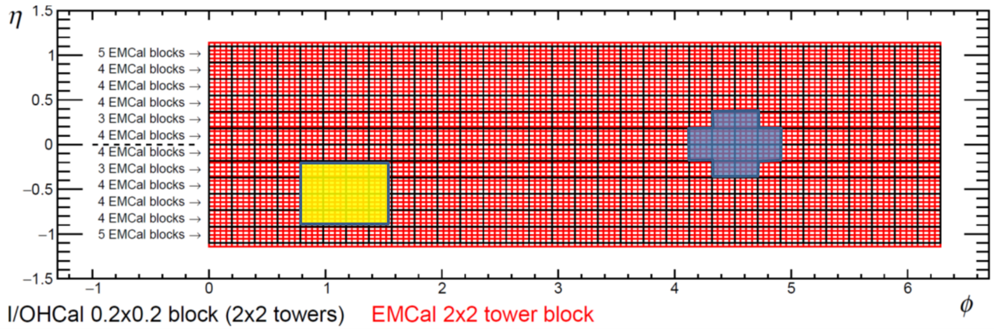

Figure 8.6: Diagram showing the calorimeter segmentation for use in the Level-1 jet patch trigger. There are 384 effective combined calorimeter energies available (in $\Delta\eta \times \Delta\phi = 0.2 \times 0.2$ regions). This grid is comprised of 12 elements in η and 32 elements in ϕ. Shown on top are the default 0.8×0.8 square jet patch region and an alternative with the corner energies removed.

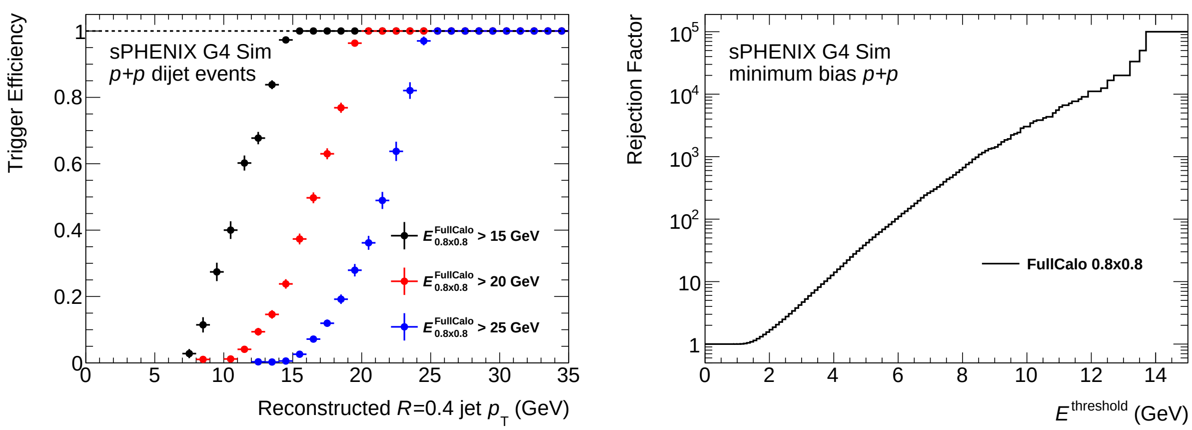

Figure 8.7: *Left:* Trigger efficiency for jets with respect to the (offline) reconstructed anti-k_t $R = 0.4$ jet p_{T}, based on requiring a minimum energy in a $\Delta\eta \times \Delta\phi = 0.8 \times 0.8$ region of the calorimeters. For this plot, PYTHIA 8 events with the hard QCD switch turned on and $\hat{p}_{\mathrm{T}} > 20$ GeV were used. The efficiency is shown for three different window energy thresholds. *Right:* Rejection factors in minimum bias p+p collisions for FullCalo 0.8×0.8 window energy thresholds.

underlying Au+Au event, which fluctuates over a large dynamic range every collision, will reduce the performance of a calorimeter-based jet patch trigger. For best operational efficiency, some estimation and subtraction of the underlying event should be performed at the trigger level. Even after this, localized underlying event fluctuations would reduce the ability of the trigger to reject minimum bias events. While a narrower jet patch area may reduce the per-event rate of such fluctuations (thus allowing a lower unprescaled p_{T} threshold), this may impose a selection bias on the profile of triggered jets. Thus, relative to p+p collisions, these issues limit the minimum p_{T} threshold above which a trigger can select hard-scattering jets with high efficiency while having sufficient rejection for underlying event fluctuations, for example to $p_T > 40$ GeV.

(4) Hadron trigger. In addition to the FullCalo jet trigger above, events containing high-p_T hadrons can be selected by requiring an energy deposit above threshold in a narrower $\Delta\eta \times \Delta\phi$ region of the calorimeters. In p+p and p+Au collisions, such a trigger could enhance the statistics for intermediate-p_T hadrons, extending the p+p and cold nuclear matter references for hadron-based measurements to a lower hadron p_T range than would naturally be selected with a (higher-p_T) jet trigger. In addition, such a trigger could be useful in selecting events with leading hadrons from heavy flavor quark jets: since these hadrons have a higher typical z than light jets, they would not fire the jet trigger until they reach substantially higher hadron p_T. Figure 8.8 demonstrates the simulated trigger efficiency curves for the FullCalo $\Delta\eta \times \Delta\phi = 0.4 \times 0.4$ hadron trigger in GEANT4-simulated p+p events. The simulations show that a 10 GeV window trigger threshold will achieve a rejection factor of over 10^4.

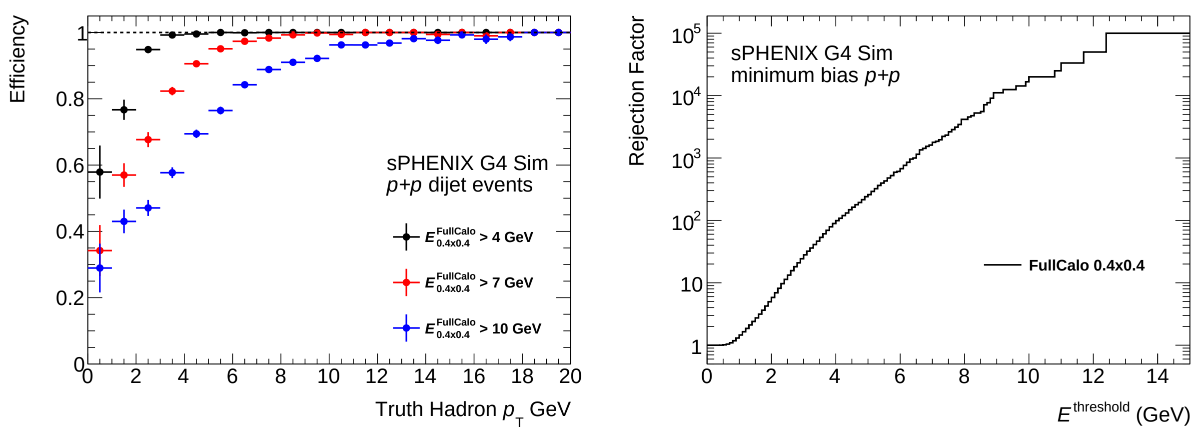

Figure 8.8: *Left:* Trigger efficiency for high-p_T hadrons with respect to the truth-level hadron p_T. The efficiency is shown for three different window energy threshold using the the FullCalo $\Delta\eta \times \Delta\phi = 0.4 \times 0.4$ hadron trigger. For this plot, the efficiency is determined in the same PYTHIA 8 hard-QCD $\hat{p}_T > 20$ GeV samples used to determine the jet trigger efficiency. In this case, for the purposes of firing the trigger, a hadron benefits from the fact that it is likely to be in close proximity to other hadrons in the jet which contribute to the energy in the FullCalo sliding windows. Thus, this estimate of the efficiency is most appropriate for the case of hadrons inside moderate-p_T quark or gluon jets (e.g. a separate study is needed to estimate the trigger efficiency for hadrons in charm or beauty jets). *Right:* Rejection factor in minimum bias p+p collisions for FullCalo 0.4×0.4 window energy thresholds.

(5) Upsilon trigger. Upsilon states decaying through the di-electron channel can be identified with a calorimeter-based trigger which requires a high-energy deposit in the EMCal consistent with an electron. For decays of the Υ states, the large mass of the parent particle sets a lower limit on the energy of its highest-energy electron daughter, potentially allowing a single-electron trigger to sample the full Upsilon production cross-section at

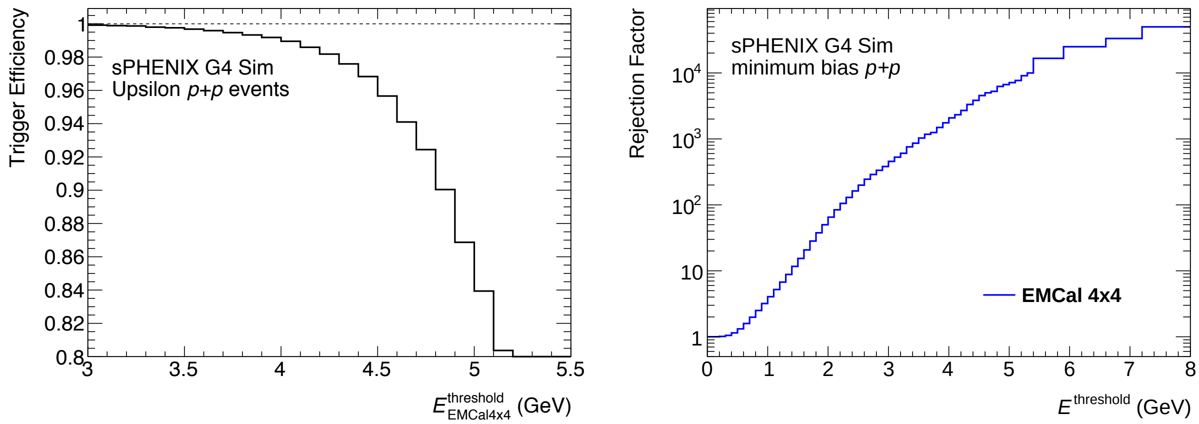

Figure 8.9: *Left:* Trigger efficiency for Upsilons decaying to two electrons, both of which are in the sPHENIX acceptance. The event sample used is PYTHIA 8 events with generator-level filtering on the decay electron and positron kinematics. The efficiency is shown as a function of the required EMCal 4x4 window threshold. *Right:* Rejection factor in minimum bias p+p collisions for EMCal 4x4 window energy thresholds (same as the right plot in Fig. 8.5).

all kinematics for which the sPHENIX detector has acceptance. In $p+p$ collisions, an Υ trigger will be critical to provide reference data for quarkonia melting measurements in Au+Au collisions. In $p+$Au collisions, such a trigger could help provide a high-statistics calibration of cold nuclear matter effects on Υ production. Since it is challenging to identify electrons at the trigger level in sPHENIX, it will be important to demonstrate that the rejection power of such a trigger is sufficient in high-rate $p+p$ and $p+$Au running to fit within the allocated bandwidth.

Figure 8.9 demonstrates the simulated trigger efficiency curves and rejection factors for such an Upsilon trigger, based on requiring some minimum energy in a 4×4 EMCal tower window, in GEANT4-simulated p+p events. At a threshold of 4.5 GeV, where the trigger is still efficient, the rejection factor for minimum bias events is ≈ 4000. While this is slightly lower than the nominal specification of $5,000$ to $10,000$, this trigger could be allocated additional bandwidth, or a trigger based on reconstructing the Upsilon invariant mass could be considered. Simulation results indicate an electron pair trigger with an invariant mass cut > 6 GeV results in a very good efficiency and a rejection in $p+p$ events of greater than 30,000.

In Au+Au collisions, an Υ trigger would allow sPHENIX to take advantage of high-luminosity running to collect additional statistics for differential quarkonia melting measurements. This is especially valuable for increasing the available statistics for the highest Υ states (which are suppressed below sensitivity at the LHC) and in peripheral collisions, which are the most statistically limited.

In addition to the considerations for an Υ trigger described above, a single-electron trigger would have partial acceptance for (predominantly high-p_{T}) J/ψ and $\psi(2S)$ mesons.

Another possibility is the use of a di-electron triggers, which selects events based on the presence of two electrons with an invariant mass in the region of the Υ mass.

8.3.1.1 Calorimeter Trigger

The ElectroMagnetic Calorimeter has 24,576 channels that are read out via the Front End Electronics (FEE) in groups of 64 channels. The FEE will perform a first pass pedestal subtraction and gain correction, and then sum the energies from adjacent 2×2 non-overlapping towers. The detector to FEE cabling will ensure that the 64 channels contain a contiguous set of nearest neighbor 2×2 towers. The trigger primitive output is bandwidth limited to 8 bits for each 2×2 sum, and these are transmitted every beam crossing through a small transition module mounted on the rear of the FEE system backplane. Including header and spacer words, the data output for the trigger primitives is ten 16-bit words per beam crossing. This fits within the bandwidth of 2 Gigabits/second for the optical output.

The Hadronic Calorimeter including both inner and outer detectors has 3,072 channels that are read out via the same FEE as the EMCal, again in groups of 64 channels. As detailed above for the EMCal, the HCal FEE will pedestal subtract, gain correct, energy sum 2×2 non-overlapping towers, and transmit 8-bit energy values via optical output. Note that for the HCal this means that the finest granularity for energies available at the Level-1 trigger are $\Delta\eta \times \Delta\phi = 0.2 \times 0.2$ (which matches the physics performance requirements).

There are several methods to collect the trigger primitives for Level-1 algorithm operations. One can directly couple primitives to the L1 boards or one can concentrate the data first to boost the optical bandwidth. Field Programmable Gate Arrays (FPGAs) available on the market, both from Altera and Xilinx, already achieve greater than 10 Gbits/sec serial speed (in the current mid-range cost FPGA) and with more than 40 link per chip. Even the new low-range cost FPGA will soon reach greater than 10 Gbits/sec serial speed, for example the Altera Cyclone 10. We find that concentrating primitives first to a higher speed may turn out to be a better match with available technology. Conservatively we can merge 4 ADC trigger primitives cables into one high speed optical cable. After removing the duplicate header words, the bandwidth will be around 7 Gbits/sec. The total number of trigger primitives cables will then be 96. If we divide the detector into 4 region, each region will only host 24 optical cables. Even with optional cross-stitching of the detector, the topology will match much better to available FPGA technology. The number of registers in the FPGA will be around 0.5 million or more. It should be enough for working multiple trigger algorithms. The outputs of the trigger calculation will be sent out via optical cable. We refer to these modules as Level-1A trigger modules, as shown in Figure 8.10.

The Level-1A boards will perform the 4×4 overlapping energy sums for the EMCal. The Level-1A main FPGA has more than enough register capacity for these calculations. The highest three energy sums are transmitted to the Level-1B board. The Level-1B board can then also make global combinations of pairs to potentially enhance the Upsilon trigger rejection with a simple invariant mass selection. From the $p+p$ event trigger simulations,

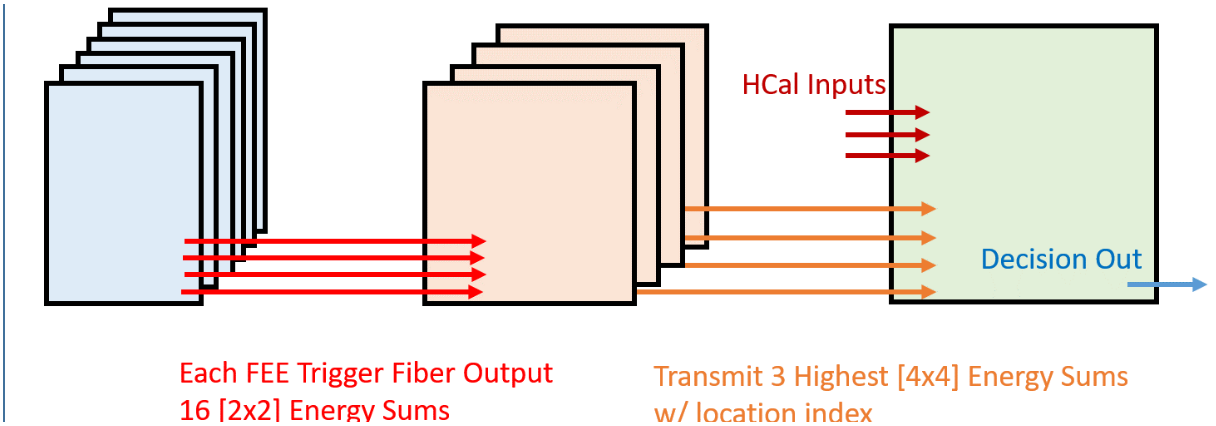

Figure 8.10: Schematic for the calorimeter Level-1 trigger systems. The FEE sends primitives with 2×2 non-overlapping tower energies to the Level-1A modules. The Level-1A modules may contain data from approximately 25% of the entire detector. The Level-1A modules then send non-overlapping energy sums in $\Delta\eta \times \Delta\phi = 0.2 \times 0.2$ regions to the Level-1B board for full jet trigger algorithm processing, where the entire detector coverage is needed. The Level-1A modules also send out a truncated list of the highest energy EMCal 4×4 overlapping towers.

this additional mass selection is not necessary but it may, for example, enable some Upsilon statistics enhancement in peripheral Au+Au collisions.

The Level-1A boards will also perform non-overlapping sums for the EMCal and HCal into $\Delta\eta \times \Delta\phi = 0.2 \times 0.2$ regions. The total number of such sums for the EMCal, Inner, and Outer HCal is 384+384+384. These energies are transmitted to the Level-1B board where jet trigger algorithms are applied and can utilize the complete event within the sPHENIX calorimeter acceptance.

The trigger simulations results shown earlier in this Section are full GEANT4 simulations of the detector performance and tower segmentation and summing. However, they do not yet include an emulation of the detailed Level-1 trigger primitives and 8-bit bandwidth matching requirement. An initial extension of the simulations to include the 8-bit ADC truncation is detailed below.

The performance of possible electron triggers for selecting di-electron Υ decays in high-luminosity p+p running in sPHENIX has been extended to mimic the first stage of the Level-1 trigger primitive processing. These triggers are based on energy sums in the electromagnetic calorimeter, and have been examined with a full event PYTHIA 8 and GEANT4 simulation of the whole sPHENIX detector. Two-dimensional projective SPACAL towers were collected into sliding tower windows made from 4×4 towers via a trigger logic emulator ($\Sigma_{4\times4}[E_{\mathrm{Tower}}]$). The top 8-bit ADC value for each tower was used in the sum in order to model the constraint from the trigger data bandwidth. The distribution of largest energy sums in minimum bias PYTHIA events was used to determine the rejection factors for the trigger. The efficiency for Υ events was determined using a cut on the largest energy sums in PYTHIA events, which contain at least one Υ(1*S*) particle that decayed into di-electrons and was reconstructed by the full tracking detector to be within an invariant mass window of $M_{\Upsilon(1S)} \pm 200$ MeV ($M_{\Upsilon(1S)} \pm 2$-σ). Figure 8.11 summarizes the performance of such an electron trigger by simultaneously plotting the rejection factor for minimum bias events and the efficiency for Υ events as a function of the minimum energy required in the electromagnetic calorimeter tower windows using both the full ADC bit-width and the top 8-bit truncated ADC information. In particular, the vertical gray band in the figure at $\Sigma_{4\times4}[E_{\mathrm{Tower}}] = 4.3$ GeV gives an example of a choice of minimum threshold energy in 4×4 windows for which the rejection factor is better than $\approx 5 \times 10^3$ while maintaining an Υ efficiency of 98% in both ADC bit-width choices. The result is quite comparable to the GEANT4 simulation without 8-bit truncation. This demonstrates the feasibility of an electron trigger for the Upsilon program in high-luminosity p+p data-taking. Extending these trigger emulated studies to the full physics channel set goes hand in hand with further specification of the trigger algorithms.

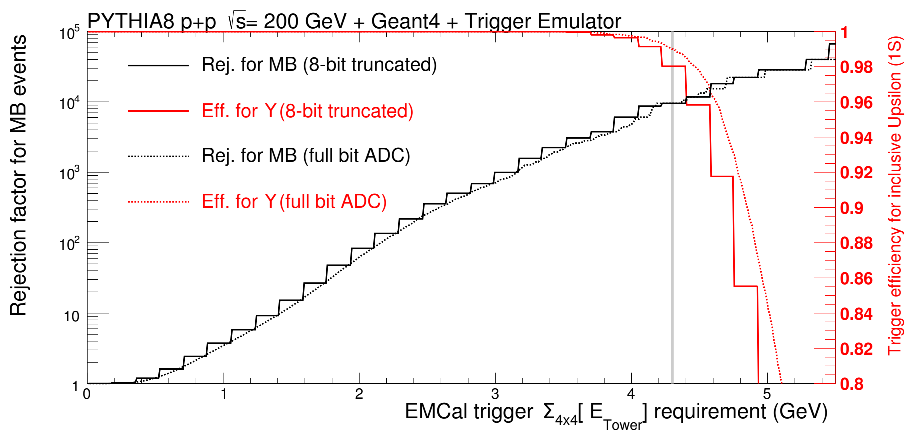

Figure 8.11: Rejection factor and efficiency for an Υ-electron trigger, which requires some minimum amount of energy in a 4x4-tower of the 2D projective SPACAL ($\Sigma_{4\times4}[E_{\mathrm{Tower}}]$). Results are shown for a full PYTHIA and GEANT4 simulation of the detector response. The rejection factor for minimum bias p+p events (black lines) and the efficiency for Υ (red lines) are plotted as a function of the required energy $\Sigma_{4\times4}[E_{\mathrm{Tower}}]$. For the dashed lines, full bit-width ADC values were used in the trigger sum, while the solid line shows trigger performance when only the top 8-bit ADC information is used.

8.3.1.2 Minimum Bias Trigger

The MBD consists of two identical arms of detectors around the beam-pipe, located both forward and backward of the collision point. Each arm consists of 64 channels, and are referred to as the North and South arms. For full details see Chapter 7.1. On every RHIC crossing, the MB LL1 trigger board will receive the following trigger primitives over 4 fibers from each of the 4 ADC boards used by the MBD:

- The mean time of all hits in one MBD ADC Board (10-12 bits)
- The number of hit channels in one MBD ADC Board (6 bits)
- The total charge sum in one MBD ADC Board (12-16 bits)

The ranges of bits in the above are determined by the lower and upper bounds on the resolution we expect to be able to achieve in the system, and will be finalized after further study. Since each ADC board reads out half of one MBD arm, it represents the data from the left or right half of an arm, which will allow scaling of left-right asymmetries during transversely polarized proton running. The MB Local Level 1 trigger will calculate the z-vertex position of the collision using the difference in the times from the two arms, and can make a cut on the collision vertex [155]. The nominal selection for sPHENIX is $|z| < 10$ cm since this is the fiducial acceptance for the silicon tracking systems. However, multiple vertex selections are possible. In PHENIX, for example, three MB triggers were defined: $|z| < 10$ cm, $|z| < 30$ cm, and the "wide" trigger in which collisions from any vertex location are accepted. With 120 ps time resolution, one expects a z-vertex resolution of about 2.5 cm for the most peripheral heavy ion events. As the centrality of the collision increases, this resolution will improve due to the statistical improvement from the larger number of hits.

The electronics upgrade allows the possibility of a couple of new features that were not available in PHENIX. The centrality of the collision can be estimated using the the number of hits or energy sums in the MBD, allowing for a trigger selection on centrality. Additionally, since the time and charge are extracted simultaneously on the ADC Board, a slew correction can be applied to the time determination, which will improve the time resolution in the Level-1 trigger compared to PHENIX.

8.4 The Global Level-1 and Timing System

At its core, the GL1 functionality is implemented in a FPGA that receives, for each beam crossing, inputs from the LL1s. After examining the input data, it arrives at a decision whether or not to accept the data from the beam crossing in question. In the end, a given crossing fulfills one or more classifications, which are usually referred to as different *trigger inputs*. For example, a collision could be characterized as (likely) containing an Upsilon signal, a high-momentum photon, or a jet, high centrality, or any of the trigger algorithms described in the previous chapter. Those properties are not exclusive; a given crossing can (and often does) fulfill more than one.

One would give priority to the most "interesting" events, usually the ones that fulfill a dedicated LL1 criterion. The least interesting crossing is one where no actual collision took place. In order to facilitate consistency checks and normalizations of the calculated cross sections, one still adds a very small fraction of those "clock" triggers to the mix.

8.4.1 Trigger Scaledowns

A given trigger mix is implemented by a set of *scaledown values*. To use an example from the PHENIX experiment, one particular run saw 18635569 collisions that satisfied the Minimum Bias criterion. Of those, 3218134 collisions happened within the desired narrow central vertex range. Obviously, we want to collect as many of the latter type as possible; however, one still needs to collect a small fraction of the former (about 0.5% of the total number of events) of the "wide vertex" collisions for normalization purposes and consistency checks.

The scaledown system counts how often a trigger signal arrives at a given trigger input while the data acquisition is not busy. If the scaledown is, for example, 10, only every 10th such collision is accepted, all others are discarded. It is of the utmost importance that the system only counts trigger signals that arrived while the DAQ system was live. In this way, the one accepted (and recorded) collision represents, other than itself, 9 others of the same statistical significance *that could have been taken*. In the analysis phase, the data from this collision must be weighted by a factor of 10 to account for the scaledown. Conversely, if that scaledown is set to 1 (no rate reduction), each triggered collision is getting accepted, and its weight is 1.

In the PHENIX run shown above, of the 18635569 minimum bias collisions, 16738539 arrived while the DAQ system was live. The scaledown for this trigger input was set to 1333, resulting in 12547 accepted collisions.

Of the 3218134 collsions in the narrow vertex range, 2891906 triggers arrived while the DAQ was live, and, with a scaledown of 1, all of them were accepted and recorded. In this way, the desired small admixture of 0.43% (12547/2891906) minimum bias events without a vertex cut was accomplished.

Similarly, a small fraction of clock triggers (7067399912 raw, 6362534485 live, 19087 accepted) was selected by a scaledown of 1/3 million (333,333). The following table summarizes those numbers:

trigger	raw count	live count	scaledown	accepted
clock	7067399912	6362534485	333333	19087
minimum bias	18635569	16738539	1333	12547
narrow vertex	3218134	2891906	1	2891906

Without the dedicated "narrow vertex" trigger, we could have taken about 2904453 (2891906 + 12547) minimum bias events in that run, but only 501563 of them, rather than 2891906, would have been in the narrow vertex. By implementing the narrow vertex trigger, and adjusting the scaledown settings properly, we were able to enhance the statistics of the most valuable collisions by almost a factor of 6.

The entire latency for the Level-1 trigger system is specified at 4.0-5.0 microseconds.

8.4.2 Timing System

The sPHENIX Timing System performs distribution of the timing information to the front end modules (FEM) for the various detector subsystems. The front-end electronics needs to be aware of the RHIC clock in order to synchronize the sampling frequencies with the arrival of the signals.

The module is housed in a 1U rack mount enclosure and interfaces with the controls network via TCP/IP over gigabit Ethernet. The actual timing information is transmitted via dedicated fiber interfaces.

The timing module performs three primary functions.

First, it provides low jitter distribution and generation of timing signals, namely the Beam Clock, Beam Clock $\times$ 6 (generated on board via PLL), and LVL-1 Accept. The Timing System distributes a copy of the generated 6 $\times$ the RHIC clock to the front-end.

Second, it provides readout enable strobes to the FEM's, and monitors the number of level-1-accepts generated by the level1 system.

Third, it is a mode bit scheduler, which outputs predetermined mode commands on a crossing-by-crossing basis to the FEM's. RHIC has 120 "buckets" in each ring that can hold beam bunches (or can be empty), giving the collider a period of 120 bunch crossings, after which the same pattern of crossings repeats itself. The bunches cross about every 110 ns, although the exact value varies slightly with the ion species that is being stored, and also changes during the acceleration phase of a RHIC store.

The scheduler always operates as multiples of a sequence of 120 values, one for each crossing in one period, which is a full rotation of a particular bunch around the ring, which takes about 1.3 microseconds.

The Timing System needs to know the RHIC bunch crossing number. The Collider provides a "fiducial tick", a hardware signal that denotes the passing of bunch number 1, which the GL1 and Timing System uses to get in sync with the accelerator state. At the start of the GL1 and Timing System operation, all its internal counters are held at reset. At the next crossing of bunch 1, the systems start counting and remain in sync with the bunch numbers.

For each beam crossing, the various front-end systems need to receive some information. Most importantly, it needs to know whether or not to prepare the data from a given collision for transmission, but there are other types of information that can be sent. For example, it would be possible to instruct the front-end to set a certain bit that results in the zero-suppression getting switched off for a small fraction of events. In this way it would be possible to acquire, for example, special events with a very low rate that can be used to check the proper settings of the pedestal subtraction (”in-beam pedestal”).

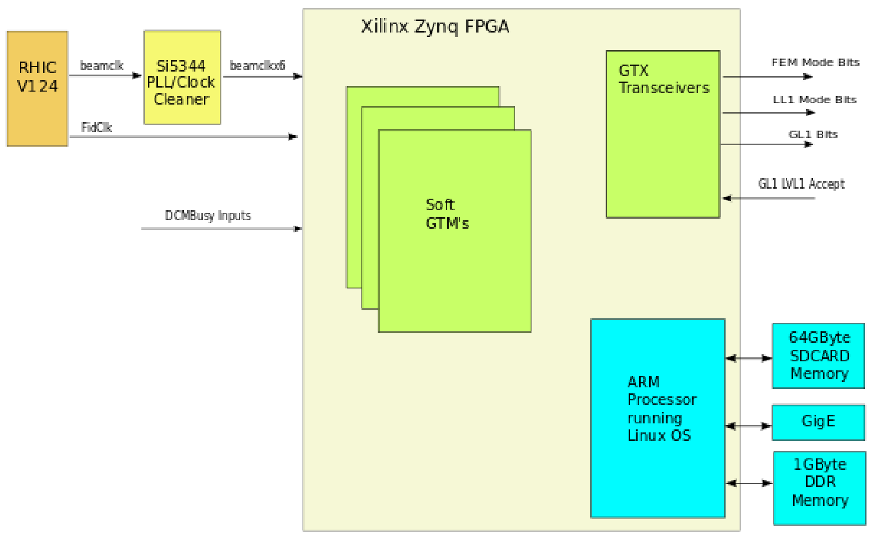

Figure 8.12: Block diagram of the Timing system, which contains a number of virtual *Granule Timing Modules* (GTMs) implemented in firmware on a FPGA. The board receives the RHIC clock from the accelerator system, as well as a *fiducial tick*, denoting the passing-by of bunch 1 in the ring. The GTMs distribute the timing and trigger information in a detector-specific way, and maintain the busy state of the DAQ.

At the core of the timing system are multiple copies of a virtual *Granule Timing Module* implemented in firmware (Fig. 8.12). A granule refers to a set of FEMs that receive identical timing information. This is most often a section of a detector system, such as the north- or south half of the electromagnetic calorimeter. Since it is possible to operate a granule in a standalone fashion during testing and debugging of the detector readout, we will likely split large detector systems up into more granules than strictly necessary just from a timing information perspective.

Each virtual GTM implements its own scheduler. The scheduler can hold 32 different sequences (internally called “mode bit groups”) of 120 per-crossing “modes” that usually repeat many times. In order to be able to execute a special sequence occasionally, as with the example of in-beam pedestals, or only one time, the GTM holds a 128 entries deep section of *scheduler memory* that schedules the proper sequences for execution. For example, sequence A might contain an instruction on bunch crossing 1 for the FEMs to reset their counters and clear their memory. Sequence B would then encode the standard operation for each rotation. In that case, one would execute sequence A once at the start of data taking, and then repeat sequence B indefinitely until the data taking ends.

Let's now assume that another pattern C contains a special instruction that injects an in-beam pedestal event, and that such an event should occur every 15 seconds. Now one would schedule sequence A once at the start as before, followed by an indefinite loop of 11538 repetitions (about 15s worth) of the standard sequence B and then one sequence C.

Each entry in the scheduler memory is 32 bits wide, and mean

31	30...5	4...0
reset	repeat count	sequence address

The entries are executed in order. The repeat count specifies how often a given sequence is repeated. The reset bit causes the scheduler to jump back to the start position after finishing the entry's execution, making it possible to program indefinite execution sequences.

To program the above example, sequence A might be stored at address 0, B at address 1, and C at address 2. Then the scheduler memory would be

31	30...5	4...0	
0	1	0	initialization
0	11538	1	15s standard operation
1	1	2	in-beam pedestal injection

A candidate board for the Timing system is shown in Fig. 8.13. The board has a Xilinx Zynq FPGA. The board has 14 individual fiber transceivers and can support 14 different granules. The Zynq FPGA has several CPU cores, and a Debian implementation for the board exists. This provides access to a standard ethernet port. The board can be configured through the network, which can also provide aggregate information such as counters.

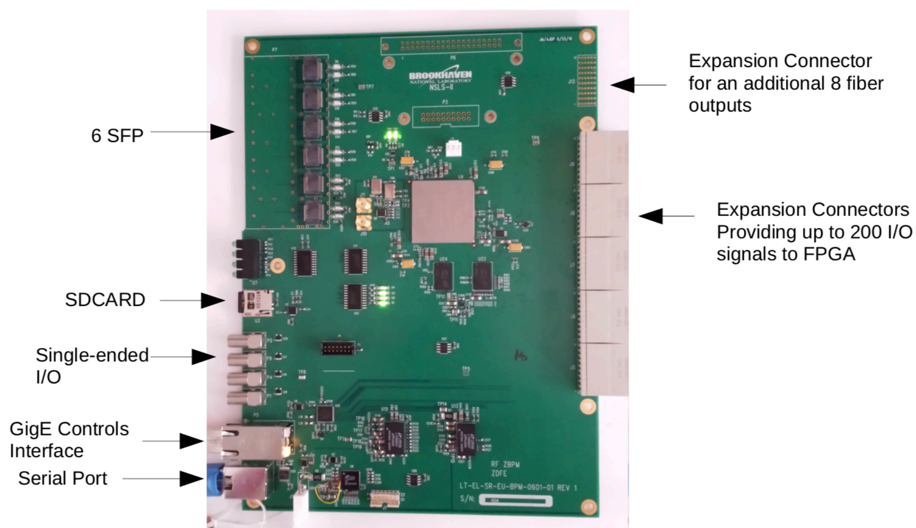

Figure 8.13: A picture of a candidate board to run the Timing System. The board has a Xilinx Zynq FPGA which, in addition to the FPGA portion, has ARM CPU cores that can run Linux and provide the slow controls interface, as well as access to aggregate information.

Appendix A

Superconducting Magnet

The magnet and tracking system should be capable of order of 1% momentum resolution at 10 GeV/c over $|\eta| < 1.1$ and the full azimuth. The BaBar solenoid, with a central field of ~ 1.5 T and an inner radius of ~ 140 cm, is an excellent match to the sPHENIX physics requirements. The magnet became available in late 2012, and the ownership of the coil and related equipment have been transferred to BNL.

A.1 Magnet Mechanical Design

The superconducting solenoid magnet was manufactured by Ansaldo and delivered to the BABAR experiment at SLAC in 1997. The magnet was successfully commissioned in 1998, and it was operated and remained in good condition through the end of the BaBar experiment in April 2008. The solenoid was then shipped to BNL in February 2015. Upon installation in sPHENIX at BNL, the magnet will remain unchanged except for an extension to the connection to the exiting power leads and cryogenic line structure (referred to as the valve box) to eliminate interference with the sPHENIX outer calorimeter.

Partly to simplify track finding and fitting, the magnitude of the magnetic field within the tracking volume should be constant within a few percent. The field will be measured to better than 1% in the whole cryostat area to correct for nonuniformities, especially close to the plug doors.

A.1.1 Conductor

The conductor is composed of a niobium titanium "Rutherford-type" superconducting cable which was co-extruded with an outer aluminum matrix. The cable is made of sixteen strands of 0.8 mm diameter wire with a copper to superconductor ratio of 1:1, filament size less than 40 μm, and twist pitch of 25 μm. The final superconducting cable is rectangular in shape and 1.4 mm by 6.4 mm in size. The aluminum matrix into which the superconductor is co-extruded is of two sizes; 8.49 mm thick by 20 mm wide in the body of the magnet, and 4.93 mm thick by 20 mm wide in the coil end regions. The thinner aluminum matrix in the ends permits higher current density in the coil ends to extend the axial region of uniform solenoid field. The critical current of the conductor is 12,680 A at 2.5 T and 4.2 K, which provides a safety margin of 2.75 over the operating current of 4,596 A. The conductor is wrapped with fiberglass cloth which is later impregnated with epoxy, the combination of which provides both electrical insulation for the conductor and mechanical support for the completed coil.

A.1.2 Coil

The solenoid coil consists of two conductor layers. Both conductor layers were internally wound inside an aluminum support mandrel — first the outer layer and then the inner layer. Winding was started at the end where the conductor leads would ultimately exit the coil, using the narrow conductor. After a specified number of windings the narrow conductor was spliced to the thick conductor using two 30 cm long soldered lap connections, spaced 20 cm on either side of a 1.5 m long region where the edges of the overlapping thin and thick aluminum matrices were welded together (Figure A.1). The completed splice region was hand wrapped with fiberglass cloth when complete and winding using the thick conductor was completed to a specified number of turns, after which a similar splice back to thin conductor was installed and the winding of the outer layer completed to the desired dimensions. A third splice, this one to connect to the inner coil layer, was installed, and inner layer winding was completed in a fashion similar to the outer layer using thin, then thick, a finally thin, conductor. The number of thin and thick conductor windings, for the inner (outer) layer, counting from the exiting lead end of the coil, are 184, 164, and 183 (188, 159, and 189). When the winding was completed, the coil was impregnated using epoxy to create a rigid structure. G-10 parts were used in transition locations and to adjust the overall length of the coil to meet the aluminum support mandrel end flanges.

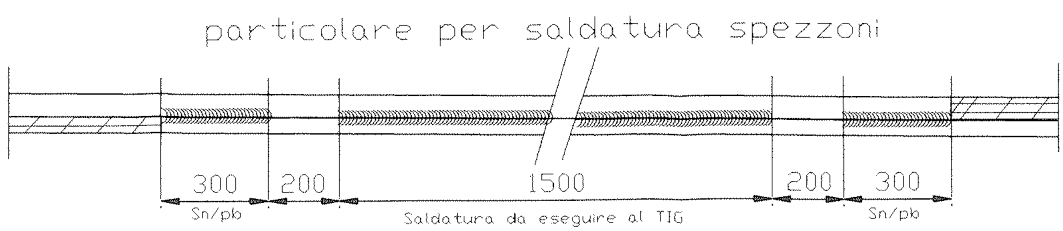

Figure A.1: Internal splices (extracted from the original Ansaldo drawing): 1500 mm weld of aluminum edges + 200 mm gap + 300 mm solder of aluminum faces on both sides of the weld. The welding was done with the TIG (Tungsten Inert Gas) technique.

A.1.3 Cold Mass and Cryostat

The aluminum support mandrel provides both mechanical support and cooling to the solenoid coil (Figure A.5). Conductive cooling is provided via helium which circulates in lines welded to the outside surface of the support mandrel. An outer heat shield which is actively cooled to 40 K using helium gas from the cold mass cooling line boil-off that is returned to the helium reservoir, along with conductively cooled heat shield end plates and inner heat shield (connected to the outer shield) assist with maintaining a uniform 4 K coil temperature. Support from outward radial and axial Lorentz forces is provided by the strength of the aluminum cylinder. Gravity loads, as well as magnetic field alignment, are provided by a system of tangential and axial Inconel tie rods which develop tension on cool down to 4 K. Tie rods connect the coil support cylinder directly to the aluminum outer cryostat (Figure A.6) but are heat stationed to the outer heat shield. The coil is positioned with a 30 mm axial offset toward the lead end with respect to the outer cryostat. The outer heat shield is independently supported by the outer cryostat by separate tie rods (Figures A.7 and Figures A.8).

A.1.4 Valve Box

The cryostat connects to a vertical tower (valve box, Figure A.2), which contains all the electrical (vapor cooled) power leads, instrumentation wire leads, helium supply and return lines for coil and heat shield, and vacuum connections. During installation in sPHENIX this valve box will be extended away from the magnet to provide clearance for the outer calorimeter, by adding a 1 m transfer line extension which carries all of the aforementioned lines from magnet to valve box.

Figures A.2 and A.3 show the placement of the cryostat, the extension and the valve box. Figure A.4 shows different portions of the extension that is connected to the valve box.

A.2 Cryogenics

A.2.1 Magnet Cryostat System

The coil of the magnet is attached to a cylindrical aluminum mandrel which is cooled by boiling liquid helium in eleven parallel aluminum tubes welded to the mandrel. A separate valve-box cryostat located above the solenoid cryostat, outside the return flux iron serves to interface the power and cryogenics to the solenoid. The valve-box contain the cryogenic valves, the siphon phase separator vessel, current leads, and relief devices. A vacuum jacketed interconnect containing the cryogenic lines and superconducting current cables, and instrument wiring, connects the solenoid cryostat to the valvebox.

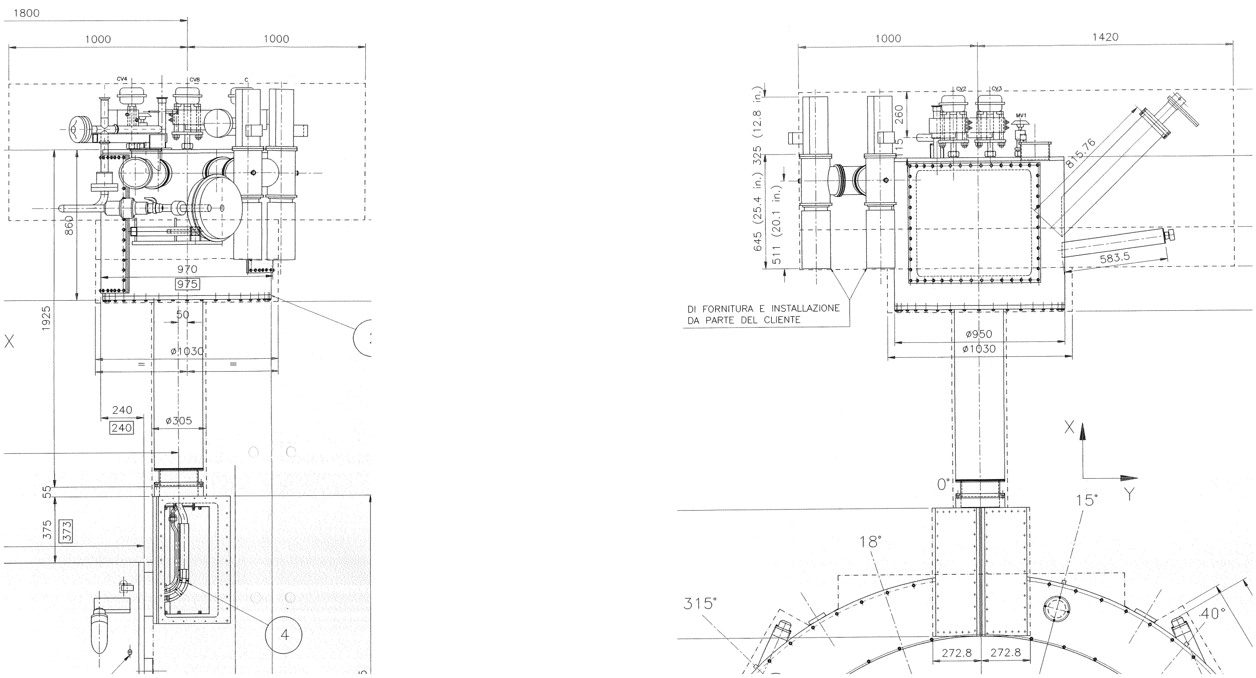

Figure A.2: Original Ansaldo drawing of the valve box.

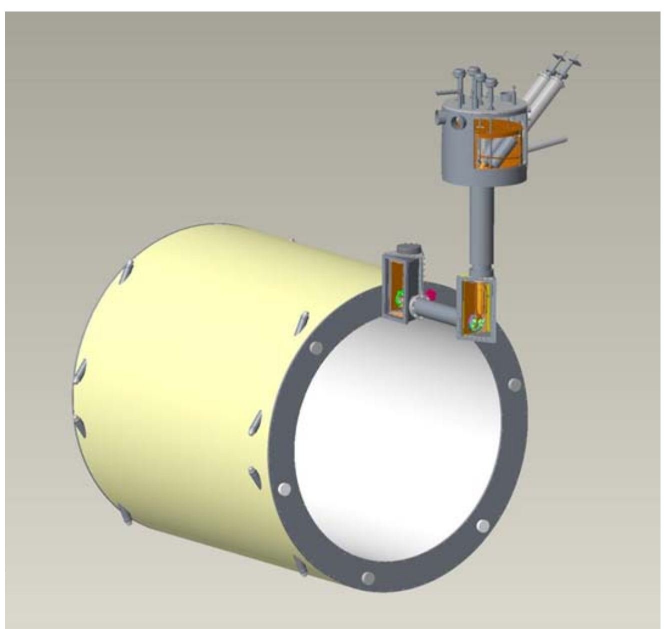

Figure A.3: The cryostat, the extension and the valve box.

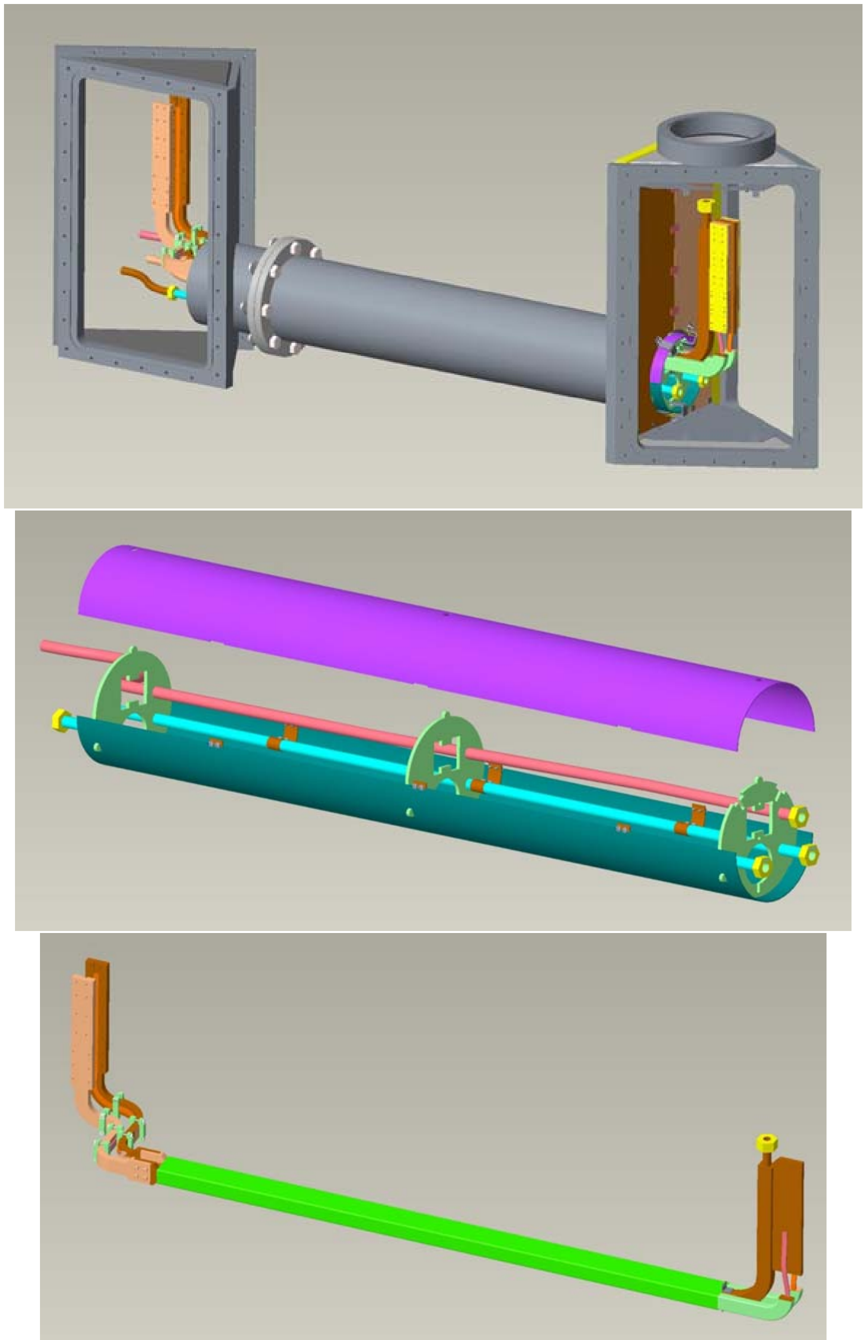

Figure A.4: Top: from the junction box (at the cryostat) to the valve box; Middle: coil helium supply line and heat shield; Bottom: extension lead assembly with flexible (laminated copper) connections to accommodate thermal contraction on the left and coil return helium to cool exiting leads on the right.

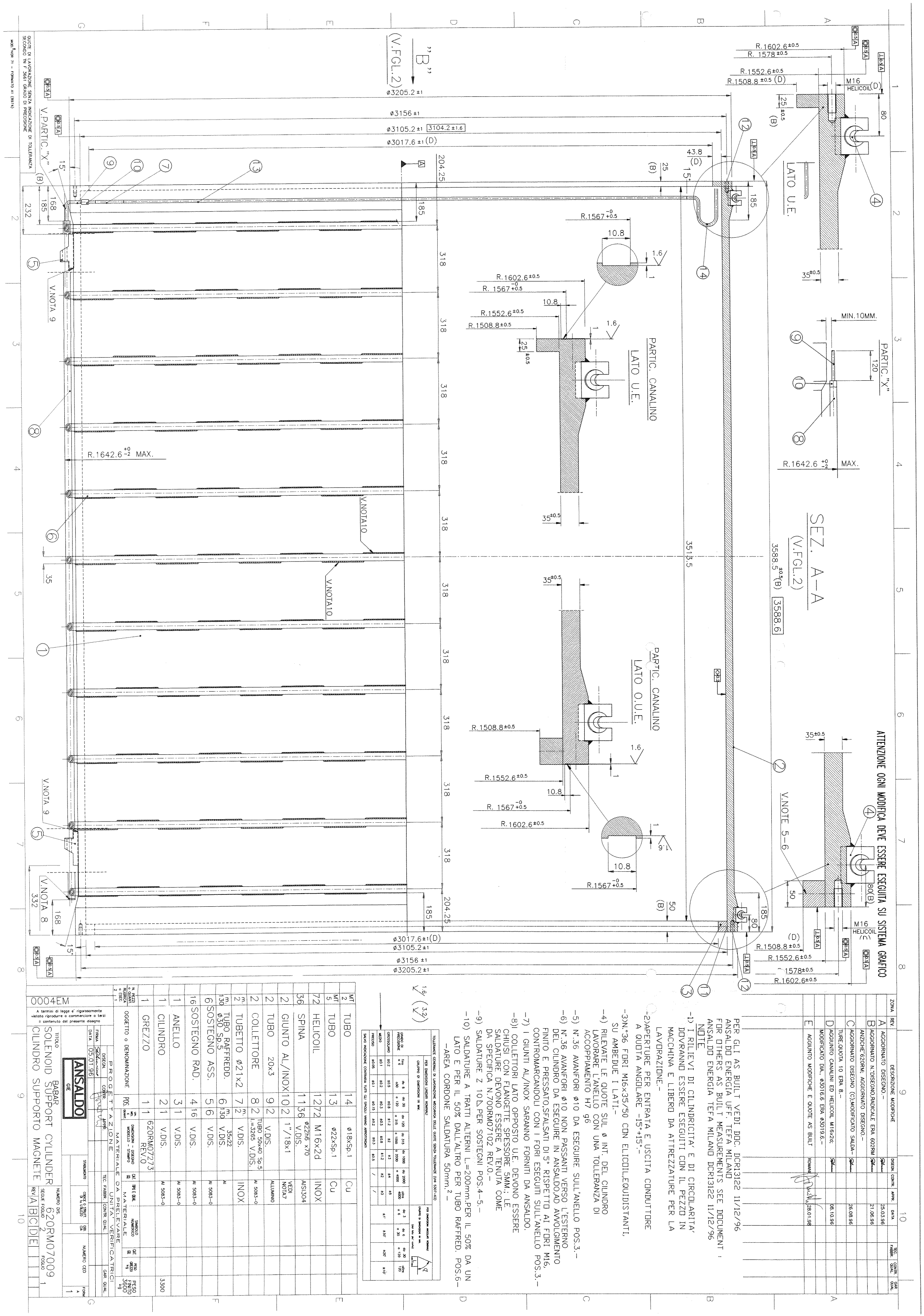

Figure A.5: Original Ansaldo drawing of the Solenoid Support Cylinder

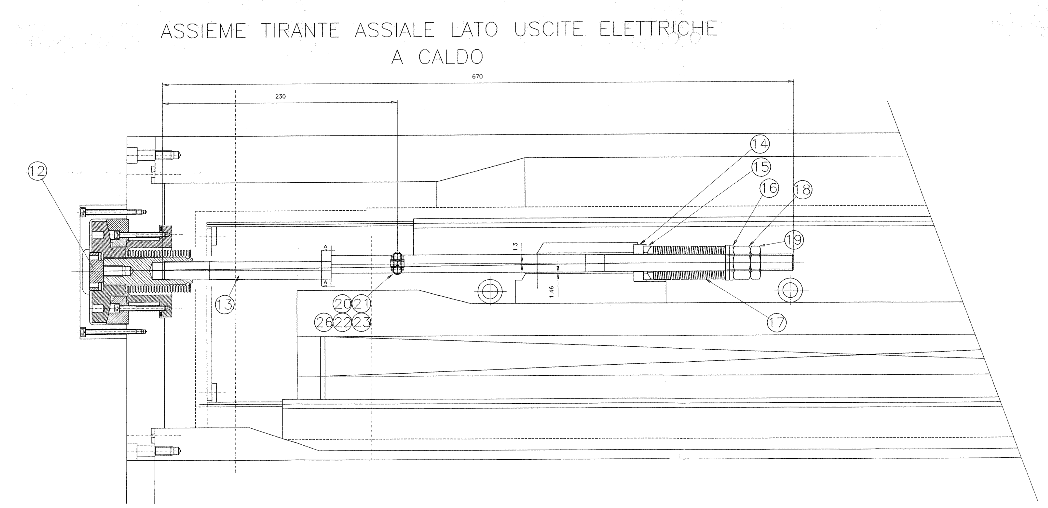

Figure A.6: Original Ansaldo drawing: Axial Tie Rod Assembly

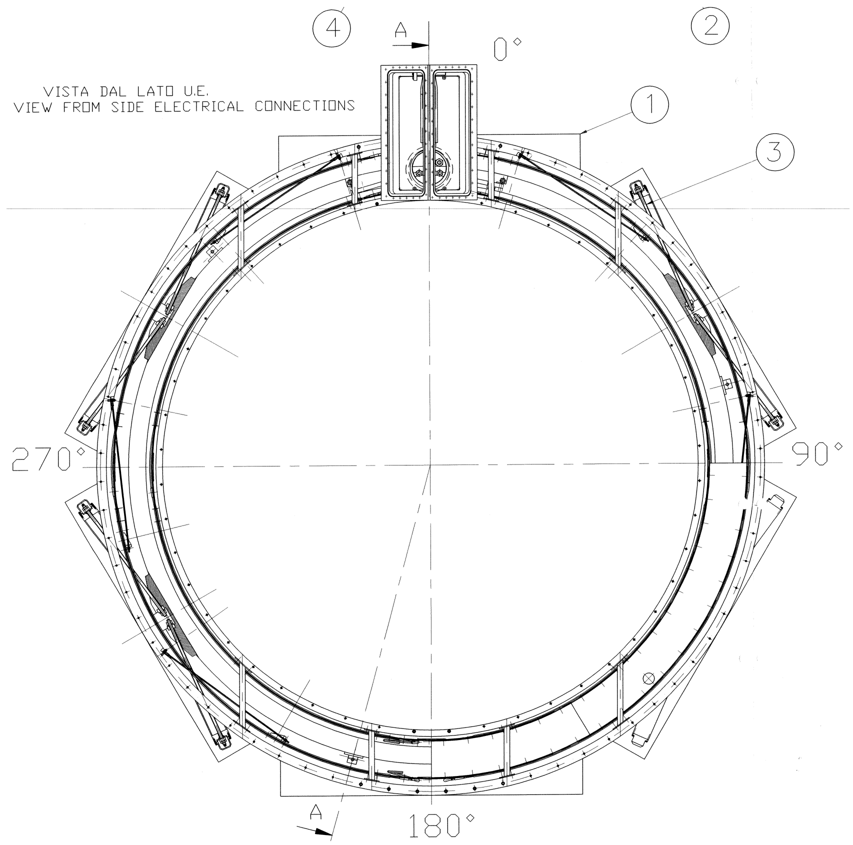

Figure A.7: Original Ansaldo drawing: Cryostat Assembly

Figure A.8: (Left) Exiting leads — aluminum removed and niobium titanium soldered to heavy copper stabilizer leads (overlapping aluminum; (Right) Outer heat shield.

A.2.2 Magnet 4.5 K Cooling

The originally design of the cooling loop is a thermo-siphon loop in which liquid is drawn from the phase separator vessel and fed to the bottom of solenoids cooling loop and returns back to the phase separator. It has not been operated in the thermo-siphon for most if its normal operating life at its previous facility. The magnet was cooled by, instead of feeding the liquid to the phase separator, the liquid helium was fed directly from the cryogenic supply to the solenoids cooling loop, with the return flow still coming back to the valve-box phase separator. This operating point was still sub-critical, and thus nucleate boiling still occurred and the flow is two phase returning to the phase separator.

Table A.1: Steady State Loads

Solenoid Valvebox Loads	Original Design / Nominal Load	Forced 2 Phase Flow Operation and Design Load
Magnet load and valvebox	35 W @ 4.5 [siphon mode]	7.5 g/s, 145W [with Valvebox separator loading heaters]
Shield	0.35 g/s, from 4.5K to 50K, 110W	0.5 g/s, from 4.5K to 50K
Vapor cooled leads	0.51 g/s, 4.5K to 300K	0.51 g/s, 4.5K to 300K
Vapor cooled leads	0.51 g/s, 4.5K to 300K	0.51 g/s, 4.5K to 300K

A.2.3 Superconducting Current Leads

The two superconducting current (SC) leads, after exiting the coil are cooled by conduction to the 2-phase flow return tube. The superconducting lead cables are attached to copper bars, which are cooled by this return line going back to the valve box. The SC leads terminate at the lead pots, which each contain the normal conducting copper vapor cooled current lead, that transitions to the room temperature connection for the external power supply. The lead pot is cooled by liquid drawn from the main siphon phase separator. The entire lead pot is electrically hot, and isolation is done with an isolator at the tubing connections that feed liquid and return cold vapor, and on the tubing connection where the lead cooling exit the warm end of the current lead, with the actual pot vessel isolated with a G-10 spacer at the flange on the warm end of the lead pot vessel. The nominal lead cooling flow is 0.2 g/s controlled by a 0.5 g/s thermal mass flow controller.

A.2.4 Thermal Shield

Thermal shields surround the solenoid coil/mandrel assembly in both annular spaces (inner and out diameter) between the coil and the cryostat vacuum vessel. Some of the 4.5 K cold vapor from the separator vessel is taken through the shield loop and returns back to the cryosystem to a warmup heater (liquefaction load on the plant) or returns cold at approximately 40 K to the cryo plants coldbox. Nominal shield flow is 0.35 g/s with a return temperature of around 60 K for a load of 110 W.

A.2.5 Valve Box

The existing valve box serves as the cryogenic, power supply, vacuum, and instrumentation interface between the solenoid and the rest of the facility. It contains the following equipment on the valve box and interfaces: cryogenic control valves, the relief devices, the electrical feedthroughs for all the solenoid instrumentation, turbo vacuum pump, vacuum gages,pressure sensors, TE, SC level, LHe bath heaters.

A.2.6 Relief Devices

The helium volume is protected by an ASME relief valve and ASME burstdisk, and a cryogenic dump globe valve from a relief line originating from the phase separator. The reliefs were sized to handle a full magnet quench and loss of insulating vacuum to air.

A.2.7 Cryogenic Supply System

The magnet will be cooled by tie-in to RHIC cryogenic distribution system. There will be one supply line that will tie-in to the S header and the H header of the cryo distribution system. This allows liquid helium supply during 4.5K operations and ability to draw from the heat shield header during cooldown.

Cold vapor returns via a return line to the U header on RHIC distribution system. The solenoid shield returns on a separate shield return which will also be used to shield the cryogenic transfer line for this interface transfer line system. The shield flow will return to the RHIC U-header or WR header. The current lead flow returns will be returned as warm gas to RHICs WR header, operating at 1.2 bar.

Thus RHIC operating conditions on the cryo distribution system will set the operating condition for the SC Solenoid.

Header name	Pressure [bar]	Temperature [K]
S	3,4	5.0
H	12-14	50-80
R/U	1.22	4.6
WR	1.19	293

Magnet operating temperature is actually set by the return pressure on the RHIC cryogenic distribution system at 8 OClock / 1008. The pressure in RHICs 4.5 K vapor line R or U header is around 1.22 bar during normal operation. In order to operate the solenoid helium at 4.5 K, the boiling point pressure needs to be 1.300 bar. This sets the 4.5 K pressure drop budget between the solenoid and R header at 80 mbar.

Tie-in from the RHIC cryogenic distribution system will occur at the valvebox via the tee-ins from the main header to the individual relief transition feedthrough lines located at one end [sextant 8/9 end] of the valvebox. The valvebox is located inside 1008B service building. The transfer line system exits the 1008 building and will penetrate the IP8 Hall via the south wall and suspends across the Hall to the platform. Cryogenic line jumpers with bayonets interface to the new interface box.

Table A.2: 4.5K loop vapor return pressure drop budget [10 g/s vapor]

Item	Pressure [bar]	DP budget [mbar]
Bath pressure	1.300	
Tubing run to valve	1.295	5
Vapor return valve	1.279	16 [$C_v = 2.8$]
Tubing run to bayonet	1.275	4
Return line to heater	1.270	5
Heater	1.250	20
Return line to RHIC tap, 1 NPS, sch10	1.240	10
Isolation valves, two	1.226	14 [$C_v = 4$]
Margin/Balance	1.216	4
U header, 5K	1.220	[overall: 80]

3980 ### A.2.8 Interfacebox

3981 The interfacebox will be located next to the solenoid valvebox and will contain the follow-
3982 ing components:

1	Liquid helium reservoir, 400L	Sufficient for magnet rampdown in 1 hour if LHe supply is interrupted
2a 2b	LN2 Boiler / Helium exchanger GN2 / Helium exchanger	LN2 exchangers to hold the magnet at 100K during shutdown using the helium circulating compressor at 1010B. LN2 Boiler and sensible heat recovery exchanger from 80K to 300K.
3a 3b 3c	heater or recovery heatexchanger*	20 kW Heater to warmup cold gas from the RHIC distribution for controlled cooldown and controlled warmup. * Recovery heatexchanger option: acts as recovery heat exchanger between solenoid helium stream and RHIC distribution system to control gradient across solenoid during cooldown and warmup
4a	Reservoir Vapor return control	Back pressure on reservoir to develop pressure difference to transfer flow to the solenoid valvebox supply
4b	Reservoir Liquid supply control	Controls liquid Helium into the reservoir from RHIC supply
4c	External dewar Liquid supply control	Controls liquid Helium into the reservoir from external dewar
4d	Heater Supply isolation	Isolates heater inlet from RHIC Helium supply
4e	Heater Exit to return side control	Controls warm Helium gas bypass to return side
4f	LN2 supply to Boiler Exchanger	Controls LN2 into LN2 boiler
4g	LN2/He HX Cooldown supply control	Controls 80K Helium flow into reservoir
5	Reliefs	Liquid helium reservoir and LN2 boiler bath, and trapped volumes
6	Temperature sensors	Reservoir, heater exit, LN2 Boiler exit
7	Pressure sensors	Liquid helium reservoir, Heater volume and LN2 boiler bath
8	Level sensors	Liquid helium reservoir and LN2 boiler bath

A 400 Liter ASME U-Stamped liquid helium reservoir will serve as the buffer to allow rampdown of the magnet in the event there is interruption from the liquid helium supply, it also serves as the phase separator to do the phase separation from the supercritical helium supplied from RHIC cryogenic distribution S-header which is slightly warmer than RHICs main M line flow. Supercritical helium at 3.55 bar and 4.8K is supplied from the S-header via shielded transfer line bundle into the 400L liquid helium reservoir and from there liquid helium at 1.4 bar, 4.6K is supplied to the solenoids valvebox. An additional bayonet is also provided to allow supply from a 500L portable liquid helium dewar from the superstructure platform. The reservoir will need to have a net liquid inventory of 300 Liters to allow liquid draw of 7.5 g/s and 1.3 g/s of vapor generation (8.8 g/s = 264 LPH) to allow rampdown of the magnet within 1 hour. [from 4600 A @1.5A/s].

The Interface box will also include the LN2/He exchanger for keeping the solenoid cold at 100K during RHIC shutdown. To handle the controlled gradient cooldown with no warm helium gas supply source available during RHIC operation, either a heater configuration or a He/He heat-exchanger and a small heater configuration is required. When the RHIC plant is not running the capability exists to use a small 18 g/s compressor located at 1010B to supply helium for circulation.

A.2.9 Liquid Nitrogen Supply Line

Liquid nitrogen is supplied to the interface valvebox for use during the shutdown to maintain the magnet at 100K. The LN2 is supplied a 500 ft long cryogenic transfer line from the liquid nitrogen storage dewar located in the front of the experimental hall building.

A.2.10 Warm Piping

N2 vent line to vent room temperature N2 to outside of the building will be run from the interface box to outside.

A.2.11 Utilities

A.2.12 Utilities Instrument Air is supplied via RHICs Cryogenic systems Instrument air system capable of providing -60C dewpoint at 90 psig.

120VAC and 480VAC power is required for the heater and controls at the solenoid and in 1008B service building.

A.2.12 Controls

Controls of the solenoid valvebox, the interfacebox will be done by a Modicon 340 series PLC and I/O chassis, located in two (2) 19 rack along with the temperature sensors controllers, SC level probe controllers and vacuum pump controllers. The PLC is interfaced to the RHIC Cryogenic Systems DCS/HMI control system via Ethernet on its own subnet.

Figure A.9 presents a flow-chart of the cryogenic control system.

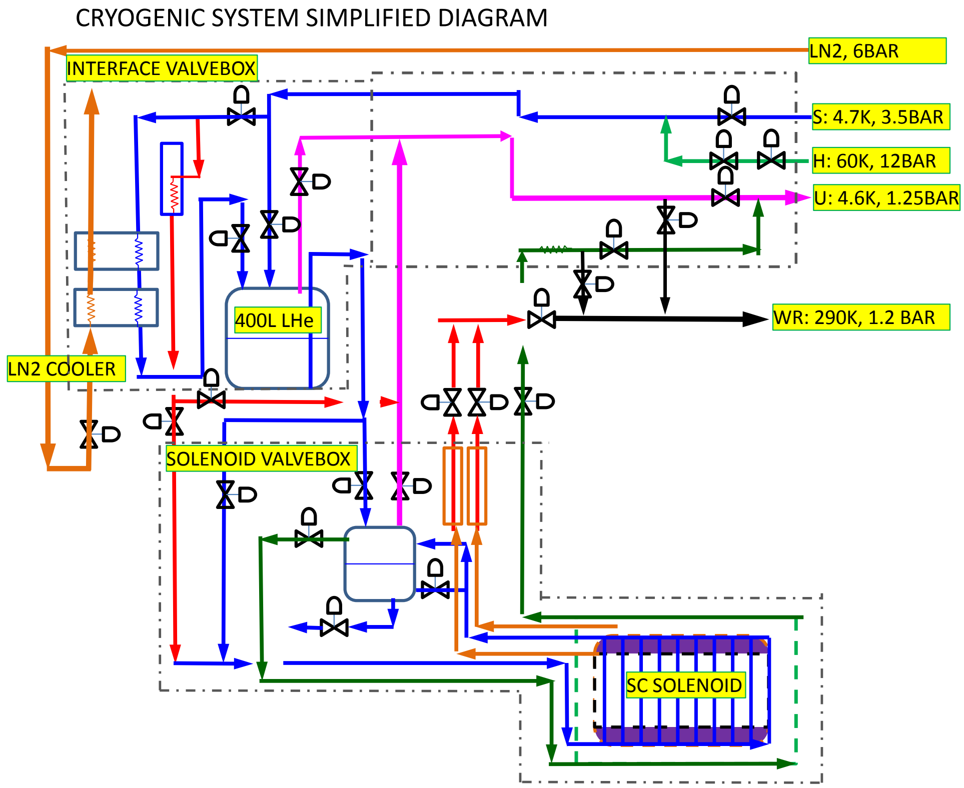

Figure A.9: sPHENIX Magnet Cryogenic Control System

A.3 Magnet Power Supply

A.3.1 Elements of the Power Supply System

Figure A.10 shows the main elements of the sPHENIX Magnet powering system.

L Solenoid = 2.5 Hy The solenoid is represented as two inductors in series, as it constructed in two layers. The connection between the two layers is brought outside the solenoid, to be used by the quench protection system. It is close, but not exactly, a true center tap. The two layers have slightly different number of turns (531 vs 536), and the inner winding has greater capacitive coupling to the support cylinder.

Rd = 68 mΩ Rd is energy dump resistor, used to quickly reduce the current in the solenoid if a quench is detected. This minimizes the energy absorbed within the solenoid. It is split in two, with a soft reference to ground at the center point. With this split, the voltage on either side of the solenoid to ground is only half the full dump voltage.

Rg = 67 mΩ Rg limits the ground current, should the coil fault to ground. The voltage

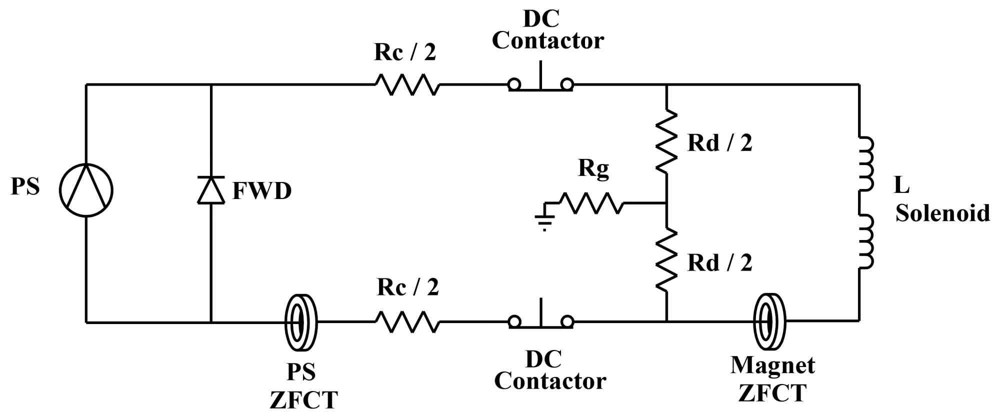

Figure A.10: sPHENIX Magnet powering system

across Rg is monitored by a ground fault detector.

Magnet ZFCT The magnet zero flux current transducer (ZFCT) accurately measures the current into the solenoid. It differs from the power supply current by the current flowing through the dump resistor. For this reason, this is the ZFCT used to regulate the current in the power supply.

DC Contactor In the event of a quench, the DC contactors are opened, and the power supply is disconnected from the solenoid. The full solenoid current is then directed through the energy dump resistor.

Rc = 1.25 mΩ (SLAC Configuration) Rc is the cable resistance. It determines the time to ramp down the current through the freewheeling diode (FWD) when the power supply turns off.

PS ZFCT The power supply ZFCT is for testing purposes, as it does not represent the solenoid current as accurately as the magnet ZFCT.

FWD The freewheeling diode (FWD) provides a current path when the power supply is turned off or trips.

PS The power supply (PS) nominally operates 4.6 kA and less than 20 V. The unit is manufactured to operate up to 8 kA and 40 V. Taps on the input transformer are used to reduce the maximum operating voltage.

A.3.2 Operating Conditions

1. Ramping Up to Full Current

Under the conditions where the current is ramped from zero to 4.6 kA at a rate of 2.5 A/sec:

(a) The time to reach full current is (4,600 A) / (2.5 A/sec) = 1,840 seconds = 30.7 minutes.

(b) The voltage across the magnet is V m = L di/dt = 2.5 Hy x 2.5 A/sec = 6.25 V.

(c) The current through Rd is Vm / Rd = 6.25 V / 68 mΩ = 92 Amps

(d) The peak power supply voltage is Rc (Im + Id) + Vm = 1.25 mΩ (4.600 + 92) + 6.25 = 12.1 V.

2. Slow Discharge through FWD and Rc

(a) Time constant τ = L / R c = 2.5 Hy / 1.25 mΩ = 2,000 seconds = 33.3 minutes

(b) Time to decay from 4.6 kA to 100 A (as an example), Td = -τ ln(I / Io) = -33.3 ln (100 / 4,600) = 127.5 minutes = 2.1 hours

3. Fast Discharge through Dump Resistor

(a) Time constant τ = L / Rd = 2.5 Hy / 68 mΩ = 36.76 seconds

(b) Time to decay from 4.6 kA to 100 A (as an example), Td = -τ ln(I / Io) = -36.76 ln (100 / 4,600) = 140.4 seconds = 2.34 minutes

A.3.3 Monitoring the Solenoid

The change in state of a conductor from superconducting to resistive is called a quench. The function of the quench detector is to measure small values of resistance by the voltage they create. Figure A.11 shows the wires connected to parts of the solenoid to sense internal voltages.

A.3.3.1 Quench Detection During Ramping

The quench detector should be sensitive to a voltage rise of about 100 mV. This is simple when the current in the solenoid is constant. But, when the current is ramping up or down, the induced voltage, $V = Ldi/dt$, is much greater than 100 mV. With a ramp rate of 2.5 A/sec, V = 6.25 V.

There is a voltage tap at the connection between the inner and outer solenoid windings. During ramping, if the inductance of these windings were identical, the voltage across the top coil (VT05 with respect to VT07) would be exactly negative of the voltage across the bottom coil with respect to the same point (VT10 with respect to VT09).

The sum of these two voltages would add to zero. An imbalance caused by a 100 mV quench voltage can then be detected in the sum.

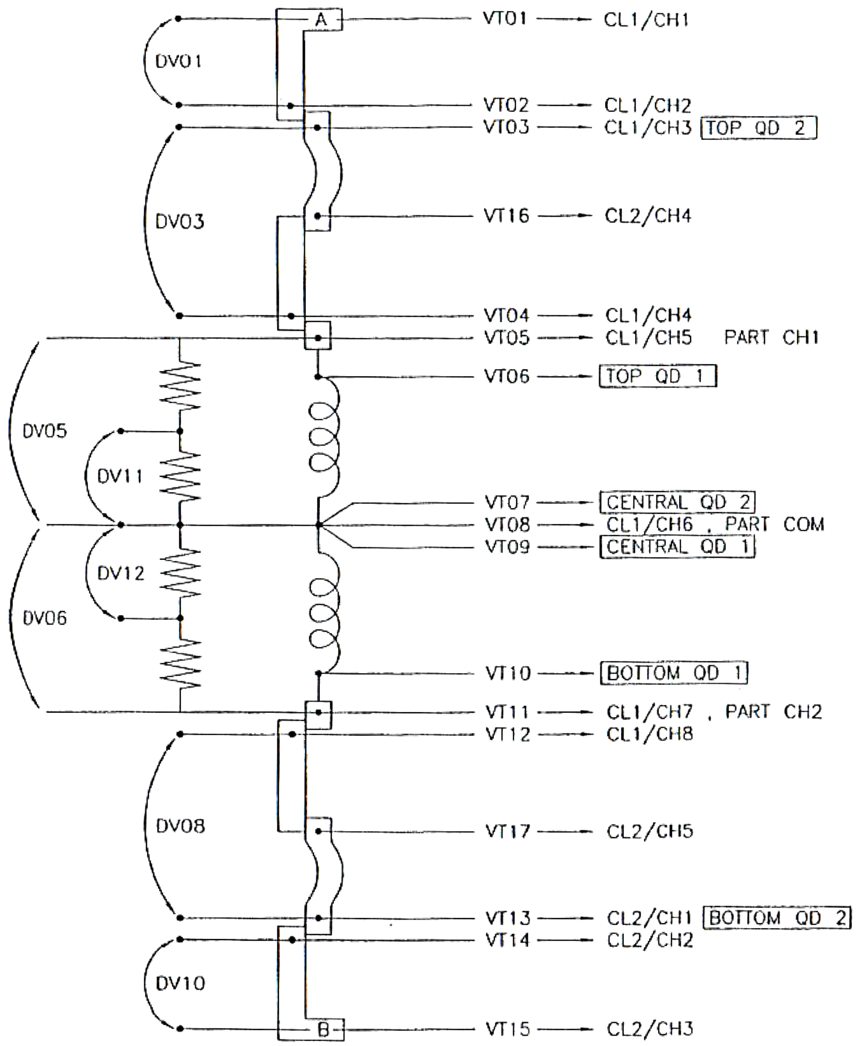

Figure A.11: sPHENIX Magnet voltage taps

A.3.3.2 Practical Considerations

The inner and outer coil inductances are not identical.

1. The winding turns are not equal. The number is slightly different, 531 vs 536. This can be corrected by scaling the voltage tap value slightly before summing the two halves of the solenoid voltages.

2. The inner coil has greater capacitive coupling to the supporting cylinder than the outer coil. Even if the coils had identical initial inductances, this coupling imbalance will cause an imbalance in induced voltage. This is effect is a function of ramp rate. To reduce this effect, the summing correction for the static inductance difference is adjusted for a given ramp rate.

A.3.3.3 Energy Extraction

When a quench is detected, DC contactors are opened, removing the power supply from the load and directing the load current through the energy dump resistor.

The energy dump resistor causes the current in the solenoid to decay with a time constant of 36.8 seconds. This minimizes the heating of the quenched portion of the magnet. The peak voltage across the magnet is approximately 640 V, which due to the center ground reference at the energy dump resistor, is a maximum of 320 V with respect to ground on either side of the solenoid. By comparison, the time constant for a slow decay through the freewheeling diode for a normal shut down is 33.3 minutes.

The quench protection of the BaBar magnet was externally reviewed in October 1996. At the end of that review, additional information was requested and a second review was held in January 1997. The final report was delivered in March 1997. The report concluded that the quench analysis was complete. Based on this analysis it was shown that, even without a fast discharge, a quench would not develop temperatures that would cause a catastrophic magnet failure. As a key component of the fast discharge, the energy dump resistor was also studied, and found to provide adequate protection for the magnet.

A.3.3.4 Development of a New Quench Detector

Fifteen years have passed since the original quench detection system in the BaBar experiment has been designed and implemented. In the future implementation which will be done by the cooperation of Superconducting Magnet Division and the Collider-Accelerator Department, new hardware and software will make more accurate and reliable quench detection possible for this Magnet.

A.3.4 Magnetic Field Simulations

As the return yoke in sPHENIX is very different than the original BaBar configuration, detailed field simulations are needed to understand the changes in shape and strength of the field. In a first step 2D simulations were done using the standard commercial opera software package.

These 2D simulations, Fig. A.12, assume a rotational symmetry of the setup and are a starting point for GEANT4 detector and physics simulations.

As the field depends on the dimensions and shape of the return yoke, which is not completely symmetric, and specifically on the distance of the two plug-doors with the beam openings, more detailed 3D simulation are necessary. To simplify the simulations the return yoke was first replaced by a solid cylinder of magnet steel with the appropriate density, Fig. A.13. The calculated magnetic field through this structure, at 4596 A, along

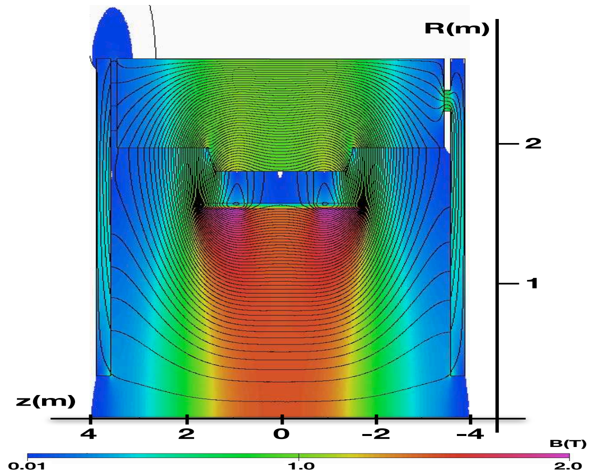

Figure A.12: 2D opera simulations of the sPHENIX setup

the longitudinal axis (beam direction) is shown in Fig. A.14.

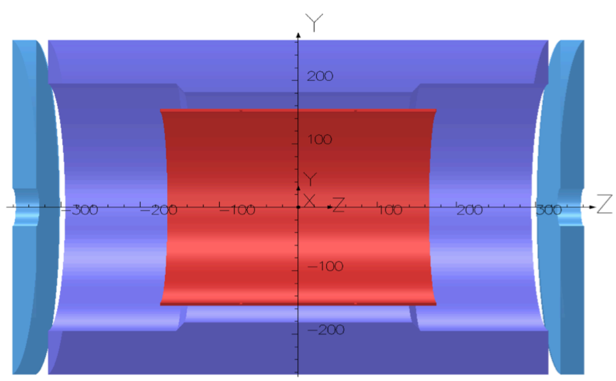

Figure A.13: 3D opera Model

These simulations can also be used to calculate the forces on the solenoid. Apart from the mechanical forces due to the cool down, the dimensions and shape of the yoke and plug doors as well as the position of the coil within the return yoke creates sizable forces on the coil.

The plate structure of the return yoke is a challenging setup for the finite-element analysis, but these details are needed for understanding possible changes in the shower shape due to the scintillator gaps, Fig. A.15.

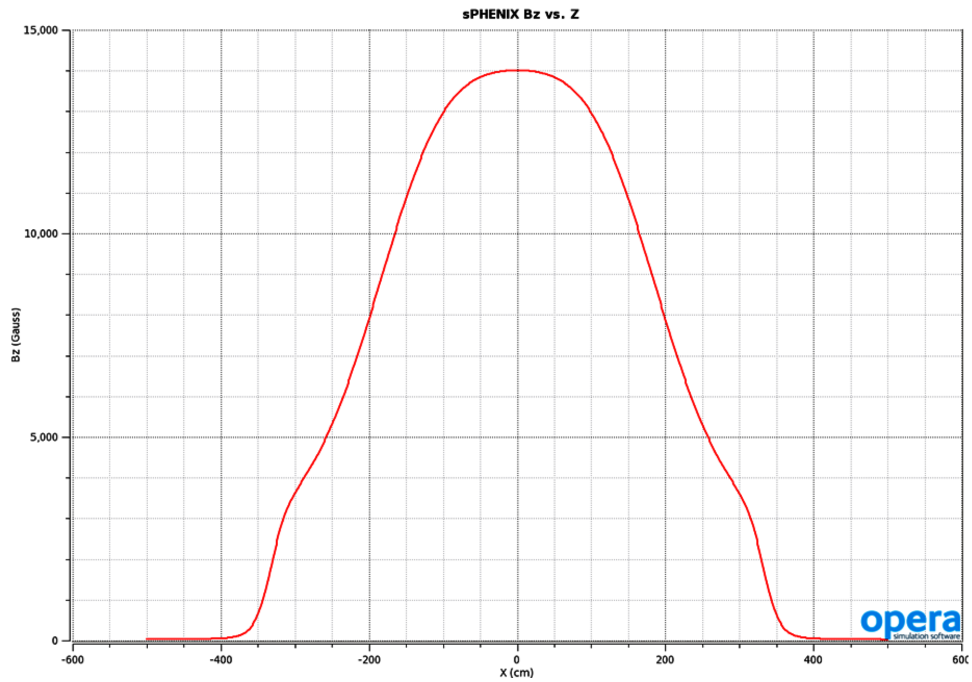

Figure A.14: Calculated magnetic field along the longitudinal axis (beam direction) for the symmetric return yoke model

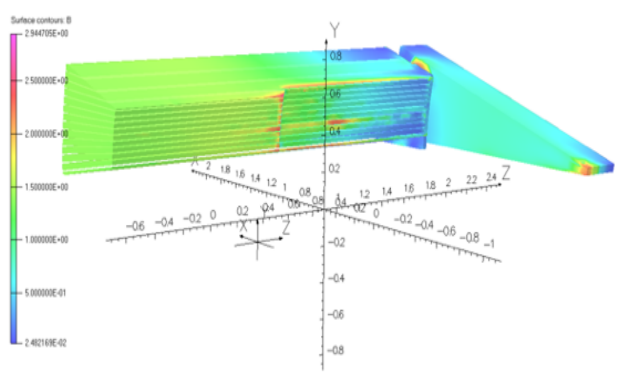

Figure A.15: 3D OPERA model detail of the field in the HCal plates

A.3.5 Magnetic Force Simulations

The BaBar superconducting coil will be placed inside a non-symmetric flux return yoke as a part of the sPHENIX magnet assembly. This can give rise to axial offset forces on the coil. Simulations with OPERA have been run to understand what these forces and torques will be on the coil during its operation at 4596 A, where the central field is about 1.4 T.

Figure A.16 shows the non-symmetric model for the sPHENIX flux return yoke in the

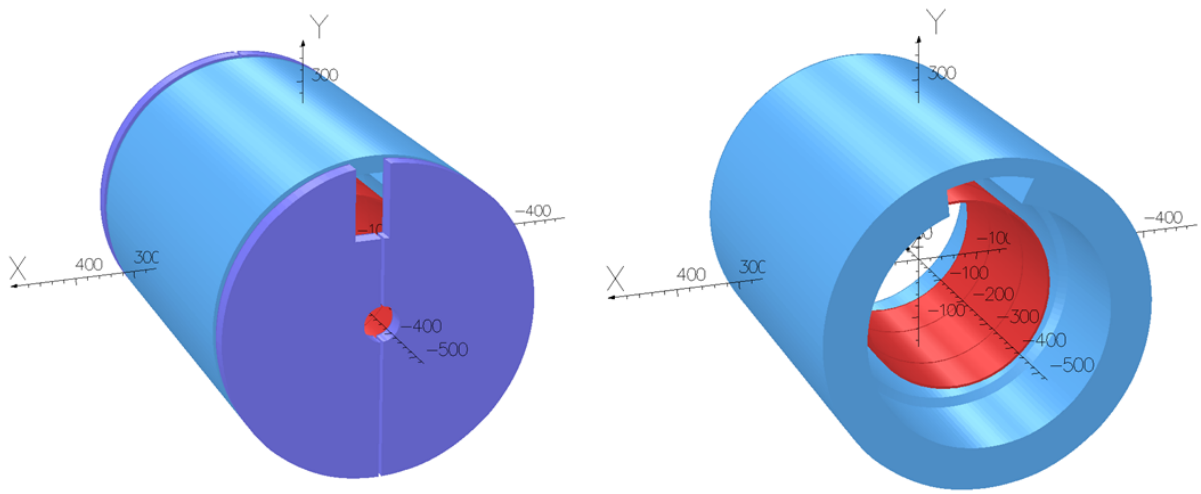

Figure A.16: Yoke and end-cap cuts from the OPERA Model, as viewed from the ”south” or the ”lead” end.

OPERA simulation, it is modelled using 1006 steel. The notch in the south end door is to allow for the valve box, as previously shown in Figure A.3.

In the symmetric model the forces along the beam axis are symmetric, the simulation for the total forces are balanced at about $\pm$ 5.65 $\times$ 10^6 N. The calculated forces on the two end doors are about $\pm$ 8 $\times$ 10^5 N.

From the simulations of this model, the magnetic forces and torques at the yoke center due to the coils being misaligned are shown in Table A.3.

Table A.3: Magnetic forces (Fx, Fy, Fz) and torques (Tx,Ty,Tz) in the non-symmetric model.

	Fx [N]	Fy [N]	Fz [N]	Tx [N-cm]	Ty [N-cm]	Tz [N-cm]
No misalignments	-1043	-14072	15640	335007	160904	0
Coils shift, dx=2 mm	9412	-14077	15647	335345	157079	-2815
Coils shift, dz=3 mm	-1033	-13903	21207	354464	159326	0

A.3.6 Field Mapping

To achieve the required momentum resolution the solenoid field has to be known in detail, specially towards the edges of the tracker acceptance where deviations from the ideal solenoidal field are expected.

There will be three separate monitoring tasks. The low and full field tests scheduled for 2016 and 2018 were just a monitoring task where we plan to use a few commercial hall probes. For the low field test we installed a 3D probe close to the center of the magnet monitoring the expected field of a few hundred Gauss.

For the full field test at a current of 4596 An additional commercial high resolution NMR probes was installed in the magnet. The NMR probes attempted to provide a high resolution measurement of the field and may later be installed as permanent monitoring probes in the final setup.

For the final setup we currently plan to install a series of NMR probes on the outside of the mapping detectors and rely on detailed field simulations.

A.4 Tests for the Superconducting Solenoid Magnet

There were a series of tests done at room temperature in April 2015 for the initial inspection and acceptance of the superconducting solenoid after it was shipped to BNL. The high potential (hipot) tests (up to 520 V) recorded a leakage current of 0.15 μA. The impulse test done at 400 V was successful in that the waveform measured didn't indicate any turn-to-turn short in the magnet coils. We also ramped the current across the solenoid slowly from 0 to 2 A and 5 V to measure the inductance of the solenoid to be about 2.3 H (very close to 2.2 H that was measured in 1997). In addition, we have also performed a leak check which found no noticeable leaks and a 6.6 bar pressure test which was also successful (even up to 85 psi).

In March 2016, a low-field and low-current test has been performed for the superconducting solenoid. We have cooled the magnet with helium down to about 4.5 K and brought the current to 100 A. This was as much a test for the entire cryogenic system as it was to test and verify the expected magnetic field (about 300 Gauss in the center). P. Joshi has also tested his quench protection system that he had used in the Superconducting Magnet Division for other purposes.

In February 2018, we have further performed a high-field and high-current test for the magnet. This time, the entire solenoid cryostat was surrounded by thick steel plates, in a box configuration, which served as the media for the return field. The above-mentioned quench protection system has been upgraded mainly by Z. Altinbas and C. Schultheiss to include a PXIe system with 3 PXIe-4300 boards (24 channels) with some circuitry (such as anti-aliasing filter) adapted from the RHIC quench protection. This system was built such that it can be used in the future sPHENIX experiment at 1008 of RHIC.

On February 13 and 16, 2018, we successfully ramped the magnet current gradually to the peak current of 4830 A, more than 5% over 4596 A, the nominal operating current that the BaBar experiment has used for this magnet during their years of operation. At the peak current, the magnetic field that we measured and recorded with our 3D gauss probe was about 1.34 T. In both occasions, we stayed at the peak current and magnetic field for about 40 minutes. This duration (that we could stay at the peak current) was limited by the amount of liquid helium available in the cryogenic system at Building 912 to keep the Magnet in the superconducting state and we needed to have another hour to perform a slow discharge for the Magnet. Figure A.17 shows the magnetic field and the ramping Magnet current. At the end, we executed a slow discharge from the peak current until it dropped below 1000 A and we then did a fast discharge as the current was deemed to be too low to do any possible damage.

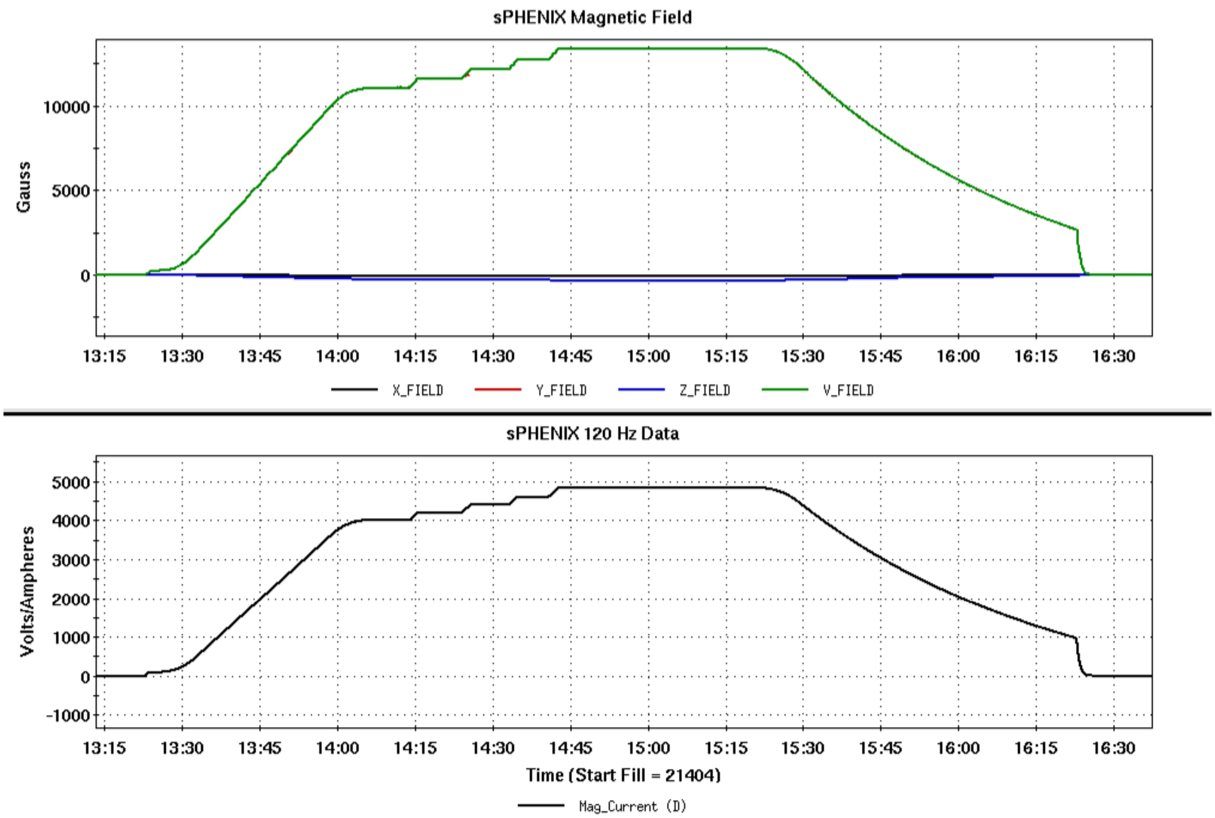

Figure A.17: The Magnetic Field and the ramping Magnet Current during the successful ramp to the peak current of 4830 A on Feb. 13, 2018. After staying at the peak current for about 40 minutes, we executed a slow discharge until the current dropped below 1000 A and then we did a fast discharge.

Appendix B

Infrastructure

The sPHENIX detector will be located in the RHIC building 1008 complex Major Facility Hall (MFH). It consists of a central hall and two expanded tunnel areas. Adjacent to the MFH is a 3700 square ft. Assembly Building, a Counting House, and Rack Room. Concrete block shielding is provided between the MFH and the assembly building. The central hall is 57 ft. long by 61 ft. wide and 47 ft. high with a 12 ton overhead crane and (2) 1-ton auxiliary cranes. A 40 ton crane is installed is installed over the assembly area. The expanded concrete tunnel areas on either side of the Central Hall are 53 ft. long by 30 ft. wide and 21.5 ft. high with a 9 6 concrete platform to raise the floor level. The Assembly Hall is steel frame with metal siding. See Figure B.1 for a plan view of the structures.

All buildings are connected to the BNL 13.8 KV AC distribution system. The electrical substations at buildings 1008A and 1008B convert 13.8 KV to 480 volts AC for distribution into the downstream distribution network of 480 V to 208/120 volt transformers and panels.

B.1 Auxiliary Buildings at the Experimental Site

Auxiliary Buildings 1008B and 1008 C contain cooling water pumping stations and HVAC equipment to service the MFH, Assembly building, and Counting House.

B.2 Cradle Carriage

The Cradle Carriage will support the sPHENIX Main Magnet. Four detector systems will be constructed in the inner and outer radius of the magnet. The Beam Pipe passes axially through the magnet/detector center.

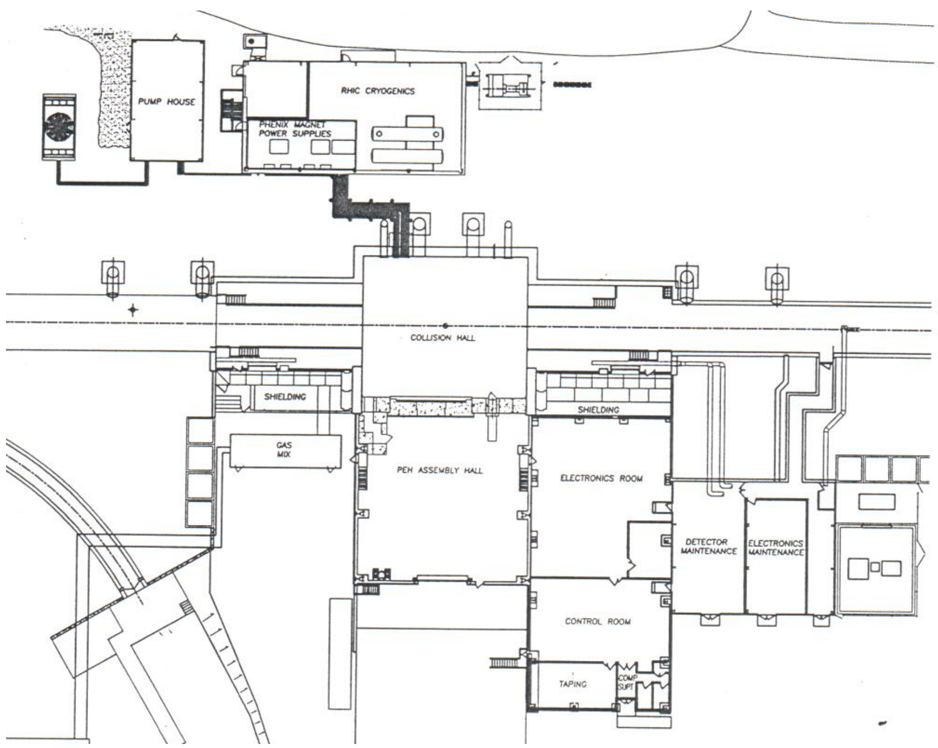

Figure B.1: sPHENIX Major Facility Hall and Auxilliary Buildings

B.3 Electronics Racks

Electronics racks for the detectors will be mounted on the Cradle Carriage and in the Counting House Rack Room. They will be fully enclosed and contain water cooled heat exchangers to remove heat. They will each contain a safety interlock system to shut their electric power & cooling water flow off during conditions such as over-temperature, smoke or water leak detected. Permanent walkways, platforms and ladders, mounted on the Central Pedestal allow for access to the racks. All will be equipped with appropriate safety railings and kick plates.

B.4 Beam Pipe

The sPHENIX Beam Pipe is a cylindrical tube with overall length of 101.2 inches. It is made up from a central 31.5 inch long beryllium section 0.030 inch thick which was gun-drilled from beryllium rod then e-beam welded to the aluminum extension pipes which were TIG welded to 2.75 inch conflat explosion bonded aluminum/stainless flanges. The flanges are bolted to the corresponding flanges on the upstream and downstream beam tube transition sections which increase the beam pipe diameter to 5 inch outside diameter in 2 steps. The sPHENIX beam pipe will be supported from the flanges and also within the central pedestal by low mass supports. sPHENIX will reuse the existing central Be section and modify the transition sections as necessary to accommodate the sPHENIX detectors. In addition, gate valves and pumping ports will be added to allow removal of the central beam pipe sections.

B.5 Shield Walls and Openings

The sPHENIX shield wall is approximately 61 wide by 48 high by 5 6 deep, made from light concrete blocks. A large rolling shied block door measures 30 wide by 36 high. The shield blocks are 20 tons each. The wall is built on a rolling platform that rides on a number of 200 ton each rated Hillman rollers. This wall can be moved away from its opening to allow large detector pieces or other equipment into and out of the MFH. There is a rolling, motor driven personnel door and emergency egress labyrinth separate from the main rolling shield door. There are PVC pipe penetrations for utilities from the assembly hall into the MFH embedded into a concrete sill . Two 3 tubes for cooling water services, twelve 4 tubes for electrical power cables, and eighteen tubes for signal cables are provided. No major modification to the PHENIX shielding configuration is anticipated for sPHENIX.

B.6 Electrical Power

Numerous distribution transformers are supplied by a 480 volt 1200 amp bus that contains eight molded case circuit breakers. This is the primary Normal Power distribution supply that powers all experimental and non-experimental loads. An emergency backup diesel generator provides 150 KW of power to critical loads in the event of on or off site power interruption. A 30 KVA Uninterruptible Power Supply (UPS) supplies battery backed-up 208/120 VAC power primarily to critical computer loads. A 3 KVA UPS supplies backup power to critical safety instruments protecting the experiment. sPHENIX will utilize the existing PHENIX power infrastructure, however, some modifications to the distribution system will be required at the 480/220 volt level.

B.7 Safety System and Control Room Monitoring & Alarm System

SPHENIX will have a real time, monitoring and control system that will take inputs from smoke and fire detection systems as well as crash buttons. Upon detection of an off normal situation from any input, safe shutdown of the experiment will be initiated. Existing PHENIX systems will be utilized to the maximum extent possible, although new components will be necessary to integrate new safety systems for potential new hazards, like oxygen deficiency.

B.8 Cooling Water

Chilled water is required at 20 degrees C for cooling the detector electronics. Pumping capacity is 300 gallons per minute (GPM).The existing cooling towers and chilled water system at the 1008 complex has the capability to meet these specifications. sPHENIX will utilize the existing PHENIX chilled water infrastructure, however, some modifications to the distribution system will be required at the rack level and to satisfy any other new water cooling needs.

B.9 Climate Control

Conventional heating, ventilation and air conditioning (HVAC) is required. Approximately 100 tons capacity currently is in use, 40 tons in the IR, 50 tons in the rack room and the remainder serving the rest of the complex. sPHENIX will utilize the existing HVAC system, with minor additions and upgrades as necessary.

B.10 Cryogenics

A cryogenics supply system is required for the sPHENIX superconducting solenoid magnet. This system is described in the Magnet section of this report.

Appendix C

Installation and Integration

sPHENIX has been conceived to be straightforward to manufacture and assemble, but it still requires significant and well thought out integration and assembly schemes to achieve the specified alignment and positioning requirements of the component detectors. In addition, the design must allow for appropriate access for maintenance and servicing of the functional components of these detectors and to optimize the integration and installation concept. The goal is to balance design tradeoffs while considering the effects on performance, cost, schedule, and reliability. Figure C.1 illustrates the overall design concept for the installed sPHENIX experiment. The following sub sections of this topic indicate how these factors will be addressed in the sPHENIX project.

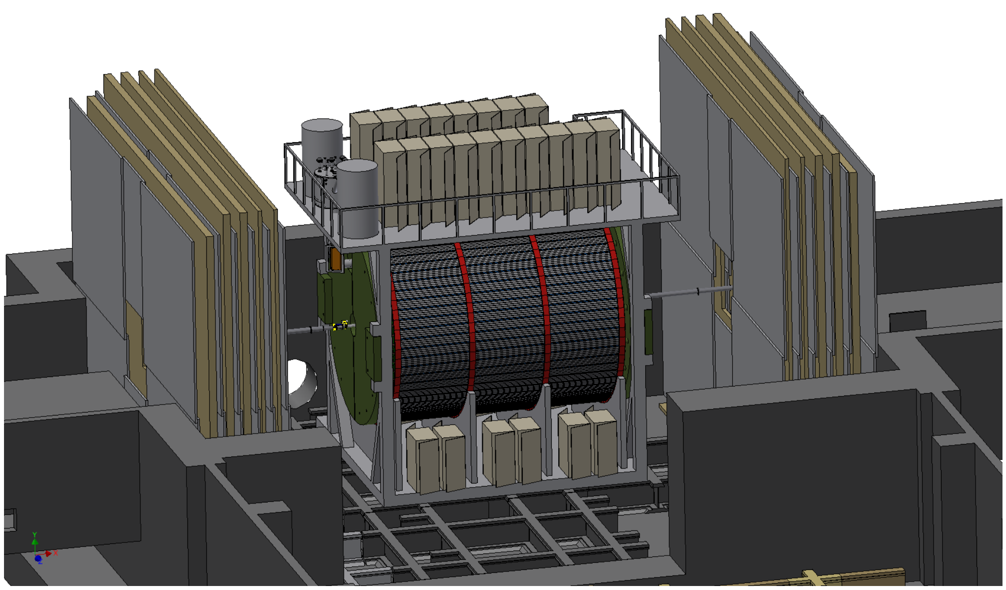

Figure C.1: sPHENIX in IR

C.1 Specifications and Requirements

C.1.1 General Limits and Requirements

The following are the key general requirements that guide the integration, inter detector assembly and installation of the sPHENIX components comprising the overall sPHENIX experimental apparatus. Requirements may be superseded by individual detector subsystem requirements (see subsystem sections).

Table C.1: sPHENIX General Limits and Requirements

Item	General Requirements
Location for final assembly/ Installation	PHENIX Assembly Hall
Assembly Hall (”AH”) Crane	rated at 40 tons
Interaction region (”IR”) Crane limit	12 tons plus 2 auxiliary, 1 ton cranes
Floor Loading Limit	4000 psi max
Assembly support surface	existing PHENIX rail system
Clearance requirements	2 inches (50 mm), between subsystems
Positional precision	0.1 mm
Angular precision	10 milliradian (roll, pitch and yaw)
Positional stability	0.5 mm
Angular stability	10 milliradian (roll, pitch and yaw)
Positional repeatability	1.0 mm
Angular repeatability	10 milliradian (roll, pitch and yaw)
Positional tolerance	(see individual detector specifications)
Angular tolerance	(see individual detector specifications)
Temperature and humidity	-10 to 50 deg C and 0-100 percent R.H.
Magnetic field	0–2T inside magnet, 0–100 Gauss field outside
Radiation environment	to be specified
Detector cooling requirements	(see individual detector subsystems)
Rack cooling requirements	2.0 gpm @ 50 deg F, for 2 kW per rack
Cryo requirements	(see Magnet Section)
Monitoring and safety system requirements	(see Infrastructure Section)
Overall size requirements	fit through the sPHENIX sill on existing rail system (see Figure C

C.1.2 Configuration Management and Control

In order to assure that the various subsystems of the sPHENIX experiment honor the space requirements for all other components, not interfere with other subsystem and/or infrastructure features of the sPHENIX experimental location, and assure that the integration and installation concepts are achievable, outline/interface drawings will be prepared for

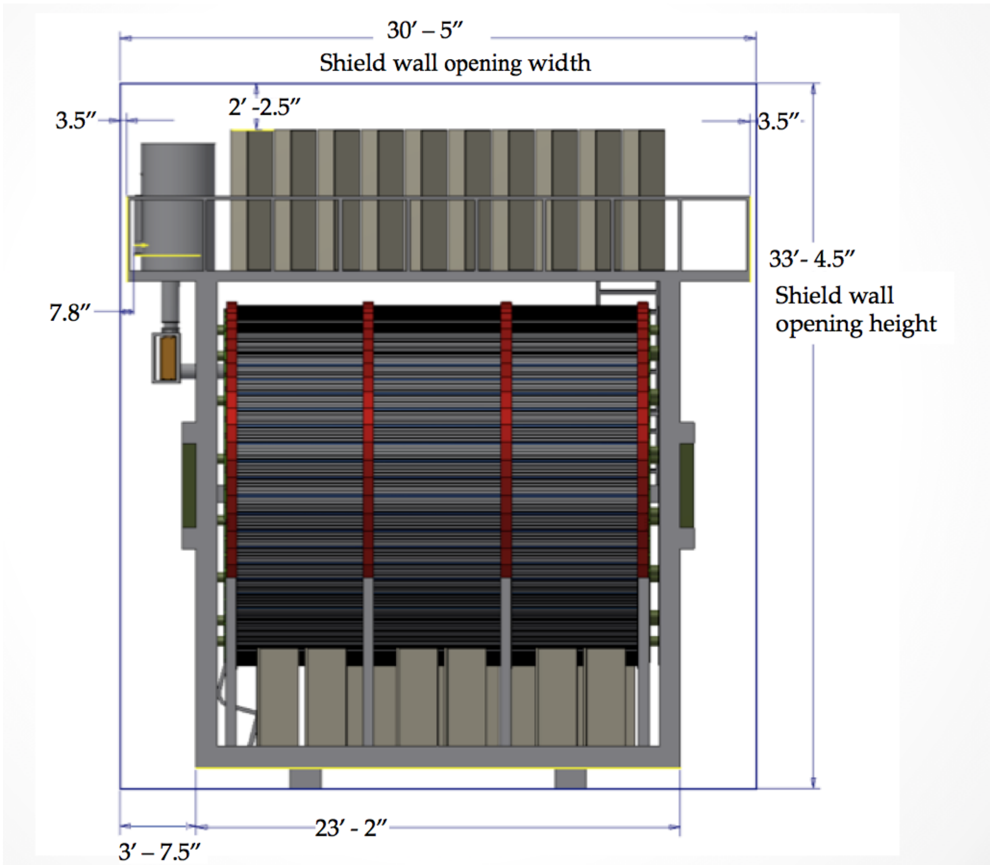

Figure C.2: sPHENIX Overall size

each detector subsystem and an overall envelope control drawing will be prepared for the integrated sPHENIX experiment.

Subsystem outline/interface drawings will provide the defining exterior envelope in to which the subsystem components fit, key dimensions for subsystem components which interface with other subsystems and/or infrastructure, and any other information pertinent to the space to be occupied by the subsystem and its relationship to adjacent subsystems and infrastructure. Figure C.3 is the subsystem outline/interface drawing for the EMCal detector subsystem.

Subsystem outline/interface drawings will provide the defining exterior envelope in to which the subsystem components fit, key dimensions for subsystem components which interface with other subsystems and/or infrastructure, and any other information pertinent to the space to be occupied by the subsystem and its relationship to adjacent subsystems and infrastructure. Figure C.3 is the subsystem outline/interface drawing for the EMCal detector subsystem.

The overall envelope control drawing will provide the limiting space allocations for each of the detector subsystems, as well as space allocations for structural support, integrating

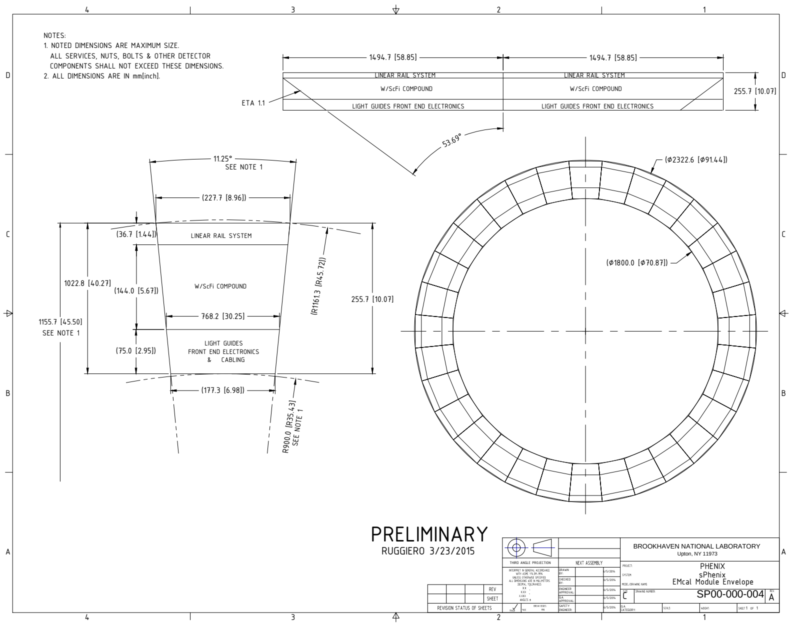

Figure C.3: EMCal Envelope Control Drawing

interfaces and all services.

Figure C.4 is the overall envelope control drawing for the sPHENIX experiment.

All subsystem design drawings, fabrication and assembly procedures and all other documentation which define the sPHENIX assembly, installation and component subsystems will comply with BNL and DOE requirements that will be governed by sPHENIX controlled documents for Configuration Management and Documentation Control Systems.

C.1.3 Weight Estimates

In order to properly evaluate the design and adequacy of the integration and installation conceptual design which will proceed parallel to the detailed design of the component detector subsystems and infrastructure, it is necessary to have reasonable estimates of weights for the major components. The following table provides the estimated weights for the major subsystem components for sPHENIX.

C.1.4 Alignment Requirements

Alignment of the detector subsystems to each other and to the RHIC nominal beam path, as reflected by the positional and angular orientations relationship of the detector subsystem components to each other and to the sPHENIX global coordinate is essential to

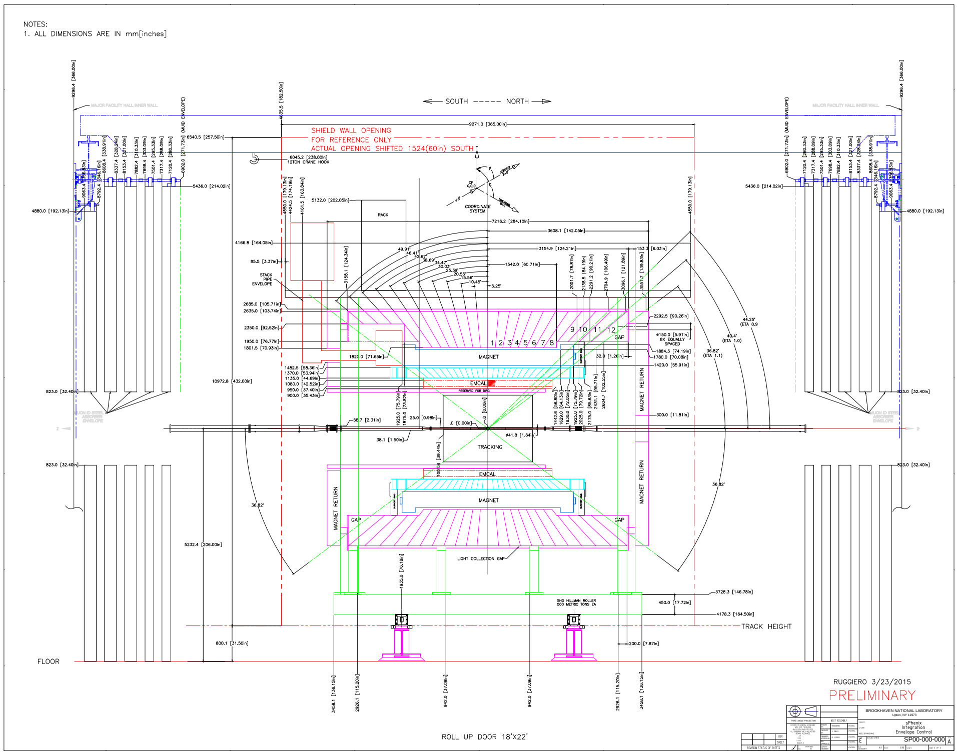

Figure C.4: sPHENIX Envelope Control Drawing

the proposed performance of the sPHENIX experiment. Internally, each detector subsystem component is aligned to the subsystem's own coordinate system as defined by each subsystem. This alignment is then reflected to the global system by means of inspection of dimensional data with respect to reference points ("fiducials") to be established on the exterior of each component. These reference points are used in the assembly and installation process to establish position and orientation of these components and by extension the internal features of each component to the sPHENIX global coordinate system.

Each component, as it is assembled and installed into the sPHENIX support structure, is to be aligned by means of built-in adjustment to achieve specified precision with respect to the experiment support structure (i.e. the Cradle Carriage) which shall have fiducial references related by survey. After the Cradle Carriage is assembled with all subsystems except the Min Bias, INTT and MVTX detectors and is moved to the Interaction Region ("IR"), THE CC is to be positioned and aligned to the sPHENIX global coordinate system at the nominal Interaction Point ("IP").

The sPHENIX global coordinate system is related to the RHIC coordinate system from the Interaction Point the center of the RHIC ring and the straight line of the RHIC ring orbit through the sPHENIX IP.

Table C.2: sPHENIX Estimated Weights of Major Components

Subsystem	Weight	Notes
Inner HCal	64,000 lb, 32 ton	2000 lb/sector
Outer HCal	854,000 lb, 427 ton	27,000 lb/sector
EMCal (with mounting)	61,000 lb, 31 ton	900 lb/sector
Inner HCal Assy Rings	1650 lb, 1 ton	total, 2 rings
Inner to Outer load transfer rings	6400 lb, 3.5 ton	total, 2 rings
Flux return end caps	226,000 lb, 113 ton	
Magnet + stack wt	42,000 lb, 21 ton	
TPC	1000 lb, 1/2 ton	
Min Bias	68 lb, 1/30 ton	17 lb/quadrant
INTT	500 lb, 1/4 ton	
MVTX	200 lb, 1/10 ton	
Detector services and support equipment	5000 lb, 2.5 tons	
Total Detector load on Cradle Carriage (CC)	1,261,000 lb, 631 tons	
CC weight without magnet and detectors	250,000 lb, 125 tons	
Total Detector load on Cradle Carriage (CC)	1,261,000 lb, 631 tons	
CC weight without magnet and detectors	250,000 lb, 125 tons	

Positional precision and alignment tolerances for the individual detector subsystem component internal features are established for each individual detector subsystem independently (see the appropriate subsystem for details). The subsystem components and/or the support structure will be designed with appropriate adjustment capability to achieve the specifications indicated in the previous section.

Precision is determined by combining the accuracy of the measurement method (survey) for locating the individual fiducial points for subsystem components directly with the fineness of adjustment provided in the subsystem mounting system.

Stability is the tendency for the assembly and its components to remain in the same location over a period of time, under normally varying environmental conditions for both operational and non-operational conditions.

Repeatability is the tendency of the assembly and its components to return to the same location after maintenance operations requiring disassembly and reassembly and/or temporary displacement and return of the entire assembly or any of the components (usually for maintenance purposes).

Tolerance is the amount by which a measured position or angle can vary from its nominal ″exact″ position or angle. This is the sum of measured variance plus the measurement precision, repeatability and stability. For internal components of subsystems, the tolerance with respect to global coordinates is calculated from a combination of the tolerance of the external fiducial points and the tolerance of the relative dimensional feature of internal features to the external fiducials. In some cases the tolerance calculations might require combining multiple relative tolerances.

C.1.5 Service Requirements

Adequate space is to be provided to route appropriate services to all of the detectors including power, signal and monitoring cables, cooling channels (air cooling) and piping (liquid cooling) for removal of heat generated by detector electronics and distribution equipment for branching and integrating electronics signals, electric power and cooling from detector service racks to module/sector front end electronic distribution panels and flow distribution manifolds to the installed detector components. Within the components these services are to be distributed to individual active components as described in the subsections describing the individual detector subsystems.

In addition, space is to be provided for cooling services and power to the subsystem racks from the cooling source(s) and line power breaker boxes, respectively. Space is to be provided as well to route signals to the rack room. Refer to the infrastructure for more detailed information on service requirements.

During the research and development process for each of the detector subsystems, prototype mockups (dimensionally accurate, non-functional) are to be developed to assist in planning the design of adequate space for services. A mockup of an Inner HCal half-sector is shown in Figure C.5.

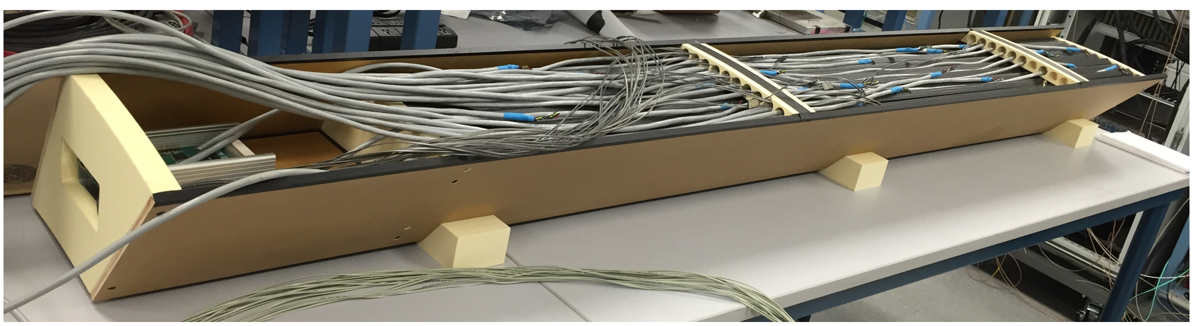

Figure C.5: Inner HCal Half-sector mockup

C.1.6 Accessibility

The sPHENIX detector subsystems will be designed to operate without maintenance for extended periods. Maintenance of the active detector components and the magnet is not possible during a run, except that access is provided to the subsystem rack electronics on all levels, to the magnet valve box and to power and cooling sources and primary distribution equipment. Limited access to the outer HCal detector electronics is possible, but it is not a requirement. Limited access to external interface electronics on all of the detectors is possible during an extended access period during a run (on the order of one or more weeks in duration), but any individual internal component of any detector subsystem is only accessible during a major shutdown of three or more months by reversing the assembly process described later in this report.

C.1.7 Quality Control

sPHENIX engineering will implement the full quality assurance program described elsewhere in this document by establishing procedures to assure that the design of sPHENIX meets the requirements of BNL, DOE and industry best practices, including implementing the appropriate configuration management, documentation control, work planning, quality control testing and inspection and performance verification.

C.2 Component Integration

C.2.1 General Integration Concepts

sPHENIX is designed to be integrated into a single structural assembly wherein a central support structure, the cradle carriage (”CC”), provides a base on a set of roller bearings, which in turn supports a set of four structural arcs (”cradles”) to support the Outer HCal detector subsystem and pillars to support an intermediate level platform, an upper platform and the north and south flux return end caps/pole tips.

The superconducting solenoid magnet is support by 12 mounting feet, six each equally distributed at the north and south ends of the magnet in the annular space between the magnet outer diameter and the Outer HCal inner diameter. These mounting feet also provide alignment adjustment for the magnet in all directions.The Outer HCal provides two additional support rings on its interior diameter onto which the interior Inner HCal and Tracking detector subsystems (TC, INTT and MVTX) are mounted. The EMCal detector subsystem is divided into 64 (32 north and 32 south) sectors which are individually mounted to adjacent Inner HCal sectors by bearing rails.

There will be two sets of four roller bearings under the base platform. They will be rotatable to allow the entire experiment assembly to move east or west and, when rotated 90 degrees, north or south. Relocation of the assembly in these directions is accomplished on the existing PHENIX rail system and allows for repositioning of the assembly in the IR and moving from the AH to the IR for installation, maintenance and upgrade operations. The 2 sets of rollers are positioned with a hydraulic lifting piston on each of the 4 points corresponding to intersection crosses of the sPHENIX rail system. This allows the entire CC to be lifted at 4 points to change the orientation of the roller bearing sets from north/south to east/west and back. Figure C.6 shows an exploded view of the detectors which comprise sPHENIX.

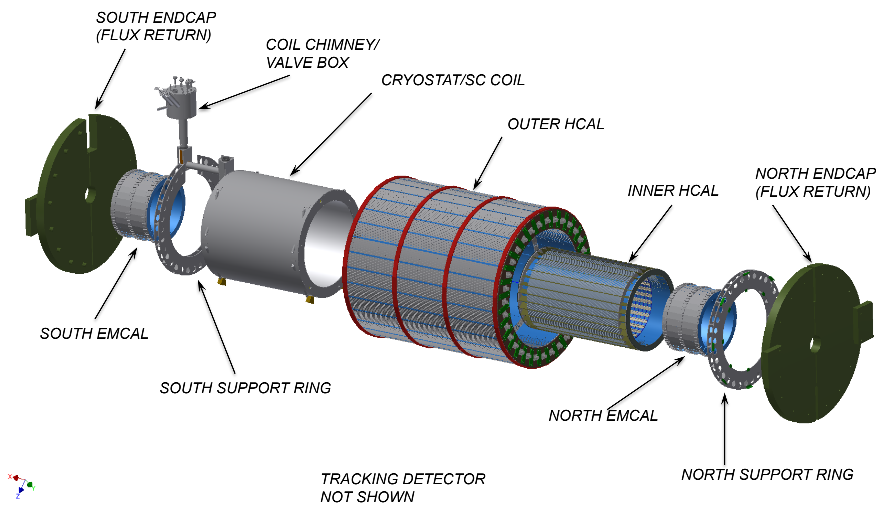

Figure C.6: sPHENIX exploded view

C.2.2 Structural Load Support

Roller bearings for the CC are to be sized for approximately twice the estimated load of the fully assembled sPHENIX experiment. The CC base will be built of structural steel and support the four cradles and four pillars which will be welded to the base as well as provide the lower level platform for detector electronics racks. The Outer HCal will be fully supported by the cradles while the mid and upper platforms and magnet flux return end caps will be supported by the pillars.

The outer HCal is comprised of 32 sectors which are tied together at their north and south ends by splice plates. The loads of each of these sectors is transferred through the splice plates to the cradles. Interior to the Outer HCal will be the magnet mounting feet and Inner HCal support rings which will transfer the magnet and inner detector structural loads separately to the base through the Outer HCal.

The Inner HCal is comprised of 32 sectors each of which has mounting provisions on its inner diameter for two EMCal sectors. Each of the 32 Inner HCal sectors is mounted on its north and south end plate to end rings. The north and south end rings that tie the 32 sectors together are then mounted to the north and south structural rings which transfer the load of the Inner HCal sectors plus the EMCal sectors to the Outer HCal and through the Outer HCal to the cradles to the base to the roller bearings to the rails and finally to the floor.

The TPC subsystem will also have a support structure which attaches to the north and south structural rings that will transfer its load in a similar manner.

The MVTX and INTT will be integrated into a dual hemisphere support frame (upper and lower). Each frame hemisphere will have a 3 point support onto a dual rail and bearing system in which the bearings will slide along pathways on the rail which allows the upper and lower frames to ride in separately and moved away from the beampipe until the frames have cleared the beampipe flanges. The lower frame is positioned first then the rail is adjusted in 3 dimensions to achieve the alignment precision required. Then the upper frame is brought into position and is mated to the lower frame by kinematic mounts. Figure C.7 shows the load path through the support structures.

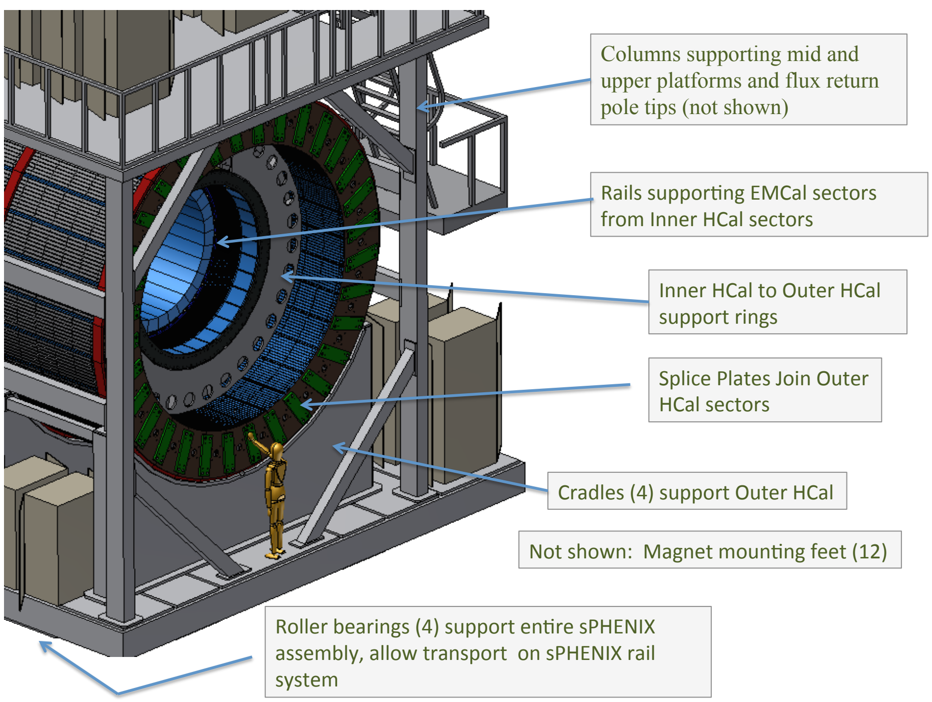

Figure C.7: sPHENIX Structural Support

C.2.3 Alignment

The sPHENIX overall alignment concept will be as follows:

- Internal alignment of detector subsystem components in the interior of the detector subsystem will be aligned as required by the subsystem at the subsystem subassembly level in accordance with the subsystem requirements, related to a set of external fiducials on the subassembly sectors/modules which are deliverables from the subsystem to the sPHENIX AH where final installation will take place. These fiducials will be documented to enable analytical reconstruction of the internal relevant features and to define a nominal axis and centerpoint relationship to the fiducials for each of the subassembly modules.

- The CC base and cradle assembly will be provided with adequate precision alignment features (reference fiducials and adjustment features) to define the nominal experiment axis and center point and the position of the initial Outer HCal sector to align its reference axis and center point to that of the CC Base and cradle assembly. Survey and shimming will be employed to fix the position of the initial Outer HCal sector within the tolerance specifications indicated in the general requirements section, above.

- As each additional Outer HCal Sector is installed it will be surveyed, adjusted and shimmed into place with respect to the required tolerances, until the lower half of the Outer HCal is completed. Figure C.8 shows the initial Outer Hcal sector installed and aligned.

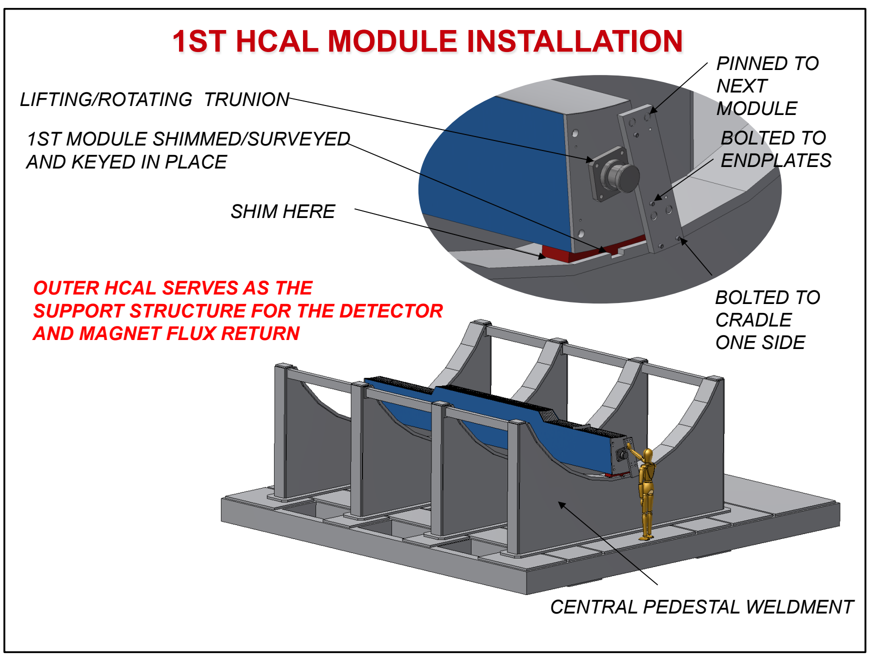

Figure C.8: sPHENIX Initial Alignment

- The Superconducting solenoid magnet will have been surveyed and been sufficiently tested to establish a nominal magnetic axis and centerpoint which will have been related to external fiducial points on the magnet and those relationships recorded. The magnet will have 12 adjustable mounting supports attached to position and secure the magnet onto the inner surface of the Outer HCal.

- After the lower half of the Outer HCal installation is completed, the magnet shall be mounted, surveyed, aligned and secured to the Outer HCal in accordance with requirements.

- The remaining Outer HCal Sectors are installed, surveyed, adjusted and shimmed into place with respect to the required tolerances, until the upper half of the Outer HCal is completed.

- The Inner HCal sectors are installed into a complete detector aligned using mechanical precision features, survey and shimming to achieve the desired alignment of each of the sectors to each other and external fiducial points. The entire assembly is then surveyed, aligned and secured onto the Inner HCal to Outer Hcal support rings.

- Each of the 64 EMCal sectors is then installed onto the rail systems on each of their respective Inner HCal sectors, surveyed, positioned, adjusted and secured into place in accordance with required tolerances. Figure C.9 shows the installation of an EMCal sector.

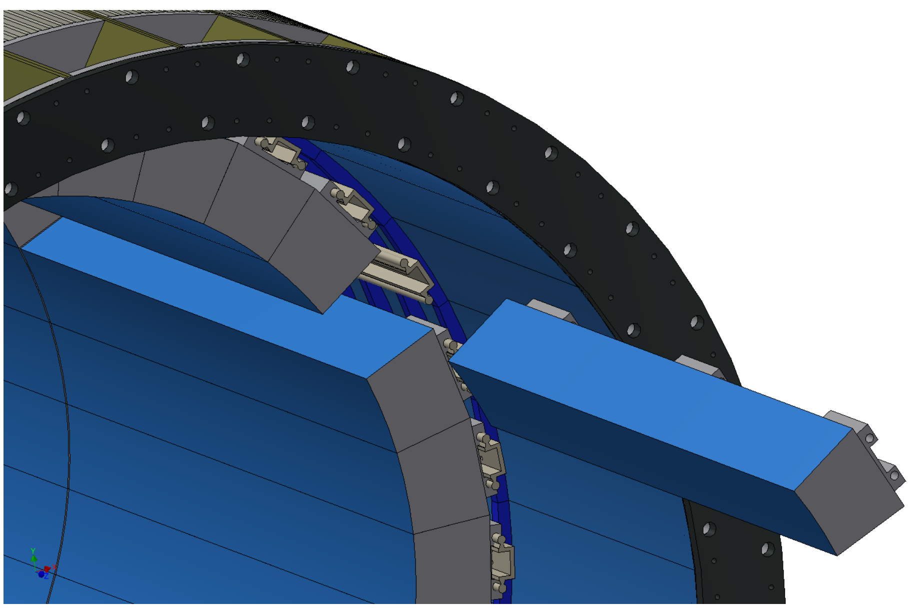

Figure C.9: EMCal Sector Installation

- The detector assembly on the CC support structure in the AH is completed by installing and aligning the TPC subsystem with the nominal axis and centerpoint using the alignment adjustments designed into the support brackets.

- Next, the entire CC is moved west on the sPHENIX rail system to the IR until its nominal axis is coaxial with the nominal RHIC beam axis then north until the CC assembly's nominal center point coincides with the sPHENIX nominal interaction point ("IP"). Survey and built in adjustments to the CC assembly are used to bring the entire assembly into tolerance as required.

The following alignments take place after the cradle carriage is moved into the Interaction Region (IR).

The beampipe is installed and surveyed into place by using the beampipe survey fixture and making adjustments on the beampipe stands. The MVTX and INTT will be integrated into a dual hemisphere support frame (upper and lower) with the upper and lower halves relatively aligned on the bench prior to installation such that mating kinematic mounting features are fully adjusted in a simulated installation. Each frame hemisphere will have a 3 point support onto a dual rail and bearing system in which the bearings will slide along pathways on the rail which allows the upper and lower frames to ride in separately and moved away from the beampipe until the frames have cleared the beampipe flanges. The lower frame is positioned first then the rail is adjusted in 3 dimensions to achieve the alignment precision required. Then the upper frame is brought into position and is mated to the lower frame by kinematic mounts.

The final detector to be installed and aligned is the Min Bias detector. It will be mounted on alignment rails which in turn mounted to horizontal and vertical brackets anchored to the Outer HCal inboard of the end caps/pole tips. These will allow X-Y-Z and angular adjustments as required.

C.2.4 Routing of Services

All services to the detectors are routed from the north or south of the overall experimental assembly to service distribution points at the north and south end of each subassembly sector/module. From that point services are routed to source points (e.g. electronics racks, cooling manifolds, etc.) which will be generally segmented into quadrants at each end for the MVTX all services are routed to the south end.

All manifolds and patch panels will be rack mounted on the Cradle Carriage platforms outside of the detector areas. In general, the services will be layered such that the outermost detector (Outer HCal) has the inner most services routes, with the Inner HCal on top of those, then the EMCal services and finally the Tracking services.

C.3 Installation

Installation is defined as the final assembly of detector support structure and detector components that will take place at the sPHENIX Assembly Hall and/or in the Interaction Region, QA testing of components at predetermined points during assembly, the relocation of the final assembly to the sPHENIX IR to its Operational location at the sPHENIX IP, installing and integrating infrastructure services, ready for final commissioning and operation.

C.3.1 Installation Concept

The Installation Concept for sPHENIX is as follows:

- Internal alignment of detector subsystem components in the interior will be completed as described in the previous section and the individual sectors or modules of the detector subsystems will be operationally tested and ready for installation when shipped to the sPHENIX AH for installation, as described in the relevant subsystem section of this report.
- The subsystem sectors/modules will be provided with handling fixtures as indicated in the tooling and support equipment section below.
- As each additional Outer HCal Sector is installed it will be surveyed, adjusted and shimmed into place with respect to the required tolerances, until the lower half of the Outer HCal is completed.
- The Superconducting solenoid magnet will have been surveyed and been sufficiently tested to establish a nominal magnetic axis and centerpoint which will have been related to external fiducial points on the magnet and those relationships recorded. The magnet will have 12 adjustable mounting supports attached to position and secure the magnet onto the inner surface of the Outer HCal. Figure C.10 shows the Outer HCal with 32 sectors installed ready for the superconducting magnet to be mounted.
- After the lower half of the Outer HCal is completed, the magnet shall be mounted surveyed, aligned and secured to the OuterHCal in accordance with requirements.
- The remaining Outer HCal Sectors are installed, surveyed, adjusted and shimmed into place with respect to the required tolerances, until the upper half of the Outer HCal is completed.
- The pillars for supporting the upper platform and flux return end caps and are then installed followed by the installation of the upper platform and end caps themselves.

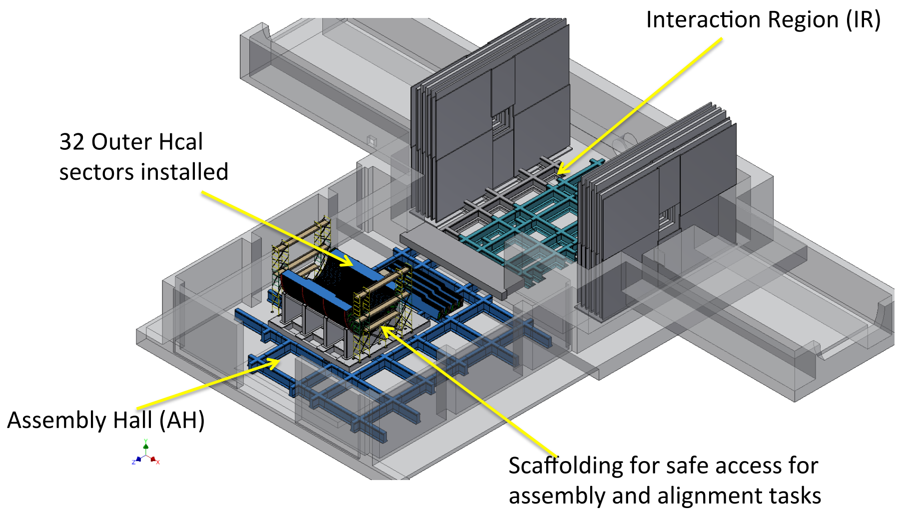

Figure C.10: Outer HCal Installation, lower half

- The Magnet valve box with extension is installed. Outer HCal services are then installed.

  The Inner HCal sectors are to be assembled into a complete detector on its dedicated assembly fixture, aligned using mechanical precision features, survey and shimming to achieve the desired alignment of each of the sectors to each other and to external fiducial points. The entire assembly is then surveyed, aligned and secured to the Inner HCal-to-Outer Hcal support rings and services are installed.Figure C.11 shows the Inner HCal nearing assembly completion and mounted on the installation fixture

- Each of the 64 EMCal sectors is then installed onto the rail systems on each of their respective Inner HCal sectors, surveyed positioned, adjusted and secured into place in accordance with required tolerances. EMCal services are then installed.

- The detector assembly on the CC support structure is made ready for movement by installing and aligning the Tracking subsystem with the nominal axis and centerpoint. The pillars for supporting the upper platform and flux return end caps/pole tips are then installed followed by the installation of the upper platform and end caps/pole tips themselves.

- Next, the entire CC is moved west on the sPHENIX rail system to the IR until its nominal axis is coaxial with the nominal RHIC beam axis then north until the CC assembly's nominal center point coincides with the sPHENIX nominal interaction point ("IP"). Survey and built in adjustments to the CC assembly are used to bring the entire assembly into tolerance as required. Once the CC is positioned and aligned in its run position, the MVTX and INTT are installed as separate detectors on a

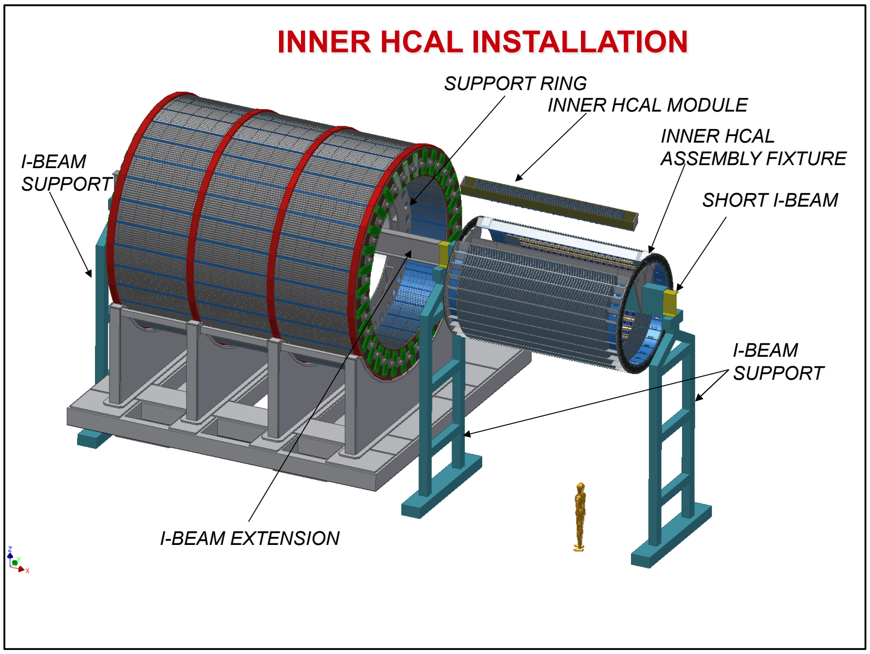

Figure C.11: Inner HCal Installation

common support structure. (Note, if necessary either of these 2 detectors could be installed without the other.) Services for the MVTX and INTT are then installed.

- Finally, the min Bias detector and its services are installed.

C.3.2 Tooling and Support Equipment Requirements

The following are the most significant tooling and support equipment needs for integration and installation:

- Central Pedestal (CC): standard lifting tools for CC base and rollers, cradle, support posts, bridge platform, access stairs), alignment tools for rollers and cradle.
- Outer HCal: module holding fixtures (4), indexed lifting/installation fixture, alignment tools, temporary inner and outer assembly support fixtures
- Inner HCal: module holding fixtures (4), module lifting fixture, assembly indexed/rotating fixture and insertion beam and insertion beam lifting fixture, alignment tools

- EMCal: module handling fixtures (8), rail alignment tool, indexed lifting/installation fixture
- TPC: Handling fixtures (2), alignment tool, installation tool
- INTT: Handling fixture, alignment tool, installation tool (common with MVTX)
- MVTX: Handling fixture, alignment tool, installation tool (common with INTT)
- Min Bias: Handling fixture, alignment tool, installation tool (common with MVTX)
- SC Magnet: Lifting fixture (spreader bar), alignment tool, stack handling/lifting tool
- Infrastructure: beampipe alignment tools/fixtures, bakeout tools/fixtures

Note: some of the tools/fixtures described above will be used in subsystem sector/module assembly operations as described in their respective sections of this report prior to being used for final installation.

C.4 Testing and Commissioning

C.4.1 Magnet

The superconducting solenoid magnet will be QA tested for integrity and function as described in the Magnet section of this report. After transport to the AH for assembly and again after installation into the CP, the magnet will be QA tested to assure that no damage has been done in transportation and installation. See the magnet section of this report for more details on magnet testing.

C.4.2 Detector Subsystem Commissioning

All detector subsystem sectors/modules are QA tested at their point of assembly, as described in the relevant subsystem sections of this report, prior to transporting the sectors/modules to the AH for installation. After transport to the AH for assembly and again after installation into the CC, the sectors/modules will be QA tested to assure that no damage has been done in transportation and installation.

The complete detector subsystems will be tested to demonstrate their operational readiness, to calibrate the detector components as necessary and to verify the chains of signals from the detector elements through to the data acquisition system. In addition, all services will be tested to demonstrate performance in accordance with requirements.

C.5 Alternative Integration/Installation Concepts Considered

The evolution of the integration and installation concept is largely driven by the design evolution of the component detector subsystems. Several alternative integration and Installation concepts have been considered during this process independent of the detector subsystems. Some of the more interesting considerations are described below, with explanation of why they have been rejected.

Multiple carriages instead of one unified Cradle Carriage. This option was considered early on, but it was rejected as unnecessarily expensive and it increases alignment difficulty.

Separate carriages for the flux return end caps. The current concept has hinged flux return caps to minimize cost, and simplify assembly.

Sliding door flux return end caps (both vertical and horizontal sliding), instead of hinged end caps. This concept was rejected because it increases space requirements for maintenance, increases cost and (in the case of the vertical sliding end caps) handling safety considerations.

Installing the EMCal as a complete detector instead of 64 separately supported sectors. This would require an assembly structure and complicated installation tooling fixtures, adding to cost. It also decreases the accessibility for maintenance.

Completing the assembly of the Inner HCal remotely and transporting the completed assembly to the AH for installation. This would require a complicated transport fixture added risk for damage during transportation and additional logistical considerations (additional assembly space). There are some merits to this alternative procedure and it may be revisited, if appropriate, after subsystem designs are finalized.

Using rail mounted gantry cranes to install the Inner HCal instead of a monorail system. Increased complexity and cost. There are some merits to this alternative procedure and it may be revisited, if appropriate, after subsystem designs are finalized.

Using separate pillars and rails to support the Inner HCal, instead of the load transfer rings. This is a more complicated design, which would increase cost and complexity of installation.

Having separate supports for the magnet instead of supporting the magnet with the Outer HCal. This was rejected due to increased complexity and cost.

Appendix D

Intermediate Silicon Strip Tracker

D.1 Detector description

The INTermediate Tracker (INTT) is part of the charged particle tracking systems of sPHENIX. The INTT consists of four layers of barrel silicon semiconductor strip detectors. The layers are noted by Layer-0, 1, 2, and 3 from the most inner to outer and the distance in radii of each layer from the interaction point is 6, 8, 10, and 12 cm, respectively. Each layer is composed of several ladders cylindrically covering rapidity range of approximately $-1.1 < \eta < 1.1$. To achieve hermeticity, alternate support and cooling structures are staggered in radius and offsets in azimuthal angle so that the alternating sensor modules overlap in azimuth as shown in Figure. D.1. Number of ladders in each layer is presented on Table D.1. Each ladder is made of two silicon modules mounted on the same Carbon-

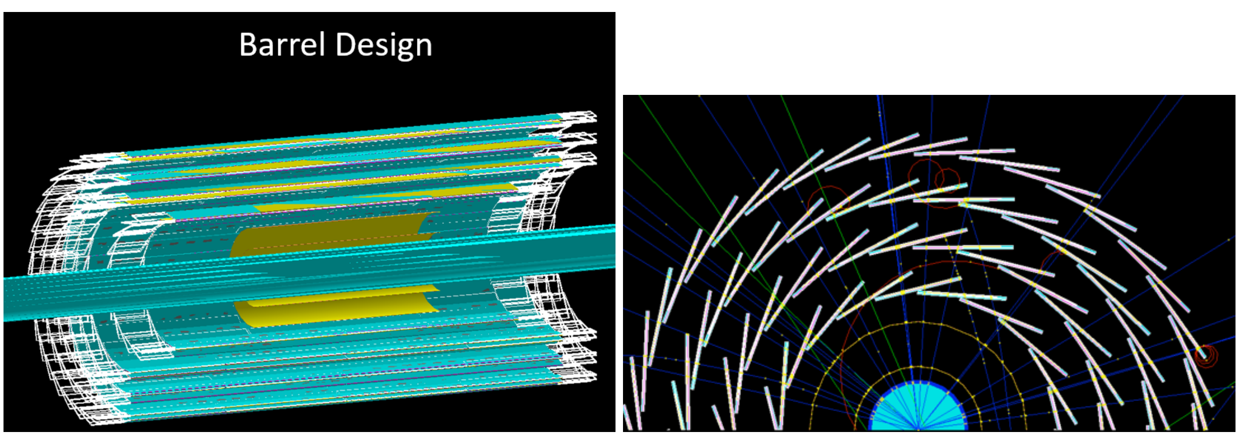

Figure D.1: The INTT tracker drawing: side view (left), and front view (right).

Fiber-Composite stave. Each silicon module is read out from one side and is composed of: (1) Two AC coupled, single-sided silicon strip sensors produced by Hamamatsu Photonics

Table D.1: Radius and number of ladders of each layers of barrel silicon strip detectors.

layer	radius [cm]	number of ladders
0	6	20
1	8	26
2	10	32
3	12	38
Total	-	116

Table D.2: Dimensions of silicon sensors (not active region) to parallel to the beam (z-) direction. The last line of the table is the $|z|$ position of $\eta = 1.1$ at the distance of each layers (6,8,10, and 12cm).

<table>
<tr><th></th><th></th><th>Layer-0</th><th>Layer-1</th><th>Layer-2</th><th>Layer-3</th></tr>
<tr><td rowspan="3">type-A</td><td>z-length/block[mm]</td><td>18</td><td colspan="3">16</td></tr>
<tr><td># of blocks</td><td>5</td><td colspan="3">8</td></tr>
<tr><td>z-length [mm]</td><td>90</td><td colspan="3">128</td></tr>
<tr><td rowspan="3">type-B</td><td>z-length/block[mm]</td><td>18</td><td colspan="3">20</td></tr>
<tr><td># of blocks</td><td>5</td><td colspan="3">5</td></tr>
<tr><td>z-length [mm]</td><td>90</td><td colspan="3">100</td></tr>
<tr><td>type-(A+B)</td><td>z-length [mm]</td><td>180</td><td colspan="3">228</td></tr>
<tr><td></td><td>$|z|$ @ $\eta = 1.1$ [mm]</td><td>174</td><td>198</td><td>223</td><td>247</td></tr>
</table>

Co. (HPK) and (2) One flexible circuit board, called the High Density Interconnect (HDI); each HDI provides power, and bias input lines as well as slow control and data output lines. The HDI was designed, manufactured and tested by Yamashita Materials Co. (3) On top of each HDI, twenty and twenty six FPHX chips[157] are mounted for ladders of layer 0 and layers 1, 2 and 3, respectively. The FPHX chip consists of a 128-channel front-end ASIC, and was designed by Fermilab for the FVTX detector[158]. The chip was optimized for fast trigger capability, a trigger-less data push architecture, and low power consumption (64 mW/chip). The HDI ends will be connected to an extender cable which is connected at the other end to a FVTX ROC used in PHENIX previously. The extender is 1.2 m long (and possibly longer) to reach the ROCs, which are in a big wheel arrangement on the inner part of the TPC endcap.

The basic design of INTT is derived from the PHENIX Forward VTX (FVTX) detector[158]. In fact, the FPHX readout chip is employed for the INTT and thus the readout chain of FVTX can be re-used for INTT. In order to avoid production of extra readout electronics beyond FVTX resources, number of readout channels are designed to be less than that of FVTX. The INTT silicon strip sensor uses conservative technology design; it is a silicon strip single sided, AC coupled, double-metal layer to route the signal from the strip to the bonding area at the edge of the sensor. In summary, The INTT tracker is driven by several ideas which it is conservative design, low risks, low-cost and high optimization for physics.

The dimensions of silicon sensors (not active region) to parallel to the beam (z-) direction are tabulated in Table D.2. The total z-coverage of Layer-0 and Layer-1 to 3 are 180 mm and 228 mm, respectively. As tabulated in the bottom of the table, the Layer-0, 1, and 2 fully cover more than $\eta = 1.1$, while z-coverage of Layer-3 is short by 19 mm from the $|z|$=247 mm where $\eta = 1.1$ at the distance of 12 mm from the beam line. The effect in the acceptance is discussed in subsection D.2.

D.2 Acceptance and efficiency

Geometrical acceptance and detection efficiency of each INTT layer are summarized in Table. D.3. Geometrical acceptance is estimated for two types of z-vertex values ($vtxz$): $vtxz < 0$ cm and $vtxz < 10$ cm. Detection efficiencies in the two rapidity regions, $|\eta| = 0$ and $|\eta| < 1$, are calculated using single electron simulation events fired from the vertex $(0, 0, 0)$ cm.

Table D.3: Summary of the geometrical acceptance and detection efficiency for each INTT layer.

Layer	Acceptance		Efficiency	
	$\lvert vtxz \rvert < 0$ cm	$\lvert vtxz \rvert < 10$ cm	$\lvert \eta \rvert = 0$	$\lvert \eta \rvert < 1$
L0	$\eta < 1.83$	$\eta < 1.12$	100 %	> 99 %
L1	$\eta < 1.79$	$\eta < 1.28$	100 %	> 99 %
L2	$\eta < 1.58$	$\eta < 1.09$	> 99 %	> 99 %
L3	$\eta < 1.41$	$\eta < 0.95$	100 %	> 99 %

D.3 Silicon strip sensors

The sensors are single sided, AC coupled sensors. For Layer-1 to 3, the active area of the type-A and type-B sensors are 128 mm $\times$ 19.96 mm and 100 mm $\times$ 19.96 mm, respectively. The active area of the type-A (type-B) sensor is divided into 8×2 (5×2) blocks. Each block has 128 short strips that are 78 μm in pitch and 16.0 mm (type-A) or 20 mm (type-B) long, and run parallel to the z (beam) direction (Table D.4). In Figure D.2, the strip runs horizontally. The read-out lines of the strips, run perpendicular to the strips and bring the signals to the read-out chips placed on the HDI at the upper and the lower edge of the sensor.

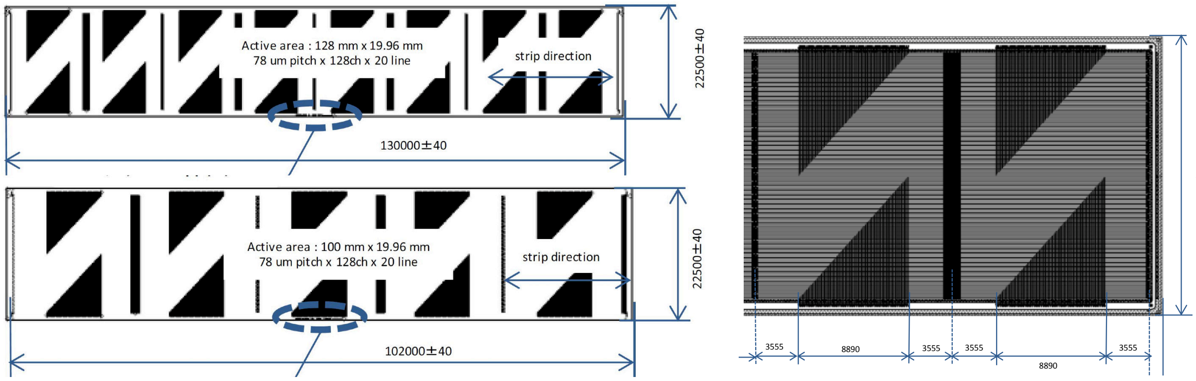

Figure D.2: The silicon strip sensor drawings of layer 1 to 3 made by HPK. (Top left) type-A, (bottom left) type-B, and (right) part of type-A sensor.

Table D.4: Silicon sensor dimensions of Layer-1 to 3.

Type	number of blocks	active area dimension	strip pitch
A	8	128 mm $\times$ 19.96 mm	78 μm
B	5	100 mm $\times$ 19.96 mm	78 μm

The silicon sensors are manufactured by Hamamatsu Photonics Co (HPK). In order to reduce the material in the tracking system, a thinner silicon sensor is under development. The thinner silicon sensors are manufactured by grinding their standard thick (320μm) silicon down to 200 to 240 μm as a trade off of the increasing dark current. The final design of the silicon thickness will be optimized based on the signal to noise ratio performance.

Shown in Figure D.3 is the prototype silicon sensor B for Layer-1,2,3.

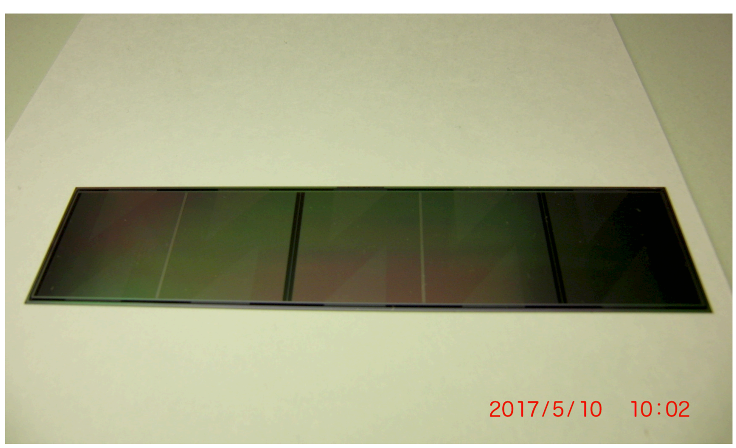

Figure D.3: The photograph of the type-B silicon sensor prototype for Layer-1,2,3.

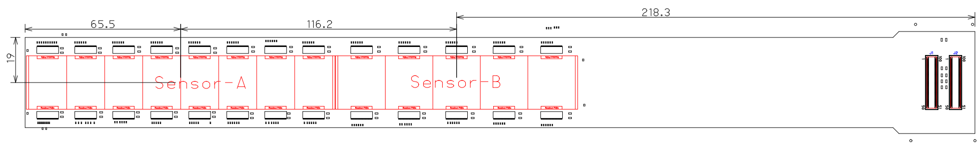

Figure D.4: Dimension of HDI for layer-1 to 3 and layout of silicon sensors, FPHX readout chips and other components.

D.4 High Density Interconnect (HDI)

The HDI is a seven layer flexible circuit board to read-out two silicon sensors. The basic layer structure design of HDI is derived from the PHENIX FVTX. On the other hand, some of parameters are slightly different particularly for those close to technological limit in FVTX are somewhat relaxed in INTT. The copper line width and pitch between copper lines are 60±10 and 120 μm, respectively. Each copper line pairs are spaced greater than 180 μm at least. The impedance is well controled to be 50Ω. The HDI will be manufactured by Yamashita Materials Co. Shown in Figure D.4 shows the dimension of HDI for layer-1 to 3 and layout of silicon sensors and FPHX chips. The width of HDI is 38mm in sensor part while 43mm in the connector end. The length is 400mm which is the longest limit of multilayer flexible cable.

Shown in Figure D.5 is the 7 layer structure of HDI. The total thickness is 493 μm. The total thickness governed by copper layers is 68 μm which is the major source of the material budget of INTT layers. In order to reduce the material budget, a mesh pattern is introduced in ground and bias copper layers for prototype model. As shown in Figure D.7, the copper line width is 300 μm and space between copper lines was kept 1.7 mm. This pattern leaves residual copper rate of 30% saving 70% of material compared to the solid copper ground. Since the main purpose of having signal layers sandwiched by ground/bias layers is to shield incoming/outgoing noise to/from signal lines, meshed design is trade off of the noise shielding performance and reducing the material. In order to minimize the noise shielding effect, the mesh design is only introduced in the area where signal lines are not running in adjacent signal layer as can be seen in Layer-2,4, and 6 in Figure D.6. The residual Copper rates for these layers are summarized in Table **??**. The final design will be optimized based on its performance by comparing prototype models between meshed and solid ground designs. Some signal lines running in sensor region in L7 is not succeeded design from FVTX. This signal lines were bi-product of saving HDI width as narrow as possible and thus couldn't fit within the signal layers. Since L7 is not shielded by the ground layers, the signal lines are exposed to the external environment, the length of the lines were kept as short as possible ($<$ a few cm).

FPHX chips[157], which was used for the FVTX silicon tracker of PHENIX[158], are mounted on HDI to read-out the sensor. A FPHX chip has 128 channels of 3 bit ADCs

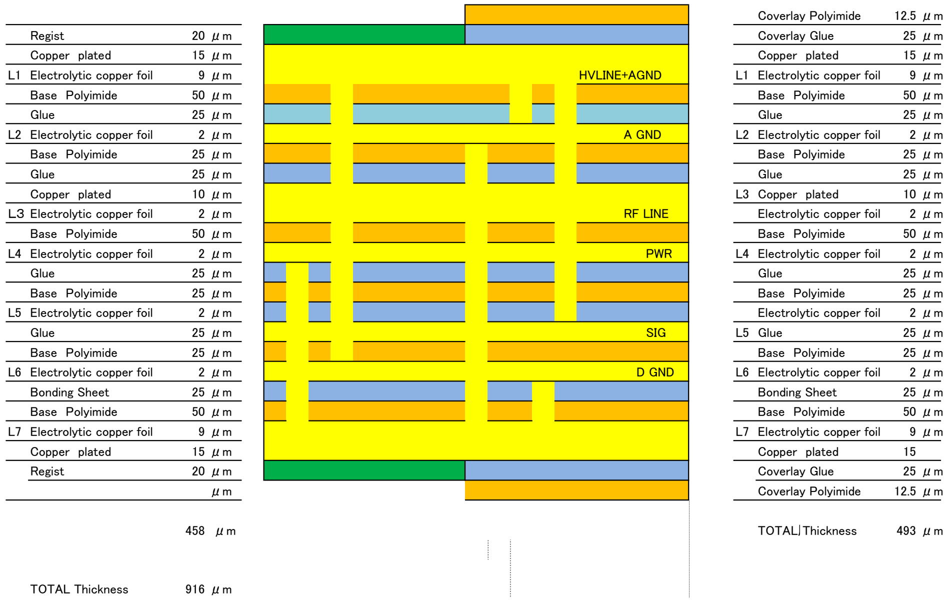

Figure D.5: 7 layer structure of HDI.

Table D.5: Residual Copper rate for ground and bias layers of HDI.

Layer	residual Copper %
2	53.99
4	62.66
6	71.92

and it can read out 128 mini-strips in one block of the sensor. The read-out pad pitch of the sensor is thus matched to that of FPHX chip (78 μm). FPHX chip has low power consumption, about 64 mW per chip, which reduces the need for cooling for the sensor module. The analog signal of each strip is digitized in the FPHX chip, and the digitized data of 128 channels are sent out through the 200 MHz data-out port of the FPHX chip.

D.5 Bus Extender

The bus extender is a cable to connect between the ROC board and the INTT ladder, and to bring all the signals from the ladder to the ROC board and power and the control commands from the ROC board to the ladders.

The requirements of the bus extender are following: (1) 1.2m long, (2) signal integrity of 200 MHz clock rate with LVDS lines, (3) small available space in the TPC. Figure D.8 shows

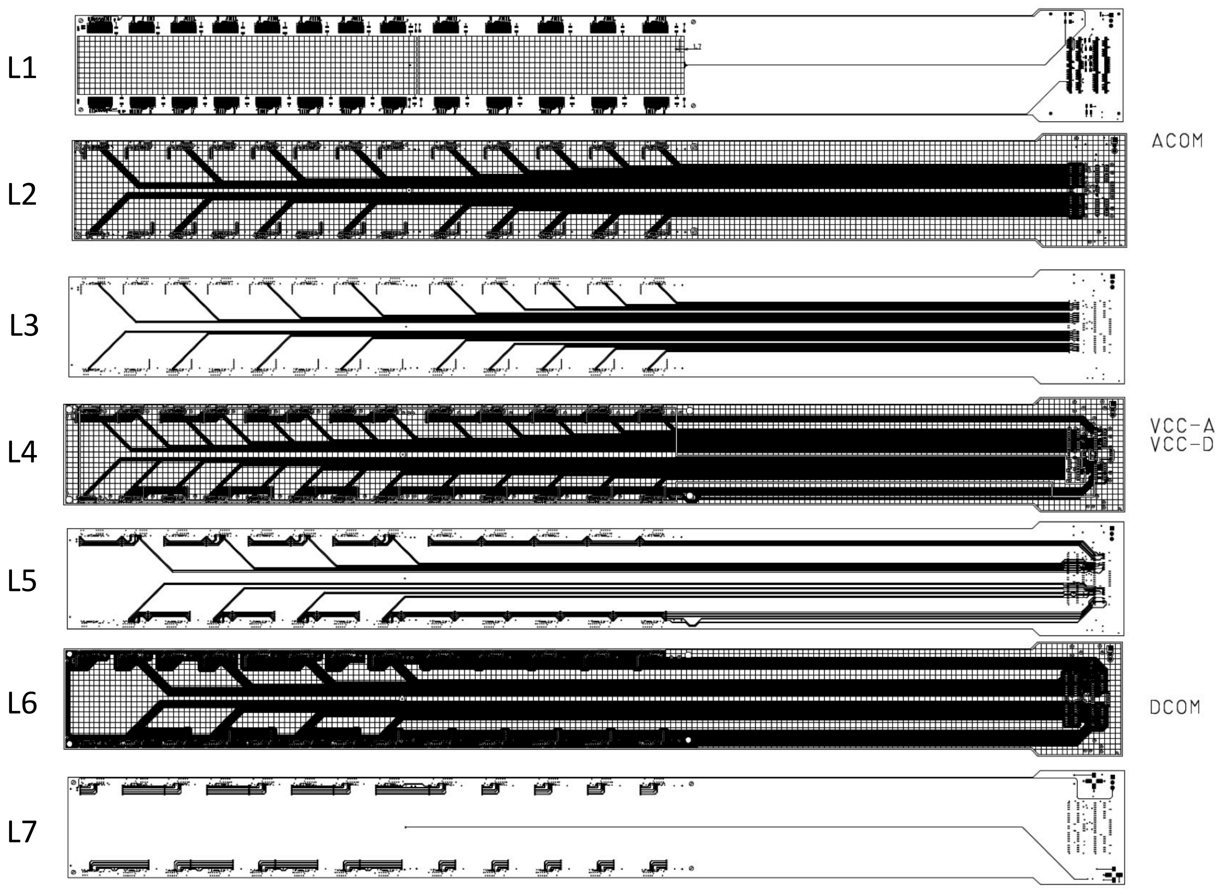

Figure D.6: 7 layer structure of HDI.

the sPHENIX tracking system. INTT detector is placed at the center of the TPC barrel and the ROC boards are outside of the barrel. The distance between the INTT ladder and the ROC boards is 1.2 m. The available space near INTT region is small. the MAPS detector has a heavy cabling systems with the mechanical support. In addition, the front edge of the the forward sPHENIX detector is rolled in to the TPC barrel and is placed near the INTT detector.

One way to meet these requirement is that the bus extender is made from a flexible PC board with having a similar stack-up design to the INTT HDIs. The flexible PCB is thin and can be arranged by bending along with the TPC barrel. The FVTX bus extender was built with the flexible PCB with multiple layers, as shown in Figure D.9. The parameters of the FVTX bus extender is summarized in Table D.6. Therefore, It is good to start with the design of the FVTX extender. It is challenging to build the extender with 1.2 m long in terms of a good signal integrity and making the long flexible PCB. We plan to do 3 steps R&D to make the extender: First, the long cable with single layer to test the signal transfer with 1.3m. Second, the long cable stacked with multiple layers for checking the multi-layer

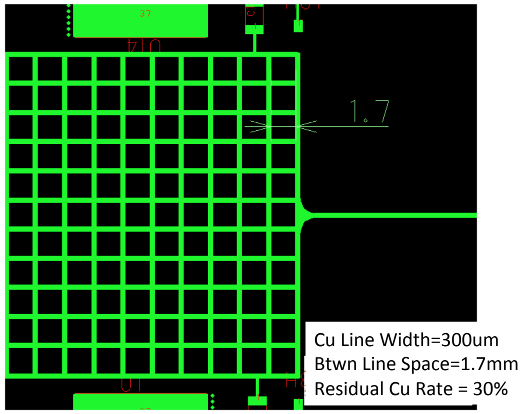

Figure D.7: Close view of the mesh pattern of the ground layer.

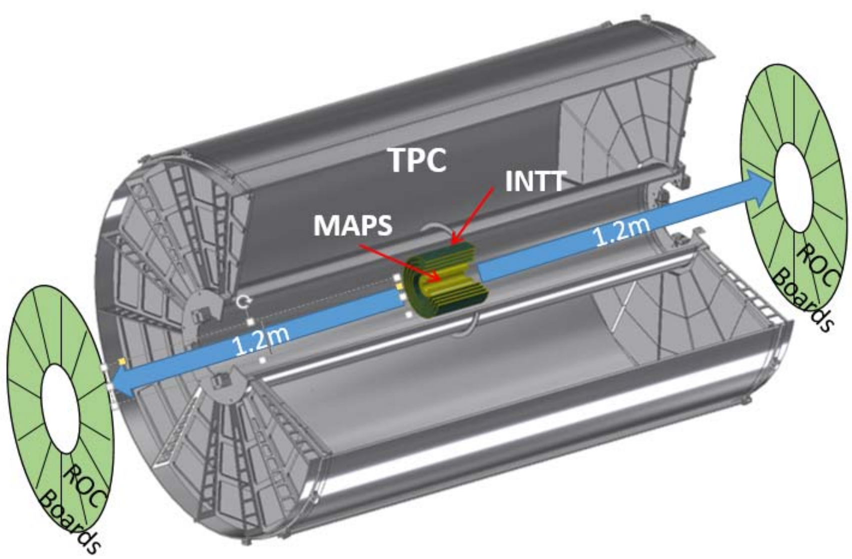

Figure D.8: sPHENIX tracking system. The bus extender should be at least 1.2m to connect between the INTT ladders and ROC boards.

cable. Third, the proto-type cable with actual 62 LVDS lines for total verification. The R&D is in progress.

D.6 Sensor module

Figure D.10 illustrates the conceptual design of the sensor module of the layer-0 (top) and layer-1 to 3 (bottom) of the INTT tracker. Each of the silicon strip module is made:

(1) Two pieces of silicon sensors type-A and type-B for layer-1 to 3, and two pieces of

Figure D.9: The bus extender for FVTX.

Table D.6: The set of parameters of the FVTX bus extender.

length	27 cm
width	2cm
Layer	7
LVDS lines	62
Powers	power, bias, GND

silicon sensors type-B for layer-0. As reminder (see silicon sensor section for more details), the active area of the type-A and type-B sensors are 128 mm $\times$ 19.96 mm and 100 mm $\times$ 19.96 mm, respectively. The active area of the type-A (type-B) sensor is divided into 8 $\times$ 2 (5 $\times$ 2) blocks. Each silicon sensor is an AC coupled silicon strip sensor single side, double-metal layer to route the signal from the strip to the bonding area at the edge of the sensor, and a strip pitch sensor of 78 μm (in ϕ). The

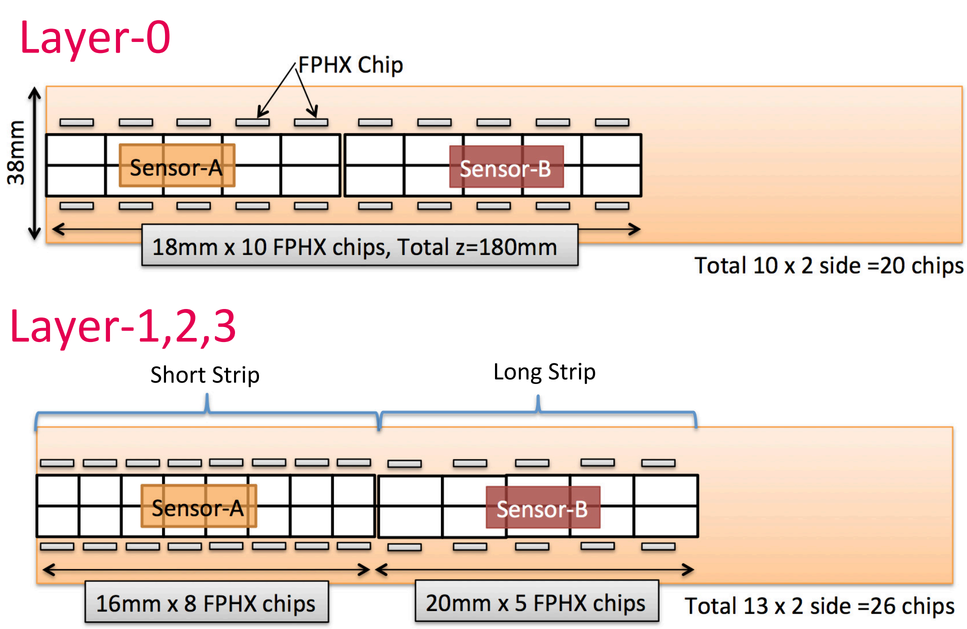

Figure D.10: Conceptual design of the Sensor Module for Layer-0 (top) Layer-1 to 3 (bottom) of the INTT detector.

silicon sensors were produced by Hamamatsu Photonics Co. (HPK).

(2) One flexible circuit board, called High Density Interconnect (HDI); each HDI provides power, and bias input lines as well as slow control and data output lines. The HDI is manufactured and tested by Yamashita Materials Co.

(3) Signals from strip sensors are digitized by 20 and 26 FPHX chips mounted on HDI for Layer-0 and Layer-1 to 3, respectively. The FPHX chip consists of a 128-channel front-end ASIC, and was designed by Fermilab for the FVTX/PHENIX detector. The chip was optimized for fast trigger capability, a trigger-less data push architecture, and low power consumption (64 mW/chip). The from-end of each chip (128 channels) is a wire-bond to the silicon sensor, and the back-end of the chip (32 channels) is wire-bonded to the HDI. All wire-bonding are encapsulated for protection.

(4) It should be point out that each sensor module contains two temperature sensors. Each ladder contains two thermistors (NCP15XH103D03) allowing us to read the temperature of each sensor module. The thermistors are part of the HDI (built in) and they are read out from the edge of the HDI. From each HDI, we will have one cable going to a readout board. The thermistors and readout board have been determined by engineer using them currently and planned to be used in sPHENIX.

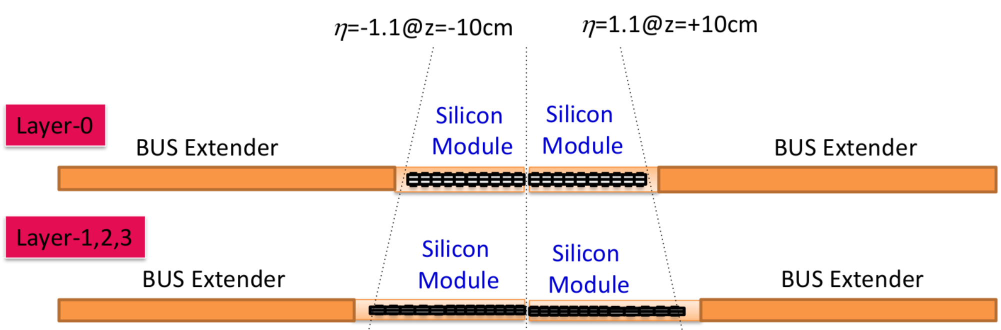

Figure D.11: Conceptual design of ladder for Layer-0 (top) Layer-1 to 3 (bottom).

D.7 Ladder

For Layer-0 to 3, each ladder is build as following:

(1) One mechanical support made of Carbon-Fiber-Composite skins called stave. The area of the stave for layer-0 (layer-1 to 3) is 40 cm × 3.3 cm (50 cm × 3.3 cm), as shown in figure D.12. Each stave contains a graphite sheet (to enhance thermal conductivity) which carries out the heat of each ladder to the top edges of the stave. Each edge of the stave is connected to a Ring which is cooled down. The temperature of each

ladder should be at 10 degrees Celsius during operation. The heat load expected from each half ladder is: 390 μW $\times$ 128ch $\times$ 26 chips = 1.3 W $\simeq$ 2 W (including power). (including power). The total heat load over the entire INTT is 300 W.

(2) Each stave carried out on top two sensor modules. Each sensor module is read out in one edge of the ladder through the HDI bus extender as shown in figure D.11. The HDI ends will be connected to an extender cable which is connected at the other end to a FVTX ROC used in PHENIX. The extender has to be at least 1.2 m long (and possibly longer) to reach the ROCs, which are in a big wheel arrangement on the inner part of the TPC endcap.

(3) Number of ladders per layer of barrel is presented on Table D.7. We have four layers of barrels silicon strip detectors made of 116 ladders in total.

(4) The four layers (layer-0 to 3) barrels silicon strip detectors will be integrated into a dual hemisphere support frame (upper and lower). Each frame hemisphere will have a 3 point support onto a dual rail and bearing system in which the bearings will slide along pathways on the rail which allows the upper and lower frames to ride in separately and move away from the beam pipe until the frames have cleared the beam pipe flanges. The lower frame is positioned first, then the rail is adjusted in 3 dimensions to achieve the alignment precision required. Then the upper frame is brought into position and is mated to the lower frame by kinematic mounts. It is almost certain that the same external supports and rail system will need to hold both the INTT and the MVTX. As a result, it will not be possible to install or remove either detector while the other is already installed. However, the support system should allow installing either of the detectors alone in the absence of the other.

Table D.7: Number of ladders per layer of barrel silicon strip detectors.

layer	number of ladders
0	20
1	26
2	32
3	38
Total	116

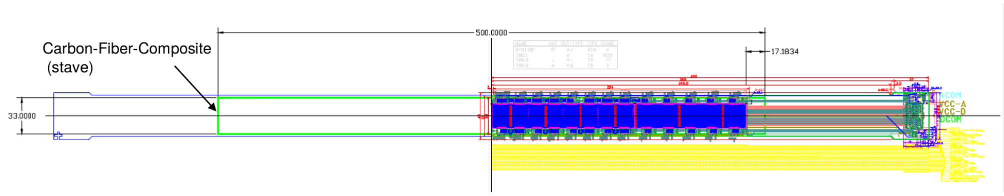

Figure D.12: Auto-Cad drawing of one stave, one silicon module, one HDI extender bus of one ladder.

D.8 Mechanical design

D.8.1 Stave

To achieve the stave requirements, 1) rigid, 2) thermally conductive, and 3) low radiation length, we have established two R&Ds programs: The Latter are progressing in parallel: 1) HoneyComb Carbon-Fiber-Composites Stave, and 2) Thermal Conductive plate stave.

D.8.1.1 HoneyComb Carbon-Fiber-Composites Stave

Each ladder consists of two silicon modules mounted on a mechanical support, called a stave. The silicon modules are oriented such that the silicon modules are immediately adjacent and symmetric on the mid-plane of the ladder. The stave itself spans the entire silicon sensors plus an extension for mechanical attachment for total length of about 50 cm. The stave, for layers 1, 2 and 3, consists of a 2 mm thick carbon-fiber honeycomb in the middle, and carbon-fiber foam on either side with an embedded 1.75 mm OD cooling tube. On the top and bottom of the stave, there is a 0.42 mm (can be reduced to 0.21) carbon-fiber sheet highly thermally conductive. At either end of the stave, there are mounting blocks allowing for accurate mechanical attachment. The entire state structure, as well as the sensor module attachment, epoxy together. The total thickness of the stave is 2.84 mm (can be reduced to 2.42 mm). This information is shown in figure D.13. Layer 0 is of the same composition; however, the carbon-fiber foam and embedded cooling tube reside only on one side of the carbon-fiber honeycomb.

D.8.1.2 Thermal Conductive Plate Stave

D.8.2 Barrels Layout

As it was required by the simulation, the INTT consists of four barrels. Each barrel consists of one type of ladder, which is implied by its naming system, are ladder 0 for Barrel 0 and ladder 1,2,3 for barrels 1, 2 and 3. Ladders within a barrel are radially offset from

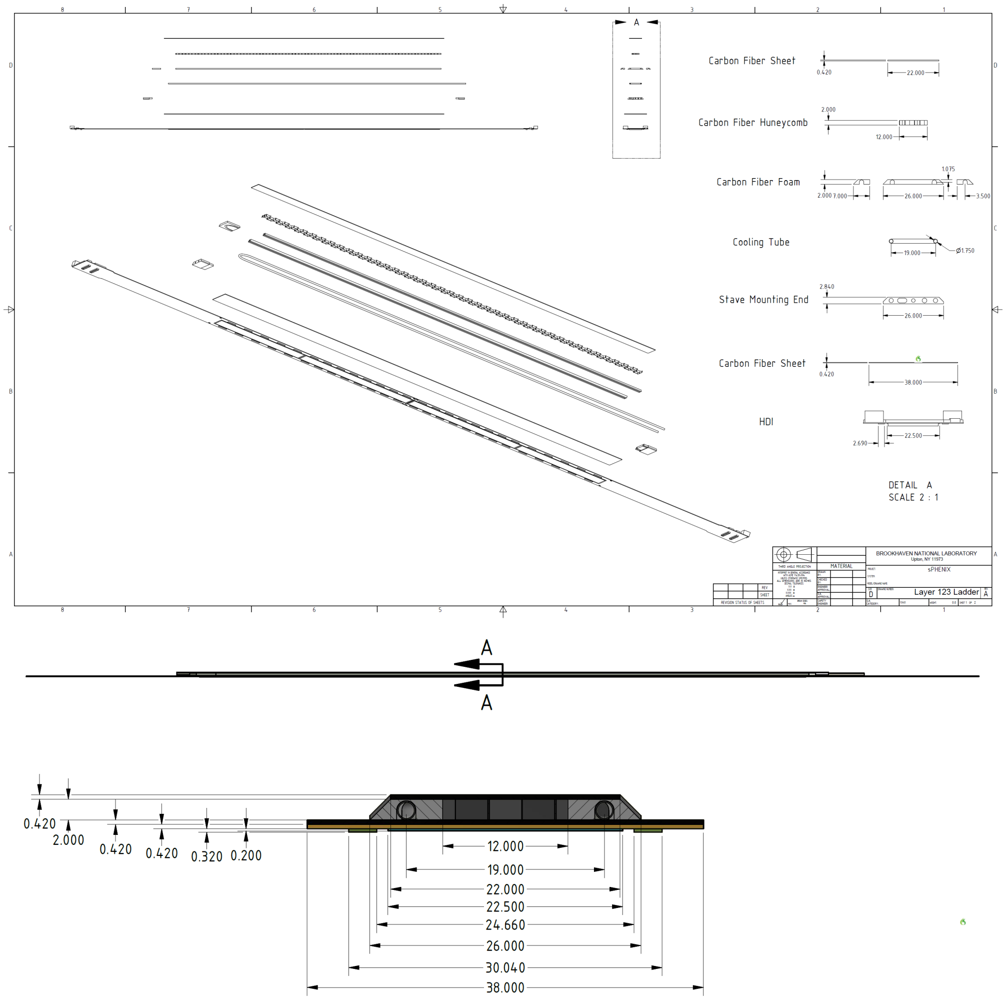

Figure D.13: Auto-Cad drawing of HoneyComb Carbon-Fiber-Composites Stave.

the central axis and tilted such that the active area of the silicon sensor modules has sufficient coverage overlap. The ladders are tilted along an axis parallel to the central axis at the mid-plane of the active area of the silicon sensor. The quantity of ladders per barrel depends on the radial location, pseudorapidity coverage, tilt angle with respect to the tangent of the radial location, and clearance. These parameters are summarized in table D.14.

D.8.3 Barrels Support Structure

For the mechanical flexibility o f installation, all four barrels are divided into two equal halves. On either end of the ladders of a given barrel there is a support ring which has grooves for easy installation of ladders as well as cutouts for the HDI, cooling tube, and

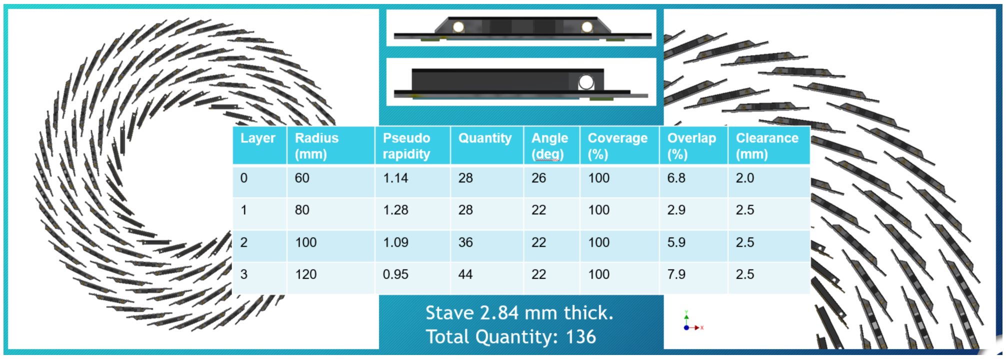

Figure D.14: Auto-Cad drawing of INTT Barrels.

locating pins alignement. Like the division of the ladders, the support ring, made of carbon infused peak. Once all the ladders are installed in a set of quarter support rings, two of these assemblies are attached to each other and then are attached to a set of half end caps. End caps have steps for each layer for the support ring to be attached to, as well as cutouts for services. A pair of half end caps are attached to an external skin to which layers three through zero can be installed in that order. The two halves of the INTT a not assembled until they are in the inner bore of the TPC.

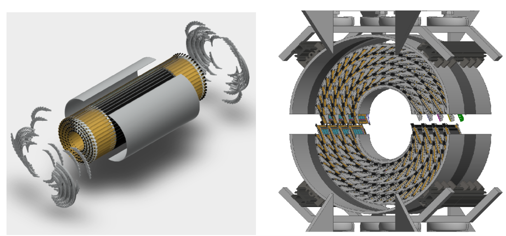

Figure D.15: Auto-Cad drawing of INTT Barrels Support Structure.

D.8.4 Cooling and Cabling

From the extension bus of each of the ladders, there is a 1.2 m extension cable to the ROCs. Extension cables are supported by a tube spanning the entire length of the TPC. The ROCs are are attached to the inner and outer faces of half of a hexagonally faceted cone. These cones allow for sufficient access and clearance for the TPC. The cones also allow for detachment of cooling tubes in order to cool the ROCs. As for the cooling of the ladders, there are several inlets and outlets per layer, however, the tube within the ladders is bent such that the individual inlets and outlets on the same side, meaning that inlets and outlets on all ladders come out the north side of the detector, opposite the MVTX. Several ladders within a layer can be daisy chained together to minimize the number of inlets and outlets supplied to the detector.

D.9 Electronics, LV&HV systems

As briefly described in the detector description section, the readout, slow control, LV, HV supply electronics chains composed by re-use boards of FVTX. These boards are mostly functional in the last year of FVTX operation and known to be kept in reasonably good condition. However, each boards are to be tested before the INTT installation and repaired up on necessity. Shown in Figure D.17 is the schematics of the readout and slow control chains for INTT.

D.10 Justification of design choices

The momentum resolution is weakly affected by multiple scattering in the material. Thus the amount of material in INTT is kept as small as possible. The design choices being pursued to minimize the material budget are as follows.

1. High thermal conductivity plate cooling.
2. Thinner Silicon Sensor.
3. Mesh pattern ground and bias layers of HDI.
4. Long multilayer bus extender.

D.10.0.1 High thermal conductivity plate cooling

The biggest advantage of the FPHX chip is the small heat generation, which allowed FVTX to avoid running cooling tubes into the acceptance. The heat generated by the wedge assemblies is conducted through the wedge carbon composite backplane to the outer radius (outside acceptance) cooling tubes which is away from the inner most chip by 5 cm (station-0) and 12 cm (station-1,2,3). The wedge carbon composite has relatively high thermal conductivity of 650 W/mK. The number of FPHX chips per HDI is identical with FVTX for Layer-0 and Layer-1 to 3 and therefore the total heat generation per HDI will be also same as FVTX. However, the spacing between adjacent chips are not as dense as FVTX. As a consequence, the distance from the chip closest $z = 0$ to the outside the acceptance is much longer in INTT (18 cm to 25 cm). Therefore the heat generated by the chip needs to be conducted longer distance and more efficiently to the location of cooling tube. The performance of high thermal conductivity $1000 \sim 1500$ W/mK sheets are under testing. It will be used in combination with the carbon composite backplane to conduct the heat.

D.10.0.2 Thinner silicon sensor

The thinner silicon sensors are manufactured by grinding their standard thick (320μm) silicon down to 200 to 240 μm as a trade off of the increasing dark current. The final design of the silicon thickness will be optimized based on the signal to noise ratio performance.

D.10.0.3 Mesh pattern ground and bias layers of HDI.

Two types of prototype HDI are under production and to be compared their noise shielding performance. An electromagnetic field simulation is to be also executed and verify the actual observation.

D.10.0.4 Long multilayer bus extender

The length of the bus extender cable of FVTX is less than 30cm. As far as we investigated within the Japanese industrial market, the length of the multilayer flexible cable is only available up to around 40 cm, while required length is approximately 1.2 meter. As discussed in subsection D.5, we established collaborative R&D contract between Tokyo Metropolitan Industrial Technology Research Institute and REPIC Co and will develop the technology within 1.5 year. In the case of unsuccessful result, the back-up solutions are 1) concatenate multiple multilayer bus extender up to 1.2 meter, 2) use single layer cable using cable adapters in both HDI and ROC board ends. The latter two has to overcome the following additional difficulties, i.e. additional connector joint can introduce new worry of unstable connection over the course of time, and spacial constraint to accommodate the cable adapter, especially in HDI side.

D.11 R&D

The first prototype INTT modules have been assembled successfully at BNL with the silicon sensors and HDI sent from Japan. The thickness of the silicon sensors used for the prototype modules are 240 and 320 μm. Figure D.18 shows the prototype module with 320 μm-thick silicon sensors. HDIs are connected one either side of the silicon sensors and 10 FPHX chips are mounted on each HDI. The silicon sensors are mechanically separated at the middle and the FPHX chips are wire-bonded to the sensors.

Tests of the prototype modules have been made with calibration pulses and the test result for a single FPHX chip on the HDI is shown in Fig. D.19. A clear correlation between calibration pulse amplitude and ADC values can be seen and all 128 channels on the chip look working correctly. Further tests with prototype modules are scheduled using cosmic rays and an available beta source.

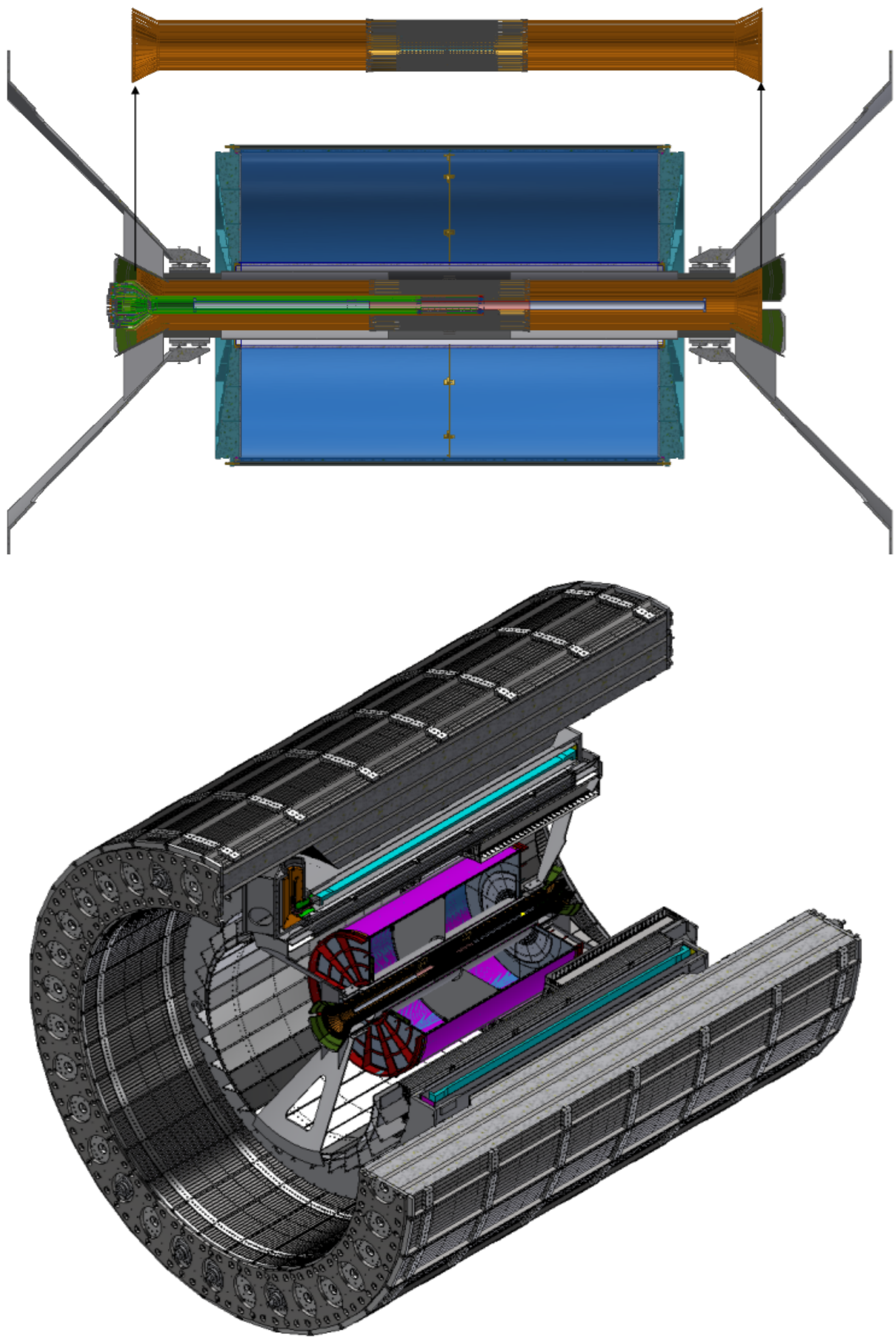

Figure D.16: Auto-Cad drawing of of extender cables and cooling in INTT mechanical structure in sPHENIX.

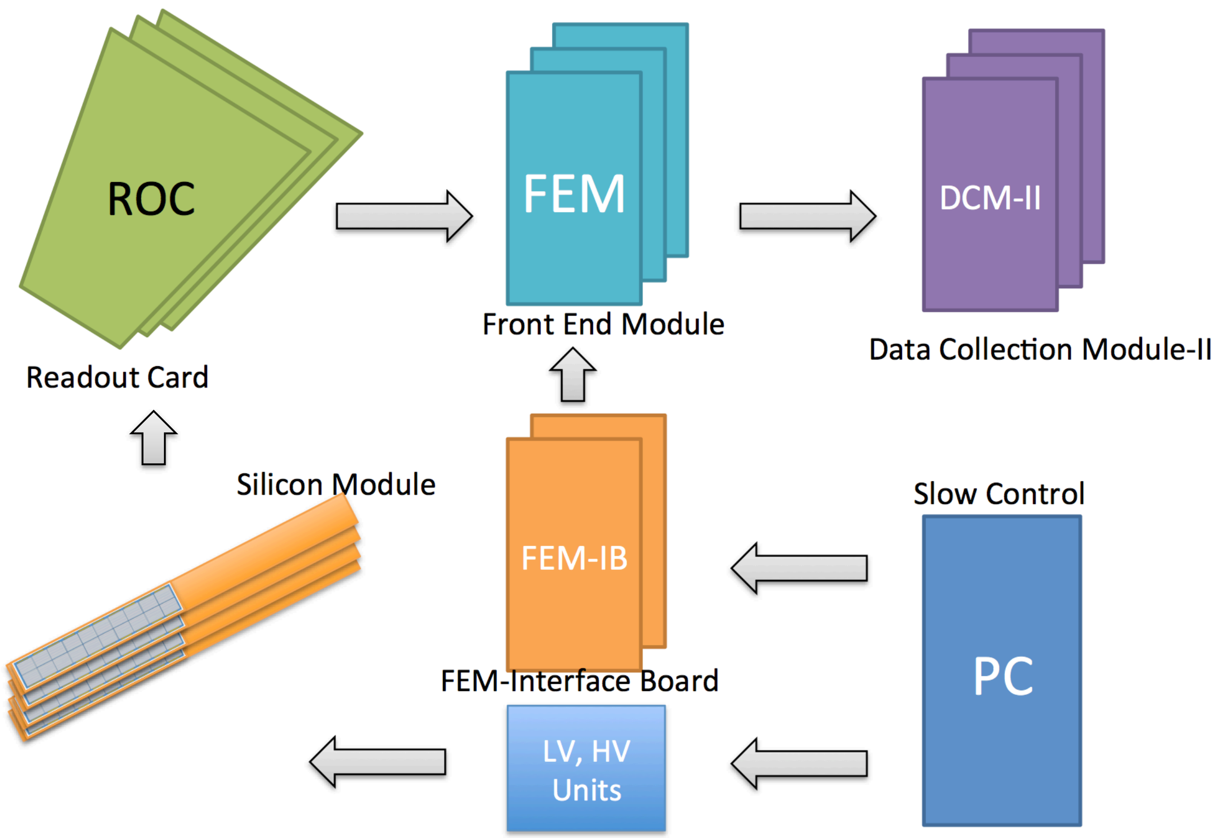

Figure D.17: Readout electronics chain for INTT. Any electronics downstream of ROC boards are re-use of resources from FVTX.

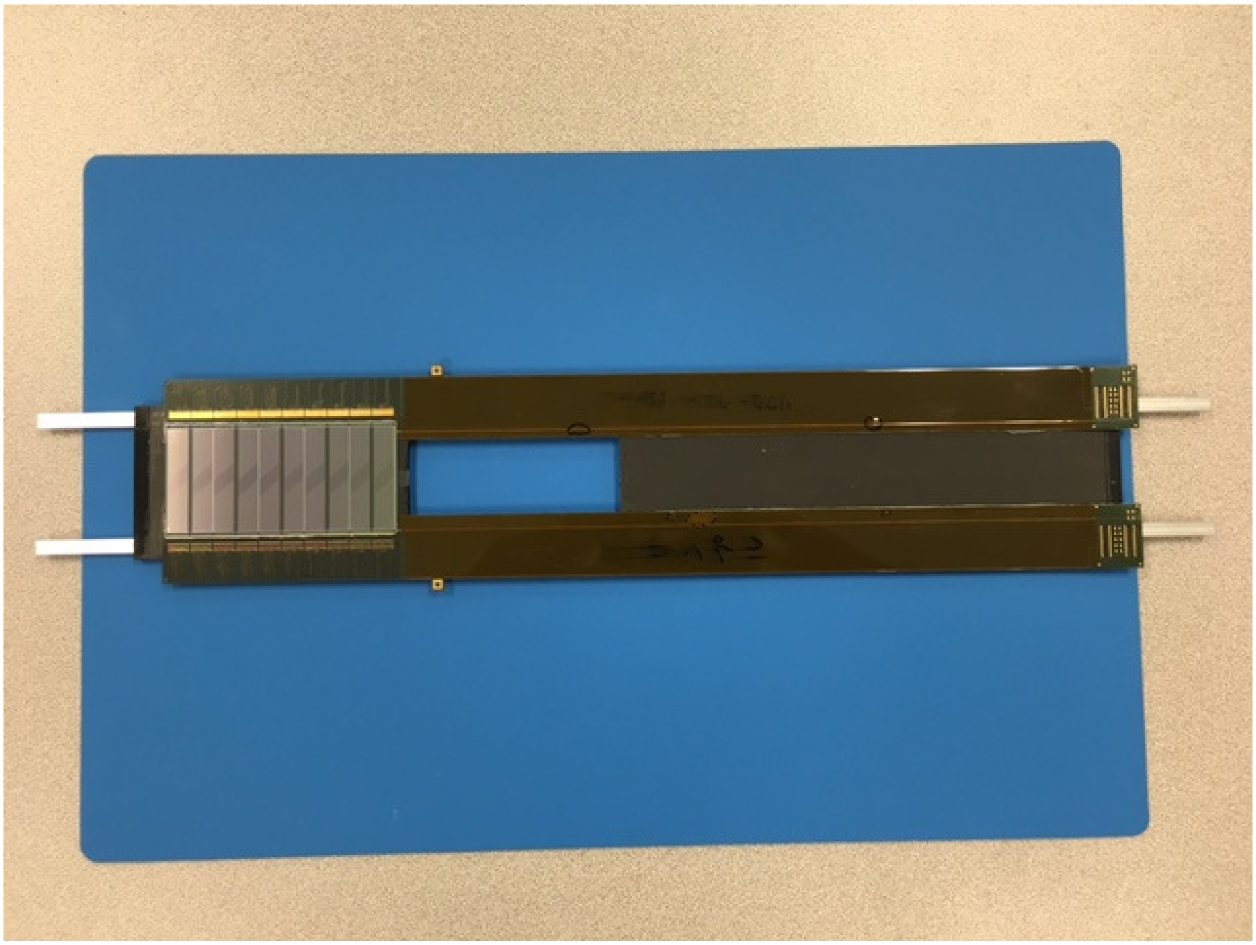

Figure D.18: The prototype module with 320 μm-thick silicon sensors.

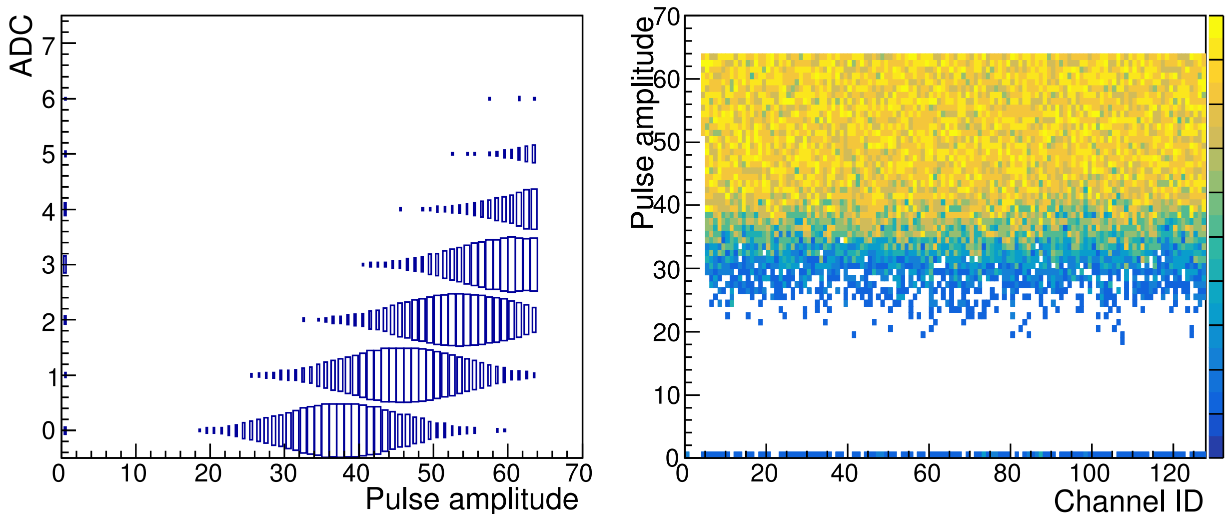

Figure D.19: The correlation between calibration pulse amplitude and ADC values (Left) and responses with the calibration pulses for all channels on the chip (Right).

List of Tables

List of Figures

Bibliography

[1] A. Adare et al. An Upgrade Proposal from the PHENIX Collaboration. 2014. arXiv:1501.06197. (document), 1, 1.8, 2.3, 8.1

[2] A. Adare et al. Enhanced production of direct photons in Au+Au collisions at $\sqrt{s_{NN}} = 200\,\text{GeV}$ and implications for the initial temperature. *Phys. Rev. Lett.*, 104:132301, 2010. arXiv:0804.4168, doi:10.1103/PhysRevLett.104.132301. 1

[3] M. Luzum and P. Romatschke. Viscous hydrodynamic predictions for nuclear collisions at the LHC. *Phys. Rev. Lett.*, 103:262302, 2009. arXiv:0901.4588, doi:10.1103/PhysRevLett.103.262302. 1

[4] K. Adcox et al. Formation of dense partonic matter in relativistic nucleus-nucleus collisions at RHIC: Experimental evaluation by the PHENIX collaboration. *Nucl. Phys.*, A757:184–283, 2005. arXiv:nucl-ex/0410003, doi:10.1016/j.nuclphysa.2005.03.086. 1.1

[5] Matthew Luzum and Paul Romatschke. Conformal Relativistic Viscous Hydrodynamics: Applications to RHIC results at s(NN)**(1/2) = 200-GeV. *Phys. Rev.*, C78:034915, 2008. [Erratum: Phys. Rev.C79,039903(2009)]. arXiv:0804.4015, doi:10.1103/PhysRevC.78.034915,10.1103/PhysRevC.79.039903. 1.1

[6] P. Danielewicz and M. Gyulassy. Dissipative phenomena in quark gluon plasmas. *Phys. Rev.*, D31:53–62, 1985. doi:10.1103/PhysRevD.31.53. 1.1

[7] P. Kovtun, Dan T. Son, and Andrei O. Starinets. Viscosity in strongly interacting quantum field theories from black hole physics. *Phys. Rev. Lett.*, 94:111601, 2005. arXiv:hep-th/0405231, doi:10.1103/PhysRevLett.94.111601. 1.1, 1.3.1

[8] H. Song and U. W. Heinz. Causal viscous hydrodynamics in 2+1 dimensions for relativistic heavy-ion collisions. *Phys. Rev.*, C77:064901, 2008. arXiv:0712.3715, doi:10.1103/PhysRevC.77.064901. 1.1

[9] B. Alver, C. Gombeaud, M. Luzum, and J.-Y. Ollitrault. Triangular flow in hydrodynamics and transport theory. *Phys. Rev.*, C82:034913, 2010. arXiv:1007.5469, doi:10.1103/PhysRevC.82.034913. 1.1

[10] D. A. Teaney. Viscous Hydrodynamics and the Quark Gluon Plasma. 2009. arXiv:0905.2433. 1.1

[11] B. Schenke, S. Jeon, and C. Gale. Elliptic and triangular flows in 3 + 1D viscous hydrodynamics with fluctuating initial conditions. *J. Phys. G*, G38:124169, 2011. 1.1

[12] A. Adare et al. Measurements of Higher-Order Flow Harmonics in Au+Au Collisions at $\sqrt{s_{NN}} = 200$ GeV. *Phys. Rev. Lett.*, 107:252301, 2011. arXiv:1105.3928, doi:10.1103/PhysRevLett.107.252301. 1.1

[13] A. Adare et al. Energy Loss and Flow of Heavy Quarks in Au+Au Collisions at s(NN)**(1/2) = 200-GeV. *Phys. Rev. Lett.*, 98:172301, 2007. arXiv:nucl-ex/0611018, doi:10.1103/PhysRevLett.98.172301. 1.1

[14] G. Aad et al. Measurement of the Azimuthal Angle Dependence of Inclusive Jet Yields in Pb+Pb Collisions at $\sqrt{s_{NN}}$= 2.76 TeV with the ATLAS detector. 2013. arXiv:1306.6469. 1.1

[15] G. Aad et al. Measurement of the jet radius and transverse momentum dependence of inclusive jet suppression in lead-lead collisions at $\sqrt{s_{NN}} = 2.76$ TeV with the ATLAS detector. *Phys. Lett.*, B719:220–241, 2013. arXiv:1208.1967, doi:10.1016/j.physletb.2013.01.024. 1.1

[16] K. Rajagopal. International Quark Matter presentation (2011). URL: http://qm2011.in2p3.fr/node/12. 1.2

[17] J. Liao and E. Shuryak. Angular Dependence of Jet Quenching Indicates Its Strong Enhancement Near the QCD Phase Transition. *Phys. Rev. Lett.*, 102:202302, 2009. arXiv:0810.4116, doi:10.1103/PhysRevLett.102.202302. 1.2, 1.3.2

[18] C. E. Coleman-Smith, G.-Y. Qin, S. A. Bass, and B. Muller. Jet modification in a brick of QGP matter. 2011. arXiv:1108.5662. 1.2, 1.6.1, 1.7

[19] C. E. Coleman-Smith, S. A. Bass, and D. K. Srivastava. Implementing the LPM effect in a parton cascade model. *Nucl. Phys.*, A862-863:275–278, 2011. arXiv:1101.4895, doi:10.1016/j.nuclphysa.2011.05.071. 1.2, 1.6, 1.6.1

[20] Laszlo P. Csernai, Joseph.I. Kapusta, and Larry D. McLerran. On the Strongly-Interacting Low-Viscosity Matter Created in Relativistic Nuclear Collisions. *Phys. Rev. Lett.*, 97:152303, 2006. arXiv:nucl-th/0604032, doi:10.1103/PhysRevLett.97.152303. 1.3.1

[21] P. B. Arnold, G. D. Moore, and L. G. Yaffe. Transport coefficients in high temperature gauge theories. 2. Beyond leading log. *JHEP*, 0305:051, 2003. arXiv:hep-ph/0302165. 1.3.1

[22] Charles Gale, Sangyong Jeon, Bjorn Schenke, Prithwish Tribedy, and Raju Venugopalan. Event-by-event anisotropic flow in heavy-ion collisions from combined Yang-Mills and viscous fluid dynamics. *Phys. Rev. Lett.*, 110:012302, 2013. arXiv:1209.6330, doi:10.1103/PhysRevLett.110.012302. 1.3.1

[23] H. Song, S. A. Bass, and U. Heinz. Elliptic flow in 200 A GeV Au+Au collisions and 2.76 A TeV Pb+Pb collisions: insights from viscous hydrodynamics + hadron cascade hybrid model. *Phys. Rev.*, C83:054912, 2011. arXiv:1103.2380, doi:10.1103/PhysRevC.83.054912. 1.3.1

[24] J. L. Nagle, I. G. Bearden, and W. A. Zajc. Quark-gluon plasma at RHIC and the LHC: perfect fluid too perfect? *New J. Phys.*, 13:075004, 2011. arXiv:1102.0680, doi:10.1088/1367-2630/13/7/075004. 1.3.1

[25] H. Niemi, G. S. Denicol, P. Huovinen, E. Molnar, and D. H. Rischke. Influence of the shear viscosity of the quark-gluon plasma on elliptic flow in ultrarelativistic heavy-ion collisions. *Phys. Rev. Lett.*, 106:212302, 2011. arXiv:1101.2442, doi:10.1103/PhysRevLett.106.212302. 1.3.1

[26] S. Chatrchyan et al. Study of high-pT charged particle suppression in PbPb compared to pp collisions at $\sqrt{s_{NN}} = 2.76$ TeV. *Eur. Phys. J.*, C72:1945, 2012. arXiv:1202.2554, doi:10.1140/epjc/s10052-012-1945-x. 1.3.2, 1.6

[27] C. N. Bo et al. Extracting jet transport coefficients from jet quenching at RHIC and the LHC. 2013. URL: https://sites.google.com/a/lbl.gov/jetwiki/documents-1/report-on-status-of-qhat. 1.3.2, 1.5, D.11

[28] Jiechen Xu, Jinfeng Liao, and Miklos Gyulassy. Anisotripic Jet Quenching in semi-Quark-Gluon Plasmas with Magnetic Monopoles in Ultrarelativistic Heavy Ion Collisions. 2014. arXiv:1411.3673. 1.5, 1.3.2, D.11

[29] Thorsten Renk. On the sensitivity of jet quenching to near T_C enhancement of the medium opacity. *Phys. Rev.*, C89:067901, 2014. arXiv:1402.5798, doi:10.1103/PhysRevC.89.067901. 1.3.2

[30] W. A. Horowitz and M. Gyulassy. The Surprising Transparency of the sQGP at LHC. *Nucl. Phys.*, A872:265–285, 2011. arXiv:1104.4958. 1.3.2

[31] K. Aamodt and C. A. Loizides. Suppression of charged particle production at large transverse momentum in central Pb–Pb collisions at $\sqrt{s_{NN}} = 2.76$ TeV. *Phys. Lett.*, B696:30–39, 2011. arXiv:1012.1004. 1.3.2

[32] X.-F. Chen, T. Hirano, E. Wang, X.-N. Wang, and H. Zhang. Suppression of high p_T hadrons in $Pb + Pb$ Collisions at LHC. *Phys. Rev.*, C84:034902, 2011. arXiv:1102.5614, doi:10.1103/PhysRevC.84.034902. 1.3.2

[33] B. G. Zakharov. Variation of jet quenching from RHIC to LHC and thermal suppression of QCD coupling constant. *JETP Lett.*, 93:683–687, 2011. `arXiv:1105.2028`, `doi:10.1134/S0021364011120162`. 1.3.2

[34] A. Buzzatti and M. Gyulassy. Jet Flavor Tomography of Quark Gluon Plasmas at RHIC and LHC. *Phys. Rev. Lett.*, 108:022301, 2012. 4 pages, 3 eps figures. `arXiv:1106.3061`, `doi:10.1103/PhysRevLett.108.022301`. 1.3.2

[35] A. Buzzatti and M. Gyulassy. A running coupling explanation of the surprising transparency of the QGP at LHC. *Nucl. Phys.A904-905*, 2013:779c–782c, 2013. `arXiv:1210.6417`, `doi:10.1016/j.nuclphysa.2013.02.133`. 1.3.2

[36] A. Adare et al. Evolution of π^0 suppression in Au+Au collisions from $\sqrt{s_{NN}}$ = 39 to 200 GeV. *Phys. Rev. Lett.*, 109:152301, 2012. `arXiv:1204.1526`, `doi:10.1103/PhysRevLett.109.152301`. 1.3.2

[37] Alexander Schmah. The beam energy scan at RHIC: Recent results from STAR. *J. Phys. Conf. Ser.*, 426:012007, 2013. `doi:10.1088/1742-6596/426/1/012007`. 1.3.2

[38] B. Muller. Parton energy loss in strongly coupled AdS/CFT. *Nucl. Phys.*, A855:74–82, 2011. `arXiv:1010.4258`, `doi:10.1016/j.nuclphysa.2011.02.022`. 1.4

[39] Thorsten Renk. Physics probed by the P_T dependence of the nuclear suppression factor. *Phys. Rev.*, C88(1):014905, 2013. `arXiv:1302.3710`, `doi:10.1103/PhysRevC.88.014905`. 1.4

[40] A. Majumder and C. Shen. Suppression of the High p_T Charged Hadron R_{AA} at the LHC. *Phys. Rev. Lett.*, 109:202301, 2012OA. `arXiv:1103.0809`, `doi:10.1103/PhysRevLett.109.202301`. 1.4

[41] A. Majumder and J. Putschke. Mass depletion: a new parameter for quantitative jet modification. 2014. `arXiv:1408.3403`. 1.4

[42] Korinna C. Zapp. JEWEL 2.0.0: directions for use. *Eur. Phys. J.*, C74:2762, 2014. `arXiv:1311.0048`, `doi:10.1140/epjc/s10052-014-2762-1`. 1.4

[43] A. Adare et al. Quantitative Constraints on the Opacity of Hot Partonic Matter from Semi-Inclusive Single High Transverse Momentum Pion Suppression in Au+Au collisions at s(NN)**(1/2) = 200-GeV. *Phys. Rev.*, C77:064907, 2008. `arXiv:0801.1665`, `doi:10.1103/PhysRevC.77.064907`. 1.4

[44] Steffen A. Bass, Charles Gale, Abhijit Majumder, Chiho Nonaka, Guang-You Qin, Thorsten Renk, and Jorg Ruppert. Systematic Comparison of Jet Energy-Loss Schemes in a realistic hydrodynamic medium. *Phys. Rev.*, C79:024901, 2009. `arXiv:0808.0908`, `doi:10.1103/PhysRevC.79.024901`. 1.4

[45] K. Adcox et al. Suppression of hadrons with large transverse momentum in central Au+Au collisions at $\sqrt{s_{NN}}$ = 130-GeV. *Phys. Rev. Lett.*, 88:022301, 2002. arXiv:nucl-ex/0109003, doi:10.1103/PhysRevLett.88.022301. 1.5

[46] C. Adler et al. Centrality dependence of high p_T hadron suppression in Au+Au collisions at $\sqrt{s_{NN}} = 130\,\text{GeV}$. *Phys. Rev. Lett.*, 89:202301, 2002. arXiv:nucl-ex/0206011. 1.5

[47] A. Adare et al. Trends in Yield and Azimuthal Shape Modification in Dihadron Correlations in Relativistic Heavy Ion Collisions. *Phys. Rev. Lett.*, 104:252301, 2010. arXiv:1002.1077, doi:10.1103/PhysRevLett.104.252301. 1.5

[48] A. Adare et al. Suppression of away-side jet fragments with respect to the reaction plane in Au+Au collisions at $\sqrt{s_{NN}} = 200$ GeV. *Phys. Rev.*, C84:024904, 2011. arXiv:1010.1521, doi:10.1103/PhysRevC.84.024904. 1.5

[49] J. Adams et al. Distributions of charged hadrons associated with high transverse momentum particles in $p+p$ and Au+Au collisions at $\sqrt{s_{NN}} = 200\,\text{GeV}$. *Phys. Rev. Lett.*, 95:152301, 2005. arXiv:nucl-ex/0501016. 1.5

[50] J. L. Nagle. Ridge, bulk, and medium response: how to kill models and learn something in the process. *Nucl. Phys.*, A830:147C–154C, 2009. arXiv:0907.2707. 1.5

[51] G. Aad et al. Observation of a centrality-dependent dijet asymmetry in lead-lead collisions at $\sqrt{s_{NN}} = 2.76\,\text{TeV}$ with the ATLAS detector at the LHC. *Phys. Rev. Lett.*, 105:252303, 2010. Accepted for publication at Physical Review Letters. arXiv:1011.6182, doi:10.1103/PhysRevLett.105.252303. 1.5.1

[52] S. Chatrchyan et al. Observation and studies of jet quenching in PbPb collisions at nucleon-nucleon center-of-mass energy = 2.76 TeV. *Phys. Rev.*, C84:024906, 2011. arXiv:1102.1957, doi:10.1103/PhysRevC.84.024906. 1.5.1, 1.6.1

[53] X.-N. Wang, Z. Huang, and I. Sarcevic. Jet quenching in the opposite direction of a tagged photon in high-energy heavy ion collisions. *Phys. Rev. Lett.*, 77:231–234, 1996. arXiv:hep-ph/9605213, doi:10.1103/PhysRevLett.77.231. 1.5.1, 1.7.1

[54] S. Chatrchyan et al. Studies of jet quenching using isolated-photon+jet correlations in PbPb and pp collisions at $\sqrt{s_{NN}} = 2.76$ TeV. 2012. Submitted to Physics Letters B. arXiv:1205.0206. 1.5.1

[55] S. Chatrchyan et al. Jet momentum dependence of jet quenching in PbPb collisions at $\sqrt{s_{NN}} = 2.76$ TeV. 2012. arXiv:1202.5022. 1.5.1

[56] P. Steinberg. Recent Heavy Ion Results with the ATLAS Detector at the LHC. 2011. arXiv:1110.3352. 1.5.1

[57] H. Caines. Jets and jet-like Correlations at RHIC. 2011. arXiv:1110.1878. 1.5.2

[58] J. Putschke. STAR: Jet reconstruction, direct gamma and multi-hadron correlations: Hard probes of the initial and final state. *Nucl. Phys.*, A855:83–91, 2011. 1.5.2

[59] J. Putschke. First fragmentation function measurements from full jet reconstruction in heavy-ion collisions at $\sqrt{s_{NN}} = 200\,\text{GeV}$ by STAR. *Eur. Phys. J.*, C61:629–635, 2009. `arXiv:0809.1419`. 1.5.2

[60] P. M. Jacobs. Background fluctuations in heavy ion jet reconstruction. 2010. `arXiv:1012.2406`. 1.5.2

[61] Y.-S. Lai. Direct jet reconstruction in p+p and Cu+Cu collisions at PHENIX. *Nucl. Phys.*, A855:295–298, 2011. 1.5.2

[62] Y.-S. Lai. Probing medium-induced energy loss with direct jet reconstruction in p+p and Cu+Cu collisions at PHENIX. *Nucl. Phys.*, A830:251C–254C, 2009. `arXiv:0907.4725`. 1.5.2

[63] JET Topical Collaboration. URL: `http://jet.lbl.gov`. 1.6

[64] K. C. Zapp, J. Stachel, and U. Wiedemann. LPM-effect in Monte Carlo models of radiative energy loss. *Nucl. Phys.*, A830:171C–174C, 2009. `arXiv:0907.4304`. 1.6

[65] T. Renk. YaJEM: a Monte Carlo code for in-medium shower evolution. *Int. J. Mod. Phys.*, E20:1594–1599, 2011. `arXiv:1009.3740`, `doi:10.1142/S0218301311019933`. 1.6

[66] C. Young, S. Jeon, C. Gale, and B. Schenke. Monte-Carlo simulation of jets in heavy-ion collisions. 2011. `arXiv:1109.5992`. 1.6, 1.6.1

[67] I. P. Lokhtin, A. V. Belyaev, and A. M. Snigirev. Jet quenching pattern at LHC in PYQUEN model. *Eur. Phys. J.*, C71:1650, 2011. `arXiv:1103.1853`, `doi:10.1140/epjc/s10052-011-1650-1`. 1.6

[68] N. Armesto, L. Cunqueiro, and C. A. Salgado. Monte Carlo for jet showers in the medium. *Nucl. Phys.*, A830:271C–274C, 2009. `arXiv:0907.4706`. 1.6

[69] J. Casalderrey-Solana, J. G. Milhano, and U. Wiedemann. Jet quenching via jet collimation. *J. Phys. G*, G38:124086, 2011. `arXiv:1107.1964`. 1.6

[70] T. Renk. Energy dependence of the dijet imbalance in Pb-Pb collisions at 2.76 ATeV. 2012. `arXiv:1204.5572`. 1.6

[71] T. Renk. Jets in medium: What RHIC and LHC measurements of R_{AA} and I_{AA} can teach about the parton-medium interaction. 2011. `arXiv:1111.0769`. 1.6

[72] T. Renk. Biased Showers — a common conceptual framework for the interpretation of High p_T observables in heavy-ion collisions. 2012. `arXiv:1212.0646`. 1.6

[73] K. Geiger and B. Muller. Dynamics of parton cascades in highly relativistic nuclear collisions. *Nucl. Phys.*, B369:600–654, 1992. doi:10.1016/0550-3213(92)90280-O. 1.6.1

[74] C. Wesp, A. El, F. Reining, Z. Xu, I. Bouras, et al. Calculation of shear viscosity using Green-Kubo relations within a parton cascade. *Phys. Rev.*, C84:054911, 2011. arXiv:1106.4306, doi:10.1103/PhysRevC.84.054911. 1.6.1

[75] C. E Coleman-Smith and B. Muller. What can we learn from Dijet suppression at RHIC? 2012. arXiv:1205.6781. 1.7

[76] G.-Y. Qin and B. Muller. Explanation of Di-jet asymmetry in Pb+Pb collisions at the Large Hadron Collider. *Phys. Rev. Lett.*, 106:162302, 2011. 4 pages, 3 figures, made corrections for numerical inaccuracies, qualitative conclusions unaffected. arXiv:1012.5280, doi:10.1103/PhysRevLett.106.162302. 1.6.1

[77] G.-Y. Qin and B. Muller. private communication. 1.6.1, 1.8

[78] B. Schenke, C. Gale, and S. Jeon. MARTINI: Monte Carlo simulation of jet evolution. *Acta Phys. Polon. Supp.*, 3:765–770, 2010. arXiv:0911.4470. 1.6.1

[79] B. Schenke, S. Jeon, and C. Gale. (3+1)D hydrodynamic simulation of relativistic heavy-ion collisions. *Phys. Rev.*, C82:014903, 2010. arXiv:1004.1408, doi:10.1103/PhysRevC.82.014903. 1.6.1

[80] C. Young, B. Schenke, S. Jeon, and C. Gale. Dijet asymmetry at the energies available at the CERN Large Hadron Collider. *Phys. Rev.*, C84:024907, 2011. arXiv:1103.5769, doi:10.1103/PhysRevC.84.024907. 1.6.1

[81] C. Young and B. Schenke. private communication. 1.8

[82] Y. He, I. Vitev, and B.-W. Zhang. Next-to-leading order analysis of inclusive jet and di-jet production in heavy ion reactions at the Large Hadron Collider. 2011. arXiv:1105.2566. 1.6.2

[83] R. B. Neufeld and I. Vitev. Parton showers as sources of energy-momentum deposition in the QGP and their implication for shockwave formation at RHIC and at the LHC. 2011. 8 pages, 4 figures. arXiv:1105.2067. 1.6.2

[84] I. Vitev and B.-W. Zhang. Jet tomography of high-energy nucleus-nucleus collisions at next-to-leading order. *Phys. Rev. Lett.*, 104:132001, 2010. arXiv:0910.1090, doi:10.1103/PhysRevLett.104.132001. 1.6.2

[85] Wei Dai, Ivan Vitev, and Ben-Wei Zhang. Momentum imbalance of isolated photon-tagged jet production at RHIC and LHC. *Phys. Rev. Lett.*, 110:142001, 2013. arXiv:1207.5177, doi:10.1103/PhysRevLett.110.142001. 1.7.1, 1.10, D.11

[86] L. Adamczyk et al. Jet-Hadron Correlations in $\sqrt{s_{NN}} = 200$ GeV $p + p$ and Central $Au + Au$ Collisions. *Phys. Rev. Lett.*, 112(12):122301, 2014. `arXiv:1302.6184`, `doi:10.1103/PhysRevLett.112.122301`. 1.7.2

[87] W. Horowitz and M. Gyulassy. Heavy quark jet tomography of Pb+Pb at LHC: AdS/CFT drag or pQCD energy loss? *Phys. Lett.*, B666:320–323, 2008. `arXiv:0706.2336`, `doi:10.1016/j.physletb.2008.04.065`. 1.8

[88] Y. Dokshitzer and D. Kharzeev. Heavy quark colorimetry of QCD matter. *Phys. Lett.*, B519:199–206, 2001. `arXiv:hep-ph/0106202`, `doi:10.1016/S0370-2693(01)01130-3`. 1.8

[89] M. Cacciari. private communication. 1.8, 1.13

[90] Jiechen Xu, Alessandro Buzzatti, and Miklos Gyulassy. Azimuthal jet flavor tomography with CUJET2.0 of nuclear collisions at RHIC and LHC. *JHEP*, 1408:063, 2014. `arXiv:1402.2956`, `doi:10.1007/JHEP08(2014)063`. 1.8, 1.14

[91] V. Abazov et al. The upgraded D0 detector. *Nucl. Instrum. Meth.*, A565:463–537, 2006. `arXiv:physics/0507191`, `doi:10.1016/j.nima.2006.05.248`. 1.8

[92] V. Abazov et al. b-Jet Identification in the D0 Experiment. *Nucl. Instrum. Meth.*, A620:490, 2010. `arXiv:1002.4224`, `doi:doi:10.1016/j.nima.2010.03.118`. 1.8

[93] Jinrui Huang, Zhong-Bo Kang, and Ivan Vitev. Inclusive b-jet production in heavy ion collisions at the LHC. *Phys. Lett.*, B726:251–256, 2013. `arXiv:1306.0909`, `doi:10.1016/j.physletb.2013.08.009`. 1.8

[94] X. Zhao and R. Rapp. Medium Modifications and Production of Charmonia at LHC. *Nucl. Phys.*, A859:114–125, 2011. 7 pages, 9 eps figures. `arXiv:1102.2194`, `doi:10.1016/j.nuclphysa.2011.05.001`. 1.9

[95] Roberta Arnaldi. J/psi production in p-A and A-A collisions at fixed target experiments. *Nucl. Phys.*, A830:345C–352C, 2009. `arXiv:0907.5004`, `doi:10.1016/j.nuclphysa.2009.10.030`. 1.9

[96] N. Brambilla, S. Eidelman, B. K. Heltsley, R. Vogt, G. T. Bodwin, et al. Heavy quarkonium: progress, puzzles, and opportunities. 2010. `arXiv:arXiv:1010.5827`. 1.9, 1.9.1, 1.9.2

[97] B. Abelev et al. J/ψ production at low transverse momentum in Pb-Pb collisions at $\sqrt{s_{NN}} = 2.76$ TeV. 2012. `arXiv:1202.1383`. 1.9

[98] Serguei Chatrchyan et al. Observation of sequential Upsilon suppression in PbPb collisions. *Phys. Rev. Lett.*, 109:222301, 2012. `arXiv:1208.2826`, `doi:10.1103/PhysRevLett.109.222301`. 1.9.1

[99] Betty Bezverkhny Abelev et al. Suppression of Υ(1S) at forward rapidity in Pb-Pb collisions at $\sqrt{s_{\rm NN}}$ = 2.76 TeV. 2014. arXiv:1405.4493. 1.9.1

[100] Betty Bezverkhny Abelev et al. Production of inclusive Υ(1S) and Υ(2S) in p-Pb collisions at $\sqrt{\mathbf{s}_{\rm NN}} = \mathbf{5.02}$ TeV. 2014. arXiv:1410.2234. 1.9.1

[101] A. Adare et al. Measurement of Υ(1S+2S+3S) production in p+p and Au+Au collisions at $\sqrt{s_{_{NN}}} = 200$ GeV. 2014. arXiv:1404.2246. 1.9.1

[102] L. Adamczyk et al. Suppression of Upsilon Production in d+Au and Au+Au Collisions at $\sqrt{s_{NN}}$ = 200 GeV. *Phys. Lett.*, B735:127, 2014. arXiv:1312.3675, doi:10.1016/j.physletb.2014.06.028. 1.9.1

[103] B. Muller, J. Schukraft, and B. Wyslouch. First results from Pb+Pb collisions at the LHC. 2012. arXiv:1202.3233. 1.9.1

[104] M. Habich, J.L. Nagle, and P. Romatschke. Particle spectra and HBT radii for simulated central nuclear collisions of C+C, Al+Al, Cu+Cu, Au+Au, and Pb+Pb from Sqrt(s)=62.4-2760 GeV. 2014. arXiv:1409.0040. 1.9.1, 1.16

[105] A. Emerick, X. Zhao, and R. Rapp. Bottomonia in the quark-gluon plasma and their production at RHIC and LHC. 2011. arXiv:1111.6537. 1.9.1

[106] L. Ruan, G. Lin, Z. Xu, K. Asselta, H. F. Chen, et al. Perspectives of a midrapidity dimuon program at RHIC: a novel and compact muon telescope detector. *J. Phys. G*, G36:095001, 2009. arXiv:0904.3774, doi:10.1088/0954-3899/36/9/095001. 1.9.1

[107] K. Eskola, H. Paukkunen, and C. Salgado. EPS09: a new generation of NLO and LO nuclear parton distribution functions. *JHEP*, 04:065, 2009. arXiv:0902.4154, doi:10.1088/1126-6708/2009/04/065. 1.9.2

[108] F. Arleo, P.B. Gossiaux, T. Gousset, and J. Aichelin. Charmonium suppression in p-A collisions. *Phys. Rev.*, C61:054906, 2000. 1.9.2

[109] D.C. McGlinchey, A.D. Frawley, and R. Vogt. Impact parameter dependence of the nuclear modification of J/ψ production in d+Au collisions at $\sqrt{S_{NN}} = 200$ GeV. *Phys. Rev.*, C87(5):054910, 2013. 1.9.2

[110] F. Arleo and S. Peigne. Heavy-quarkonium suppression in p-A collisions from parton energy loss in cold QCD matter. *JHEP*, 03:122, 2013. 1.9.2

[111] Betty Abelev et al. Long-range angular correlations on the near and away side in p-Pb collisions at $\sqrt{s_{NN}} = 5.02$ TeV. *Phys. Lett.*, B719:29–41, 2013. 1.9.2

[112] Georges Aad et al. Measurement with the ATLAS detector of multi-particle azimuthal correlations in p+Pb collisions at $\sqrt{s_{NN}}$=5.02 TeV. *Phys. Lett.*, B725:60–78, 2013. 1.9.2

[113] Serguei Chatrchyan et al. Multiplicity and transverse momentum dependence of two- and four-particle correlations in pPb and PbPb collisions. *Phys. Lett.*, B724:213–240, 2013. 1.9.2

[114] A. Adare et al. Quadrupole Anisotropy in Dihadron Azimuthal Correlations in Central d+Au Collisions at $\sqrt{s_{NN}}$=200 GeV. *Phys. Rev. Lett.*, 111:212301, 2013. 1.9.2

[115] W. Fischer. RHIC Luminosity Upgrade Program. *Conf. Proc.*, C100523:TUXMH01, 2010. 1

[116] RHIC Beam Projections [online]. URL: `http://www.rhichome.bnl.gov/RHIC/Runs/RhicProjections.pdf`. 1, 8.1

[117] W. Vogelsang. private communication. 1.10.1, 1.19

[118] C. Marquet and T. Renk. Jet quenching in the strongly-interacting quark-gluon plasma. *Phys. Lett.*, B685:270–276, 2010. `arXiv:0908.0880`, `doi:10.1016/j.physletb.2010.01.076`. 1.10.2

[119] A. Adare et al. Azimuthal anisotropy of neutral pion production in Au+Au collisions at $\sqrt(s_N N)$ = 200 GeV: Path-length dependence of jet quenching and the role of initial geometry. *Phys. Rev. Lett.*, 105:142301, 2010. `arXiv:1006.3740`, `doi:10.1103/PhysRevLett.105.142301`. 1.10.2

[120] J. Casalderrey-Solana, Doga Can Gulhan, Jose Guilherme Milhano, Daniel Pablos, and Krishna Rajagopal. Jet quenching within a hybrid strong/weak coupling approach. *Nucl. Phys.*, A, 2014. `arXiv:1408.5616`. 1.10.2

[121] Jorge Casalderrey-Solana, Doga Can Gulhan, Guilherme, Daniel Pablos, and Krishna Rajagopal. A Hybrid Strong/Weak Coupling Approach to Jet Quenching. *JHEP*, 1410:19, 2014. `arXiv:1405.3864`, `doi:10.1007/JHEP10(2014)019`. 1.10.2

[122] S. Afanasiev et al. Measurement of Direct Photons in Au+Au Collisions at $\sqrt{s_{NN}} =$ 200 GeV. 2012. `arXiv:1205.5759`. 1.21

[123] A. Adare et al. Direct-Photon Production in $p + p$ Collisions at $\sqrt{s} = 200$ GeV at Midrapidity. 2012. `arXiv:1205.5533`. 1.21

[124] R. Fr?hwirth. Application of kalman filtering to track and vertex fitting. *Nuclear Instruments and Methods in Physics Research Section A: Accelerators, Spectrometers, Detectors and Associated Equipment*, 262(2):444 – 450, 1987. URL: `http://www.sciencedirect.com/science/article/pii/0168900287908874`, `doi:https://doi.org/10.1016/0168-9002(87)90887-4`. 3.4

[125] Johannes Rauch and Tobias Schl?ter. GENFIT - a Generic Track-Fitting Toolkit. *J. Phys. Conf. Ser.*, 608(1):012042, 2015. `arXiv:1410.3698`, `doi:10.1088/1742-6596/608/1/012042`. 3.4

[126] Wolfgang Waltenberger. RAVE: A detector-independent toolkit to reconstruct vertices. *IEEE Trans. Nucl. Sci.*, 58:434–444, 2011. doi:10.1109/TNS.2011.2119492. 3.4

[127] B. D. Leverington et al. Performance of the prototype module of the GlueX electromagnetic barrel calorimeter. *Nucl. Instrum. Meth.*, A596:327–337, 2008. doi:10.1016/j.nima.2008.08.137. 4.2.1

[128] S. A. Sedykh et al. Electromagnetic calorimeters for the BNL muon (g-2) experiment. *Nucl. Instrum. Meth.*, A455:346–360, 2000. doi:10.1016/S0168-9002(00)00576-3. 4.2.1

[129] T. Armstrong et al. The E864 lead-scintillating fiber hadronic calorimeter. *Nucl. Instrum. Meth.*, A406:227–258, 1998. doi:10.1016/S0168-9002(98)91984-2. 4.2.1

[130] R. D. Appuhn et al. The H1 lead / scintillating fiber calorimeter. *Nucl. Instrum. Meth.*, A386:397–408, 1997. doi:10.1016/S0168-9002(96)01171-0. 4.2.1

[131] D. W. Hertzog, P. T. Debevec, R. A. Eisenstein, M. A. Graham, S. A. Hughes, P. E. Reimer, and R. L. Tayloe. A HIGH RESOLUTION LEAD SCINTILLATING FIBER ELECTROMAGNETIC CALORIMETER. *Nucl. Instrum. Meth.*, A294:446–458, 1990. doi:10.1016/0168-9002(90)90285-E. 4.2.1

[132] O. D. Tsai et al. Development of a forward calorimeter system for the STAR experiment. *J. Phys. Conf. Ser.*, 587(1):012053, 2015. doi:10.1088/1742-6596/587/1/012053. 4.2.1, 4.3.1, 4.3.2, 4.4.1

[133] O.D. Tsai, L.E. Dunkelberger, C.A. Gagliardi, S. Heppelmann, H.Z. Huang, et al. Results of & on a new construction technique for W/ScFi Calorimeters. *J. Phys. Conf. Ser.*, 404:012023, 2012. doi:10.1088/1742-6596/404/1/012023. 4.2.1, 4.4.1

[134] R. McNabb, J. Blackburn, J. D. Crnkovic, D. W. Hertzog, B. Kiburg, et al. A Tungsten / Scintillating Fiber Electromagnetic Calorimeter Prototype for a High-Rate Muon g-2 Experiment. *Nucl. Instrum. Meth.*, A602:396–402, 2009. arXiv:0910.0818, doi:10.1016/j.nima.2009.01.007. 4.2.2

[135] S. Agostinelli et al. GEANT4: A Simulation toolkit. *Nucl. Instrum. Meth.*, A506:250–303, 2003. doi:10.1016/S0168-9002(03)01368-8. 4.3.1, 4.3.7, 5.3

[136] M. Hirschberg, R. Beckmann, U. Brandenburg, H. Brueckmann, and K. Wick. Precise measurement of Birks kB parameter in plastic scintillators. *IEEE Trans. Nucl. Sci.*, 39:511–514, 1992. doi:10.1109/23.159657. 4.3.1, 2

[137] Klaus Alexander Tadday. *Scintillation Light Detection and Application of Silicon Photomultipliers in Imaging Calorimetry and Positron Emission Tomography*. PhD thesis, Heidelberg U., 2011. URL: http://www.ub.uni-heidelberg.de/archiv/12959. 4.3.2

[138] C. A. Aidala et al. Design and Beam Test Results for the sPHENIX Electromagnetic and Hadronic Calorimeter Prototypes. *Submitted to: IEEE Trans. Nucl. Sci.*, 2017. `arXiv:1704.01461`. 4.3.2, 4.4.1, 4.4.1

[139] M. E. Connors et al. Test Results and Status of the sPHENIX Calorimeter System. *Submitted to: IEEE 2017 NSS/MIC Conf. Rec. Proc.*, 2017. 4.4.2

[140] A. Izmaylov, S. Aoki, J. Blocki, J. Brinson, A. Dabrowska, et al. Scintillator counters with WLS fiber/MPPC readout for the side muon range detector (SMRD)of the T2K experiment. *Nucl. Instrum. Meth.*, A623:382–384, 2010. `arXiv:0904.4545`, `doi:10.1016/j.nima.2010.03.009`. 5.2.1

[141] Inc. Saint-Gobain Ceramics & Plastics. Scintillating optical fibers. 5.2.1

[142] Kuraray Co. Ltd. Scintillation materials catalogue. 5.2.1

[143] *Geant4 Reference Physics Lists*, 2017 (accessed February 14, 2018). URL: `http://geant4.cern.ch/support/proc_mod_catalog/physics_lists/useCases.shtml`. 5.3

[144] J. B. Birks. Scintillations from Organic Crystals: Specific Fluorescence and Relative Response to Different Radiations. *Proc. Phys. Soc.*, A64:874–877, 1951. `doi:10.1088/0370-1298/64/10/303`. 2

[145] sPHENIX collaboration. sphenix software repository. `https://github.com/sPHENIX-Collaboration`, 2015. 5.3

[146] F. James and M. Roos. Minuit: A System for Function Minimization and Analysis of the Parameter Errors and Correlations. *Comput. Phys. Commun.*, 10:343–367, 1975. `doi:10.1016/0010-4655(75)90039-9`. 5.3

[147] W. Anderson et al. Design, Construction, Operation and Performance of a Hadron Blind Detector for the PHENIX Experiment. *Nucl. Instrum. Meth.*, A646:35, 2011. `arXiv:1103.4277`, `doi:10.1016/j.nima.2011.04.015`. 6.3

[148] T. Matsumura et al. Effects of radiation damage caused by proton irradiation on Multi-Pixel Photon Counters (MPPCs) . *Nucl. Instrum. Meth.*, pages 301–308, 2009. `doi:10.1016/j.nima.2009.02.022`. 6.6.1

[149] Y. Qiang et al. Radiation Hardness Test of SiPMs for the JLab Hall D Barrel Calorimeter. *Nucl. Instrum. Meth.*, pages 301–308, 2009. `doi:10.1016/j.nima.2012.10.015`. 6.6.1

[150] Y Musienko. Radiation Damage Studies of Silicon Photomultipliers for the CMS HCAL Phase 1 Upgrade. *New Developments in Photodetection Conference Presentation*, 2014. 6.6.1

[151] Y. Fisyak et al. Thermal neutron flux measurements in the STAR experiemental hall. *Nucl. Instrum. Meth.*, pages 68–72, 2014. `doi:10.1016/j.nima.2014.04.035`. 6.6.1

[152] M. Garcia-Valderas et al. The Effects of Proton Irradiation in CoolRunner-II^{TM} CPLD Technology. *Radiation and Its Effects on Components and Systems (RADECS), 2008 European Conference on*, pages 131–135, 2008. `doi:10.1109/RADECS.2008.5944064`. 6.6.1

[153] K. Ikematsu et al. A Start - timing detector for the collider experiment PHENIX at RHIC-BNL. *Nucl. Instrum. Meth.*, A411:238–248, 1998. `arXiv:physics/9802024`, `doi:10.1016/S0168-9002(98)00307-6`. 7.1

[154] M. Allen et al. PHENIX inner detectors. *Nucl. Instrum. Meth.*, A499:549–559, 2003. `doi:10.1016/S0168-9002(02)01956-3`. 7.1

[155] Stephen Scott Adler et al. PHENIX on-line systems. *Nucl. Instrum. Meth.*, A499:560–592, 2003. `doi:10.1016/S0168-9002(02)01957-5`. 8.2, 8.3.1.2

[156] Markus F. X. J. Oberhumer. oberhumer.com: LZO data compression library. http://www.oberhumer.com/opensource/lzo/, July 2002. 8.2.3

[157] J.S. Kapustinsky. Production and performance of the silicon sensor and custom readout electronics for the PHENIX FVTX tracker. *Nucl. Instrum. Meth.*, A617:546–548, 2010. `doi:10.1016/j.nima.2014.04.017`. D.1, D.4

[158] C. Aidala. The PHENIX Forward Silicon Vertex Detector. *Nucl. Instrum. Meth.*, A755:44–61, 2014. `doi:10.1016/j.nima.2014.04.017`. D.1, D.4